FWM in a gas-filled hollow core capillary

Olivia Zurita Miranda

Olivia Zurita Miranda. FWM in a gas-filled hollow core capillary. Optics / Photonic. Université Bourgogne Franche-Comté, 2022. English. NNT : 2022UBFCD012 . tel-03881377

THÈSE DE DOCTORAT DE L'ÉTABLISSEMENT UNIVERSITÉ
BOURGOGNE FRANCHE-COMTÉ
PRÉPARÉE À L'UNIVERSITÉ DE FRANCHE-COMTÉ
École doctorale n°37
Sciences Pour l'Ingénieur et Microtechniques
Doctorat d'Optique et Photonique
Par

Olivia Zurita Miranda

Mélange à quatre ondes dans un capillaire à cœur creux rempli de gaz.

FWM in a gas-filled hollow core capillary.

Thèse présentée et soutenue à Talence, le 25 Mars 2022 à 10:00 hrs.

Composition du Jury:

Frédéric Gérôme	**Chargé de recherche. Université de Limoges, (XLIM)**	***Rapporteur***
Philipe Balcou	**Directeur de recherche. Centre Lasers Intenses et Applications, (CELIA)**	***Rapporteur***
Amelle Zaïr	**Maître de conférences. King's College London**	***Examinatrice***
Camille Brès	**Professeure associée. École polytechnique fédérale de Lausanne.**	***Examinatrice***
Pierre Béjot	**Chargé de recherche. Université Bourgogne-Franche-Comté, (ICB)**	***Examinateur***
Maxime Jacquot	**Professeur. Université Bourgogne -Franche-Comté, (FEMTO-ST)**	***Examinateur***
Hervé Maillotte	**Directeur de recherche. Université Bourgogne-Franche-Comté, (FEMTO-ST)**	***Directeur de thèse***
Damien Bigourd	**Chargé de recherche. Laboratoire de l'Intégration du Matériau au Système, (IMS)**	***CoDirecteur de thèse***

école doctorale **sciences pour l'ingénieur et microtechniques**

Titre: Mélange à quatre ondes dans un capillaire à cœur creux rempli de gaz.

Mots-clés: Mélange à quatre ondes, Génération de fréquence, Capillaire à cœur creux, Optique non linéaire, Amplificateurs paramétriques optiques.

Résume : L'objectif de ce travail est de produire des impulsions infrarouges en utilisant des phénomènes non linéaires dits de mélange à quatre ondes générés dans un environnement gazeux. Le concept général repose sur le transfert de l'énergie d'une forte impulsion de pompe à deux impulsions plus faibles (le signal et le complémentaire). Le processus de transfert d'énergie ne se produit que lorsque les trois champs se déplacent à la même vitesse. Comme milieu de propagation, nous avons utilisé un capillaire rempli de gaz qui permet de modifier la dispersion de la fibre et la non-linéarité simplement en changeant la pression du gaz. L'accordabilité de l'impulsion de le complémentaire (infrarouge) est obtenue en ajustant le temps de recouvrement entre les champs. Nous avons obtenu une impulsion complémentaire à spectre accordable dans le proche infrarouge de 1,2 à 1,5 μm avec la potentialité d'atteindre la gamme de l'infrarouge moyen. Le complémentaire est généré le plus efficacement à 1,2 μm et possède une durée de 220 fs avec une énergie évaluée à quelques nJ. Dans la deuxième partie de ce manuscrit, nous nous intéressons à l'interaction spatiale non linéaire. Où, en considérant que les champs se propageant ont une distribution spatiale différente qui conduit à un couplage spatio-temporel. En conséquence, le signal et le complémentaire peuvent être générés dans diverses combinaisons de modes de fibre HE_{1n}. Une nouvelle approche numérique basée sur l'équation de propagation unidirectionnelle multimode des impulsions a été réalisée en collaboration avec le laboratoire ICB. Les simulations ont montré une oscillation longitudinale de la puissance et de l'intensité du laser le long de la fibre due à l'interaction entre les modes fondamentaux et les modes d'ordre supérieur. Dans cette condition, nous avons mis en évidence la génération et l'amplification de nouveaux modes à d'autres domaines spectraux permettant non seulement de comprendre le couplage spatio-temporel dans le HCC rempli de gaz mais aussi d'ouvrir la voie à de nouvelles perspectives comme la mise en forme assistée non linéaire du faisceau.Dans notre cas, nous observons également la génération et l'amplification de nouveaux modes dans un HCC. Ces études nous a permis non seulement de mettre en avant le couplage spatiotemporel dans le HCC rempli de gaz, mais également d'ouvrir de nouvelles perspectives sur le façonnage spatial de faisceau assisté par un mélange à quatre ondes multimodal.

Title : FWM in a gas-filled hollow core capillary.

Keywords: Four-wave mixing, Frequency generation, Hollow core fiber, Nonlinear optics, Optical parametric amplifier.

Summary: The objective of this work is to produce infrared pulses using non-linear phenomena known as four wave mixing generated in a gaseous environment. The general concept relies on to transfer the energy from a strong pump pulse to two weaker pulses (the signal and/or idler). The energy transfer process occurs only when the three fields travel at the same speed. As a propagation medium, we used a capillary filled with gas that allows to modify the dispersion of the fiber and the non-linearity just by changing the gas pressure. The tunability of the idler pulse (infrared) is obtained by adjusting the time overlapping between the fields. From the experiment, we get a near infrared tunable pulse of 1.2 to 1.5 µm with potentiality to reach the mid-infrared. The idler generated at 1.2 μm has a duration of 220 fs with an energy of few nJ. In the second part of this manuscript, we take an interest in non-linear spatial interaction. Where, by considering the propagating fields have a different spatial distribution that leads to a spatiotemporal coupling. As a result, the signal and the idler can be generated in various combinations of fiber HE_{1n} modes. A new numerical approach based on the multimode unidirectional pulse propagation equation was performed in collaboration with the ICB laboratory. We found a longitudinal oscillation of the power and the beam intensity along the fiber because of an interaction between the fundamental and the generated high order modes. In this condition, we highlighted the generation and amplification of new modes at another spectral ranges allowing not only to understand the spatio-temporal coupling in the gas filled HCC but also to open the way to new perspectives as nonlinear assisted beam shaping.

Université Bourgogne Franche-Comté
32, avenue de l'Observatoire
25000 Besançon, France

To my family and
to all those who have come my way in this project.

"Nothing rest; everything moves; everything vibrates"
The kybalion

Acknowledgements

I would first like to thank the Science and Technology Council of Mexico (Consejo Nacional de Ciencia y Tecnología, CONACYT) that has sponsored this research, and all the people there that helped me with all my academic and financial issues.

Second, I wish to thank my two supervisors, Damien Bigourd and Herve Maillote, for accepting me as a PhD student in Non-linear optics at the Femto-ST. Especially to Damien because he invites me to continue working together at the IMS Laboratory in Bordeaux. Damien, thank you very much for sharing your knowledge, always having a good style of work and for all your endless patience. I've learned many things from you. Also, thank you, Coralie for your assistance, ideas and solutions you always give us when I got lost. Thanks to the nonlinear optics team from Femto-St. Thank you to Thérèse Leblois for your assistance and for facilitating my leaving to Bordeaux. Vincent, thanks for being my first friend in France for listening to me and helping me. You're a boy who has a big heart. Xavier thanks for telling me about books and getting me to enjoy jazz music with a beer. Joseline thanks you so much for being with me in Besançon, for all your support and good advice, to motivate me to go on and never give up. I don't have any way to pay you for all your help. You're a beautiful girl in all senses of the word. Thanks Fernando for your friendship and company on the trip to Italy.

I am also grateful to the Laser team of the IMS laboratory for the warm welcome it has given me. Thank you for always coming to the lab to help me and provide feedback or suggestions. Thank you very much, Patrick, Jean Paul, Fréderic Daracq, and Fréderic Fauquet. I am grateful for the technical support provided by Fréderic Fauquet as part of my experimental research. Also, all Ph.D. students, Mingming, Adrian, Margeux, Quentin, Marine, Thomas, Jean-Batiste, Oussama, Marco, Florent, Nolwenn. Thank many trips and parties together. Also, thanks, the micro-electronics team, who welcomed me, Andres, Denis, Sebastian, Marie, Aude and Stefania. Thank you, guys, for all your support and spending time together, mojitos, pizzas and karaoke time which has always helped to relax. We discovered Bordeaux together, you will always be in my heart. The Brazilians, thank you for taking a Mexican on your team and invite me to the churrascos and to all the Portuguese you taught me *"muito obrigada".*

Andres, thanks you for your friendship and support, for motivating me to improve my French. You're a wonderful person who always brings good things to the people around you. The most recent group of friends; Alex, Mateo, Frédéricque and Rosa, thank you for calling me "Adelita" and accepting me as I am. Thank you for showing me a different lifestyle that helped me in my personal development. *Los amo princesos.*

Finally, I want to thank my big family for their support on this project. Gracias papá y mamá por apoyarme para poder cumplir esta meta, gracias por absolutamente todo sin ustedes no tendría nada, los amo mucho. Gracias Mike por tu infinito apoyo, por estar siempre conmigo en las buenas y malas, eres un gran hermano que amo con toda el alma.

Thanks to that girl I met on my way one day and she shared her enthusiasm for research and inspired me to keep going and go for more. If she hadn't met you, none of this would have happened. Gracias a Dios y al universo que conspiro para que todo esto sucediera.

Author expresses its gratitude to the Mexican National Council for Science and Technology (CONACYT) for financing this work through PhD fellowship CONACyT-GOB-Frances 2018, N° 710318.

List of publications

Conference contributions

O. Zurita Miranda, C. Fourcade-Dutin, P. Béjot, F. Fauquet, H. Maillotte, P. Mounaix, and D. Bigourd, *"Four-wave mixing process induced by a self-phase modulated pulse in a hollow core capillary,"* in OSA Advanced Photonics Congress 2021, OSA Technical Digest (Optical Society of America, 2021), paper NoTu3C.2.

C. Fourcade-Dutin, **O. Zurita Miranda**, P. Mounaix, and D. Bigourd, *"Toward Mid-Infrared Ultra-Short Pulse Generation in a Gas-Filled Hollow-Core Photonic Crystal fiber,"* in OSA Advanced Photonics Congress 2021, OSA Technical Digest (Optical Society of America, 2021), paper NoTu3C.5.

O. Zurita Miranda, C. Fourcade-Dutin, P. Béjot, F. Fauquet, J. Guillet, F. Darracq, P. Mounaix, H. Maillotte, and D. Bigourd, *"Tunable source of infrared pulses in gas-filled hollow core capillary,"* in Laser Congress 2020 (ASSL, LAC), OSA Technical Digest (Optical Society of America, 2020), paper JTh2A.22.

O. Zurita Miranda, C. Fourcade Dutin, P. Béjot, F. Fauquet, J. Guillet, F. Darracq, P. Mounaix, H. Maillotte, D. Bigourd, *"Optical parametric amplification in gas-filled hollow core capillary for the generation of tunable pulses in the infrared,"* 9TH EPS-QEOD EUROPHOTON, EPS, Prague, Czech Republic, Sep, (2020)

Journal articles

C. Fourcade-Dutin, **O. Zurita Miranda**, P. Mounaix, D Bigourd, *"Mid-Infrared Ultra-Short Pulse Generation in a Gas-Filled Hollow-Core Photonic Crystal Fiber Pumped by Two-Color Pulses,"* Fibers 9 (4), 21, (2021)

O. Zurita Miranda, C. Fourcade Dutin, F. Fauquet, F. Darracq, J. Guillet, P. Mounaix, H. Maillotte, D. Bigourd. *"Tunable ultra-fast infrared generation in a gas-filled hollow core capillary by a four-wave mixing process,"* JOSA B 39, 662-670, (2022).

O. Zurita Miranda, C. Fourcade-Dutin, P. Béjot, F. Fauquet, H. Maillotte, P. Mounaix, and D. Bigourd, *"Four-wave mixing process induced by a self-phase modulated pulse in a hollow core capillary,"* (in preparation).

List of abbreviations

CL: Coherence Length
CPA: Chirped Pulse Amplification
DFG: Different Frequency Generation
FROG: Frequency Resolved Optical Grating
fs: Femtosecond (10^{-15} second)
FMF: Few Multimode Fiber
FWHM: Full Width at Half Maximum
FWM: Four-Wave Mixing
GDM: Group Delay Mismatched
GNLSE: Generalized Nonlinear Schrödinger Equation
GRIN: Graded-Index
GRINMF: Graded-Index Multimode Fiber
GVD: Group Velocity Dispersion
HCC: Hollow Core Capillary
HOMs: High Order Modes
iFWM: Intermodal Four-Wave-Mixing
IR: Infrared
MM-UPPE: Multimode Unidirectional Pulse Propagation Equation
MMFs: Multimode Fibers
NLO: Nonlinear Optics
NLSE: Nonlinear Schrödinger Equation
OPA: Optical Parametric Amplification
OPCPA: Optical Parametric Chirped Pulse Amplification
PCF: Photonic Crystal Fiber
RDW: Resonant Dispersive Wave
SDM: Space Division Multiplexing
SFG: Sum Frequency Generation
SHG: Second Harmonic Generation
SPM: Self-Phase Modulation
SRS: Stimulates Raman Scattering
SSFM: Split-Step Fourier Method
SSI: Spatial Self Imaging
SVEA: Slowly Varying Envelope Approximation
THG: Third Harmonic Generation
TOD: Third Order Dispersion
UPPE: Pulse Propagation Equation
VUV: Vacuum Ultraviolet
XPM: Cross Phase Modulation
YAG: Yttrium Aluminum Garnet
ZDW: Zero Dispersion Wavelength

Abstract

This work is associated with the study of four-wave mixing (FWM) based on optical parametric amplification of broadband pulses in a gas-filled hollow-core capillary (HCC). Numerical and experimental investigations have been considered to achieve a tunable source generating ultra-short pulses in the near-infrared. The general principle relies on a four-wave mixing process achieved in a monoatomic gas that offers a degree of freedom with the pressure to control dispersion and the non-linearity in real time. In addition, the selection of different gases as a non-linear medium offers a wide range of light-matter interactions with different dynamics. Another advantage of HCC is to overcome the limitations of damage occurring in bulk materials and absorption in the infrared. The general goal is to transfer the energy from a strong pump pulse to two weaker pulses (the signal and/or idler) through a phase-matched FWM process. One important feature of this technique is the generation of the idler simultaneously at different wavelengths as respect to the injected signal spectrum; the accessible bandwidth is therefore enhanced. In order to add spectral tunability, the pump and the signal can be chirped, as the specific spectral components of both pulses temporally overlap. In addition, as the peak power is reduced by stretching the input pulses, the energy transfer can be improved without undesirable nonlinearities.

Numerical simulations have been performed to quantify the contribution of all parameters in the phase-matched FWM process. We begin to use an undepleted regime with a monochromatic pump wave to analytically describe the FWM. We highlight the importance of the sign of the fiber second order dispersion term to predict the signal and idler positions, and to evaluate the walk-off length related to the group velocity. In addition, an important point for ultra-fast amplifiers is its spectral bandwidth. Since the pump acquires a chirp during its propagation in the gas, the signal and idler sidebands are generated from the chirped pump pulse. Therefore, they will be temporally delayed inducing a spectro-temporal distribution.

The propagation of a chirped pump pulse and a chirped broadband signal in a gas-filled-HCC has been numerically studied by solving the generalized nonlinear Schrödinger equation with the split-step Fourier method, to accurately explore the chirp contribution. In this way, we found a combination of parameters which served to develop an experimental configuration with fundamental mode profiles. From the experiment, we get a near infrared tunable pulse of 1.2 to 1.5 μm with potentiality to reach the mid-infrared. The idler generated at 1.2 μm has a duration of 220 fs with an energy of few nJ.

In the second part of this manuscript, we focus on the nonlinear interaction between the fundamental and high order modes in the gas filled HCC. Because of the large core diameter, the HCC can handle ultra-short pulses with high power in a nonlinear medium supporting a multimode content. This leads to a spatiotemporal coupling due to spatial and temporal Kerr effects occurring during the pulse propagation. Thus, the analytical

solution of FWM was solved using various combinations of fiber HE_{1n} modes. The preliminary numerical results confirm the possibility to amplify or generate infrared pulses with a multimodal phase matching. The experimental implementation did not conclude that this effect is predominant, but instead, other original phenomena were observed and studied more deeply during experiments and numerical simulations.

A new numerical approach based on the multimode unidirectional pulse propagation equation was also performed in collaboration with the laboratory Interdisciplinaire Carnot de Bourgogne (ICB). We found a longitudinal oscillation of the power and the beam intensity along the fiber because of an interaction between the fundamental and the generated high order modes. As similar effect reported in GRIN fibers, a periodic modulation of the refractive index and intensity exists and leads to some local intense area and nonlinearities. In this condition, we highlighted the generation and amplification of new modes at another spectral ranges allowing not only to understand the spatio-temporal coupling in the gas filled HCC but also to open the way to new perspectives as nonlinear assisted beam shaping.

Résumé

Ce travail porte sur l'étude de l'amplification paramétrique optique d'impulsions à dérive de fréquence large bande dans un capillaire à cœur creux rempli de gaz (ou *Hollow Core Capillary*, HCC). Nous avons développé des codes de simulation et des expériences pour réaliser une source accordable à impulsions ultra-courtes dans l'infrarouge proche. Le principe général repose sur le mélange à quatre ondes (ou *Four-Wave Mixing*, FWM) généré dans un gaz monoatomique qui permet de contrôler en temps réel la dispersion et la non-linéarité en ajustant la pression. De plus, il est possible d'utiliser différents gaz afin d'obtenir une large variété d'interaction avec la lumière. Un autre avantage des HCC par rapport à des systèmes à base de matériaux massifs est d'augmenter le seuil de dommage et de limiter l'absorption dans l'infrarouge. L'objectif général est de transférer l'énergie d'une impulsion de pompe à forte puissance vers deux impulsions à puissance plus faible (le signal et le complémentaire) via un processus de mélange à quatre ondes. Une des caractéristiques importantes est que l'onde complémentaire soit générée simultanément au signal à différentes longueurs d'onde. La bande spectrale est ainsi élargie. Afin de modifier ou d'améliorer l'accordabilité spectrale, des dérives de fréquence peuvent être appliquées sur la pompe et le signal. Ainsi, un ensemble de composantes spectrales des deux impulsions se recouvrent temporellement. De plus, la puissance crête des impulsions d'entrée est diminuée pour éviter les dommages et les effets non linéaires indésirables.

Des simulations numériques ont été effectuées pour comprendre la contribution de tous les paramètres importants influençant la condition d'accord de phase du FWM. Nous avons également réalisé un code analytique, dans le cas d'une onde de pompe monochromatique en régime non saturé, pour décrire qualitativement le FWM et pour connaitre l'importance des paramètres comme le signe de la dispersion, la vitesse de groupe, la pression et la puissance.

Un autre point important pour développer les amplificateurs à impulsions ultra-courtes est sa bande spectrale. Puisque la pompe acquiert une phase spectrale pendant la propagation dans le gaz, les bandes latérales du signal et du complémentaire sont générées à partir d'une impulsion de pompe à dérive de fréquence. Par conséquent, elles présentent une distribution spectro-temporelle. Pour accentuer cet effet, la propagation d'une pompe et d'un signal étirées a été étudiée numériquement dans une fibre creuse remplie de gaz en résolvant l'équation de Schrödinger non-linéaire. Cette méthode a été utilisée principalement pour comprendre l'impact et l'influence de la dérive de fréquence sur le FWM. Nous avons trouvé une combinaison de paramètres pour développer l'expérience avec toutes les impulsions dans un mode fondamental. Nous avons obtenu une impulsion complémentaire à spectre accordable dans le proche infrarouge de 1,2 à 1,5 μm avec la possibilité d'atteindre la gamme de l'infrarouge moyen. Le complémentaire est généré le plus efficacement à 1,2 μm et possède une durée de 220 fs avec une énergie évaluée à quelques nJ.

Dans la deuxième partie de ce manuscrit, nous nous concentrons sur l'interaction non linéaire entre des ondes dans un mode fondamental et des modes d'ordre supérieurs. En raison du grand diamètre du cœur, le HCC peut facilement supporter des impulsions de forte puissante avec plusieurs modes spatiaux. Il se produit ainsi un couplage spatiotemporel dû à l'effet Kerr survenant durant la propagation de l'impulsion. Le FWM a été ensuite décrit analytiquement en tenant compte diverses combinaisons de modes de fibres (HE_{1n}). Les résultats confirment la possibilité d'amplifier ou de générer des impulsions infrarouges avec plusieurs combinaisons différentes d'accord de phase en ajustant la pression du gaz. Cependant, cet effet n'a pas été observé d'une façon prédominante. Par conséquente, nous avons travaillé sur une autre analyse et des simulations complémentaires. Cette nouvelle approche est basée sur la résolution de l'équation de la propagation unidirectionnelle multimodale des impulsions en collaboration avec le laboratoire ICB. Les simulations ont montré une oscillation longitudinale de la puissance et de l'intensité du laser le long de la fibre due à l'interaction entre les modes fondamentaux et les modes d'ordre supérieur. Un effet similaire a été également observé dans les fibres GRIN lorsqu'une modulation périodique de l'indice de réfraction et de l'intensité produit une concentration de l'énergie. Dans notre cas, nous observons également la génération et l'amplification de nouveaux modes dans un HCC. Ces études nous a permis non seulement de mettre en avant le couplage spatiotemporel dans le HCC rempli de gaz, mais également d'ouvrir de nouvelles perspectives sur le façonnage spatial de faisceau assisté par un mélange à quatre ondes multimodal.

Contents

Chapter 1. Introduction

Based on the theoretical work by Arthur Leonard Schawlow and Charles Hard Townes[1] Theodore H. Maiman has first shown the concept of lasing in a ruby crystal [2]. A few years later, the concept of solid-state laser [3] and gas laser [4] has also been developed to bring a revolutionary change to the way we live today, because lasers are highly used in scientific and industrial applications. The principal objectives of laser research are: increase the pulse energy, generate ultra-short pulses, and produce laser light a specific wavelength. Thus, in relation to the first task, the rapid evolution of the technology creates the shortest pulses by Q switching and mode-locking techniques. The Chirped pulse amplification (**CPA**) has also emerged as a solution to amplify ultra-short pulse at high peak power. This technique was developed by D. Strickland and G. Mourou and they receive the Nobel Prize in Physics 2018 [5]. CPA consists to stretch the incoming pulse by adding dispersion from a prism or a grating. Since the pulse is temporally stretched, its peak power decreases keeping the same amount of energy. To increase the power, the pulse goes to the amplification stage and after the dispersion is compensated. Finally, the amplified pulse is recompressed to reach a high peak power.

Following these progresses, the invention of optical fibers in the 1970s brought the invention of the first fiber laser by Elias Snitzer [6]. The significant advantage of the fiber is that the beam is confined to the transverse plane, so that the beam intensity can be maintained over a long propagation distance. Another advantage to use fibers is to generate laser light at a specific wavelength by doping the fiber with rare earth elements such as ytterbium, erbium and thulium [7]. During the 1990s there were a lot of research behind fiber laser amplifiers resulting in ytterbium doped fiber amplifier. This is now a well matured system that provides a high average power (~100 W) of ultra-short pulse at ~1 µm [8].

The ultra-fast processes were studied in the optical fibers even before the invention of the fiber laser, since that time many non-linear phenomena have been discovered [9]. The progress achieved on fiber laser, and nonlinear materials have created the field related to nonlinear optics and non-liner photonic as well. The first nonlinear optical process reported was a second harmonic generation (at 342 nm) in crystal line quartz [10]. This event was followed by reports on frequency mixing [11] parametric generation [12] and supercontinuum generation [13] in various configurations like crystalline and isotropic bulk materials. The process linked to the third order susceptibility includes the third harmonic generation [14], optical Kerr [15], four-wave mixing [16], self-focusing, among others. As most wavelength regions are not directly accessible using only available laser materials, non-linear effects allows to extend the spectral bandwidth and tunability. For example, recently in hollow capillary fibers have been used to generate few-femtosecond pulses tunable from the ultraviolet (300 nm) to the infrared (740 nm) with an energy up to 25 µJ [17].

In relation with the pulse energy, since the 1980s, one of the most widely used non-linear effects has been the Optical Parametric Amplification (**OPA**), particularly in non-linear materials with second order susceptibility. The researches have been focused on crystals, because it allows to get a wide spectral tunability and or an amplification of few-optical cycle pulses with energy above the µJ-level [18]. Particularly OPA has been well developed to generate or amplify fs pulses in the visible [19,20], near-IR [21] and Mid-infrared [22].

Lately, the Optical Parametric Chirped Pulse Amplifiers (**OPCPA**), has been used to achieve systems with high peak power in the near-IR, with an energy above the mJ-level by using a different type of crystals such as BBO [23], BiB3O6 [24], and PPMgLN [25]. Despite its great success, the OPA systems are designed with multiple nonlinear stages to optimize the phase matching and the conversion efficiency. Additionally, the process is limited by the optical transparency of the materials, the availability of the non-linear crystals and the damage threshold.

Using guided systems in association with the OPCPA provides significant benefits, such as; robustness and compactness systems. Moreover, in guided system the optical interactions between the involved pulses shall be more efficient thanks to the beam collinearity and excellent spatial beam profile. In particular, these processes were studied in single-mode solid-core photonic crystal fibers (**PCF**) in which the generation and the amplification are achieved from a Four Wave Mixing (**FWM**) mechanism [26–28]. In this case, the phase matching is given by the nonlinear phase of the pump and the overall (chromatic and geometric) dispersion of the fiber [29]. The FWM also arises as a solution for frequency conversion from a high-intense ultrashort laser pulse. Optical damage is also an important potential issue. Therefore, the power scalability by using solid core fibers can be performed by increasing the fiber-core diameter while keeping the suitable dispersion profile [30] or by stretching involved pulses [31] as for CPA and OPCPA.

Lately, gas filled-hollow core waveguide is of great interest because the optical damage threshold is much higher than in silica. In this case, the dispersion can be controlled by the pressure in real time, allowing a tunable phase-matched process. Regarding a specific type of hollow core waveguide, the Hollow Core Capillary (**HCC**) which is a dielectric tube that can contain gas inside, has emerged as an interesting solution that allows to work in a gas environment [32]. The HCC has been included in many applications, such as vacuum ultraviolet (**VUV**) generation [33,34], spatial and temporal self-compression [30,35], high harmonic generation [36–38]. Recently, applications in frequency conversion and amplification from FWM and Resonant dispersive wave (**RDW**) have been emerged, and it also allows the creation of tunable ultra-fast source from UV up to IR in the few-femtosecond regime [39]. The gas-filled HCC has many advantages for non-linear phenomena because the gas pressure is the key to simultaneously adjust dispersion and non-linearity. Few groups have focused their research on the amplification in gas filled HCC with a large core to generate or amplified pulses in the visible [40], ultra-violet [41,42] and infrared ranges [43–45].

Nonlinear phenomena in multimode optical fiber were heavily studied in the early years of optical communications to increase the capacity of optical communication systems [46–48]. One of the main current limitations to the transmission capacity of both single-mode and multimode fiber optical communication links is due to nonlinearity. Thus, the nonlinear phenomena in multicore and multimode fibers (**MMFs**), particularly four-wave mixing (FWM), have received renewed attention [49–52]. Another important motivation for research in this area is the potential to use multimode optical fibers in the development of multimode mode-locking laser [53–56]. Lately, graded-index multimode fiber (**GRINMFs**) has become an ideal platform to explore the nonlinear interaction of multiple modes because all guided modes can propagate with nearly identical group velocities at special wavelengths [57]. Therefore, the non-linear coupling between all the short pulses is reached at a maximum along the fiber[58,59]. Moreover, the propagation constants of the modes in this case is quantized with equally spaced values; therefore, just a specific mode can be amplified [60].

For the multimode propagation in a HCC, Kida et al.[31] have achieved parametric amplification of a supercontinuum with a gain up to 100 in the visible from 500 to 600 nm. The amplification bandwidth obtained supports a duration of around 10 fs. Faccio et al. [61] reported the light amplification using a fundamental pulse and its harmonics to generate a near-infrared pulse through FWM by considering a phase matching with high order modes. In most cases, the amplification is done with a multi-modal phase matching, however, the key parameters by which the process can be optimized are not yet clear. It is noteworthy that investigation also has been performed in gas filled hollow-core photonic crystal fibers [62–65] but usually with limited experimental results obtained with a large fiber-core. When a strong laser beam propagates in a material, it induces an increase in the refractive index proportional to the local intensity. Thus, the beam is exposed to a high index at the center a lower index at the edges. This means different nonlinear phenomena occur such as self-focusing, plasma, diffraction, intra-modal phenomena [66–70], etc., therefore a rich dynamic can be associated.

This manuscript will be dedicated to the investigation of nonlinear processes, mostly FWM in large core HCC. Therefore, it is necessary to include in the investigation the intermodal nonlinear phenomena and spatiotemporal coupling, mainly associated with broadband frequency conversion. In fact, understanding the various non-linear effects that occur within the multimode waveguide is a prerequisite for applying intermodal non-linear phenomena as the basis for future laser systems.

Chapter 2, discusses the nonlinear process and the pulse propagation and introduces fundamental equations required for the full understanding and used in the next chapter. The second part summarizes the properties of a gas-filled HCC.

The FWM process is deeply described in **chapter 3**. It introduces general equations, including discussion related to the phase matching and gain factor. The phenomena is also briefly described when the fundamental modes are considered and then the role of high order modes (**HOMs**) is also discussed.

Chapter 4 develops the theory and an experimental configuration to highlight FWM in a HCC and to generate tunable pulse in the near-infrared. The fundamental modes are mostly considered guaranteeing a beam profile with a high-quality profile at the source output.

In **Chapter 5,** we firstly focus on the intermediate region, between quasi-single mode and highly multimode interaction. Numerical and experimental configuration were implemented. From the experimental results, we found a similar effect that exists in GRIN fibers, where spatial self-imaging results in a longitudinal oscillation of the beam width and beam intensity along the fiber. This oscillation is also explained as an interchange of energy between different modes of the fiber. The numerical approach based on the multimode unidirectional pulse propagation equation (**MM-UPPE)** was developed to fit with the experimental results. The comparison between the numerical results and experimental data is given at the end of the chapter.

1.1 References to Chapter 1

1. Schawlow, A. L. and Townes, C. H. Infrared and optical masers. *Physical Review* **112**, 1940–1949 (1958).
2. Maiman, T. H. Stimulated optical radiation in Ruby. *Nature* **187**, 493–494 (1960).
3. Hall, R. N., Fenner, G. E., Kingsley, J. D., Soltys, T. J. and Carlson, R. O. Coherent light emission from GaAs junctions. *Physical Review Letters* **9**, 366–368 (1962).
4. Javan, A., Bennett, W. R. and Herriott, D. R. Population inversion and continuous optical maser oscillation in a gas discharge containing a He-Ne mixture. *Physical Review Letters* **6**, 106–110 (1961).
5. Strickland, D. and Mourou, G. Compression of amplified chirped optical pulses. *Optics Communications* **56**, 219–221 (1985).
6. Koester, C. J. and Snitzer, E. Amplification in a Fiber Laser. *Appl. Opt* **3**, RP1 (2017).
7. Nilsson, J. *et al.* High-power wavelength-tunable cladding-pumped rare-earth-doped silica fiber lasers. *Optical Fiber Technology* **10**, 5–30 (2004).
8. Lavenu, L. *et al.* High-energy few-cycle Yb-doped fiber amplifier source based on a single nonlinear compression stage. *Optics Express* **25**, 7530 (2017).
9. Blow, K. J. and Wood, D. Theoretical Description of Transient Stimulated Raman Scattering in Optical Fibers. *IEEE Journal of Quantum Electronics* **25**, 2665–2673 (1989).
10. Franken, P. A., Hill, A. E., Peters, C. W. and Weinreich, G. Generation of optical harmonics. *Physical Review Letters* **7**, 118–119 (1961).
11. Bass, M., Franken, P. A., Hill, A. E., Peters, C. W. and Weinreich, G. Optical mixing. *Physical Review Letters* **8**, 18–18 (1962).
12. Giordmaine, J. A. and Miller, R. C. Tunable coherent parametric oscillation in LiNbO3 at optical frequencies. *Physical Review Letters* **14**, 973–976 (1965).
13. Maker, P. D. and Terhune, R. W. Study of optical effects due to an induced polarization third order in the electric field strength. *Physical Review* **137**, 507–509 (1965).
14. New, G.H.C. and Ward, J. F. Optical third-harmonic generation in gases,. *Phys. Rev. Lett.* **19**, 556–559 (1967).
15. McWane, P. D. and Sealer, D. A. New measurements of intensity-dependent changes in the refractive index of liquids. *Applied Physics Letters* **8**, 278–279 (1966).
16. Carman, R. L., Chiao, R. Y. and Kelley, P. L. Observation of degenerate stimulated four-photon interaction and four-wave parametric amplification. *Physical Review Letters* **17**, 1281–1283 (1966).
17. Brahms, C., Belli, F. and Travers, J. C. Infrared attosecond field transients and UV to IR few-femtosecond pulses generated by high-energy soliton self-compression. *Physical Review Research* **2**, 043037 1–8 (2020).
18. Manzoni, C. and Cerullo, G. Few-optical-cycle pulses from near-IR to UV by non linear frequency conversion. in *2015 IEEE Photonics Conference, IPC 2015* 206–207 (2015).
19. Tzankov, P. *et al.* 300 μJ noncollinear optical parametric amplifier in the visible at 1 kHz repetition rate. *Optics Letters* **31**, 3629–3631 (2006).
20. Odhner, J. H. and Levis, R. J. High-energy noncollinear optical parametric amplifier producing 4 fs pulses in the visible seeded by a gas-phase filament. *Optics Letters* **40**, 3814–3817 (2015).

21. Viotti, A.-L. *et al.* Supercontinuum generation and soliton self-compression in χ (2)-structured KTiOPO 4. *Optica* **5**, 711–717 (2018).
22. Andriukaitis, G. *et al.* 90 GW peak power few-cycle mid-infrared pulses from an optical parametric amplifier. *Optics Letters* **36**, 2755–2757 (2011).
23. Shamir, Y. *et al.* High-average-power 2 μm few-cycle optical parametric chirped pulse amplifier at 100 kHz repetition rate. *Optics Letters* **40**, 5546–5549 (2015).
24. Silva, F., Bates, P. K., Esteban-Martin, A., Ebrahim-Zadeh, M. and Biegert, J. High-average-power, carrier-envelope phase-stable, few-cycle pulses at 21 μm from a collinear BiB3O6 optical parametric amplifier. *Optics Letters* **37**, 933 (2012).
25. Gu, X. *et al.* Generation of carrier-envelope-phase-stable 2-cycle 740-μJ pulses at 21-μm carrier wavelength. *Optics Express* **17**, 62–69 (2009).
26. Robert, P. *et al.* Spectral correlation of four-wave mixing generated in a photonic crystal fiber pumped by a chirped pulse. *Optics Letters* **45**, 4148–4151 (2020).
27. Fourcade-Dutin, C. *et al.* Temporal distribution measurement of the parametric spectral gain in a photonic crystal fiber pumped by a chirped pulse. *Photonics* **6**, 1–9 (2019).
28. Fourcade-Dutin, C., Miranda, O. Z., Mounaix, P. and Bigourd, D. Toward mid-infrared ultra-short pulse generation in a gas-filled hollow-core photonic crystal fiber. in *Advanced Photonics Congress 2021* (2021).
29. J. C. Travers, C. Brahms, F. Belli, T. F. Grigorova, A. L. M. S. Advances in nonlinear optics in gas-filled hollow-core fibers. in *in OSA Nonlinear Optics 2021, R. Boyd, C. Conti, D. Christodoulides, and P. Rakich, eds., OSA Technical Digest (Optical Society of America, 2021), paper NM2A.1.* (2021).
30. Travers, J. C., Grigorova, T. F., Brahms, C. and Belli, F. High-energy pulse self-compression and ultraviolet generation through soliton dynamics in hollow capillary fibres. *Nature Photonics* **13**, 547–554 (2019).
31. Kida, Y. and Imasaka, T. Optical parametric amplification of a supercontinuum in a gas. *Applied Physics B: Lasers and Optics* **116**, 673–680 (2014).
32. Ippen, E. P. Low-power quasi-cw raman oscillator. *Applied Physics Letters* **16**, 303–305 (1970).
33. Misoguti, L. *et al.* Generation of broadband VUV light using third-order cascaded processes. *Physical Review Letters* **87**, 013601/1-013601/4 (2001).
34. Adamu, A. I. *et al.* Deep-UV to Mid-IR Supercontinuum Generation driven by Mid-IR Ultrashort Pulses in a Gas-filled Hollow-core Fiber. *Scientific Reports* **9**, 1–8 (2019).
35. Wagner, N. L. *et al.* Self-compression of ultrashort pulses through ionization-induced spatiotemporal reshaping. *Physical Review Letters* **93**, 173902–173906 (2004).
36. Popmintchev, T. *et al.* Bright coherent ultrahigh harmonics in the kev x-ray regime from mid-infrared femtosecond lasers. *Science (1979)* **336**, 1287–1291 (2012).
37. Cabasse, A., Machinet, G., Dubrouil, A., Cormier, E. and Constant, E. Optimization and phase matching of fiber-laser-driven high-order harmonic generation at high repetition rate. *Optics Letters* **37**, 4618–4620 (2012).
38. Couch, D. E. *et al.* Ultrafast 1 MHz vacuum-ultraviolet source via highly cascaded harmonic generation in negative-curvature hollow-core fibers. *Optica* **7**, 832–837 (2020).
39. Brahms, C., Belli, F. and Travers, J. C. Infrared attosecond field transients and UV to IR few-femtosecond pulses generated by high-energy soliton self-compression. *Physical Review Research* **2**, 0–1 (2020).

40. Ciriolo, A. G. *et al.* Generation of ultrashort pulses by four wave mixing in a gas-filled hollow core fiber. *Journal of Optics* **20**, 125503-1 /125503-9 (2018).
41. Belli, F., Abdolvand, A., Travers, J. C. and Russell, P. St. J. Highly efficient deep UV generation by four-wave mixing in gas-filled hollow-core photonic crystal fiber. *Optics Letters* **44**, 5509 (2019).
42. Durfee, C. G., Backus, S., Kapteyn, H. C. and Murnane, M. M. Intense 8-fs pulse generation in the deep ultraviolet. *Optics Letters* **24**, 697 (1999).
43. Faccio, D., Grün, A., Bates, P. K., Chalus, O. and Biegert, J. Optical amplification in the near-infrared in gas-filled hollow-core fibers. *Optics Letters* **34**, 2918 (2009).
44. Kida, Y. and Kobayashi, T. Generation of sub-10 fs ultraviolet Gaussian pulses. *Journal of the Optical Society of America B* **28**, 139 (2011).
45. Fourcade-Dutin, C., Zurita-Miranda, O., Mounaix, P. and Bigourd, D. Mid-infrared ultra-short pulse generation in a gas-filled hollow-core photonic crystal fiber pumped by two-color pulses. *Fibers* **9**, 21 (2021).
46. Stolen, R. H., Bjorkholm, J. E. and Ashkin, A. Phase-matched three-wave mixing in silica fiber optical waveguides. *Applied Physics Letters* **24**, 308–310 (1974).
47. Hill, K. O., Johnson, D. C. and Kawasaki, B. S. Efficient conversion of light over a wide spectral range by four-photon mixing in a multimode graded-index fiber: erratum. *Applied Optics* **20**, 2769 (1981).
48. Agrawal, G. P. Nonlinear fiber optics: its history and recent progress [Invited]. *Journal of the Optical Society of America B* **28**, A1 (2011).
49. Nazemosadat, E., Pourbeyram, H. and Mafi, A. Phase matching for spontaneous frequency conversion via four-wave mixing in graded-index multimode optical fibers. *Journal of the Optical Society of America B* **33**, 144 (2016).
50. Rademacher, G., Warm, S. and Petermann, K. Analytical description of cross-modal nonlinear interaction in mode multiplexed multimode fibers. *IEEE Photonics Technology Letters* **24**, 1929–1932 (2012).
51. Mecozzi, A., Antonelli, C. and Shtaif, M. Nonlinear propagation in multi-mode fibers in the strong coupling regime. *Optics Express* **20**, 11673 (2012).
52. Mafi, A. Pulse Propagation in a Short Nonlinear Graded-Index Multimode Optical Fiber. *Journal of Lightwave Technology* **30**, 2803–2811 (2012).
53. Ding, E., Lefrancois, S., Kutz, J. N. and Wise, F. W. Scaling fiber lasers to large mode area: An investigation of passive mode-locking using a multi-mode fiber. *IEEE Journal of Quantum Electronics* **47**, 597–606 (2011).
54. Nazemosadat, E. and Mafi, A. Nonlinear switching in multicore versus multimode waveguide junctions for mode-locked laser applications. *Optics Express* **21**, 30739 (2013).
55. Mafi, E. N. and A. Nonlinear switching in a two- concentric-core chalcogenide glass optical fiber for passively mode-locking a fiber laser. *Opt. Lett.* **39**, 4675–4678 (2014).
56. Fu, S. *et al.* Passive Q-switching of an all-fiber laser induced by the Kerr effect of multimode interference. *Optics Express* **23**, 17255 (2015).
57. Einarsson, G. Pulse broadening in graded-index optical fibers: correction. *Applied Optics* **25**, 1030 (1986).
58. Renninger, W. H. and Wise, F. W. Optical solitons in graded-index multimode fibres. *Nature Communications* **4**, 1719 (2013).
59. S. Raghavan G. P. Agrawal. Spatiotemporal solitons in inhomogeneous nonlinear media. *Opt. Commun* **180**, 377–382 (2000).

60. Kibler, B. and Béjot, P. Discretized Conical Waves in Multimode Optical Fibers. *Physical Review Letters* **126**, (2021).
61. Faccio, D. *et al.* Spatio-temporal reshaping and X Wave dynamics in optical filaments. *Optics Express* **15**, 13077 (2007).
62. Konorov, S. O., Fedotov, A. B. and Zheltikov, A. M. Enhanced four-wave mixing in a hollow-core photonic-crystal fiber. *Optics Letters* **28**, 1448 (2003).
63. Ding, X., Selim Habib, Md., Amezcua-Correa, R. and Moses, J. Near-octave intense mid-infrared by adiabatic down-conversion in hollow anti-resonant fiber. *Optics Letters* **44**, 1084 (2019).
64. Finger, M. A., Joly, N. Y., Russell, P. S. J. and Chekhova, M. v. Characterization and shaping of the time-frequency Schmidt mode spectrum of bright twin beams generated in gas-filled hollow-core photonic crystal fibers. *Physical Review A* **95**, 053814 (2017).
65. Cordier, M. *et al.* Active engineering of four-wave mixing spectral correlations in multiband hollow-core fibers. *Optics Express* **27**, 9803 (2019).
66. Tempea, G. and Brabec, T. Theory of self-focusing in a hollow waveguide. *Optics Letters* **23**, 762 (1998).
67. Crego, A., Conejero Jarque, E. and San Roman, J. Influence of the spatial confinement on the self-focusing of ultrashort pulses in hollow-core fibers. *Scientific Reports* **9**, 9546 (2019).
68. Chapman, R. T. *et al.* Modal effects on pump-pulse propagation in an Ar-filled capillary. *Optics Express* **18**, 13279 (2010).
69. Mangini, F. *et al.* Self-imaging dynamics in nonlinear GRIN multimode optical fibers. *Frontiers in Optics / Laser Science* **28**, 24005–24021 (2020).
70. Wright, L. G., Wabnitz, S. W., Christodoulides, D. N. and Wise, F. W. Ultrabroadband dispersive radiation by spatiotemporal oscillation of multimode waves. in *Photonics and Fiber Technology 2016* (2016).
71. Marhic, M. E. *Fiber optical parametric amplifiers, oscillators and related devices*. *Fiber Optical Parametric Amplifiers, Oscillators and Related Devices* vol. 9780521861 (Cambridge University Press, 2007).
72. Couairon, A. *et al.* Practitioner's guide to laser pulse propagation models and simulation. *European Physical Journal: Special Topics* **199**, 5–76 (2011).
73. Brabec, T. and Krausz, F. Intense few-cycle laser fields: Frontiers of nonlinear optics. *Reviews of Modern Physics* **72**, 545–591 (2000).
74. Agrawal, G. P. *Nonlinear fiber optics*. *Nonlinear Fiber Optics* (Academic Press, 2019).
75. Boyd, R. W. *Nonlinear Fiber Optics*. (2008).
76. Marcatili, E. A. J. and Schmeltzer, R. A. Hollow Metallic and Dielectric Waveguides for Long Distance Optical Transmission and Lasers. *Bell System Technical Journal* **43**, 1783–1809 (1964).
77. Lehmeier, H. J., Leupacher, W. and Penzkofer, A. Nonresonant third order hyperpolarizability of rare gases and N2 determined by third harmonic generation. *Optics Communications* **56**, 67–72 (1985).
78. Couairon, A., Chakraborty, H. S. and Gaarde, M. B. From single-cycle self-compressed filaments to isolated attosecond pulses in noble gases. *Physical Review A - Atomic, Molecular, and Optical Physics* **77**, (2008).
79. Sinkin, O. V., Holzlöhner, R., Zweck, J. and Menyuk, C. R. Optimization of the split-step Fourier method in modeling optical-fiber communications systems. *Journal of Lightwave Technology* **21**, 61–68 (2003).

80. Marburger, J. H. Self-focusing: Theory. *Progress in Quantum Electronics* **4**, 35–110 (1975).
81. Milosevic, N., Tempea, G. and Brabec, T. Optical pulse compression: bulk media versus hollow waveguides. *Optics Letters* **25**, 672–674 (2000).
82. Stolen, R. H. and Lin, C. Self-phase-modulation in silica optical fibers. *Physical Review A* **17**, 1448–1453 (1978).
83. Dudley, J. M. and Taylor, J. R. *Supercontinuum generation in optical fibers*. *Supercontinuum Generation in Optical Fibers* vol. 9780521514 (2010).
84. Snitzer, E. Cylindrical Dielectric Waveguide Modes*. *J Opt Soc Am* **51**, 491 (1961).
85. Archambault, J. L., Black, R. J., Lacroix, S. and Bures, J. Loss Calculations for Antiresonant Waveguides. *Journal of Lightwave Technology* **11**, 416–423 (1993).
86. Hesketh, G. D., Poletti, F. and Horak, P. Spatio-Temporal Self-Focusing in Femtosecond Pulse Transmission Through Multimode Optical Fibers. *Journal of Lightwave Technology* **30**, 2764–2769 (2012).
87. Börzsönyi, A., Heiner, Z., Kalashnikov, M. P., Kovács, A. P. and Osvay, K. Dispersion measurement of inert gases and gas mixtures at 800 nm. *Applied Optics* **47**, 4856–4863 (2008).
88. Cros, B. *et al.* Eigenmodes for capillary tubes with dielectric walls and ultraintense laser pulse guiding. *Physical Review E - Statistical Physics, Plasmas, Fluids, and Related Interdisciplinary Topics* **65**, (2002).
89. M. Nisoli, S. Stagira, S. De Silvestri, O. Svelto, S. Sartinia Z. Cheng, G. Tempea, C. Spielmann, and F. K. Towards a terawatt-scale sub-10-fs laser technology. *IEEE J. of selected topics in quantum ELECTRONICS* **4**, (1998).
90. Trebino, R. *Frequency-Resolved Optical Gating: The Measurement of Ultrashort Laser Pulses*. *Frequency-Resolved Optical Gating: The Measurement of Ultrashort Laser Pulses* (2000). doi:10.1007/978-1-4615-1181-6.
91. Trebino, R. *et al.* Measuring ultrashort laser pulses in the time-frequency domain using frequency-resolved optical gating. *Review of Scientific Instruments* **68**, 3277–3295 (1997).
92. Stolen, R. Phase-matched-stimulated four-photon mixing in silica-fiber waveguides. *IEEE Journal of Quantum Electronics* **11**, 100–103 (1975).
93. Russell, P. Photonic Crystal Fibers. *Science (1979)* **299**, 358–362 (2003).
94. Knight, J. C. Photonic crystal fibres. *Nature* **424**, 847–851 (2003).
95. Bigourd, D., D'Augerès, P. B., Dubertrand, J., Hugonnot, E. and Mussot, A. Ultra-broadband fiber optical parametric amplifier pumped by chirped pulses. *Optics Letters* **39**, 3782 (2014).
96. Bigourd, D. *et al.* Parametric gain shaping from a structured pump pulse. *IEEE Photonics Technology Letters* **31**, 214–217 (2019).
97. Vanvincq, O., Fourcade-Dutin, C., Mussot, A., Hugonnot, E. and Bigourd, D. Ultrabroadband fiber optical parametric amplifiers pumped by chirped pulses Part 1: analytical model. *Journal of the Optical Society of America B* **32**, 1479 (2015).
98. Fourcade-Dutin, C., Vanvincq, O., Mussot, A., Hugonnot, E. and Bigourd, D. Ultrabroadband fiber optical parametric amplifier pumped by chirped pulses Part 2: sub-30-fs pulse amplification at high gain. *Journal of the Optical Society of America B* **32**, 1488 (2015).
99. Bigourd, D. *et al.* High-gain fiber, optical-parametric, chirped-pulse amplification of femtosecond pulses at 1 μm. *Optics Letters* **35**, 3480 (2010).

100. Bigourd, D., Lago, L., Mussot, A., Kudlinski, A. and Hugonnot, E. High gain fiber optical parametric chirped pulse amplification of femtosecond pulses at 1 µm. *Optics InfoBase Conference Papers* **35**, (2011).
101. Qin, Y., Batjargal, O., Cromey, B. and Kieu, K. All-fiber high-power 1700 nm femtosecond laser based on optical parametric chirped-pulse amplification. *Optics Express* **28**, 2317 (2020).
102. Qin, Y. *et al.* Watt-level all-fiber optical parametric chirped-pulse amplifier working at 1300 nm. *Optics Letters* **44**, 3422 (2019).
103. Ho, M. C., Uesaka, K., Marhic, M., Akasaka, Y. and Kazovsky, L. G. 200-nm-bandwidth fiber optical amplifier combining parametric and Raman gain. *Journal of Lightwave Technology* **19**, 977–981 (2001).
104. Lesvigne, C. *et al.* Visible supercontinuum generation controlled by intermodal four-wave mixing in microstructured fiber. *Optics Letters* **32**, 2173 (2007).
105. Tu, H., Jiang, Z., Marks, D. L. and Boppart, S. A. Intermodal four-wave mixing from femtosecond pulse-pumped photonic crystal fiber. *Applied Physics Letters* **94**, 101109 (2009).
106. Yuan, J. *et al.* Polarization-dependent intermodal four-wave mixing in a birefringent multimode photonic crystal fiber. *Optics Letters* **42**, 1644 (2017).
107. Dupiol, R. *et al.* Far-detuned cascaded intermodal four-wave mixing in a multimode fiber. *Optics Letters* **42**, 1293 (2017).
108. Yuan, J. *et al.* Experimental generation of discrete ultraviolet wavelength by cascaded intermodal four-wave mixing in a multimode photonic crystal fiber. *Optics Letters* **42**, 3537 (2017).
109. Velazquez-Ibarra, L., Diez, A., Silvestre, E. and Andres, M. V. Tunable Four-Wave Mixing Light Source Based on Photonic Crystal Fibers with Variable Chromatic Dispersion. *Journal of Lightwave Technology* **37**, 5722–5726 (2019).
110. Delagnes, J.-C. *et al.* High-power widely tunable ps source in the visible light based on four wave mixing in optimized photonic crystal fibers. *Optics Express* **26**, 11265 (2018).
111. Ryf, R. *et al.* Mode-Division Multiplexing Over 96 km of Few-Mode Fiber Using Coherent 6x6 MIMO Processing. *Journal of Lightwave Technology* **30**, 521–531 (2012).
112. Wright, L. G., Christodoulides, D. N. and Wise, F. W. Controllable spatiotemporal nonlinear effects in multimode fibres. *Nature Photonics* **9**, 306–310 (2015).
113. Krupa, K. *et al.* Multimode nonlinear fiber optics, a spatiotemporal avenue. *APL Photonics* **4**, 110901 (2019).
114. Rashleigh, S. C. Origins and Control of Polarization Effects in Single-Mode Fibers. *Journal of Lightwave Technology* **1**, 312–331 (1983).
115. Taylor, J. R. *Theory of Dielectric Optical Waveguides. 2nd Edition*. *Journal of Modern Optics* vol. 39 (1992).
116. Stolen, R. and Bjorkholm, J. Parametric amplification and frequency conversion in optical fibers. *IEEE Journal of Quantum Electronics* **18**, 1062–1072 (1982).
117. Ferguson, A. I. *The Elements of Nonlinear Optics*. *Journal of Modern Optics* vol. 38 (1991).
118. Musheghyan, M. *et al.* Tunable, few-cycle, CEP-stable mid-IR optical parametric amplifier for strong field applications. *Journal of Physics B: Atomic, Molecular and Optical Physics* **53**, (2020).
119. B. Shao, Y. Li, Y. Peng, P. Wang, J. Qian,Y. Leng, R. L. Broad-bandwidth high-temporal-contrast carrier-envelope-phase-stabilized laser seed for 100 PW lasers. *Opt. Lett.* **45**, (2020).

120. E. Rubino, J. Darginavičius, D. Faccio, P. Di Trapani, A. Piskarskas, A. D. Generation of broadly tunable sub-30-fs infrared pulses by four-wave optical parametric amplification. *Opt. Lett* **36**, 382–384 (2011).
121. J. Bromage, S.-W. Bahk, I. A. Begishev, C. Dorrer, M. J. Guardalben, B. N. Hoffman, J. B. Oliver, R. G. Roides, E. M. Schiesser, M. J. Shoup III, M. Spilatro, B. Webb, D. Weiner, J. D. Z. Technology development for ultra-intense all-OPCPA systems. *High Power Laser Science and Engineering* **7**, (2019).
122. Fu, W. and Wise, F. W. Normal-Dispersion Fiber Optical Parametric Chirped-Pulse Amplification. *2018 Conference on Lasers and Electro-Optics, CLEO 2018 - Proceedings* **43**, 5331 (2018).
123. Fourcade-Dutin, C. and Bigourd, D. Modulation instability in a dispersion oscillating fibre pumped by a broad band pulse. *Journal of Modern Optics* **64**, 500–506 (2017).
124. Dubietis, A. and Couairon, A. *Ultrafast Supercontinuum Generation in Transparent Solid-State Media*. (Springer Nature, 2019).
125. Ding, Y., Xu, J., Ou, H. and Peucheret, C. Mode-selective wavelength conversion based on four-wave mixing in a multimode silicon waveguide. *IET Conference Publications* **2013**, 198–200 (2013).
126. Pan, W., Jin, Q., Li, X. and Gao, S. All-optical wavelength conversion for mode-division multiplexing signals using four-wave mixing in a dual-mode fiber. *Journal of the Optical Society of America B* **32**, 2417 (2015).
127. C. Fourcade Dutin. *et al.* Post-compression of high-energy femtosecond pulses using gas ionization. *Optics Letters* **35**, 253 (2010).
128. Kolesik, M., Katona, G., Moloney, J.V., Wright, E. M. Physical factors limiting the spectral extent and band gap dependence of supercontinuum generation. *Phys. Rev. Lett* **91**, (2003).
129. Saari, P. and Reivelt, K. X-Shaped Propagation-Invariant localized light waves. *Physical Review Letters* **79**, 4135–4138 (1997).
130. Tzortzakis, S. *et al.* Formation of a conducting channel in air by self-guided femtosecond laser pulses. *Physical Review E - Statistical Physics, Plasmas, Fluids, and Related Interdisciplinary Topics* **60**, R3505 (1999).
131. Poletti, F. and Horak, P. Description of ultrashort pulse propagation in multimode optical fibers. *Journal of the Optical Society of America B* **25**, 1645 (2008).
132. Poletti, F. and Horak, P. Dynamics of femtosecond supercontinuum generation in multimode fibers. *Optics Express* **17**, 6134 (2009).
133. Mussot, A., Sylvestre, T., Provino, L. and Maillotte, H. Generation of a broadband single-mode supercontinuum in a conventional dispersion-shifted fiber by use of a subnanosecond microchiplaser. *Optics Letters* **28**, 1820 (2003).
134. Köttig, F., Tani, F., Travers, J. C. and Russell, P. S. J. Self-focusing below the critical power in gas-filled hollow-core PCF. in *Optics InfoBase Conference Papers* vol. Part F81-E (2017).
135. Mecozzi, A., Antonelli, C. and Shtaif, M. Coupled Manakov equations in multimode fibers with strongly coupled groups of modes. *Optics Express* **20**, 23436 (2012).
136. Tani, F., Travers, J. C. and St.J. Russell, P. Multimode ultrafast nonlinear optics in optical waveguides: numerical modeling and experiments in kagomé photonic-crystal fiber. *Journal of the Optical Society of America B* **31**, 311 (2014).
137. Benabid, F., Knight, J. C., Antonopoulos, G. and Russell, P. S. J. Stimulated Raman Scattering in Hydrogen-Filled Hollow-Core Photonic Crystal Fiber. *Science (1979)* **298**, 399–402 (2002).

138. Poletti, F. Nested antiresonant nodeless hollow core fiber. *Optics Express* **22**, 23807 (2014).
139. Cregan, R. F. *et al.* Single-Mode Photonic Band Gap Guidance of Light in Air. *Science (1979)* **285**, 1537–1539 (1999).
140. Knight, J. C., Broeng, J., Birks, T. A. and Russell, P. S. J. Photonic band gap guidance in optical fibers. *Science (1979)* **282**, 1476–1478 (1998).
141. Alharbi, M. *et al.* Hypocycloid-shaped hollow-core photonic crystal fiber Part II: Cladding effect on confinement and bend loss. *Optics Express* **21**, 28609 (2013).
142. Agrawal, G. *Nonlinear Fiber Optics*. (Academic Press, 2012).
143. Hansson, T. *et al.* Nonlinear beam self-imaging and self-focusing dynamics in a GRIN multimode optical fiber: theory and experiments. *Optics Express* **28**, 24005 (2020).

Chapter 2. Nonlinear optics in gas-filled Hollow Core Capillary

2.1 Introduction

Nowadays, many light sources for different scientific, medical, and industrial fields are created using non-linear optics. Nonlinear optic (**NLO**) is based on the phenomena related to the interaction of intense light radiation with matter. In a weak regime, the induced polarisation depends linearly with the electric field amplitude such as $\mathbf{P}=\varepsilon_0\chi^{(1)}\mathbf{E}$ where $\chi^{(1)}$ represents the linear susceptibility. In NLO since the optical response is nonlinear, the polarization is expressed as a power series of the electric field as, $\mathrm{P}=\varepsilon_0\left[\chi^{(1)}\mathrm{E}+\chi^{(2)}\mathrm{E}^2+\chi^{(3)}\mathrm{E}^3+\ldots\right]$The NLO effects are determined by the optical properties of the material, i.e the susceptibility. For example, a material with a $\chi^{(2)}$ value could be used for second harmonic generation (SHG), sum-frequency generation (SFG) and different-frequency generation (DFG). Materials with $\chi^{(3)}$ give rise to other nonlinear effects such as Self-focusing, third harmonic generation (THG), Self-phase modulation, (SPM), Cross phase modulation (XPM), Four Wave Mixing (FWM), stimulated Raman scattering (SRS), etc. All these effects can modify the temporal and spatial profiles of a laser beam.

In the last decades, although a lot of work have been made in bulk materials to create the nonlinear processes, gas environment has attracted attention for NLO with ultrafast pulse. Gas filled-HCC has a broadband transmission, high damage threshold and the dispersion and nonlinearity can be controlled. Consequently, in this chapter, we will explain some nonlinear phenomena related to $\chi^{(3)}$ We introduce the fundamental propagation equations for ultrashort pulses starting with the Maxwell equations.

2.2 Propagation of femtosecond pulses in a HCC

The propagation of the electric and magnetic fields through a dielectric media is described by the Maxwell equations [71].

$$\nabla\times\mathbf{E}=-\frac{\partial B}{\partial t}, \qquad (2-1)$$

$$\nabla\times\mathbf{H}=\mathbf{J}+\frac{\partial D}{\partial t}, \qquad (2-2)$$

$$\nabla\bullet\mathbf{D}=\rho, \qquad (2-3)$$

$$\nabla\bullet\mathbf{B}=0, \qquad (2-4)$$

here **E** and **H** are the electric and magnetic field vectors, whereas **B** and **D** are the magnetic and the electric displacement fields. **J** is the current density of free charges and

ρ is the charge density. In absence of free charges in a medium such as monoatomic gases $\mathrm{J}=0$ and $\rho = 0$. All fields (amplitude and phase) depend on space variables $\mathbf{r}=(x,y)$ time t and the propagation variable z.

The relations between electric displacement field, the electric field and the polarization is given by [71]

$$\mathbf{D}(\mathbf{r},t) = \varepsilon_0 \mathbf{E} + \mathbf{P} \qquad (2-5)$$

$$\mathbf{B}(\mathbf{r},t) = \mu_0 \mathbf{H} + \mathbf{M}, \qquad (2-6)$$

where ε_0 is the permittivity and μ_0 the permeability of free space and **P** and **M** are the induced electric and magnetic polarizations. In a non-magnetic material, **M** = 0.

The equation that describes the propagation of light is obtained from of the Maxwell equations, (Eq. (2-1)-Eq. (2-4)). Considering $\mathbf{J}=0$, the derivation, in terms of electric field **E**, is [72]

$$\nabla \times \nabla \times \mathbf{E} = -\frac{1}{c^2}\frac{\partial^2 \mathbf{E}}{\partial t^2} - \mu_0\left(\frac{\partial^2 \mathbf{P}}{\partial t^2}\right) \qquad (2-7)$$

where, $c=(\varepsilon_0\mu_0)^{-1/2}$, represents the speed of propagation of these waves in vacuum. The bound electron response of the medium to the electric field constitutes the polarization $\mathbf{P}$ and it can be separated into a linear part and non-linear part, such as; $\mathbf{P}=\mathbf{P}_{\mathrm{L}}+\mathbf{P}_{\mathrm{NL}}$ where $\mathbf{P}_{\mathrm{L}}$describes the medium response for a weak electric field
For laser intensities, up to 10^{15} Wcm^{-2} in gases [73] the nonlinearity become relevant, thus $\mathbf{P}_{\mathrm{NL}}$ must be included into the polarization equation. In addition, the linear medium response is non-instantaneous for the general case, thus, the linear polarization is given by [74].

$$\mathbf{P}_{\mathrm{L}}(\mathbf{r},t) = \varepsilon_0 \int_{-\infty}^{t} \chi^1(r,\ t-t')\ \mathbf{E}(\mathbf{r},t')\,dt'. \qquad (2-8)$$

Whereas the non-linear part is written as:

$$\mathrm{P}_{\mathrm{NL}}(\mathrm{r},t) = \varepsilon_0 \iiint_{-\infty}^{t} \chi^3(t-t_1,t-t_2,t-t_3)\ \mathrm{E}(\mathrm{r},t_1)\ \mathrm{E}(\mathrm{r},t_2)\mathrm{E}(\mathrm{r},t_3)\,dt_1dt_2dt_3 \qquad (2-9)$$

Since noble gases and diatomic gases are homogeneous and isotropic, they present a null inversion symmetry, $\chi^2=0$ (m/V) [75]. Considering the nonlinear response is instantaneous [73], the polarization equation can be simplified, such as

$$\mathbf{P}_{\mathrm{L}} = \varepsilon_0\chi^{(1)}\mathbf{E} \qquad (2-9a)$$

$$\mathbf{P}_{\mathrm{NL}} = \varepsilon_0\chi^{(3)}\mathbf{E}^3. \qquad (2-9b)$$

The identity $\nabla \times [\nabla \times \mathbf{E}] = \nabla [\nabla \bullet \mathbf{E}] - \nabla^2 \mathbf{E}$can be applied to derive the optical Helmholtz equation from Eq. (2-7). Since the wavelength of the laser pulses is much smaller than the radius of the fiber [76] the longitudinal component of the E can be neglected. Therefore, the propagation equation for current-free medium is given by:

$$\nabla^2 \mathbf{E} - \frac{1}{c^2}\frac{\partial^2 \mathbf{E}}{\partial t^2} = \mu_0 \left(\frac{\partial^2 \mathbf{P}_{\mathrm{L}}}{\partial t^2} + \frac{\partial^2 \mathbf{P}_{\mathrm{NL}}}{\partial t^2} \right) \qquad (2-10)$$

Introducing the polarization expressions, the equation becomes:

$$\nabla^2 \mathbf{E} - \frac{1}{c^2}\frac{\partial^2 \mathbf{E}}{\partial t^2} = \mu_0 \frac{\partial^2}{\partial t^2} \left(\varepsilon_0 \chi^{(1)} \mathbf{E} + \mathbf{P}_{\mathrm{NL}} \right) \qquad (2-11)$$

In the slowly varying envelope approximation, the pulse propagation can be advantageously described by considering the electric field as a superposition of the pulse envelope $\mathcal{E}$ with a carrier wave frequency ω_0, such as:

$$\mathbf{E} = \frac{1}{2}\left[\mathcal{E} \exp\left(ik_0 z - i\omega_0 t \right) + \mathcal{E}^* \exp\left(-ik_0 z + i\omega_0 t \right) \right] \qquad (2-12)$$

The polarization can be described in a similar way:

$$\mathbf{P}_{\mathrm{L}} = \frac{1}{2}\left[\mathscr{P}_L \exp\left(ik_0 z - i\omega_0 t \right) + \mathscr{P}_L^* \exp\left(-ik_0 z + i\omega_0 t \right) \right] \qquad (2-13)$$

$$\mathbf{P}_{\mathrm{NL}} = \frac{1}{2}\left[\mathscr{P}_{NL} \exp\left(ik_0 z - i\omega_0 t \right) + \mathscr{P}_{NL}^* \exp\left(-ik_0 z + i\omega_0 t \right) \right], \qquad (2-14)$$

where $k_0 = \omega / c$.

The expression for $\mathbf{E}^3$ is**:**

$$\mathrm{E}^3 = \frac{1}{8}\left[\mathcal{E}^3 \exp\left(i3k_0 z - i3\omega_0 t \right) + 3|\mathcal{E}|^2 \mathcal{E} \exp\left(ik_0 z - i\omega_0 t \right) + c.c. \right], \qquad (2-15)$$

where c.c. denotes complex conjugate. By introducing Eq. (2-15) into Eq. (2-9b) and by neglecting the third harmonic frequency, we identify the nonlinear polarization envelope $\mathscr{P}_{NL}$ from its carrier envelope decomposition.

$$\mathscr{P}_{NL} \equiv \varepsilon_0 \chi^{(3)} \frac{3}{4} |\mathcal{E}|^2 \mathcal{E} \qquad (2-16)$$

In the same way, the nonlinear refractive index n_2 can be defined from $\chi^{(3)}$ such that:

$$\mathrm{n}_2(\omega) = \left(\frac{3\chi^3}{4n^2(\omega)\, \varepsilon_0 c} \right)^{\frac{1}{2}} \qquad (2-17)$$

By introducing the above definition for the nonlinear index coefficient n_2 in Eq. (2-16), and by using the definition of the intensity $I \equiv \varepsilon_0 c n_0 |\mathcal{E}|^2/2$, an expression is obtained for the nonlinear polarization envelope modeling an instantaneous Kerr response of the medium [72]:

$$\mathscr{P}_{NL} = 2\varepsilon_0 \mathrm{c}\mathrm{n}_2 n_0 I\mathcal{E}. \qquad (2-18)$$

The linear refraction index n_0 and $\mathrm{n}_2 I$ are dimensionless, since I have units of Wm^{-2} and n_2 in $(\mathrm{m}^2\mathrm{W}^{-1})$.

To get the wave equation for the slowly varying envelope approximation (SVEA), the Eq. (2-11) is transferred to the frequency domain, resulting in:

$$\nabla^2 \tilde{\boldsymbol{\mathcal{E}}} + n^2(\omega)\frac{\omega^2}{c^2}\tilde{\mathcal{E}} = \mu_0 \omega^2 \tilde{\mathscr{P}}_{\mathrm{NL}} \qquad (2-19)$$

2.2.1 Pulse propagation in single mode waveguides

This section focusses on the pulse propagation in a waveguide with a cylindrical symmetry, such as optical fibers. Rewriting Eq. (2-19) in cylindrical coordinates results:

$$\frac{\partial^2 \tilde{\boldsymbol{\mathcal{E}}}}{\partial^2 \rho^2} + \frac{1}{\rho}\frac{\partial \tilde{\boldsymbol{\mathcal{E}}}}{\partial \rho} + \frac{1}{\rho^2}\frac{\partial^2 \tilde{\boldsymbol{\mathcal{E}}}}{\partial^2 \phi^2} + \frac{\partial^2 \tilde{\boldsymbol{\mathcal{E}}}}{\partial^2 z^2} + n^2(\omega) k^2(\omega)\tilde{\mathcal{E}} = \mu_0 \omega^2 \tilde{\mathscr{P}}_{\mathrm{NL}} \qquad (2-20)$$

where, ρ and ϕ are the radial and azimuthal coordinates and z is the longitudinal direction and $k(\omega)$ is the vacuum vector given as $k(\omega) = \frac{2\pi}{\lambda} = \frac{\omega}{c}$. In gas-filled core hollow core capillary, the wave vector can be written as $\beta_z(\omega) = n\, k(\omega)$

The Eq. (2-20) can be solved by using the method of variable separation, to results in a solution of the form:

$$\tilde{\boldsymbol{\mathcal{E}}}\left(r, \omega-\omega_0\right) = \tilde{\mathrm{A}}\left(z, \omega-\omega_0\right) \mathbf{F}(\rho, \phi) \exp(i\beta_0 z), \qquad (2-21)$$

where, $\mathbf{F}(\rho, \phi)$ is the transverse profile and $\tilde{\mathbf{A}}(\omega)$ is the envelope of the pulse and β_0 is the propagation constant of the wave along the z-axis. The equation (2-21) can be separated into an eigenvalue equation for the transverse profile $\mathbf{F}(\rho, \phi)$ and the envelope propagation along the z direction. Following the procedure describe in Agrawal book [74], it results in the pulse propagation equation:

$$\frac{\partial \mathrm{A}}{\partial z} = -\frac{\alpha}{2}\mathrm{A} + \left(\sum_{k\geq 2}\beta_n \frac{i^{n-1}}{n!}\frac{\partial^n}{\partial T^n}\right)\mathrm{A} + i\gamma\left(1 + \frac{i}{\omega_0}\frac{\partial}{\partial T}\right)\left(|A|^2 A\right) \qquad (2-22)$$

This equation describes the propagation of an optical pulse in a single mode fiber and it is related to the nonlinear Schrödinger equation under certain conditions. When the frequency spacing are not very large, it is often a good approximation to assume χ^3 is frequency independent of frequency so the four mode profiles are essentially identical. Hence the nonlinear coefficient, γ, is constant and it is defined as:

$$\gamma = \frac{\omega_0 n_2}{c}\left[\frac{\int_0^a |\mathbf{F}(\rho)|^4 \rho d\rho}{2\pi\left(\int_0^a |\mathbf{F}(\rho)|^2 \rho d\rho\right)^2}\right] \qquad (2-23)$$

$\beta(\omega)$ is often expanded in a Taylor series around the carrier frequency ω_0 such as:

$$\beta(\omega) = \beta_0 + \left(\omega-\omega_0\right)\beta_1 + \frac{1}{2}\left(\omega-\omega_0\right)^2\beta_2 + \frac{1}{6}\left(\omega-\omega_0\right)^3\beta_3 + \ldots \qquad (2-24)$$

The high-order parameters are defined as:

$$\beta_m = \left.\frac{\partial^m \beta}{\partial \omega^m}\right|_{\omega=\omega_0} \quad (m=1,2,3\ldots), \qquad (2-25)$$

The first derivative, β_1 also known as the group delay T_g. It corresponds to the flight time of the pulse when it propagates through a material of a length, L, at group velocity V_g. The first-order spectral phase produces a delay in the pulse without changing its temporal profile (Fig. 2.1a).

The subsequent order phase terms correspond to β_2 and represent the group velocity dispersion (**GVD**). This term is responsible for the temporal broadening of the pulse, because different frequency components propagate at different speeds. β_2 produces a linear delay, thus the frequency components arrive one after the other (Fig. 2.1b). When $\beta_2 > 0$, the lower frequencies of the pulse move faster than the higher ones and the reverse occurs in the anomalous dispersion region GVD ($\beta_2 < 0$), where the high frequencies are faster.
The zero-dispersion wavelength (**ZDW)** is when $\beta_2 = 0$ (fs^{2}m^{-1}), and it means the spectral component can maintain their constant phase over a long distance because the dispersive effects almost vanish.

The third order dispersion term, β_3, (**TOD**) produces an asymmetric broadening of the pulse because its central frequency arrives first, while the frequencies on each side arrive later or vice versa depending on the β_3 sign. The appearance of oscillations after or before the pulse characterizes the presence of TOD (Fig. 2.1c).

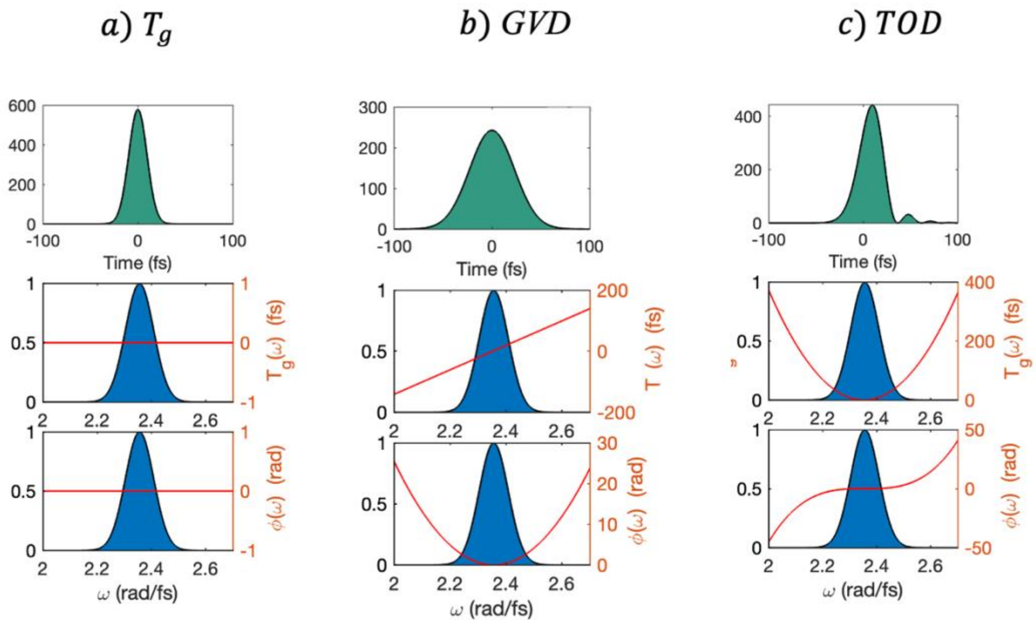

Fig. 2.1 Green graphs, temporal Intensity I(t), blue graphs, spectral intensity I(ω), spectral phase $\phi(\omega)$ and group delay $T_g(\omega)$. The Gaussian laser pulse is centered at 800 nm, the Fourier Transform Limited pulse duration is 15 fs at FWHM.

2.2.2 Nonlinear effects

In monoatomic gases, the linear $\chi^{(1)}$ and nonlinear susceptibility $\chi^{(3)}$ linearly scale with pressure, because of the atomic number, **N**, of the gas, which depends on pressure p and temperature T, [77].

$$\chi^{(3)}(p,T) = \frac{p}{p_0}\frac{T_0}{T}\,\chi^{(3)}\Big|_{p_0,T_0} \qquad (2-26)$$

Nonlinear polarization considers only the non-resonant electronic contribution, coming from the real part of the susceptibility. It leads to an intensity dependent with an instantaneous nonlinear response. Monoatomic gases present a weak nonlinear response in comparison with glass as fused silica.

The n_2 values used in this work are displayed in Table 2-1. They are computed at 800 nm in [78].

Table 2-1 Parameters corresponding values of nonlinear index coefficient n_2 [78]

Gas types	n_2 (10^{-19}cm^{2}W^{-1})
Ne	0.14
Ar	1.74
Kr	4.03
Xe	11.15

2.2.3 The Split-Step Fourier Method

In a numerical simulation, it is convenient to perform a change of the reference frame. The pulse is translated to a local frame $(z,t) \rightarrow (z,\tau)$ where τ represents the retarded time in the pulse frame such as:

$$\tau = t - z/v_g \equiv t - \beta_1 z, \tag{2-27}$$

The propagation equation (Eq. (2-22) is numerically simulated by using the transformation of the local frame. In addition, we can add the intensity dependence of the group velocity. We arrive to the widely used nonlinear Schrödinger equation (**NLSE**) and by neglecting the loss $\alpha=0$, we obtained :

$$\frac{\partial \mathrm{A}}{\partial z} - \frac{i\beta_2}{2}\frac{\partial^2 \mathrm{A}}{\partial \tau^2} = i\gamma\left(1 + \frac{i}{\omega_0}\frac{\partial}{\partial \tau}\right)(|A|^2 A) \tag{2-28}$$

The NLSE (Eq. 2.28) represents the pulse propagation in nonlinear dispersive media [74], and is usually solved by the split-step Fourier method. In order to get the pulse propagation, the equation is split into two main operators for dispersion and nonlinearity, such that;

$$\frac{\partial A}{\partial z} = (\mathrm{D} + \mathrm{N})\ A, \tag{2-29}$$

where N is a non-linear operator that governs the nonlinear effects whereas the D is a differential operator for dispersion. The nonlinear operator in time domain is defined as:

$$\mathrm{N} = i\gamma\left(1 + \frac{i}{\omega_0}\frac{\partial}{\partial \tau}\right)|A|^2, \tag{2-30}$$

In the equation (2-29), D is described in the time domain but it is more convenient to express this quantity in the frequency domain:

$$\mathfrak{F}^{-1}\left[\mathrm{D}\right] = i\left[\beta(\omega) - \beta_0(\omega_0) - \beta_1(\omega - \omega_0)\right], \tag{2-31}$$

where, $\mathfrak{F}^{-1}$ stands for inverse Fourier transform. This explicit relation is usually implemented such that all the full dispersion profile is taken into account in the numerical model. The zero and first order term are subtracted in agreement with the definition of Eq. (2-27).

In the symmetrical split-step Fourier method, the propagation on one step h is approximated by.

$$\mathrm{A}(z+\mathrm{h},\ \tau) = \exp\left(\frac{\mathrm{h}}{2}\widehat{\mathrm{D}}\right)\exp\left(\int_{z}^{z+\mathrm{h}} \widehat{\mathrm{N}}(z')\,dz'\right) \times \exp\left(\frac{\mathrm{h}}{2}\widehat{\mathrm{D}}\right)\mathrm{A}(z,\tau)\ , \tag{2-32}$$

where the exponential dispersion operator is ideally evaluated in the Fourier domain through the use of Fast Fourier Transform. The pulse propagates step by step with a small value of h until it reaches the end of the fiber.
In the symmetric method, the pulse propagates successively in half a linear step, in a full step that corresponds to the nonlinear part, and finally in half linear step.

In this work, the adaptive step size method was used, based on the algorithm described by Sinkin et al.[79]. The selection of the step size is based on an estimate of the relative error from the step size. The real local error cannot be found because the real solution is not known. Hence, the local error δ is estimated by comparing a rough and a fine solution.

$$\delta = \frac{\left\| A_{fine} - A_{coarse} \right\|}{\left\| A_{fine} \right\|}, \qquad (2-33)$$

where $\| \tilde{A}(z, \omega) \| = \left(\int |\tilde{A}(z, \omega)|^2 d\omega \right)^{1/2}$.

The algorithm tries to estimate the local error by taking a complete step to calculate a coarse solution and then independently by taking two half steps, resulting in a fine solution. The h-step size is adapted to maintain δ within the range $(\delta_G, 2\delta_G)$ where δ_G is the acceptable error. If δ> $2\delta_G$, the solution is discarded, and the process is recalculated with half of the step size. If δ is in the range $(\delta_G, 2\delta_G)$ is divided by 2 for the next step. If $\delta < 1/2\delta_G$, h is multiplied by $2^{(1/3)}$ for the next step.

2.2.4 Kerr effect

The relation between nonlinear polarization and Kerr response is given in Eq. (2-16). The total polarization is also describing by the linear susceptibility and the refractive index of the medium and is expressed as following:

$$\mathrm{n} = \sqrt{1 + \chi^{(1)} + \frac{3}{4} \frac{\chi^{(3)}}{n^2(\omega)\, \varepsilon_0 c} I} \approx \mathrm{n}_0 + \mathrm{n}_2 I, \qquad (2-34)$$

where, n_2 is the Kerr coefficient. Thus, the refractive index of the medium become intensity-dependent, leading to effects such as self-focusing, self-phase modulation (**SPM**) and cross-phase modulation (**XPM**) [74]. The SPM is responsible for the spectral broadening of ultrashort pulses and the formation of optical solitons whereas the XPM refers to the nonlinear phase shift of an optical field induced by another field having different wavelength, direction, or state of polarization. These phenomena will be covered in the following sections.

Other spatial phenomena can be produced due to an high intensity. For example, it is known that beams with power above a certain threshold, called critical power, P_{cr} undergo self-focusing [67] at finite distance [80]. When the power approach the critical value, other phenomena (self-focusing, plasma, etc.) should be considered during pulse propagation. Since the spatial confinement of the beam favors the self-focusing, in absence of an analytical formula A. Crego et al.[80] used the numerical results to obtain curve-fitted formula to predict the location of the singularity as a function of the Gaussian input beams.

$$\frac{z_c}{z_R} = \frac{0.625}{\left(\mathbf{P}_{\mathbf{in}}/\mathbf{P}_{\mathbf{cr}} - 0.715\right)^{0.6346}}, \qquad (2-35)$$

The critical power of the fundamental mode of the HCC is as follow[81],

$$\boldsymbol{P}_{cr} = \frac{\lambda_0^{\;2}}{2\nu_2 p}, \qquad (2-36)$$

where, ν_2 is the ratio between the nonlinear refractive index and the gas pressure p, and where $z_R = \pi W_0^2/\lambda$ known as the Rayleigh length (diffraction limit).

2.2.5 Self-phase modulation

Self-phase modulation is a non-linearity that modifies the effective refractive index of the capillary with the phase intensity. Thus, the temporal dependence of the refractive index produces a nonlinear change of the temporal phase ϕ_{nl} given by [82],

$$\phi_{nl}(t) = \frac{\omega_0}{c} n_2 \int_O^L I(t,z)\, dz, \qquad (2-37)$$

where L is the length of the nonlinear medium, ω_0 is the carrier frequency and z is the propagation distance. The nonlinear phase shift is accumulated during the pulse propagation. The SPM leads to the generation of new frequencies where the spectral enlargement has a negative shift from the central frequency on the pulse leading edge and a positive shift at the trailing edge (Fig. 2.2). In addition, the chirp is linear in the central part of the pulse but becomes nonlinear on the edges.

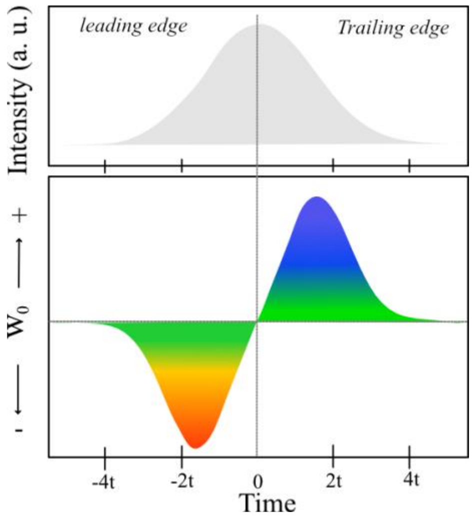

Fig. 2.2 Schematic representation of spectral broadening due to self-phase modulation on a Gaussian pulse

By neglecting the dispersion and self-steepening, the solution of the NLS equation Eq. (2-28) is given by:

$$A(z,\tau) = A(0,\tau)\exp\left[i\phi_{nl}(z,\tau)\right], \qquad (2-38)$$

where the initial condition $A(0,T)$ is the pulse at the input of the fiber with a power $|A(0,T)|^2 = P_0$ and $\phi_{nl}(z,\tau) = i\gamma|A(0,T)|^2 z$ is the nonlinear phase that the pulse acquires as it propagates through a Kerr medium. Thus, the strength of SPM depends on the nonlinear fiber parameter and peak power. It is quantified with the nonlinear length defined as [82]:

$$L_{NL} = \frac{1}{\gamma P_0}, \qquad (2-39)$$

As the pulse propagates, its spectrum broadens through SPM and its characteristic structure comes from the interference of spectral components with identical frequencies generated at different times (Fig. 2.3). The spectrum can broaden due to SPM to more than 100 THz, especially when it is combined with other nonlinear processes such as Raman scattering and FWM. An extreme spectral broadening is known as supercontinuum generation [83].

The nonlinear pulse propagation in a gas-filled hollow core capillary with a core diameter of 150 μm and filled with argon a 1 bar is shown in Fig. 2.3. A Gaussian pulse is launched with at a central wavelength at 800 nm and a pulse duration of 120 fs. The output spectra are displayed after propagation length of 20, 40, and 70 cm.

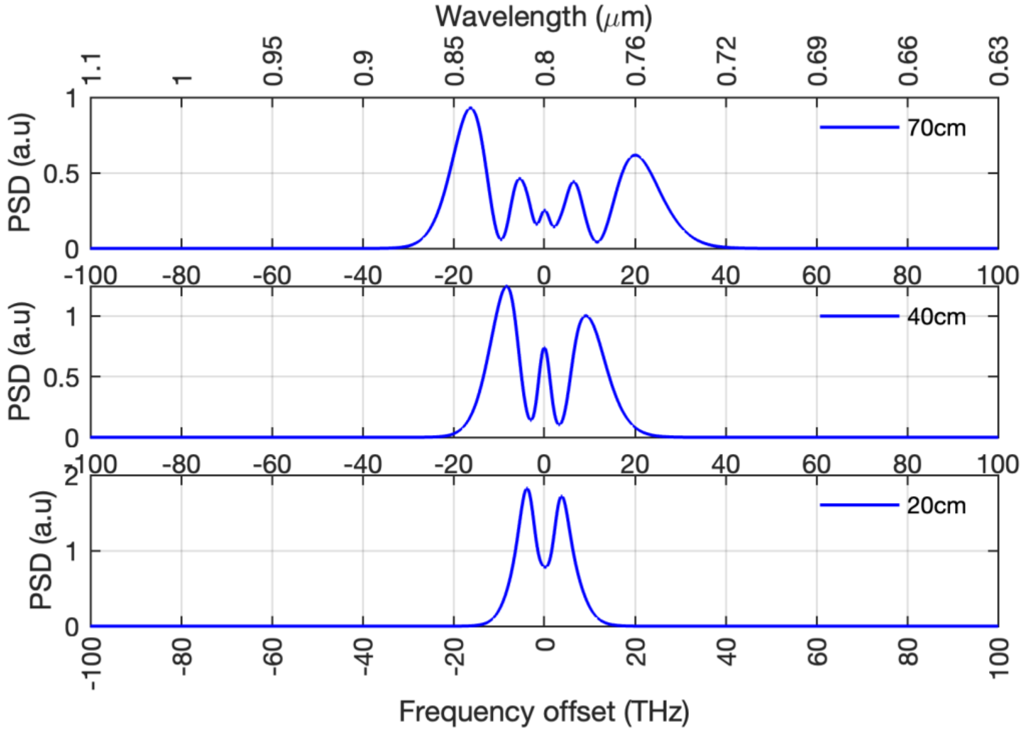

Fig. 2.3 Output spectrum of a Gaussian pulse after propagation through HCC filled with argon at 1 bar at different fiber lengths with constant peak power (1.67 GW) and core diameter of 150 μm.

In Fig. 2.3 for a given peak power and pressure, the maximum phase shift ϕ_{max} increases linearly with the fiber length. Therefore, the number of peaks depends on ϕ_{max} and increase linearly with it. The spectral broadening scales with the inverse of the pulse duration even if the pulse peak power is kept constant. In our case if the system is limited by a given fiber length, the nonlinearity can be increased by selecting a gas with higher $\chi^{(3)}$ value.

2.2.6 Self-Steepening

Self-steepening occurs when the group velocity becomes intensity dependent. This means the Gaussian pulse is modified so that its trailing edge becomes steeper and the leading-edge flatter. This is because the most intense part of the pulse moves at lower speed than the edges, conducting the creation of a shock on the trailing edge of the pulse (also called optical shock).

A steeper trailing edge means that spectral enlargement extends far more on the blue side than the red side, whereas the power on the red is superior to those on the blue side. To illustrate the self-steeping effect by using NLS equation, Fig. 2.4 shows the output spectrum of a Gaussian pulse after a propagation in a 100 cm-long-argon filled HCC at a pressure of 1.5 bar. It is clear that we can observe the asymmetric broadening, where the red-shifted peaks are more intense than blue ones. The nonlinearity increases with the gas pressure, i.e at a higher pressure the self-steeping effect becomes more significant (especially on heavy gas, like argon or krypton).

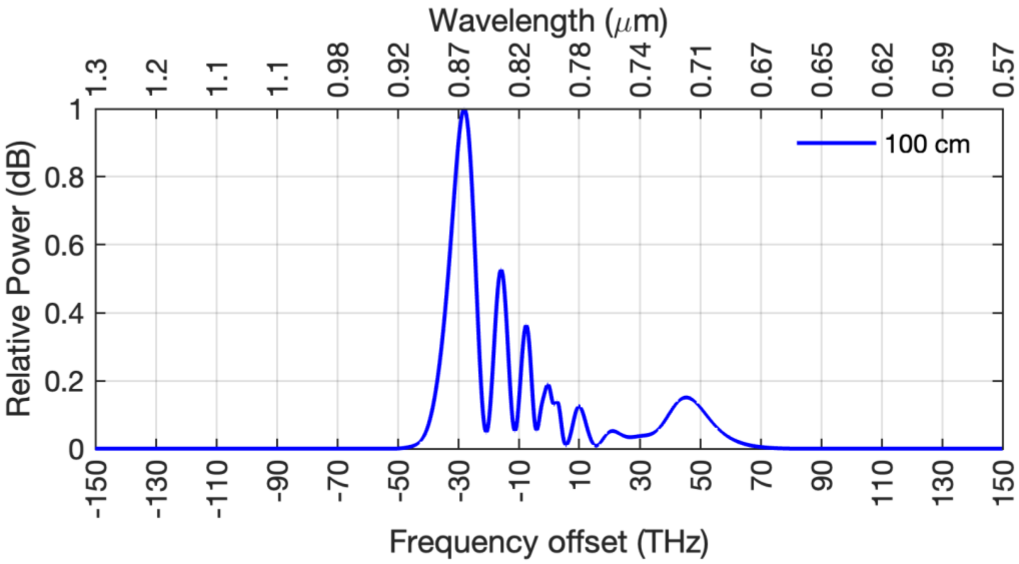

Fig. 2.4 Output spectrum of Gaussian pulse after propagation in a 100 cm long HCC filled with argon at 1.5 bar. The peak power is 1.67 GW and the core diameter is 150 μm.

2.2.7 Four Wave Mixing

Four Wave Mixing (FWM) is a parametric process in which four waves or photons interact with each other because of the third-order nonlinearity in the media. Considering four CW oscillating at angular frequencies ω_1, ω_2, ω_3 and ω_4 The total electric field is expressed as:

$$\mathbf{E}=\frac{1}{2}\sum_{n=1,2,3,4}\mathcal{E}_n\left[\exp\left(i\beta_n z-i\omega_n t\right)\right]+c.c, \qquad (2-40)$$

where β_n is the propagation constant for a given mode and frequency. Next, we express the nonlinear polarization (**NPL**), in the same form.

$$\mathbf{P}_{\mathbf{NL}}=\frac{1}{2}\sum_{n=1,2,3,4}\mathscr{P}^{n}_{NL}\left[\exp\left(ik_0 z-i\omega_0 t\right)\right]+c.c. \qquad (2-41)$$

Including the Eq. (2-40) in the nonlinear polarization equation Eq. (2-9b) results in many frequency components. For example, the polarization associated to P_4 is given by the expression:

$$\mathbf{P}^{4}_{\mathbf{NL}}=\varepsilon_0\chi^{(3)}\frac{3}{4}\left[|\mathcal{E}_4|^2\mathcal{E}_4+2\left(|\mathcal{E}_1|^2+|\mathcal{E}_2|^2+|\mathcal{E}_3|^2\right)\mathcal{E}_4+2\mathcal{E}_1\mathcal{E}_2\mathcal{E}_3\exp(i\theta^+)+2\mathcal{E}_1\mathcal{E}_2\mathcal{E}_3^*\exp(i\theta^-)\right], \qquad (2-42)$$

Where θ^- and θ^+ represent the phase between the four waves.
$\theta^+=(\beta_1+\beta_2+\beta_3+\beta_4)z-(\omega_1+\omega_2+\omega_3+\omega_4)t$. $\theta^-=(\beta_1+\beta_2-\beta_3-\beta_4)z-(\omega_1+\omega_2-\omega_3-\omega_4)t$.
They are defined by the propagation constant and angular frequencies (energy and momentum conservation).

The SPM and XPM are contained in the first four terms and the remaining terms result from the frequency combination of all the four waves. From the equation, two types of

FWM appear [74]. One associated with the term θ^{+} that corresponds to the case in which three photons are annihilated and transfer their energy to a single photon at frequency ω_4 . This process is also known as third-harmonic generation for $\omega_1=\omega_2=\omega_3$

The other one is related to the term θ^{-}. It corresponds to the case when two photons at frequencies ω_1 and ω_2 are annihilated, while two photons at frequencies ω_3 and ω_4 are generated. In this case the photons must fulfil the conservation laws; the photon energy and the photon momentum given by [71]:

$$\omega_3+\omega_4=\omega_1+\omega_2, \tag{2-43}$$

$$\Delta\beta=\beta_3+\beta_4-\beta_1-\beta_2, \tag{2-44}$$

The last relation, Eq. 2.44, is the phase matching condition, where the maximum conversion efficiency is achieved when the phase mismatch vanishes, $\Delta\beta=0$. In this case, the energy flows in an efficient way from the pump to the new frequencies at ω_3 and ω_4.

On the other hand, if a weak signal at ω_3 is also launched into the fiber together with the pump, the signal will be amplified. The configuration is known as optical parametric amplification. In Chapter 3, the FWM mixing process will be explained in detail and some expressions will be derived to evaluate the parametric gain and conversion efficiency.

2.3 Hollow-Core Capillary

The optical wave guides emerged as a solution to overcome the diffraction of the propagation in the free space and to confine the light over a long trajectory with low loss. They are made of different materials such as metal, silica glass, crystals or even polymers. They also exist with different geometry and designs, like step-index fiber or microstructured with a solid or hollow core. Regarding hollow-core fibers, the optical properties are determined by the inner radius a, the filling gas with refractive index n_1, and the refractive index of the waveguide, n_2.

The Hollow Core Capillary HCC is a cylindrical waveguide with a central hollow in the core. Their properties have been known since the 1960s [84]. The presence of a micro-capillary greatly changes the properties of the fibers due to the high contrast of the refractive index between the hollow and the glass. As the hollow can be filled with rare gases, the refractive index is about 1, which is inferior to the silica glass. Consequently, this fiber does not support any guided modes and its transmission capabilities are therefore limited by leakage loss [85]. Leaky is the case where the electric field decays monotonically for a finite distance in the transverse direction. Thus, the radiation field travels through a relatively long distances mostly when it propagates along the fiber axis (in the core) [84].

The light guiding mechanism is originated from the partial internal reflection [76]. Since the losses caused by these reflections greatly affect the high order modes, the fundamental mode will be mostly transmitted in a sufficiently long fiber. In fact, the loss of the fundamental mode HE11 scales as 1/a^3, so it becomes very high for diameters smaller than~100 µm.

2.3.1 Capillary modes

The modes supported by the cylindrical waveguide are represented by Bessel functions. When the capillary core is large compared to the laser wavelength, analytic expressions are used to describe the vectorial modes using the cylinder coordinates (r,θ) [76].

$$e_{n,m}(r,\theta) = e^{r}_{n,m}(r,\theta)\,\hat{r} + e^{\theta}_{n,m}(r,\theta)\,\hat{\theta}, \qquad (2-45)$$

$$e^{r}_{n,m} = J_{n-1}\left(\frac{u_{n,m}}{a}r\right)\sin[(n-1)\theta], \qquad (2-46)$$

$$e^{\theta}_{n,m}(r) = J_{n-1}\left(\frac{u_{n,m}}{a}r\right)\cos[(n-1)\theta], \qquad (2-47)$$

where $\hat{r}$ and $\hat{\theta}$ are the unit vectors in the radial and azimuthal directions, $J_{n-1}$is the first kind Bessel function of order $n-1$ and $u_{n,m}$ is the mth zero root of the equation $J_{n-1}(u_{n,m})$, i.e., $u_{1,m} = 2.405(m=1)$, $5.52(m=2)$, $8.654(m=3)$

Inside the hollow region, $|n|$ is the number of periods of each field component in the θ-direction, and m, is both the order of the Bessel root and the maxima and minima of each component in the radial direction. As the laser beam is usually linearly polarized, the modes that are expected in HCC can be approximated as linearly polarized modes LP$_{n,m}$. [66,86]. i.e., the transverse intensity distribution of the modes remains radially symmetric. The analytic expression to describe the transversal spatial profile is.

$$e_{1,m}(r,\theta) = J_0\left(\frac{u_{1,m}}{a}r\right), \qquad (2-48)$$

In this notation, the fundamental mode is the EH$_{11}$ mode and the root is $u_{1,1}=2.405$. The representations of the three lowest orders are shown in Fig. 2.5.

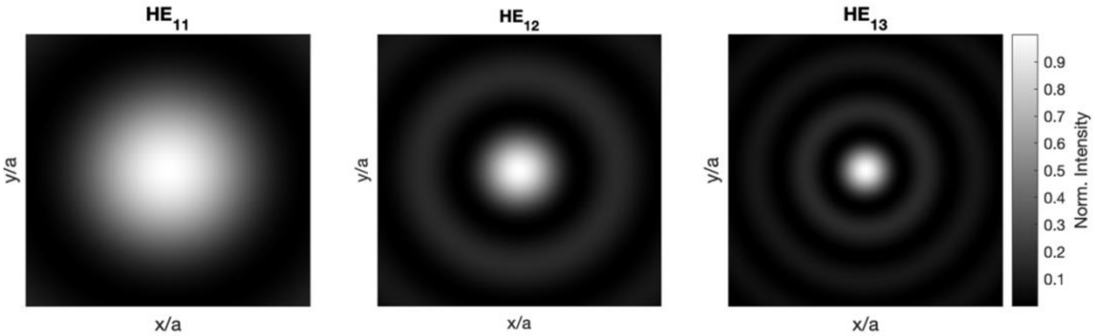

Fig. 2.5 Normalized intensity profiles of the EH1m modes in the transverse plane (x,y), where a represents the core radius of the capillary.

Refractive index in HCC

The Sellmeier equation also allows to calculate the refractive index of the gas n_{gas} which depends on the gas pressure (p) and temperature (T) .

$$n_{gas}(\lambda, \mathrm{p}, \mathrm{T}) = 1 + \left(\frac{T_0}{T}\right)\left(\frac{p}{p_0}\right)\delta(\lambda) \;, \qquad (2-49)$$

where, $\delta(\lambda)$ is the Sellmeier equation and its coefficients are available in the literature for different gases as a function of the wavelength [87].

$$\delta(\lambda) = \left[\frac{B_1\lambda^2}{\lambda^2 - C_1} + \frac{B_2\lambda^2}{\lambda^2 - C_2}\right]_{p_0, T_0} \;, \qquad (2-50)$$

T_0 and p_0 are the standard temperature and pressure, respectively.
The Sellmeier coefficients for argon, neon, krypton, and xenon are displayed in Table 2-2

Table 2-2 Sellmeier coefficients at $p_0 = 1000$ mbar and $T_0 = 273$ K, λ is in micrometers [87].

Gas	$B_1 \times 10^8$	$C_1 \times 10^6$	$B_2 \times 10^8$	$C_2 \times 10^3$
Argon	20332.29	206.12	34458.31	8.066
Neon	9154.48	656.97	4018.63	5.728
Krypton	26102.88	2.01	56946.82	10.043
Xenon	103701.61	12.75	31228.61	0.561

The refractive index calculated for different noble gases is displayed in Fig. 2.6, by using the values of the Table 2-2 and Eq. (2-49).

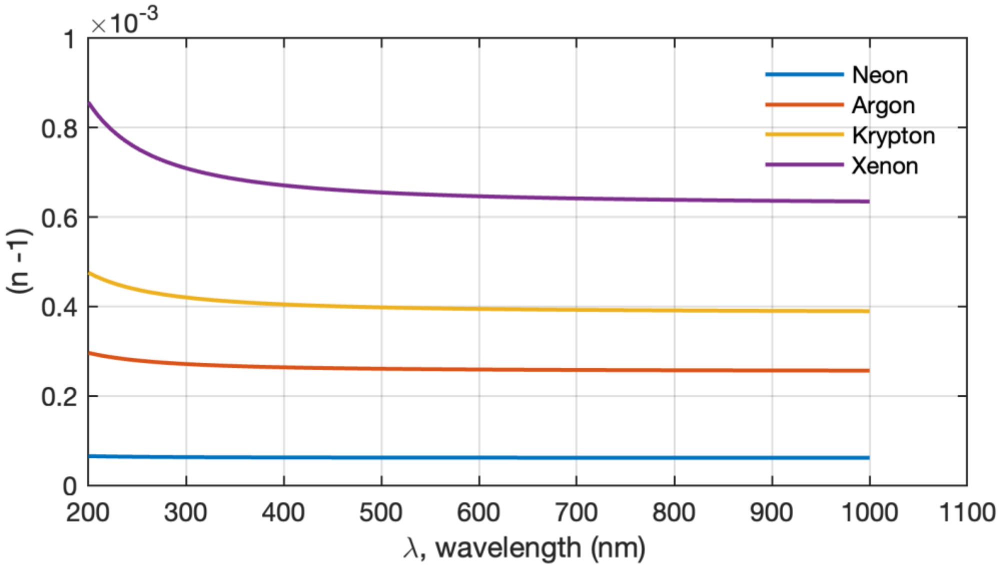

Fig. 2.6 Refractive index as a function of wavelength for different noble gases at pressure 1 bar at T=293 K.

2.3.2 Dispersion Properties

The linear dispersion of a HCC is described by Marcatili and Schmetlzer model [76]. In the leaky guiding, the electric field goes to zero outside the core fiber, i.e., the light propagates mostly in the core. Mathematical relation that expresses the transverse wavevector $\beta_\perp$is:

$$J_0(\beta_\perp a) = 0 \tag{2-51}$$

The longitudinal propagation constant β_z can be written in terms of the wave-vectors as:

$$\beta_z = \sqrt{\beta^2 - \beta_\perp^2}, \tag{2-52}$$

such that $\beta_\perp a = u_{n,m}$. Thus, it leads to:

$$\beta_z = \sqrt{\beta^2 - \frac{u_{m,n}^2}{a^2}} \tag{2-53}$$

In a gas filled HCC, the refractive index in the core is related to the one of the gas n_{gas}. The wave vector is written as $\beta = n_{gas}k$, with $k = \omega / c$. By substituting in eq. (2-53), it becomes :

$$\beta_z \approx k\sqrt{n_{gas}^2 - \frac{u_{n,m}{}^2}{a^2k^2}}, \tag{2-54}$$

or

$$\beta_z(\lambda,p,T) = \left(\frac{2\pi}{\lambda}\right)\sqrt{n_{gas}^2(\lambda,p,T) - \left(\frac{u_{n,m}\lambda}{2\pi a}\right)^2}, \tag{2-55}$$

From Eq. (2-55) we conclude that the dispersion in an HCC depends on: (i) the filling properties of the gases according to the temperature and pressure, and (ii) the geometry of the fiber according to the core radius.

In HCC with a small core size, the loss α becomes important and scales as[76]:

$$\alpha_{n,\mathrm{m}}\left[\frac{\mathrm{dB}}{\mathrm{m}}\right] \approx 8.686\left(\frac{u_{n,\mathrm{m}}}{2}\right)^2 \frac{\lambda^2}{a^3} \tag{2-56}$$

At 800 nm the core diameter must be larger than 100 µm in order to keep the loss below 10 dB/m. When the light is coupled in the fundamental mode EH_{11}, the power is attenuated according to $P(z) = P(0)\,e^{-\alpha_{1,m}z}$. The mode that presents the lowest loss is EH_{11}, and the spatial profile is close to Gaussian shape.

The group velocity dispersion

Since in the hollow core capillary, it is possible to have a wide variety of gas species, temperatures, and pressures, the properties of dispersion and non-linearity can be tuned to target specific effects.

The second order dispersion term β_2 is usually used to quantify the dispersion. As an example, Fig. 2.7 shows the spectral evolution of β_2 for several core radius when no gas is injected in the core. The β_2 value is completely negative and decreases with the core radius, when $n_{gas}=1$, such as:

$$\beta_2(\lambda) \approx -\frac{\lambda^3 u_{m,n}^2}{8\pi^3 a^2 c^2} \qquad (2-57)$$

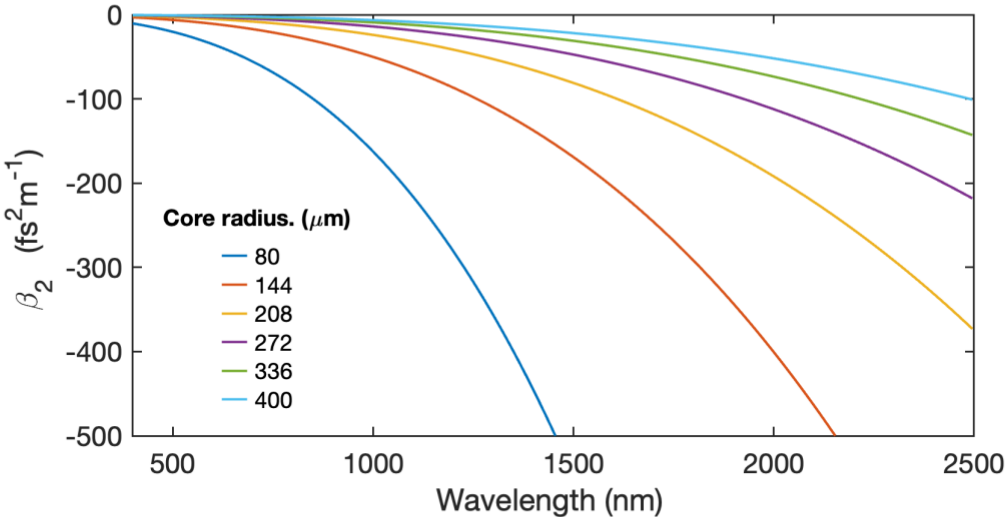

Fig. 2.7 Calculated dispersion term, β_2 in an evacuated HCC with a core radius from 80 to 400 μm.

Together with the broadband transmission, HCC also offers the possibility to tune the dispersion profile. The tunability arises from the balance of the dispersion of the gas with the negative dispersion of the waveguide. Then, ZDW ($\beta_2=0$ fs^{2}m^{-1}) is also an important parameter because it can be easily tuned with the pressure and the core radius capillary, see Fig. 2.8.

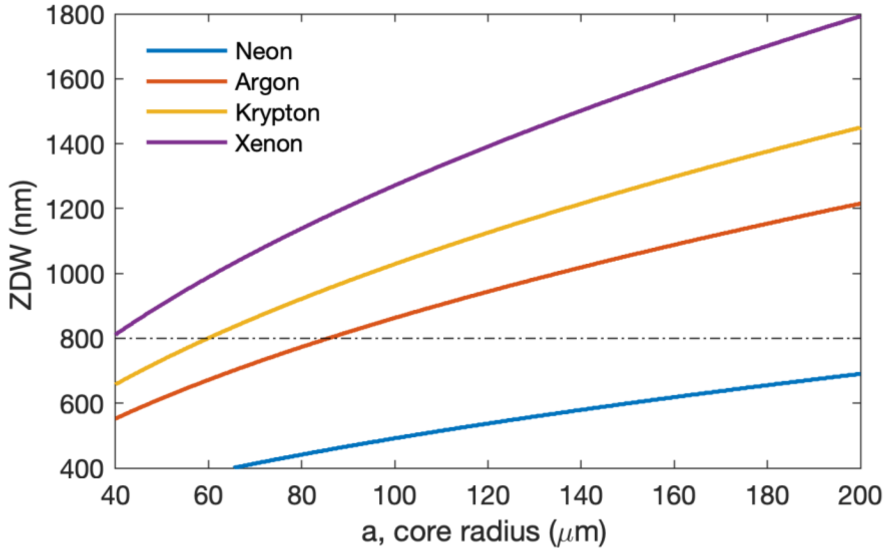

Fig. 2.8 Zero dispersion wavelength (ZDW) as the function of the core radius for various rare gases, at a pressure of 1 bar at T=293 K.

The GVD in an argon-filled HCC at various pressures is shown in the Fig. 2.9. A positive dispersion contribution from the gas compensates the negative dispersion coming from the waveguide. This makes possible to change the ZDW position, and set a pump with a central wavelength in normal or anomalous dispersion regime.
For example, for a core radius of 75 μm filled with argon, at 800 nm the regime changes when the gas pressure is over 1.2 bar.

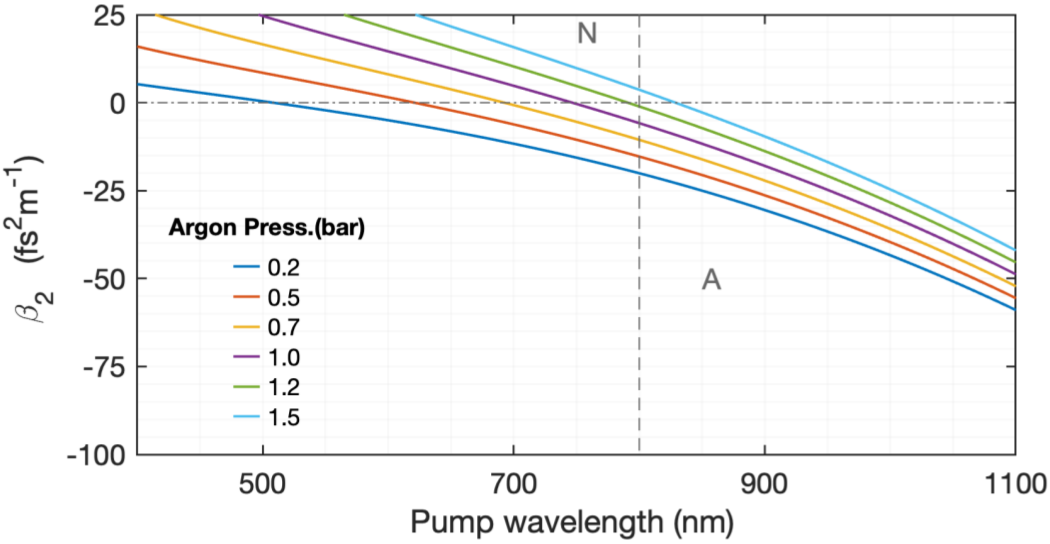

Fig. 2.9 Group velocity dispersion as the function the argon gas at a pressure from 0.2 to 1.5 bar in a HCC with a core radius of 75 μm.

2.3.3 Coupling in HCC

A hollow core capillary makes possible the propagation of intense laser beams in comparison with a solid material. The fundamental mode, EH_{11}, is of particular interest, since it has the lowest loss and the highest group velocity [88]. However, the coupling is achieved from a beam propagating in a free space.

Assuming an incident beam with a Gaussian shape and linearly polarized, the electric field is written as $E_i = E_0 \exp(-r^2/W_0^2)$. In order to achieve the maximum amount of power inside the capillary, it is necessary to get a spatial overlap between the input beam and the fundamental mode of the HCC.

The analytic expression that represents the coupling efficiency between an injected beam with a Gaussian profile and the fundamental EH_{1m} modes is given by [89]:

$$\eta_{1m}=\frac{\left|\int_0^a e^{-r^2/W_0^2}J_0\left(\frac{u_{1m}r}{a}\right)\ rdr\right|^2}{\left(\int_0^{+\infty} e^{-2\left(\frac{r}{W_0}\right)^2} rdr\right)\left(\int_0^a J_0^2\left(\frac{u_{1m}r}{a}\right)rdr\right)}, \qquad (2-58)$$

where, W_0 represents the beam waist and r, the radial coordinate.

Fig. 2.10 shows the calculated coupling efficiency of EH_{1m} modes as the function of the input beam spot size and the capillary radius (W_0/a) .The optimum coupling is when $W_0=0.645a$ and it leads to a coupling efficiency of 98%.

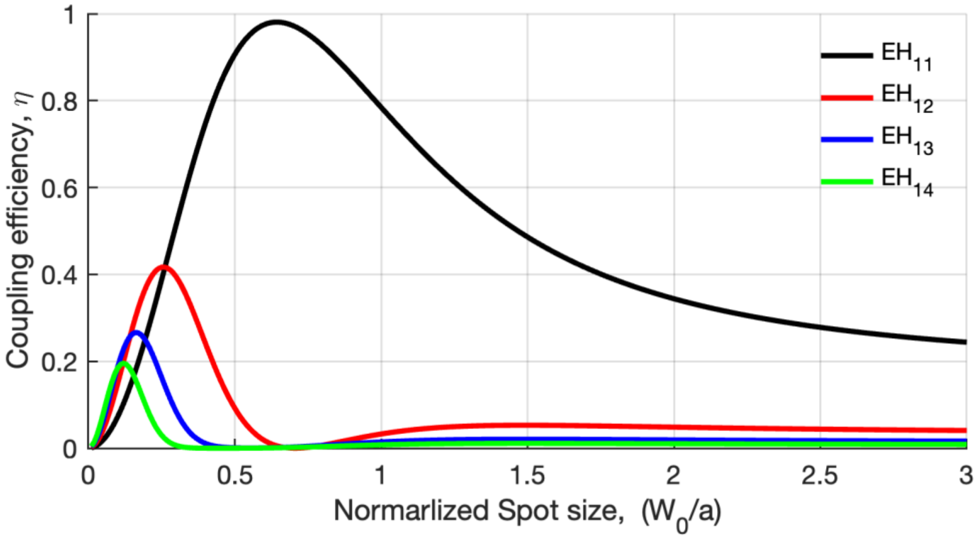

Fig. 2.10 Coupling efficiency for four HCC modes EH_{1m} as a function of the normalized input spot size, (W_0/a).

For a spot size value smaller than the optimum, an excitation of the higher order modes can be produced. Additionally, using heavy gases at high pressure can lead instabilities at the fiber entrance, affecting the coupling. Especially at high power, the misaligned incoming laser beam could cause damage to the surrounding glass in the cladding.

2.4 Characterization techniques of ultrashort pulses

Before and during experiments, it is important to know the pulse shape and the pulse duration in order to control the ultra-short phenomena. Likewise, the measurements of the output pulses generated by the nonlinear optical process can help to better understand the behavior. Therefore, I will outline some techniques used in this work to characterize the laser pulses.

2.4.1 Intensity autocorrelation

A well-known technique to measure the pulse duration by using the pulse itself is the autocorrelation [90]. The pulse under investigation is divided into two parts. One replica is delayed respect to the other. The two pulses are recombined into a second-order non-linear medium to generate a signal proportional to the intensity product of the two pulses, i.e., with the second-harmonic generation (**SHG**).

The intensity autocorrelation is directly obtained, when the two delayed pulses are focused non collinearly into the nonlinear crystal.

$$S(\tau) \propto \int_{-\infty}^{\infty} I(t)\, I(t+\tau)\; dt \qquad (2-59)$$

The signal is measured as function of the delay, τ. The measurement provides the information on the pulse shape. To estimate the pulse duration by using this method, we need to assume a pulse form and then calculate the pulse duration for the assumed shape. The coefficient changes according to the pulse shape and the coefficients are given in Table 2-3.

Table 2-3 Ratio factor for a determine pulse shapes

Pulse shape	**Square**	**Gaussian**	**Hyperbolic Secant**	**Lorentzian**
$\Delta_{AC}/\Delta t$	1	1.41	1.54	2

The intensity autocorrelation technique has been used in the experimental part of this work. The task was challenging, given that the power was low and the bandwidth was broad. Different crystal thickness was tested to ensure the efficient phase matching for SHG.

2.4.2 Frequency Resolved Optical Gating, FROG

Frequency Resolved Optical Gating (**FROG**) is a technique that combines the temporal frequency domain resolutions simultaneously [91]. FROG is a spectrally resolved autocorrelation. This advantage makes it possible to determine completely the shape of the pulse.

In the FROG, the signal is generated by SHG and measured with a spectrometer instead of a photodetector, see Fig. 2.11. The intensity autocorrelation can be retrieved by projecting the FROG trace onto the frequency axis [90]. Thus, the phase and amplitude of an unknown pulse can be reconstructed.

The FROG trace $I_{FROG}(\omega,\tau)$ is a plot of frequency versus delay, such as

$$\mathrm{I}_{\mathrm{FROG}}^{\mathrm{SHG}}(\omega,\tau) \propto \left| \int_{-\infty}^{\infty} \mathrm{E}(t)\, \mathrm{E}(t+\tau)\, e^{-i\omega t}\, dt \right|^2 \qquad (2-60)$$

One disadvantage of Second Harmonic Frequency Resolved Optical Gating (**SHG FROG**) (1) is the invariance with the phase sign. The SHG FROG trace is always symmetric around τ, $I_{FROG}(\omega,\tau) = I_{FROG}(\omega,-\tau)$. In other words, the SHG FROG trace is identical for a pulse with positive or negative linear chirp.

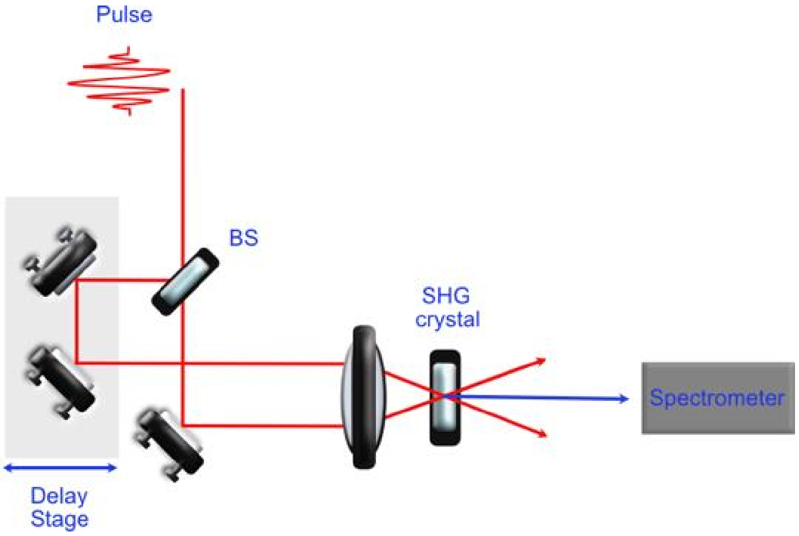

Fig. 2.11 Scheme of the configuration for SHG FROG.

2.5 References to Chapter 2

1. Schawlow, A. L. and Townes, C. H. Infrared and optical masers. *Physical Review* **112**, 1940–1949 (1958).
2. Maiman, T. H. Stimulated optical radiation in Ruby. *Nature* **187**, 493–494 (1960).
3. Hall, R. N., Fenner, G. E., Kingsley, J. D., Soltys, T. J. and Carlson, R. O. Coherent light emission from GaAs junctions. *Physical Review Letters* **9**, 366–368 (1962).
4. Javan, A., Bennett, W. R. and Herriott, D. R. Population inversion and continuous optical maser oscillation in a gas discharge containing a He-Ne mixture. *Physical Review Letters* **6**, 106–110 (1961).
5. Strickland, D. and Mourou, G. Compression of amplified chirped optical pulses. *Optics Communications* **56**, 219–221 (1985).
6. Koester, C. J. and Snitzer, E. Amplification in a Fiber Laser. *Appl. Opt* **3**, RP1 (2017).
7. Nilsson, J. *et al.* High-power wavelength-tunable cladding-pumped rare-earth-doped silica fiber lasers. *Optical Fiber Technology* **10**, 5–30 (2004).
8. Lavenu, L. *et al.* High-energy few-cycle Yb-doped fiber amplifier source based on a single nonlinear compression stage. *Optics Express* **25**, 7530 (2017).
9. Blow, K. J. and Wood, D. Theoretical Description of Transient Stimulated Raman Scattering in Optical Fibers. *IEEE Journal of Quantum Electronics* **25**, 2665–2673 (1989).
10. Franken, P. A., Hill, A. E., Peters, C. W. and Weinreich, G. Generation of optical harmonics. *Physical Review Letters* **7**, 118–119 (1961).
11. Bass, M., Franken, P. A., Hill, A. E., Peters, C. W. and Weinreich, G. Optical mixing. *Physical Review Letters* **8**, 18–18 (1962).
12. Giordmaine, J. A. and Miller, R. C. Tunable coherent parametric oscillation in LiNbO3 at optical frequencies. *Physical Review Letters* **14**, 973–976 (1965).
13. Maker, P. D. and Terhune, R. W. Study of optical effects due to an induced polarization third order in the electric field strength. *Physical Review* **137**, 507–509 (1965).
14. New, G.H.C. and Ward, J. F. Optical third-harmonic generation in gases,. *Phys. Rev. Lett.* **19**, 556–559 (1967).

15. McWane, P. D. and Sealer, D. A. New measurements of intensity-dependent changes in the refractive index of liquids. *Applied Physics Letters* **8**, 278–279 (1966).
16. Carman, R. L., Chiao, R. Y. and Kelley, P. L. Observation of degenerate stimulated four-photon interaction and four-wave parametric amplification. *Physical Review Letters* **17**, 1281–1283 (1966).
17. Brahms, C., Belli, F. and Travers, J. C. Infrared attosecond field transients and UV to IR few-femtosecond pulses generated by high-energy soliton self-compression. *Physical Review Research* **2**, 043037 1–8 (2020).
18. Manzoni, C. and Cerullo, G. Few-optical-cycle pulses from near-IR to UV by non linear frequency conversion. in *2015 IEEE Photonics Conference, IPC 2015* 206–207 (2015).
19. Tzankov, P. *et al.* 300 μJ noncollinear optical parametric amplifier in the visible at 1 kHz repetition rate. *Optics Letters* **31**, 3629–3631 (2006).
20. Odhner, J. H. and Levis, R. J. High-energy noncollinear optical parametric amplifier producing 4 fs pulses in the visible seeded by a gas-phase filament. *Optics Letters* **40**, 3814–3817 (2015).
21. Viotti, A.-L. *et al.* Supercontinuum generation and soliton self-compression in χ (2)-structured KTiOPO 4. *Optica* **5**, 711–717 (2018).
22. Andriukaitis, G. *et al.* 90 GW peak power few-cycle mid-infrared pulses from an optical parametric amplifier. *Optics Letters* **36**, 2755–2757 (2011).
23. Shamir, Y. *et al.* High-average-power 2 μm few-cycle optical parametric chirped pulse amplifier at 100 kHz repetition rate. *Optics Letters* **40**, 5546–5549 (2015).
24. Silva, F., Bates, P. K., Esteban-Martin, A., Ebrahim-Zadeh, M. and Biegert, J. High-average-power, carrier-envelope phase-stable, few-cycle pulses at 21 μm from a collinear BiB3O6 optical parametric amplifier. *Optics Letters* **37**, 933 (2012).
25. Gu, X. *et al.* Generation of carrier-envelope-phase-stable 2-cycle 740-μJ pulses at 21-μm carrier wavelength. *Optics Express* **17**, 62–69 (2009).
26. Robert, P. *et al.* Spectral correlation of four-wave mixing generated in a photonic crystal fiber pumped by a chirped pulse. *Optics Letters* **45**, 4148–4151 (2020).
27. Fourcade-Dutin, C. *et al.* Temporal distribution measurement of the parametric spectral gain in a photonic crystal fiber pumped by a chirped pulse. *Photonics* **6**, 1–9 (2019).
28. Fourcade-Dutin, C., Miranda, O. Z., Mounaix, P. and Bigourd, D. Toward mid-infrared ultra-short pulse generation in a gas-filled hollow-core photonic crystal fiber. in *Advanced Photonics Congress 2021* (2021). doi:10.1364/noma.2021.notu3c.5.
29. J. C. Travers, C. Brahms, F. Belli, T. F. Grigorova, A. L. M. S. Advances in nonlinear optics in gas-filled hollow-core fibers. in *in OSA Nonlinear Optics 2021, R. Boyd, C. Conti, D. Christodoulides, and P. Rakich, eds., OSA Technical Digest (Optical Society of America, 2021), paper NM2A.1.* (2021).
30. Travers, J. C., Grigorova, T. F., Brahms, C. and Belli, F. High-energy pulse self-compression and ultraviolet generation through soliton dynamics in hollow capillary fibres. *Nature Photonics* **13**, 547–554 (2019).
31. Kida, Y. and Imasaka, T. Optical parametric amplification of a supercontinuum in a gas. *Applied Physics B: Lasers and Optics* **116**, 673–680 (2014).
32. Ippen, E. P. Low-power quasi-cw raman oscillator. *Applied Physics Letters* **16**, 303–305 (1970).

33. Misoguti, L. *et al.* Generation of broadband VUV light using third-order cascaded processes. *Physical Review Letters* **87**, 013601/1-013601/4 (2001).
34. Adamu, A. I. *et al.* Deep-UV to Mid-IR Supercontinuum Generation driven by Mid-IR Ultrashort Pulses in a Gas-filled Hollow-core Fiber. *Scientific Reports* **9**, 1–8 (2019).
35. Wagner, N. L. *et al.* Self-compression of ultrashort pulses through ionization-induced spatiotemporal reshaping. *Physical Review Letters* **93**, 173902–173906 (2004).
36. Popmintchev, T. *et al.* Bright coherent ultrahigh harmonics in the kev x-ray regime from mid-infrared femtosecond lasers. *Science (1979)* **336**, 1287–1291 (2012).
37. Cabasse, A., Machinet, G., Dubrouil, A., Cormier, E. and Constant, E. Optimization and phase matching of fiber-laser-driven high-order harmonic generation at high repetition rate. *Optics Letters* **37**, 4618–4620 (2012).
38. Couch, D. E. *et al.* Ultrafast 1 MHz vacuum-ultraviolet source via highly cascaded harmonic generation in negative-curvature hollow-core fibers. *Optica* **7**, 832–837 (2020).
39. Brahms, C., Belli, F. and Travers, J. C. Infrared attosecond field transients and UV to IR few-femtosecond pulses generated by high-energy soliton self-compression. *Physical Review Research* **2**, 0–1 (2020).
40. Ciriolo, A. G. *et al.* Generation of ultrashort pulses by four wave mixing in a gas-filled hollow core fiber. *Journal of Optics* **20**, 125503-1 /125503-9 (2018).
41. Belli, F., Abdolvand, A., Travers, J. C. and Russell, P. St. J. Highly efficient deep UV generation by four-wave mixing in gas-filled hollow-core photonic crystal fiber. *Optics Letters* **44**, 5509 (2019).
42. Durfee, C. G., Backus, S., Kapteyn, H. C. and Murnane, M. M. Intense 8-fs pulse generation in the deep ultraviolet. *Optics Letters* **24**, 697 (1999).
43. Faccio, D., Grün, A., Bates, P. K., Chalus, O. and Biegert, J. Optical amplification in the near-infrared in gas-filled hollow-core fibers. *Optics Letters* **34**, 2918 (2009).
44. Kida, Y. and Kobayashi, T. Generation of sub-10 fs ultraviolet Gaussian pulses. *Journal of the Optical Society of America B* **28**, 139 (2011).
45. Fourcade-Dutin, C., Zurita-Miranda, O., Mounaix, P. and Bigourd, D. Mid-infrared ultra-short pulse generation in a gas-filled hollow-core photonic crystal fiber pumped by two-color pulses. *Fibers* **9**, 21 (2021).
46. Stolen, R. H., Bjorkholm, J. E. and Ashkin, A. Phase-matched three-wave mixing in silica fiber optical waveguides. *Applied Physics Letters* **24**, 308–310 (1974).
47. Hill, K. O., Johnson, D. C. and Kawasaki, B. S. Efficient conversion of light over a wide spectral range by four-photon mixing in a multimode graded-index fiber: erratum. *Applied Optics* **20**, 2769 (1981).
48. Agrawal, G. P. Nonlinear fiber optics: its history and recent progress [Invited]. *Journal of the Optical Society of America B* **28**, A1 (2011).
49. Nazemosadat, E., Pourbeyram, H. and Mafi, A. Phase matching for spontaneous frequency conversion via four-wave mixing in graded-index multimode optical fibers. *Journal of the Optical Society of America B* **33**, 144 (2016).
50. Rademacher, G., Warm, S. and Petermann, K. Analytical description of cross-modal nonlinear interaction in mode multiplexed multimode fibers. *IEEE Photonics Technology Letters* **24**, 1929–1932 (2012).
51. Mecozzi, A., Antonelli, C. and Shtaif, M. Nonlinear propagation in multi-mode fibers in the strong coupling regime. *Optics Express* **20**, 11673 (2012).

52. Mafi, A. Pulse Propagation in a Short Nonlinear Graded-Index Multimode Optical Fiber. *Journal of Lightwave Technology* **30**, 2803–2811 (2012).
53. Ding, E., Lefrancois, S., Kutz, J. N. and Wise, F. W. Scaling fiber lasers to large mode area: An investigation of passive mode-locking using a multi-mode fiber. *IEEE Journal of Quantum Electronics* **47**, 597–606 (2011).
54. Nazemosadat, E. and Mafi, A. Nonlinear switching in multicore versus multimode waveguide junctions for mode-locked laser applications. *Optics Express* **21**, 30739 (2013).
55. Mafi, E. N. and A. Nonlinear switching in a two- concentric-core chalcogenide glass optical fiber for passively mode-locking a fiber laser. *Opt. Lett.* **39**, 4675–4678 (2014).
56. Fu, S. *et al.* Passive Q-switching of an all-fiber laser induced by the Kerr effect of multimode interference. *Optics Express* **23**, 17255 (2015).
57. Einarsson, G. Pulse broadening in graded-index optical fibers: correction. *Applied Optics* **25**, 1030 (1986).
58. Renninger, W. H. and Wise, F. W. Optical solitons in graded-index multimode fibres. *Nature Communications* **4**, 1719 (2013).
59. S. Raghavan G. P. Agrawal. Spatiotemporal solitons in inhomogeneous nonlinear media. *Opt. Commun* **180**, 377–382 (2000).
60. Kibler, B. and Béjot, P. Discretized Conical Waves in Multimode Optical Fibers. *Physical Review Letters* **126**, (2021).
61. Faccio, D. *et al.* Spatio-temporal reshaping and X Wave dynamics in optical filaments. *Optics Express* **15**, 13077 (2007).
62. Konorov, S. O., Fedotov, A. B. and Zheltikov, A. M. Enhanced four-wave mixing in a hollow-core photonic-crystal fiber. *Optics Letters* **28**, 1448 (2003).
63. Ding, X., Selim Habib, Md., Amezcua-Correa, R. and Moses, J. Near-octave intense mid-infrared by adiabatic down-conversion in hollow anti-resonant fiber. *Optics Letters* **44**, 1084 (2019).
64. Finger, M. A., Joly, N. Y., Russell, P. S. J. and Chekhova, M. v. Characterization and shaping of the time-frequency Schmidt mode spectrum of bright twin beams generated in gas-filled hollow-core photonic crystal fibers. *Physical Review A* **95**, 053814 (2017).
65. Cordier, M. *et al.* Active engineering of four-wave mixing spectral correlations in multiband hollow-core fibers. *Optics Express* **27**, 9803 (2019).
66. Tempea, G. and Brabec, T. Theory of self-focusing in a hollow waveguide. *Optics Letters* **23**, 762 (1998).
67. Crego, A., Conejero Jarque, E. and San Roman, J. Influence of the spatial confinement on the self-focusing of ultrashort pulses in hollow-core fibers. *Scientific Reports* **9**, 9546 (2019).
68. Chapman, R. T. *et al.* Modal effects on pump-pulse propagation in an Ar-filled capillary. *Optics Express* **18**, 13279 (2010).
69. Mangini, F. *et al.* Self-imaging dynamics in nonlinear GRIN multimode optical fibers. *Frontiers in Optics / Laser Science* **28**, 24005–24021 (2020).
70. Wright, L. G., Wabnitz, S. W., Christodoulides, D. N. and Wise, F. W. Ultrabroadband dispersive radiation by spatiotemporal oscillation of multimode waves. in *Photonics and Fiber Technology 2016* (2016). doi:10.1364/NP.2016.NW4A.1.

71. Marhic, M. E. *Fiber optical parametric amplifiers, oscillators and related devices*. *Fiber Optical Parametric Amplifiers, Oscillators and Related Devices* vol. 9780521861 (Cambridge University Press, 2007).
72. Couairon, A. *et al.* Practitioner’s guide to laser pulse propagation models and simulation. *European Physical Journal: Special Topics* **199**, 5–76 (2011).
73. Brabec, T. and Krausz, F. Intense few-cycle laser fields: Frontiers of nonlinear optics. *Reviews of Modern Physics* **72**, 545–591 (2000).
74. Agrawal, G. P. *Nonlinear fiber optics*. *Nonlinear Fiber Optics* (Academic Press, 2019). doi:10.1016/C2018-0-01168-8.
75. Boyd, R. W. *Nonlinear Fiber Optics*. (2008).
76. Marcatili, E. A. J. and Schmeltzer, R. A. Hollow Metallic and Dielectric Waveguides for Long Distance Optical Transmission and Lasers. *Bell System Technical Journal* **43**, 1783–1809 (1964).
77. Lehmeier, H. J., Leupacher, W. and Penzkofer, A. Nonresonant third order hyperpolarizability of rare gases and N2 determined by third harmonic generation. *Optics Communications* **56**, 67–72 (1985).
78. Couairon, A., Chakraborty, H. S. and Gaarde, M. B. From single-cycle self-compressed filaments to isolated attosecond pulses in noble gases. *Physical Review A - Atomic, Molecular, and Optical Physics* **77**, (2008).
79. Sinkin, O. V., Holzlöhner, R., Zweck, J. and Menyuk, C. R. Optimization of the split-step Fourier method in modeling optical-fiber communications systems. *Journal of Lightwave Technology* **21**, 61–68 (2003).
80. Marburger, J. H. Self-focusing: Theory. *Progress in Quantum Electronics* **4**, 35–110 (1975).
81. Milosevic, N., Tempea, G. and Brabec, T. Optical pulse compression: bulk media versus hollow waveguides. *Optics Letters* **25**, 672–674 (2000).
82. Stolen, R. H. and Lin, C. Self-phase-modulation in silica optical fibers. *Physical Review A* **17**, 1448–1453 (1978).
83. Dudley, J. M. and Taylor, J. R. *Supercontinuum generation in optical fibers*. *Supercontinuum Generation in Optical Fibers* vol. 9780521514 (2010).
84. Snitzer, E. Cylindrical Dielectric Waveguide Modes*. *J Opt Soc Am* **51**, 491 (1961).
85. Archambault, J. L., Black, R. J., Lacroix, S. and Bures, J. Loss Calculations for Antiresonant Waveguides. *Journal of Lightwave Technology* **11**, 416–423 (1993).
86. Hesketh, G. D., Poletti, F. and Horak, P. Spatio-Temporal Self-Focusing in Femtosecond Pulse Transmission Through Multimode Optical Fibers. *Journal of Lightwave Technology* **30**, 2764–2769 (2012).
87. Börzsönyi, A., Heiner, Z., Kalashnikov, M. P., Kovács, A. P. and Osvay, K. Dispersion measurement of inert gases and gas mixtures at 800 nm. *Applied Optics* **47**, 4856–4863 (2008).
88. Cros, B. *et al.* Eigenmodes for capillary tubes with dielectric walls and ultraintense laser pulse guiding. *Physical Review E - Statistical Physics, Plasmas, Fluids, and Related Interdisciplinary Topics* **65**, (2002).
89. M. Nisoli, S. Stagira, S. De Silvestri, O. Svelto, S. Sartinia Z. Cheng, G. Tempea, C. Spielmann, and F. K. Towards a terawatt-scale sub-10-fs laser technology. *IEEE J. of selected topics in quantum ELECTRONICS* **4**, (1998).
90. Trebino, R. *Frequency-Resolved Optical Gating: The Measurement of Ultrashort Laser Pulses*. *Frequency-Resolved Optical Gating: The Measurement of Ultrashort Laser Pulses* (2000). doi:10.1007/978-1-4615-1181-6.

91. Trebino, R. *et al.* Measuring ultrashort laser pulses in the time-frequency domain using frequency-resolved optical gating. *Review of Scientific Instruments* **68**, 3277–3295 (1997).
92. Stolen, R. Phase-matched-stimulated four-photon mixing in silica-fiber waveguides. *IEEE Journal of Quantum Electronics* **11**, 100–103 (1975).
93. Russell, P. Photonic Crystal Fibers. *Science (1979)* **299**, 358–362 (2003).
94. Knight, J. C. Photonic crystal fibres. *Nature* **424**, 847–851 (2003).
95. Bigourd, D., D'Augerès, P. B., Dubertrand, J., Hugonnot, E. and Mussot, A. Ultra-broadband fiber optical parametric amplifier pumped by chirped pulses. *Optics Letters* **39**, 3782 (2014).
96. Bigourd, D. *et al.* Parametric gain shaping from a structured pump pulse. *IEEE Photonics Technology Letters* **31**, 214–217 (2019).
97. Vanvincq, O., Fourcade-Dutin, C., Mussot, A., Hugonnot, E. and Bigourd, D. Ultrabroadband fiber optical parametric amplifiers pumped by chirped pulses Part 1: analytical model. *Journal of the Optical Society of America B* **32**, 1479 (2015).
98. Fourcade-Dutin, C., Vanvincq, O., Mussot, A., Hugonnot, E. and Bigourd, D. Ultrabroadband fiber optical parametric amplifier pumped by chirped pulses Part 2: sub-30-fs pulse amplification at high gain. *Journal of the Optical Society of America B* **32**, 1488 (2015).
99. Bigourd, D. *et al.* High-gain fiber, optical-parametric, chirped-pulse amplification of femtosecond pulses at 1 µm. *Optics Letters* **35**, 3480 (2010).
100. Bigourd, D., Lago, L., Mussot, A., Kudlinski, A. and Hugonnot, E. High gain fiber optical parametric chirped pulse amplification of femtosecond pulses at 1 µm. *Optics InfoBase Conference Papers* **35**, (2011).
101. Qin, Y., Batjargal, O., Cromey, B. and Kieu, K. All-fiber high-power 1700 nm femtosecond laser based on optical parametric chirped-pulse amplification. *Optics Express* **28**, 2317 (2020).
102. Qin, Y. *et al.* Watt-level all-fiber optical parametric chirped-pulse amplifier working at 1300 nm. *Optics Letters* **44**, 3422 (2019).
103. Ho, M. C., Uesaka, K., Marhic, M., Akasaka, Y. and Kazovsky, L. G. 200-nm-bandwidth fiber optical amplifier combining parametric and Raman gain. *Journal of Lightwave Technology* **19**, 977–981 (2001).
104. Lesvigne, C. *et al.* Visible supercontinuum generation controlled by intermodal four-wave mixing in microstructured fiber. *Optics Letters* **32**, 2173 (2007).
105. Tu, H., Jiang, Z., Marks, D. L. and Boppart, S. A. Intermodal four-wave mixing from femtosecond pulse-pumped photonic crystal fiber. *Applied Physics Letters* **94**, 101109 (2009).
106. Yuan, J. *et al.* Polarization-dependent intermodal four-wave mixing in a birefringent multimode photonic crystal fiber. *Optics Letters* **42**, 1644 (2017).
107. Dupiol, R. *et al.* Far-detuned cascaded intermodal four-wave mixing in a multimode fiber. *Optics Letters* **42**, 1293 (2017).
108. Yuan, J. *et al.* Experimental generation of discrete ultraviolet wavelength by cascaded intermodal four-wave mixing in a multimode photonic crystal fiber. *Optics Letters* **42**, 3537 (2017).
109. Velazquez-Ibarra, L., Diez, A., Silvestre, E. and Andres, M. V. Tunable Four-Wave Mixing Light Source Based on Photonic Crystal Fibers with Variable Chromatic Dispersion. *Journal of Lightwave Technology* **37**, 5722–5726 (2019).

110. Delagnes, J.-C. *et al.* High-power widely tunable ps source in the visible light based on four wave mixing in optimized photonic crystal fibers. *Optics Express* **26**, 11265 (2018).

111. Ryf, R. *et al.* Mode-Division Multiplexing Over 96 km of Few-Mode Fiber Using Coherent 6x6 MIMO Processing. *Journal of Lightwave Technology* **30**, 521–531 (2012).

112. Wright, L. G., Christodoulides, D. N. and Wise, F. W. Controllable spatiotemporal nonlinear effects in multimode fibres. *Nature Photonics* **9**, 306–310 (2015).

113. Krupa, K. *et al.* Multimode nonlinear fiber optics, a spatiotemporal avenue. *APL Photonics* **4**, 110901 (2019).

114. Rashleigh, S. C. Origins and Control of Polarization Effects in Single-Mode Fibers. *Journal of Lightwave Technology* **1**, 312–331 (1983).

115. Taylor, J. R. *Theory of Dielectric Optical Waveguides. 2nd Edition*. *Journal of Modern Optics* vol. 39 (1992).

116. Stolen, R. and Bjorkholm, J. Parametric amplification and frequency conversion in optical fibers. *IEEE Journal of Quantum Electronics* **18**, 1062–1072 (1982).

117. Ferguson, A. I. *The Elements of Nonlinear Optics*. *Journal of Modern Optics* vol. 38 (1991).

118. Musheghyan, M. *et al.* Tunable, few-cycle, CEP-stable mid-IR optical parametric amplifier for strong field applications. *Journal of Physics B: Atomic, Molecular and Optical Physics* **53**, (2020).

119. B. Shao, Y. Li, Y. Peng, P. Wang, J. Qian,Y. Leng, R. L. Broad-bandwidth high-temporal-contrast carrier-envelope-phase-stabilized laser seed for 100 PW lasers. *Opt. Lett.* **45**, (2020).

120. E. Rubino, J. Darginavičius, D. Faccio, P. Di Trapani, A. Piskarskas, A. D. Generation of broadly tunable sub-30-fs infrared pulses by four-wave optical parametric amplification. *Opt. Lett* **36**, 382–384 (2011).

121. J. Bromage, S.-W. Bahk, I. A. Begishev, C. Dorrer, M. J. Guardalben, B. N. Hoffman, J. B. Oliver, R. G. Roides, E. M. Schiesser, M. J. Shoup III, M. Spilatro, B. Webb, D. Weiner, J. D. Z. Technology development for ultra-intense all-OPCPA systems. *High Power Laser Science and Engineering* **7**, (2019).

122. Fu, W. and Wise, F. W. Normal-Dispersion Fiber Optical Parametric Chirped-Pulse Amplification. *2018 Conference on Lasers and Electro-Optics, CLEO 2018 - Proceedings* **43**, 5331 (2018).

123. Fourcade-Dutin, C. and Bigourd, D. Modulation instability in a dispersion oscillating fibre pumped by a broad band pulse. *Journal of Modern Optics* **64**, 500–506 (2017).

124. Dubietis, A. and Couairon, A. *Ultrafast Supercontinuum Generation in Transparent Solid-State Media*. (Springer Nature, 2019).

125. Ding, Y., Xu, J., Ou, H. and Peucheret, C. Mode-selective wavelength conversion based on four-wave mixing in a multimode silicon waveguide. *IET Conference Publications* **2013**, 198–200 (2013).

126. Pan, W., Jin, Q., Li, X. and Gao, S. All-optical wavelength conversion for mode-division multiplexing signals using four-wave mixing in a dual-mode fiber. *Journal of the Optical Society of America B* **32**, 2417 (2015).

127. C. Fourcade Dutin. *et al.* Post-compression of high-energy femtosecond pulses using gas ionization. *Optics Letters* **35**, 253 (2010).

128. Kolesik, M., Katona, G., Moloney, J.V., Wright, E. M. Physical factors limiting the spectral extent and band gap dependence of supercontinuum generation. *Phys. Rev. Lett* **91**, 043905 (2003).
129. Saari, P. and Reivelt, K. X-Shaped Propagation-Invariant localized light waves. *Physical Review Letters* **79**, 4135–4138 (1997).
130. Tzortzakis, S. *et al.* Formation of a conducting channel in air by self-guided femtosecond laser pulses. *Physical Review E - Statistical Physics, Plasmas, Fluids, and Related Interdisciplinary Topics* **60**, (1999).
131. Poletti, F. and Horak, P. Description of ultrashort pulse propagation in multimode optical fibers. *Journal of the Optical Society of America B* **25**, 1645 (2008).
132. Poletti, F. and Horak, P. Dynamics of femtosecond supercontinuum generation in multimode fibers. *Optics Express* **17**, 6134 (2009).
133. Mussot, A., Sylvestre, T., Provino, L. and Maillotte, H. Generation of a broadband single-mode supercontinuum in a conventional dispersion-shifted fiber by use of a subnanosecond microchiplaser. *Optics Letters* **28**, 1820 (2003).
134. Köttig, F., Tani, F., Travers, J. C. and Russell, P. S. J. Self-focusing below the critical power in gas-filled hollow-core PCF. in *Optics InfoBase Conference Papers* vol. Part F81-E (2017).
135. Mecozzi, A., Antonelli, C. and Shtaif, M. Coupled Manakov equations in multimode fibers with strongly coupled groups of modes. *Optics Express* **20**, 23436 (2012).
136. Tani, F., Travers, J. C. and St.J. Russell, P. Multimode ultrafast nonlinear optics in optical waveguides: numerical modeling and experiments in kagomé photonic-crystal fiber. *Journal of the Optical Society of America B* **31**, 311 (2014).
137. Benabid, F., Knight, J. C., Antonopoulos, G. and Russell, P. S. J. Stimulated Raman Scattering in Hydrogen-Filled Hollow-Core Photonic Crystal Fiber. *Science (1979)* **298**, 399–402 (2002).
138. Poletti, F. Nested antiresonant nodeless hollow core fiber. *Optics Express* **22**, 23807 (2014).
139. Cregan, R. F. *et al.* Single-Mode Photonic Band Gap Guidance of Light in Air. *Science (1979)* **285**, 1537–1539 (1999).
140. Knight, J. C., Broeng, J., Birks, T. A. and Russell, P. S. J. Photonic band gap guidance in optical fibers. *Science (1979)* **282**, 1476–1478 (1998).
141. Alharbi, M. *et al.* Hypocycloid-shaped hollow-core photonic crystal fiber Part II: Cladding effect on confinement and bend loss. *Optics Express* **21**, 28609 (2013).
142. Agrawal, G. *Nonlinear Fiber Optics*. (Academic Press, 2012).
143. Hansson, T. *et al.* Nonlinear beam self-imaging and self-focusing dynamics in a GRIN multimode optical fiber: theory and experiments. *Optics Express* **28**, 24005 (2020).

Chapter 3. Four-Wave Mixing process in Hollow core capillary.

3.1 Introduction

Four Wave Mixing (**FWM**) is a third-order nonlinear parametric process which, in the general case, involves the interaction of four optical waves at different angular frequencies. As a result, the two main waves called "pumps" (at angular frequencies ω_1 and ω_2) give rise to new optical waves, i.e., the pumps transfer the energy to one signal and one idler at the angular frequency ω_3 and ω_4, respectively, Fig. 3.1a. The efficiency of these phenomena depends strongly on the phase matched conditions.

The existence of the FWM in optical fibers was observed for the first time by Stolen et al.[1] using a 9 cm long fiber pumped by a doubled-pulse YAG laser. Since the first demonstration, the FWM in fibers have attracted much attention, especially after the invention of photonic crystal fiber (**PCF**) [2,3]. PCFs are ideal candidates for FWM [4,5] because they can provide custom dispersion profile and improved non-linearity as well. The fiber optic parametric amplifier (**FOPA**) based on the four-wave mixing can be used for linear signal amplification and wavelength conversion. Therefore, FOPA is widely used to achieve high gain and high bandwidth [6–10].

For ultra-short pulse amplification, there are a lot of efforts related to fiber-based optical parametric chirped pulse amplification (**FOPCPA**),[11–14], where the key step is to stretch the seed signal before the injection into the amplifier. An idler is also generated during the process. At the end, the amplified signal is re-compressed to reach ultrashort pulses. Another reported method to increase the gain bandwidth is by using the highly nonlinear fibers (**HNLF**) and combination with Raman effect to get a bandwidth of 200 nm[15]. Most of the previous works with FWM in fibers are related to the generation of signal and idler (anti-Stokes and Stokes waves) in the same mode, i .e., the fundamental mode. However, other systems are based on multi-mode propagation, in which the ultrashort pulses propagate inside a multi-mode optical fiber. Nonlinear spatiotemporal effects such as intermodal FWM, produce a coupling between modes [16,17]. For example, the intermodal FWM in PFC has been used to generate green light [18,19] in the UV [20] and the IR [21,22].

Multi-mode FWM has also been used for application such as space-division multiplexing (**SDM**) with few multi-mode fiber (**FMF**), multicore fibers, for telecommunications systems [23]. Recently, the renew of interest for multi-mode fiber (**MMFs**) has led to numerous investigations of intermodal nonlinear phenomena and spatiotemporal coupling, mainly associated with broadband frequency conversion processes [24,25]. This seems relevant for intermediate platform to investigate nonlinear optic and random linear coupling between the modes [26,27].

As the FWM process is fundamental for the frequency generation and amplification, the associated theory is well described in this chapter. Initially, the general case of FWM is examined, considering the contribution of higher order modes. Later we focus on the distribution when all the waves propagate in the fundamental mode of the gas filled hollow core capillary. The propagation equations of the signal and idler are also derived.

The propagation by using the NLS equations allows to discuss deeply the FWM. Particularly, we highlight how the FWM process is affected by the waveguide geometries, such as the core diameter and gas pressure.

3.2 Description of FWM

When the pumps at angular frequencies $\omega_1$and ω_2 propagate in a fiber, their interaction gives rise to new waves at frequencies, the signal and idler at ω_3 and ω_4 Fig. 3.1a.

$$\omega_1 + \omega_2 = \omega_3 + \omega_4 \qquad (3-1)$$

The FWM process become efficient when the following phase matching condition are satisfied, such as $\Delta\kappa=0$:

$$\Delta\kappa=\Delta\beta_L + \Delta\beta_{NL} = \beta^{n,k}(\omega_3) + \beta^{n,l}(\omega_4) - \beta^{n,m}(\omega_2) - \beta^{n,m}(\omega_1) + \Delta\beta_{NL}, \qquad (3-2)$$

Where, $\beta^{n,m}(\omega_q)$ is the propagation constant of the q^{th} wave propagating in the m^{th} fiber mode. $\Delta\beta_L$ is the linear mismatch and $\Delta\beta_{NL}$ is the phase caused by non-linear effects.

In case of MMFs whose spatial modes have different propagation constant, it is also possible to achieve $\Delta\beta_L=0$ by propagating different waves in different fiber modes [28]. If the frequency spacing $\Delta\omega$ between the pumps equals to zero, the pump frequencies coincide such as $\omega_1=\omega_2=\omega_c$. In this case, the FWM is called "degenerate case", Fig. 3.1b. The new frequencies will be symmetrically positioned around the pump, ω_c , and these sidebands are referred to as the Stokes and anti-Stokes bands, respectively.
In a degenerated case, the corresponding energy conservation is given by

$$\omega_3 + \omega_4 = 2\omega_c \qquad (3-3)$$

The frequency shift of the two sidebands is defined as,

$$\Delta\omega = \omega_c - \omega_3 = \omega_4 - \omega_c \qquad (3-4)$$

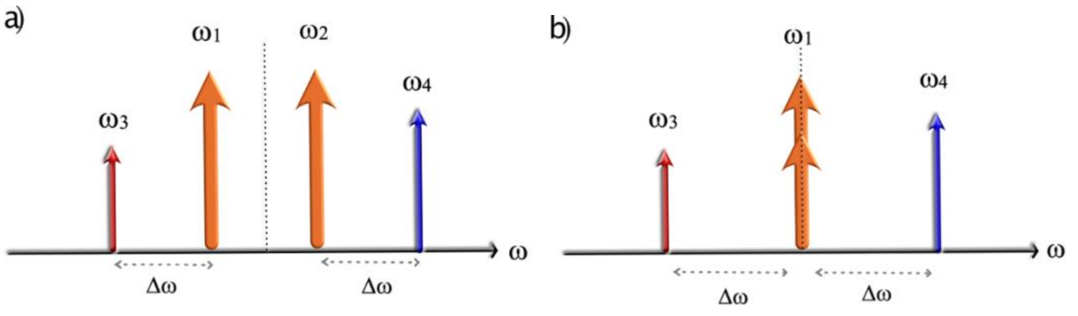

Fig. 3.1 a) Scheme for the non-degenerated FWM b) degenerated FWM

3.3 Theory of FWM

Since FWM process relies on an energy transfer, it is necessary to calculate the conversion efficiency from the pump to the signal and idler waves. The starting point is to calculate $\mathbf{P}_{\mathrm{NL}}$ the non-linear polarization which is linked to the third order susceptibility, such as [29].

$$\mathbf{P}_{\mathrm{NL}} = \varepsilon_0 \chi^3 EEE \qquad (3-5)$$

The total electric field can be described as a superposition of four waves in frequency domain, with a transverse field distribution of each mode, $\mathbf{F}_n(\rho,\phi)$ and the longitudinal field envelopes $\tilde{\mathrm{A}}_n\left(z,\omega-\omega_0\right)$

$$\mathrm{E}(\mathbf{r},\mathbf{t}) = \int \sum_{n=1}^{4} \tilde{\mathrm{A}}_n\left(z,\omega-\omega_0\right)\, \mathbf{F}_n(\rho,\phi)\, e^{-i\omega t} d\omega, \qquad (3-6)$$

By substituting Eq. (3-6) into Eq. (3-5), the non-linear polarization can also be written as a superposition of terms in the form:

$$\mathbf{P}_{\mathrm{NL}} = \frac{1}{2}\sum_{n=1}^{4}\left[\, \mathscr{P}^{\mathrm{n}}_{\mathrm{NL}}(r,t)\,\right], \qquad (3-7)$$

By placing Eq. (3-7) and Eq. (3-6) into the wave equation, Eq. (2-10), it leads to a set of four coupled equations [29]. In the following, the time dependence of the field components is neglected, and the spatial distribution of the fiber mode is included.

$$\frac{d\mathrm{A}_1}{dz} = \frac{i\mathrm{n}_2\omega_1}{c}\left[\left(\mathrm{f}_{11}|A_1|^2 + 2\sum_{m\neq 1} f_{1m}|A_m|^2\right)A_1 + 2\mathrm{f}_{1234}\,\mathrm{A}_3\mathrm{A}_4\mathrm{A}_2^* e^{i\Delta\beta z}\right] \qquad (3-8)$$

$$\frac{d\mathrm{A}_2}{dz} = \frac{i\mathrm{n}_2\omega_2}{\mathrm{c}}\left[\left(\mathrm{f}_{22}|A_2|^2 + 2\sum_{m\neq 2} f_{2m}|A_m|^2\right)A_2 + 2\mathrm{f}_{2134}\,\mathrm{A}_3\mathrm{A}_4\mathrm{A}_1^* e^{i\Delta\beta z}\right] \qquad (3-9)$$

$$\frac{d\mathrm{A}_3}{dz} = \frac{i\mathrm{n}_2\omega_3}{c}\left[\left(\mathrm{f}_{33}|A_3|^2 + 2\sum_{m\neq 3} f_{3m}|A_m|^2\right)A_3 + 2\mathrm{f}_{3412}\,\mathrm{A}_1\mathrm{A}_2\mathrm{A}_4^* e^{-i\Delta\beta z}\right] \qquad (3-10)$$

$$\frac{d\mathrm{A}_4}{dz} = \frac{i\mathrm{n}_2\omega_4}{c}\left[\left(\mathrm{f}_{44}|A_4|^2 + 2\sum_{m\neq 4} f_{4m}|A_m|^2\right)A_4 + 2\mathrm{f}_{4312}\mathrm{A}_1\mathrm{A}_2\mathrm{A}_3^* e^{-i\Delta\beta z}\right] \qquad (3-11)$$

The asterisk represents the conjugated complex and n_2, the nonlinear refractive index. We assume that n_2 is wavelength independent[30].

In the FWM process, the conversion efficiency is highly determined by the mode field integral, because the involved waves present different spatial profile distributions. Therefore, their interaction is quantified by the overlapping integral such as:

$$\mathbf{f}_{\mathbf{ijkl}} = \frac{\langle F_i^* F_j^* F_k F_l \rangle}{\left[\langle |F_i|^2 \rangle \langle |F_j|^2 \rangle \langle |F_k|^2 \rangle \langle |F_l|^2 \rangle\right]^{1/2}}, \qquad (3-12a)$$

$$\mathbf{f}_{\mathbf{jk}} = \frac{\langle |F_j|^2 |F_k|^2 \rangle}{\left[\langle |F_j|^2 \rangle \langle |F_k|^2 \rangle\right]}, \qquad (3-12b)$$

Where $F_{i,j,k,l}$ is the transverse spatial distribution of the fiber modes, the brackets $\langle\ \rangle$ represents the integration over the transverse cross-section of the fiber.
By definition, $f_{jk} = f_{ijkl}$ when only two modes exist with different transversal modal distributions; i.e $i=j$ and $k=l$.

3.4 Coupled equations of multi-mode FWM

In the degenerate FWM case, the coupled wave equations are reduced to three equations; the signal, idler and pump. The energy conservation becomes $2\omega_1 = \omega_3 + \omega_4$. The electrical field of the three waves is therefore provided by:

$$\frac{d\mathrm{A}_1}{dz} = \frac{i\mathrm{n}_2\omega_1}{c}\left[\left(\mathrm{f}_{11}|A_1|^2 + 2\left(\mathrm{f}_{13}|A_3|^2 + \mathrm{f}_{14}|A_4|^2\right)\right)A_1 + 2\mathrm{f}_{1134}A_3A_4A_1^* e^{i\Delta\beta z}\right] \qquad (3-13)$$

$$\frac{d\mathrm{A}_3}{dz} = \frac{i\mathrm{n}_2\omega_3}{c}\left[\left(\mathrm{f}_{33}|A_3|^2 + 2\left(\mathrm{f}_{31}|A_1|^2 + \mathrm{f}_{34}|A_4|^2\right)\right)A_3 + \mathrm{f}_{3411}A_1^2A_4^* e^{-i\Delta\beta z}\right] \qquad (3-14)$$

$$\frac{d\mathrm{A}_4}{dz} = \frac{i\mathrm{n}_2\omega_4}{c}\left[\left(\mathrm{f}_{44}|A_4|^2 + 2\left(\mathrm{f}_{41}|A_1|^2 + \mathrm{f}_{43}|A_3|^2\right)\right)A_4 + \mathrm{f}_{4311}A_1^2A_3^* e^{-i\Delta\beta z}\right] \qquad (3-15)$$

The first term inside the brackets describes the SPM effect whereas the second term is related to XPM. The generation of new frequency components by FWM is provided by the latest terms. Considering only the dispersion effect the linear phase mismatch is given by

$$\Delta\beta = \beta^{n,k}(\omega_3) + \beta^{n,l}(\omega_4) - 2\beta^{n,m}(\omega_1) \qquad (3-16)$$

To derive an analytical solution of the equations, the time dependence of the field is not taken into account, and we consider a quasi-continuous wave (CW). We assume the pump is much stronger than the signal and idler and the fiber loss is neglected. It also means that the pump remains un-depleted during the processes. We also assume that the signal and idler waves are weak and are therefore not affected by SPM. Thus, Eq. (3-13) to (3-15) are reduced to:

$$\frac{d\mathbf{A}_1}{dz} = \frac{i\mathrm{n}_2\omega_1}{c}\left[\mathrm{f}_{11}\left(\left|\mathrm{A}_1\right|^2\right) A_1\right] \qquad (3-17)$$

$$\frac{d\mathbf{A}_3}{dz} = \frac{i\mathrm{n}_2\omega_3}{c}\left[2\mathrm{f}_{31}\left(\left|\mathrm{A}_1\right|^2\right) A_3 + \mathrm{f}_{3411}\,(\mathrm{A}_1)^{2} A_4^* \exp(-i\Delta\beta z)\right] \qquad (3-18)$$

$$\frac{d\mathbf{A}_4}{dz} = \frac{i\mathrm{n}_2\omega_4}{c}\left[2\mathrm{f}_{41}\left(\left|\mathrm{A}_1\right|^2\right) A_4 + \mathrm{f}_{4311}\,(\mathrm{A}_1)^{2} A_3^* \exp(-i\Delta\beta z)\right] \qquad (3-19)$$

The solution of the initial equation (Eq. 3-17) is included in Eq. (3-18) and (3-19). Through a variable transformation, the problem is reduced to two equations for the signal and idler waves [31].

$$\frac{d\mathbf{A}_3}{dz} = i\delta_3\left[\left(2\mathrm{f}_{31}|A_1|^2\right)A_3 + \mathrm{f}_{3411}\,A_1(0)\,A_1(0)\,A_4^*[\mathrm{exp}i\left(2\left(\delta_1 f_{11}|A_1|^2\right) - \Delta\beta\right)z]\right] \qquad (3-20)$$

$$\frac{d\mathbf{A}_4}{dz} = i\delta_4\left[\left(2\mathrm{f}_{41}|A_1|^2\right)A_4 + \mathrm{f}_{4311}\,A_1(0)\,A_1(0)\,A_3^*[\mathrm{exp}i\left(2\left(\delta_1 f_{11}|A_1|^2\right) - \Delta\beta\right)z]\right] \qquad (3-21)$$

where,

$$\delta_n = \frac{n_2\omega_n}{c} \qquad n = 1, 3, 4 \qquad (3-22)$$

We then assume the power difference between the signal and idler is constant $P_3(z) - P_4(z) = const = P_3(0)$. It leads to the signal and idler power equation given by:

$$P_3(z) = \mathrm{P}_3(0)\left[1 + \delta_3\delta_4\left(\frac{\mathrm{f}_{1134}\mathrm{P}_1}{g}\right)^2 \sinh^2 gz\right] \qquad (3-23)$$

$$P_4(z) = \mathrm{P}_3(0)\left[\left(\frac{\mathrm{f}_{1134}\,\delta_3\,\mathrm{P}_1}{g}\right)^2 \sinh^2 gz\right], \qquad (3-24)$$

where, g represents the parameter gain. It can be calculated as:

$$g^2 = \delta_3\delta_4\left(\mathrm{f}_{1134}\mathrm{P}_1\right)^2 - \left(\frac{\kappa}{2}\right)^2, \qquad (3-25)$$

where κ is the effective phase mismatch, which is expressed as:

$$\kappa = 2\mathrm{P}_1\left(\delta_3\mathrm{f}_{13} + \delta_4\mathrm{f}_{14} - \delta_1\mathrm{f}_{11}\right) + \Delta\beta, \qquad (3-26)$$

3.5 Coupled equations of single mode FWM

In the case of a FWM in which all the waves are in the fundamental mode, all the overlap integrals are nearly the same [29].

$$f_{ijkl} \approx 1/\,A_{eff}, \tag{3-27}$$

where A_{eff} is the effective mode area.

$$A_{eff} = \frac{2\pi\left(\int_0^a |F(\rho)|^2 \rho d\rho\right)^2}{\int_0^a |F(\rho)|^4 \rho d\rho}, \tag{3-28}$$

In view of a single-mode fiber, we introduce the non-linear coefficient using the definition:

$$\gamma_j = \frac{n_2 \omega_j}{c\,A_{eff}} \approx \gamma \tag{3-29}$$

In this case, the nonlinear coefficient does not vary with the wavelength. Thus, the overlapping integral and non-linear coefficient are constants. Consequently, the coupled equations are simplified as.

$$\frac{d\mathbf{A}_1}{dz} = i\gamma\left[|A_1|^2\right] A_1 \tag{3-30}$$

$$\frac{d\mathbf{A}_3}{dz} = i2\gamma\left(|A_1|^2\right)A_3 + i\gamma(A_1)^2 A_4^* \exp\left(-i\Delta\beta z\right) \tag{3-31}$$

$$\frac{d\mathbf{A}_4}{dz} = i2\gamma\left(|A_1|^2\right)A_4 + i\gamma(A_1)^2 A_3^* \exp\left(-i\Delta\beta z\right) \tag{3-32}$$

The pump field is solved as:

$$A_1(z) = A_1(0)\exp i\left[\gamma P_1 z\right], \tag{3-33}$$

where, $P_1 = |A_1(0)|^2$. By introducing the pump field at $z = 0$ in Eq (3-31) and (3-32) we obtain:

$$\frac{d\mathbf{A}_3}{dz} = i2\gamma P_1 A_3 + i\gamma A_1(0)\,A_1(0)\,A_4^* \exp i(2\gamma P_1 - \Delta\beta)\,z \tag{3-34}$$

$$\frac{d\mathrm{A}_4}{dz} = i2\gamma P_1 A_4 + i\gamma A_1(0)\,A_1(0)\,A_3^* \exp i(2\gamma P_1 - \Delta\beta)\,z \qquad (3-35)$$

With the same procedure as before, by using a variable transformation and considering no idler wave at the HCC input, i.e., $A_4(0) = 0,$ the amplitude of the signal and idler at a distance $z = L$writes as:

$$\mathbf{A}_3(z) = \left\{A_3(0)\left[\left[\cosh(gz)\right] + \frac{i}{g}\left[\frac{\kappa}{2}\right]\left[\sinh(gz)\right]\right] + \left[\frac{i\gamma\,[A_1(0)]^2}{g}\left[\sinh(gz)\right]\right]\left[A_4^*(0)\right]\right\}\exp\left[i\left(\gamma 2\right.\right. \qquad (3-36)$$

$$\mathbf{A}_4^*(z) = \left\{-\left[\frac{i\gamma\,[A_1(0)]^2}{g}\left[\sinh(gz)\right]\right]\left[A_3(0)\right]\right\}\exp\left[-i\left(\gamma 2P_1 - \frac{\kappa}{2}\right)z\right], \qquad (3-37)$$

where g is the parametric gain.

$$g^2 = (\gamma P_1(0))^2 - (\kappa/2)^2 \qquad (3-38)$$

The effective phase mismatch parameter, $\boldsymbol{\kappa}$, is defined as:

$$\boldsymbol{\kappa} = \Delta\beta_L + 2\gamma P_1 \qquad (3-39)$$

The signal and idler power, $P_3(z) = |A_3(z)|^2$ is expressed by

$$\mathrm{P}_3(z) = \mathrm{P}_3(0)\left[1 + (1 + \kappa^2/4g^2)\ \sinh^2(gz)\right] \qquad (3-40)$$

$$\mathrm{P}_4(z) = \mathrm{P}_3(0)\left[(1 + \kappa^2/4g^2)\ \sinh^2(gz)\right] \qquad (3-41)$$

The linear phase mismatch depends on the material and waveguide geometry, and it can be expressed as the function of the frequency shift, $\Delta\omega,$ from the pump centered at frequency ω_0. Then we can do an expansion up to the fourth-order term:

$$\boldsymbol{\kappa} = \beta_2(\Delta\omega)^2 + \frac{\beta_4}{12}(\Delta\omega)^4 + 2\gamma P_1, \qquad (3-42)$$

The phase matching with the pump in the normal dispersion regimen $(\beta_2 > 0)$ could be achieved if the β_4, term is negative. Whereas for a pump in the anomalous dispersion region, the negative value of $\beta_2$compensates the nonlinear term $2\gamma P$, which is always positive [32]. Then the phase matching can be always achieved even for a pump in the normal or anomalous dispersion regime.

Another common representation of the phase-matched conditions is the coherence length, given by:

$$\mathrm{CL}=\frac{2\pi}{|\kappa|} \qquad (3-43)$$

CL represents the maximum HCC length allowed from the wave-vector mismatch. This means that the FWM can occur if the HCC length is smaller than CL. Therefore, the frequency generation occurs in a wavelength range where the coherence length is large.

3.6 Analytical solution

3.6.1 Phase-matching dependence on pressure and HCC core radius.

Since the nonlinear refractive index n_2 can be defined from, χ^3 as[33]:

$$\mathrm{n}_2=\left(\frac{3}{4}\frac{\chi^3(p,T)}{\mathbf{n}_0^2(\omega)\,\varepsilon_0 c}\right)^{1/2}, \qquad (3-44)$$

by substituting Eq. (3-44) into the non-linear coefficient Eq. (3-29) it can easily see how nonlinearity in gases can be controlled by pressure [34].

$$\gamma\approx\left(\frac{\omega_m}{c\,\mathrm{A}_{\mathrm{eff}}}\right)(\mathrm{n}_2)\approx\left(\frac{\omega_m}{c\,\mathrm{A}_{\mathrm{eff}}}\right)\left(\frac{3}{4}\frac{\chi^3(p,T)}{\mathbf{n}_0^2(\omega)\,\varepsilon_0 c}\right)^{1/2} \qquad (3-45)$$

,

As discussed in the preceding section, HCC dispersion also can be adjusted by the pressure. Then the positive contribution of the GVD coming from the filling gas increases with the pressure. This property enables us to switch from an anomalous to a normal dispersion regime, affecting the phase matching process and changing the frequency position of the two spontaneous lateral bands (in the Stokes and anti-Stokes sides).
For example, the evolution of the CL as a function of the gas pressure is displayed in Fig. 3.2. The pump is centered at 800 nm and is launched into an argon-filled HCC. The pressure is raised from 0 to 2 bar (y-axes) for various core radius from 40 to 200 µm. The pump power is 1.60 GW.

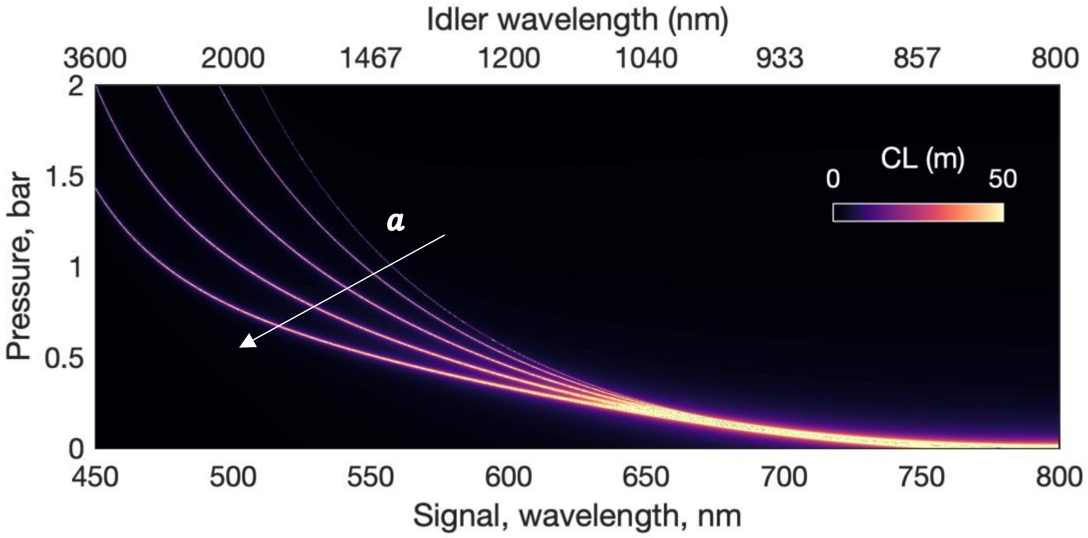

Fig. 3.2 Coherence length calculated for an argon filled HCC and pumped by a CW at 800 nm. The peak power is 1.60 GW. The lines represent the Coherence Length for different core radius, *a*, starting from 40 up to 200 µm.

In Fig. 3.2 the limit of the CL is from 0 to 50 meters and is represented by the color bar. When the core radius is small, the coherence length value is shorter. This is because the field is strongly affected by the non-linear contribution, due to decreasing of the effective area. As the core radius increases, the coherence length reaches higher values, closer to 50 meters. However, the position of the signal and idler wavelength moves further away from the pump when the pressure increases. As the gain of the signal and idler depends on the interaction length, having a high CL is always a good point that improves the amplifier performance.

3.6.2 Gain relative to different types of gas.

The signal and idler powers are calculated by the analytical solutions (Eq. (3-40) and Eq. (3-41)) considering a phase-matched FWM in the single mode case. Since the non-linear phase depends on the properties of the medium (in this case noble gases) several rare gases have been used to see how FWM can be affected. As an example, the gain is displayed in Fig. 3.3 for helium, argon, krypton and xenon. The pump wave is at 800 nm. and its pump power is 1.60 GW. The HCC has a radius of 75 µm and is filled with 1 bar.

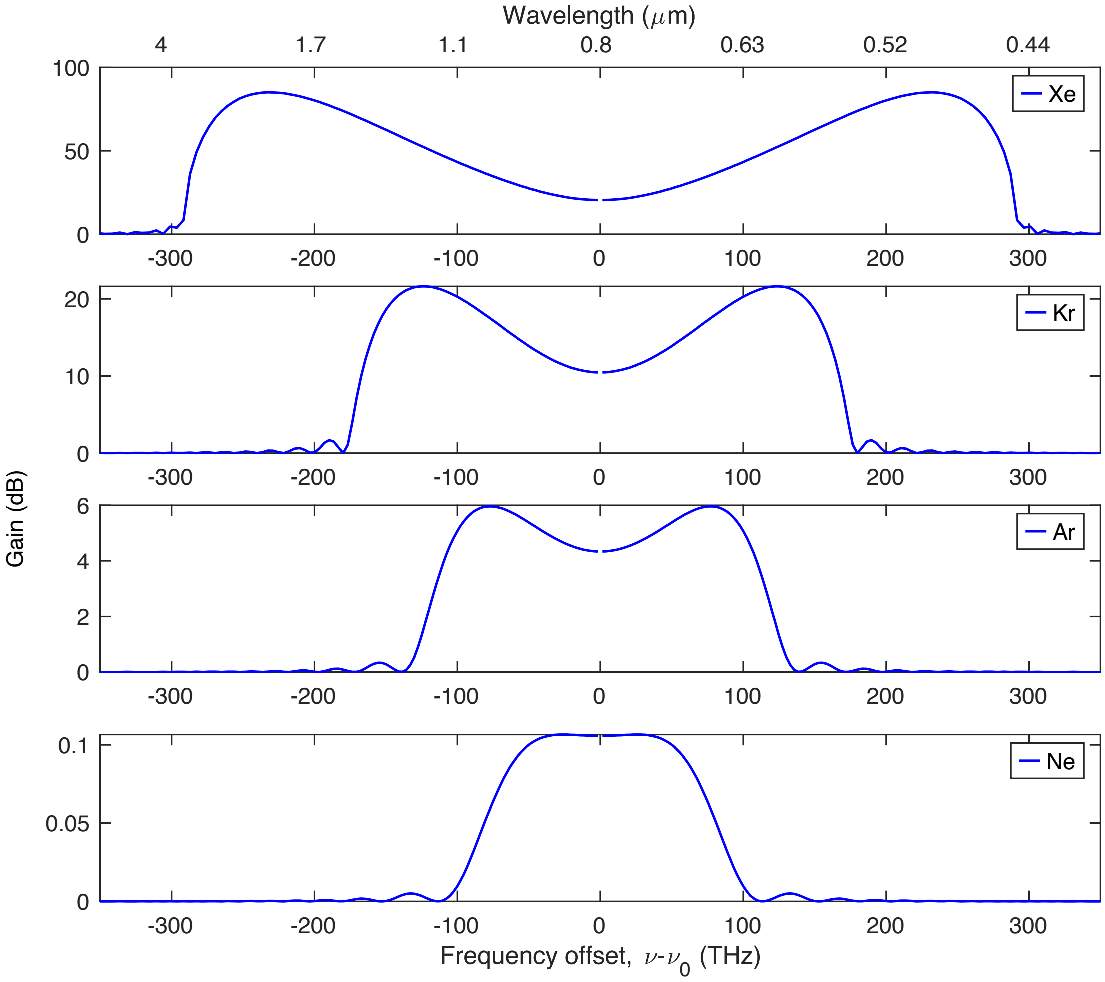

Fig. 3.3 Analytical gain calculated with Eq. 3-41.The 50 cm long HCC has a radius of 75 μm. The gas pressure is 0.15 bar. The input pump power is 1.60 GW.

The signal/idler power increases depend on the nonlinear coefficient, $\mathbf{n_2}$. As each gas present different value, the process gets more efficient in a heavy gas such as Krypton and Xenon.

It is also noteworthy that the phase-matched frequency at the maximum gain is different for each gas species. The frequencies of the signal and idler move away from the pump because of the different dispersion and nonlinear values (Eq. (3-42)). Since the dispersion properties of HCC depend on the filling gas, the pump wave can propagate in the anomalous or normal dispersion regime. Therefore, the change in frequency is not just related to the input pump power, as in silica fibers with at fixed pump wavelength.

Finally, in the case of a low input pump power, one can select a noble gas with a higher $\mathbf{n_2}$ to increase the frequency shift and to enhance the gain. This is another way to generate a higher nonlinearity at low pressure instead of using a smaller core diameter.

3.7 Simulation by integrating the NLS equation

3.7.1 Gain relative to different types of gas

To predict the power of the idler and signal waves generated by FWM, it is necessary to solve the NLSE developed in the previous chapter. Therefore, by using the split-step Fourier method, it is possible also to include the GVD effects and other nonlinearity effects.

We used in the numerical propagation 2^{15} points and a temporal resolution of 1.3 fs. This leads to a total window of ~±21 ps and a frequency span of ~± 374 THz. We select and error of $\delta_G = 1e^{-5}$.

As in the previous section, various types of rare gases (neon, argon, krypton and xenon) are considered, with the same input variables. For this numerical simulation, a single mode propagation is only considered and the self-steepening effect and loss are neglected. The pump is launched in a 50-cm-length HCC with a 75- µm core radius. The pulse is at the FT limit and the pulse duration at full width at half maximum (FWHM) of 120 fs. The central wavelength is 800 nm and the pump power is 1.61 GW. The gas pressure is 0.15 bar. The spectral output power is displayed in the Fig. 3.4 for several types of gases. For the case with neon gas, there is no FWM and only spectral broadening is observed due to the SPM effect.

With xenon gas, a strong spectral broadening is observed together with side band lobes, that corresponds to FWM. As we have seen in the previous case, by using the analytical solution with a heavy gas, the spectral gain is also high.

If we make a comparison with the analytical solution and split-step Fourier method, in both cases the behaviors are qualitatively similar. For xenon, the lobes are localized far from the pump frequency whereas in argon and neon the lobes are not seen with NLSE because the lobes are closer to the pump and it gain is week. With NLSE result just the pump spectral broadening is observed.

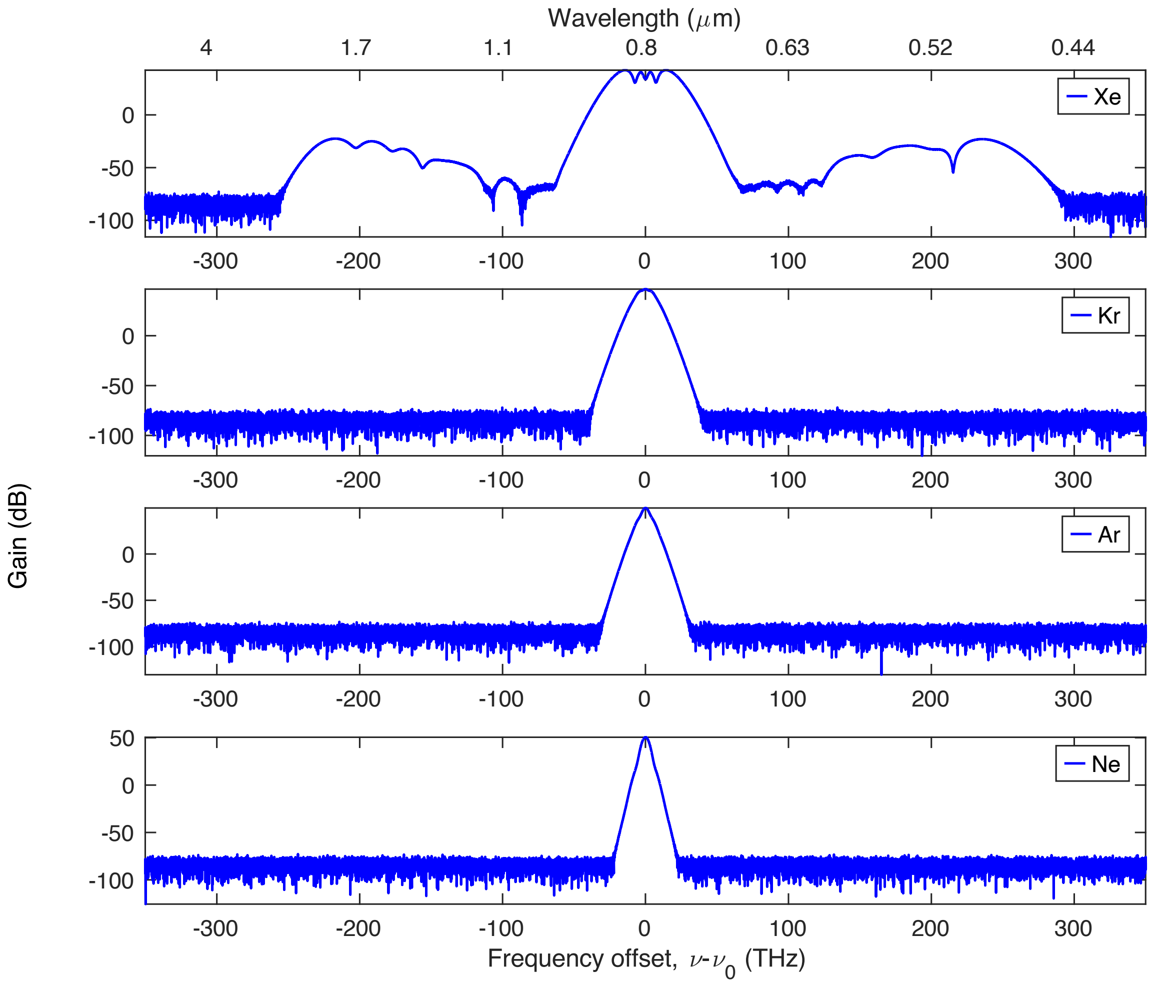

Fig. 3.4 The output spectral intensities for different noble gas after propagation in a 50 cm long HCC The core radius is 75 µm and the pressure is 0.15 bar. The pump wavelength is centered at 800 nm and the pulse duration is 120 fs at FWHM. The peak power is 1.60 GW

3.8 Conclusion

The general purpose of this chapter was to develop the standard equations referring to FWM. It makes a link between the filling gas, core radio, and pressure with the phase matching conditions. The effective core radius can be estimated by optimizing the CL. As the pressure increases, the refractive index of the gas also increases linearly, which has a direct impact on the phase matching conditions.

In addition, the phase-matched can be also adjusted by the geometry of the waveguide, consequently, there is a strong interplay between the properties of the gas and the waveguide with the linear dispersion and the non-linear phase. All these degrees of freedom in the HCC allow to reach different gain and spectral location of the generated lobes.

From numerical simulations, we conclude that the signal and idler can be generated even at a low pump power, for a relatively high-pressure, high n2, and long fiber. Another important point is that the signal/idler bandwidth decreases when the lobes are located further away from the pump due to the effect of chromatic dispersion and GVM. The FWM generation in an HCC can evolved to a supercontinuum including several other nonlinearities such as ionization, plasma recombination, high order Kerr effect. In this work, the parameter is selected to focus on the dynamic of FWM.

3.9 References to Chapter 3

1. Schawlow, A. L. and Townes, C. H. Infrared and optical masers. *Physical Review* **112**, 1940–1949 (1958).
2. Maiman, T. H. Stimulated optical radiation in Ruby. *Nature* **187**, 493–494 (1960).
3. Hall, R. N., Fenner, G. E., Kingsley, J. D., Soltys, T. J. and Carlson, R. O. Coherent light emission from GaAs junctions. *Physical Review Letters* **9**, 366–368 (1962).
4. Javan, A., Bennett, W. R. and Herriott, D. R. Population inversion and continuous optical maser oscillation in a gas discharge containing a He-Ne mixture. *Physical Review Letters* **6**, 106–110 (1961).
5. Strickland, D. and Mourou, G. Compression of amplified chirped optical pulses. *Optics Communications* **56**, 219–221 (1985).
6. Koester, C. J. and Snitzer, E. Amplification in a Fiber Laser. *Appl. Opt* **3**, RP1 (2017).
7. Nilsson, J. *et al.* High-power wavelength-tunable cladding-pumped rare-earth-doped silica fiber lasers. *Optical Fiber Technology* **10**, 5–30 (2004).
8. Lavenu, L. *et al.* High-energy few-cycle Yb-doped fiber amplifier source based on a single nonlinear compression stage. *Optics Express* **25**, 7530 (2017).
9. Blow, K. J. and Wood, D. Theoretical Description of Transient Stimulated Raman Scattering in Optical Fibers. *IEEE Journal of Quantum Electronics* **25**, 2665–2673 (1989).
10. Franken, P. A., Hill, A. E., Peters, C. W. and Weinreich, G. Generation of optical harmonics. *Physical Review Letters* **7**, 118–119 (1961).
11. Bass, M., Franken, P. A., Hill, A. E., Peters, C. W. and Weinreich, G. Optical mixing. *Physical Review Letters* **8**, 18–18 (1962).
12. Giordmaine, J. A. and Miller, R. C. Tunable coherent parametric oscillation in LiNbO3 at optical frequencies. *Physical Review Letters* **14**, 973–976 (1965).
13. Maker, P. D. and Terhune, R. W. Study of optical effects due to an induced polarization third order in the electric field strength. *Physical Review* **137**, 507–509 (1965).
14. New, G.H.C. and Ward, J. F. Optical third-harmonic generation in gases,. *Phys. Rev. Lett.* **19**, 556–559 (1967).
15. McWane, P. D. and Sealer, D. A. New measurements of intensity-dependent changes in the refractive index of liquids. *Applied Physics Letters* **8**, 278–279 (1966).
16. Carman, R. L., Chiao, R. Y. and Kelley, P. L. Observation of degenerate stimulated four-photon interaction and four-wave parametric amplification. *Physical Review Letters* **17**, 1281–1283 (1966).
17. Brahms, C., Belli, F. and Travers, J. C. Infrared attosecond field transients and UV to IR few-femtosecond pulses generated by high-energy soliton self-compression. *Physical Review Research* **2**, 043037 1–8 (2020).

18. Manzoni, C. and Cerullo, G. Few-optical-cycle pulses from near-IR to UV by non linear frequency conversion. in *2015 IEEE Photonics Conference, IPC 2015* 206–207 (2015).
19. Tzankov, P. *et al.* 300 µJ noncollinear optical parametric amplifier in the visible at 1 kHz repetition rate. *Optics Letters* **31**, 3629–3631 (2006).
20. Odhner, J. H. and Levis, R. J. High-energy noncollinear optical parametric amplifier producing 4 fs pulses in the visible seeded by a gas-phase filament. *Optics Letters* **40**, 3814–3817 (2015).
21. Viotti, A.-L. *et al.* Supercontinuum generation and soliton self-compression in χ (2)-structured KTiOPO 4. *Optica* **5**, 711–717 (2018).
22. Andriukaitis, G. *et al.* 90 GW peak power few-cycle mid-infrared pulses from an optical parametric amplifier. *Optics Letters* **36**, 2755–2757 (2011).
23. Shamir, Y. *et al.* High-average-power 2 µm few-cycle optical parametric chirped pulse amplifier at 100 kHz repetition rate. *Optics Letters* **40**, 5546–5549 (2015).
24. Silva, F., Bates, P. K., Esteban-Martin, A., Ebrahim-Zadeh, M. and Biegert, J. High-average-power, carrier-envelope phase-stable, few-cycle pulses at 21 µm from a collinear BiB3O6 optical parametric amplifier. *Optics Letters* **37**, 933 (2012).
25. Gu, X. *et al.* Generation of carrier-envelope-phase-stable 2-cycle 740-µJ pulses at 21-µm carrier wavelength. *Optics Express* **17**, 62–69 (2009).
26. Robert, P. *et al.* Spectral correlation of four-wave mixing generated in a photonic crystal fiber pumped by a chirped pulse. *Optics Letters* **45**, 4148–4151 (2020).
27. Fourcade-Dutin, C. *et al.* Temporal distribution measurement of the parametric spectral gain in a photonic crystal fiber pumped by a chirped pulse. *Photonics* **6**, 1–9 (2019).
28. Fourcade-Dutin, C., Miranda, O. Z., Mounaix, P. and Bigourd, D. Toward mid-infrared ultra-short pulse generation in a gas-filled hollow-core photonic crystal fiber. in *Advanced Photonics Congress 2021* (2021).
29. J. C. Travers, C. Brahms, F. Belli, T. F. Grigorova, A. L. M. S. Advances in nonlinear optics in gas-filled hollow-core fibers. in *in OSA Nonlinear Optics 2021, R. Boyd, C. Conti, D. Christodoulides, and P. Rakich, eds., OSA Technical Digest (Optical Society of America, 2021), paper NM2A.1.* (2021).
30. Travers, J. C., Grigorova, T. F., Brahms, C. and Belli, F. High-energy pulse self-compression and ultraviolet generation through soliton dynamics in hollow capillary fibres. *Nature Photonics* **13**, 547–554 (2019).
31. Kida, Y. and Imasaka, T. Optical parametric amplification of a supercontinuum in a gas. *Applied Physics B: Lasers and Optics* **116**, 673–680 (2014).
32. Ippen, E. P. Low-power quasi-cw raman oscillator. *Applied Physics Letters* **16**, 303–305 (1970).
33. Misoguti, L. *et al.* Generation of broadband VUV light using third-order cascaded processes. *Physical Review Letters* **87**, 013601/1-013601/4 (2001).
34. Adamu, A. I. *et al.* Deep-UV to Mid-IR Supercontinuum Generation driven by Mid-IR Ultrashort Pulses in a Gas-filled Hollow-core Fiber. *Scientific Reports* **9**, 1–8 (2019).
35. Wagner, N. L. *et al.* Self-compression of ultrashort pulses through ionization-induced spatiotemporal reshaping. *Physical Review Letters* **93**, 173902–173906 (2004).
36. Popmintchev, T. *et al.* Bright coherent ultrahigh harmonics in the kev x-ray regime from mid-infrared femtosecond lasers. *Science (1979)* **336**, 1287–1291 (2012).

37. Cabasse, A., Machinet, G., Dubrouil, A., Cormier, E. and Constant, E. Optimization and phase matching of fiber-laser-driven high-order harmonic generation at high repetition rate. *Optics Letters* **37**, 4618–4620 (2012).
38. Couch, D. E. *et al.* Ultrafast 1 MHz vacuum-ultraviolet source via highly cascaded harmonic generation in negative-curvature hollow-core fibers. *Optica* **7**, 832–837 (2020).
39. Brahms, C., Belli, F. and Travers, J. C. Infrared attosecond field transients and UV to IR few-femtosecond pulses generated by high-energy soliton self-compression. *Physical Review Research* **2**, 0–1 (2020).
40. Ciriolo, A. G. *et al.* Generation of ultrashort pulses by four wave mixing in a gas-filled hollow core fiber. *Journal of Optics* **20**, 125503-1 /125503-9 (2018).
41. Belli, F., Abdolvand, A., Travers, J. C. and Russell, P. St. J. Highly efficient deep UV generation by four-wave mixing in gas-filled hollow-core photonic crystal fiber. *Optics Letters* **44**, 5509 (2019).
42. Durfee, C. G., Backus, S., Kapteyn, H. C. and Murnane, M. M. Intense 8-fs pulse generation in the deep ultraviolet. *Optics Letters* **24**, 697 (1999).
43. Faccio, D., Grün, A., Bates, P. K., Chalus, O. and Biegert, J. Optical amplification in the near-infrared in gas-filled hollow-core fibers. *Optics Letters* **34**, 2918 (2009).
44. Kida, Y. and Kobayashi, T. Generation of sub-10 fs ultraviolet Gaussian pulses. *Journal of the Optical Society of America B* **28**, 139 (2011).
45. Fourcade-Dutin, C., Zurita-Miranda, O., Mounaix, P. and Bigourd, D. Mid-infrared ultra-short pulse generation in a gas-filled hollow-core photonic crystal fiber pumped by two-color pulses. *Fibers* **9**, 21 (2021).
46. Stolen, R. H., Bjorkholm, J. E. and Ashkin, A. Phase-matched three-wave mixing in silica fiber optical waveguides. *Applied Physics Letters* **24**, 308–310 (1974).
47. Hill, K. O., Johnson, D. C. and Kawasaki, B. S. Efficient conversion of light over a wide spectral range by four-photon mixing in a multimode graded-index fiber: erratum. *Applied Optics* **20**, 2769 (1981).
48. Agrawal, G. P. Nonlinear fiber optics: its history and recent progress [Invited]. *Journal of the Optical Society of America B* **28**, A1 (2011).
49. Nazemosadat, E., Pourbeyram, H. and Mafi, A. Phase matching for spontaneous frequency conversion via four-wave mixing in graded-index multimode optical fibers. *Journal of the Optical Society of America B* **33**, 144 (2016).
50. Rademacher, G., Warm, S. and Petermann, K. Analytical description of cross-modal nonlinear interaction in mode multiplexed multimode fibers. *IEEE Photonics Technology Letters* **24**, 1929–1932 (2012).
51. Mecozzi, A., Antonelli, C. and Shtaif, M. Nonlinear propagation in multi-mode fibers in the strong coupling regime. *Optics Express* **20**, 11673 (2012).
52. Mafi, A. Pulse Propagation in a Short Nonlinear Graded-Index Multimode Optical Fiber. *Journal of Lightwave Technology* **30**, 2803–2811 (2012).
53. Ding, E., Lefrancois, S., Kutz, J. N. and Wise, F. W. Scaling fiber lasers to large mode area: An investigation of passive mode-locking using a multi-mode fiber. *IEEE Journal of Quantum Electronics* **47**, 597–606 (2011).
54. Nazemosadat, E. and Mafi, A. Nonlinear switching in multicore versus multimode waveguide junctions for mode-locked laser applications. *Optics Express* **21**, 30739 (2013).

55. Mafi, E. N. and A. Nonlinear switching in a two- concentric-core chalcogenide glass optical fiber for passively mode-locking a fiber laser. *Opt. Lett.* **39**, 4675–4678 (2014).
56. Fu, S. *et al.* Passive Q-switching of an all-fiber laser induced by the Kerr effect of multimode interference. *Optics Express* **23**, 17255 (2015).
57. Einarsson, G. Pulse broadening in graded-index optical fibers: correction. *Applied Optics* **25**, 1030 (1986).
58. Renninger, W. H. and Wise, F. W. Optical solitons in graded-index multimode fibres. *Nature Communications* **4**, 1719 (2013).
59. S. Raghavan G. P. Agrawal. Spatiotemporal solitons in inhomogeneous nonlinear media. *Opt. Commun* **180**, 377–382 (2000).
60. Kibler, B. and Béjot, P. Discretized Conical Waves in Multimode Optical Fibers. *Physical Review Letters* **126**, (2021).
61. Faccio, D. *et al.* Spatio-temporal reshaping and X Wave dynamics in optical filaments. *Optics Express* **15**, 13077 (2007).
62. Konorov, S. O., Fedotov, A. B. and Zheltikov, A. M. Enhanced four-wave mixing in a hollow-core photonic-crystal fiber. *Optics Letters* **28**, 1448 (2003).
63. Ding, X., Selim Habib, Md., Amezcua-Correa, R. and Moses, J. Near-octave intense mid-infrared by adiabatic down-conversion in hollow anti-resonant fiber. *Optics Letters* **44**, 1084 (2019).
64. Finger, M. A., Joly, N. Y., Russell, P. S. J. and Chekhova, M. v. Characterization and shaping of the time-frequency Schmidt mode spectrum of bright twin beams generated in gas-filled hollow-core photonic crystal fibers. *Physical Review A* **95**, 053814 (2017).
65. Cordier, M. *et al.* Active engineering of four-wave mixing spectral correlations in multiband hollow-core fibers. *Optics Express* **27**, 9803 (2019).
66. Tempea, G. and Brabec, T. Theory of self-focusing in a hollow waveguide. *Optics Letters* **23**, 762 (1998).
67. Crego, A., Conejero Jarque, E. and San Roman, J. Influence of the spatial confinement on the self-focusing of ultrashort pulses in hollow-core fibers. *Scientific Reports* **9**, 9546 (2019).
68. Chapman, R. T. *et al.* Modal effects on pump-pulse propagation in an Ar-filled capillary. *Optics Express* **18**, 13279 (2010).
69. Mangini, F. *et al.* Self-imaging dynamics in nonlinear GRIN multimode optical fibers. *Frontiers in Optics / Laser Science* **28**, 24005–24021 (2020).
70. Wright, L. G., Wabnitz, S. W., Christodoulides, D. N. and Wise, F. W. Ultrabroadband dispersive radiation by spatiotemporal oscillation of multimode waves. in *Photonics and Fiber Technology 2016* (2016).
71. Marhic, M. E. *Fiber optical parametric amplifiers, oscillators and related devices*. *Fiber Optical Parametric Amplifiers, Oscillators and Related Devices* vol. 9780521861 (Cambridge University Press, 2007).
72. Couairon, A. *et al.* Practitioner's guide to laser pulse propagation models and simulation. *European Physical Journal: Special Topics* **199**, 5–76 (2011).
73. Brabec, T. and Krausz, F. Intense few-cycle laser fields: Frontiers of nonlinear optics. *Reviews of Modern Physics* **72**, 545–591 (2000).
74. Agrawal, G. P. *Nonlinear fiber optics*. *Nonlinear Fiber Optics* (Academic Press, 2019). doi:10.1016/C2018-0-01168-8.
75. Boyd, R. W. *Nonlinear Fiber Optics*. (2008).

76. Marcatili, E. A. J. and Schmeltzer, R. A. Hollow Metallic and Dielectric Waveguides for Long Distance Optical Transmission and Lasers. *Bell System Technical Journal* **43**, 1783–1809 (1964).
77. Lehmeier, H. J., Leupacher, W. and Penzkofer, A. Nonresonant third order hyperpolarizability of rare gases and N2 determined by third harmonic generation. *Optics Communications* **56**, 67–72 (1985).
78. Couairon, A., Chakraborty, H. S. and Gaarde, M. B. From single-cycle self-compressed filaments to isolated attosecond pulses in noble gases. *Physical Review A - Atomic, Molecular, and Optical Physics* **77**, (2008).
79. Sinkin, O. V., Holzlöhner, R., Zweck, J. and Menyuk, C. R. Optimization of the split-step Fourier method in modeling optical-fiber communications systems. *Journal of Lightwave Technology* **21**, 61–68 (2003).
80. Marburger, J. H. Self-focusing: Theory. *Progress in Quantum Electronics* **4**, 35–110 (1975).
81. Milosevic, N., Tempea, G. and Brabec, T. Optical pulse compression: bulk media versus hollow waveguides. *Optics Letters* **25**, 672–674 (2000).
82. Stolen, R. H. and Lin, C. Self-phase-modulation in silica optical fibers. *Physical Review A* **17**, 1448–1453 (1978).
83. Dudley, J. M. and Taylor, J. R. *Supercontinuum generation in optical fibers*. *Supercontinuum Generation in Optical Fibers* vol. 9780521514 (2010).
84. Snitzer, E. Cylindrical Dielectric Waveguide Modes*. *J Opt Soc Am* **51**, 491 (1961).
85. Archambault, J. L., Black, R. J., Lacroix, S. and Bures, J. Loss Calculations for Antiresonant Waveguides. *Journal of Lightwave Technology* **11**, 416–423 (1993).
86. Hesketh, G. D., Poletti, F. and Horak, P. Spatio-Temporal Self-Focusing in Femtosecond Pulse Transmission Through Multimode Optical Fibers. *Journal of Lightwave Technology* **30**, 2764–2769 (2012).
87. Börzsönyi, A., Heiner, Z., Kalashnikov, M. P., Kovács, A. P. and Osvay, K. Dispersion measurement of inert gases and gas mixtures at 800 nm. *Applied Optics* **47**, 4856–4863 (2008).
88. Cros, B. *et al.* Eigenmodes for capillary tubes with dielectric walls and ultraintense laser pulse guiding. *Physical Review E - Statistical Physics, Plasmas, Fluids, and Related Interdisciplinary Topics* **65**, (2002).
89. M. Nisoli, S. Stagira, S. De Silvestri, O. Svelto, S. Sartinia Z. Cheng, G. Tempea, C. Spielmann, and F. K. Towards a terawatt-scale sub-10-fs laser technology. *IEEE J. of selected topics in quantum ELECTRONICS* **4**, (1998).
90. Trebino, R. *Frequency-Resolved Optical Gating: The Measurement of Ultrashort Laser Pulses*. *Frequency-Resolved Optical Gating: The Measurement of Ultrashort Laser Pulses* (2000). doi:10.1007/978-1-4615-1181-6.
91. Trebino, R. *et al.* Measuring ultrashort laser pulses in the time-frequency domain using frequency-resolved optical gating. *Review of Scientific Instruments* **68**, 3277–3295 (1997).
92. Stolen, R. Phase-matched-stimulated four-photon mixing in silica-fiber waveguides. *IEEE Journal of Quantum Electronics* **11**, 100–103 (1975).
93. Russell, P. Photonic Crystal Fibers. *Science (1979)* **299**, 358–362 (2003).
94. Knight, J. C. Photonic crystal fibres. *Nature* **424**, 847–851 (2003).
95. Bigourd, D., D'Augerès, P. B., Dubertrand, J., Hugonnot, E. and Mussot, A. Ultra-broadband fiber optical parametric amplifier pumped by chirped pulses. *Optics Letters* **39**, 3782 (2014).

96. Bigourd, D. *et al.* Parametric gain shaping from a structured pump pulse. *IEEE Photonics Technology Letters* **31**, 214–217 (2019).
97. Vanvincq, O., Fourcade-Dutin, C., Mussot, A., Hugonnot, E. and Bigourd, D. Ultrabroadband fiber optical parametric amplifiers pumped by chirped pulses Part 1: analytical model. *Journal of the Optical Society of America B* **32**, 1479 (2015).
98. Fourcade-Dutin, C., Vanvincq, O., Mussot, A., Hugonnot, E. and Bigourd, D. Ultrabroadband fiber optical parametric amplifier pumped by chirped pulses Part 2: sub-30-fs pulse amplification at high gain. *Journal of the Optical Society of America B* **32**, 1488 (2015).
99. Bigourd, D. *et al.* High-gain fiber, optical-parametric, chirped-pulse amplification of femtosecond pulses at 1 µm. *Optics Letters* **35**, 3480 (2010).
100. Bigourd, D., Lago, L., Mussot, A., Kudlinski, A. and Hugonnot, E. High gain fiber optical parametric chirped pulse amplification of femtosecond pulses at 1 µm. *Optics InfoBase Conference Papers* **35**, (2011).
101. Qin, Y., Batjargal, O., Cromey, B. and Kieu, K. All-fiber high-power 1700 nm femtosecond laser based on optical parametric chirped-pulse amplification. *Optics Express* **28**, 2317 (2020).
102. Qin, Y. *et al.* Watt-level all-fiber optical parametric chirped-pulse amplifier working at 1300 nm. *Optics Letters* **44**, 3422 (2019).
103. Ho, M. C., Uesaka, K., Marhic, M., Akasaka, Y. and Kazovsky, L. G. 200-nm-bandwidth fiber optical amplifier combining parametric and Raman gain. *Journal of Lightwave Technology* **19**, 977–981 (2001).
104. Lesvigne, C. *et al.* Visible supercontinuum generation controlled by intermodal four-wave mixing in microstructured fiber. *Optics Letters* **32**, 2173 (2007).
105. Tu, H., Jiang, Z., Marks, D. L. and Boppart, S. A. Intermodal four-wave mixing from femtosecond pulse-pumped photonic crystal fiber. *Applied Physics Letters* **94**, 101109 (2009).
106. Yuan, J. *et al.* Polarization-dependent intermodal four-wave mixing in a birefringent multimode photonic crystal fiber. *Optics Letters* **42**, 1644 (2017).
107. Dupiol, R. *et al.* Far-detuned cascaded intermodal four-wave mixing in a multimode fiber. *Optics Letters* **42**, 1293 (2017).
108. Yuan, J. *et al.* Experimental generation of discrete ultraviolet wavelength by cascaded intermodal four-wave mixing in a multimode photonic crystal fiber. *Optics Letters* **42**, 3537 (2017).
109. Velazquez-Ibarra, L., Diez, A., Silvestre, E. and Andres, M. V. Tunable Four-Wave Mixing Light Source Based on Photonic Crystal Fibers with Variable Chromatic Dispersion. *Journal of Lightwave Technology* **37**, 5722–5726 (2019).
110. Delagnes, J.-C. *et al.* High-power widely tunable ps source in the visible light based on four wave mixing in optimized photonic crystal fibers. *Optics Express* **26**, 11265 (2018).
111. Ryf, R. *et al.* Mode-Division Multiplexing Over 96 km of Few-Mode Fiber Using Coherent 6x6 MIMO Processing. *Journal of Lightwave Technology* **30**, 521–531 (2012).
112. Wright, L. G., Christodoulides, D. N. and Wise, F. W. Controllable spatiotemporal nonlinear effects in multimode fibres. *Nature Photonics* **9**, 306–310 (2015).
113. Krupa, K. *et al.* Multimode nonlinear fiber optics, a spatiotemporal avenue. *APL Photonics* **4**, 110901 (2019).
114. Rashleigh, S. C. Origins and Control of Polarization Effects in Single-Mode Fibers. *Journal of Lightwave Technology* **1**, 312–331 (1983).

115. Taylor, J. R. *Theory of Dielectric Optical Waveguides. 2nd Edition*. *Journal of Modern Optics* vol. 39 (1992).
116. Stolen, R. and Bjorkholm, J. Parametric amplification and frequency conversion in optical fibers. *IEEE Journal of Quantum Electronics* **18**, 1062–1072 (1982).
117. Ferguson, A. I. *The Elements of Nonlinear Optics*. *Journal of Modern Optics* vol. 38 (1991).
118. Musheghyan, M. *et al.* Tunable, few-cycle, CEP-stable mid-IR optical parametric amplifier for strong field applications. *Journal of Physics B: Atomic, Molecular and Optical Physics* **53**, (2020).
119. B. Shao, Y. Li, Y. Peng, P. Wang, J. Qian,Y. Leng, R. L. Broad-bandwidth high-temporal-contrast carrier-envelope-phase-stabilized laser seed for 100 PW lasers. *Opt. Lett.* **45**, (2020).
120. E. Rubino, J. Darginavičius, D. Faccio, P. Di Trapani, A. Piskarskas, A. D. Generation of broadly tunable sub-30-fs infrared pulses by four-wave optical parametric amplification. *Opt. Lett* **36**, 382–384 (2011).
121. J. Bromage, S.-W. Bahk, I. A. Begishev, C. Dorrer, M. J. Guardalben, B. N. Hoffman, J. B. Oliver, R. G. Roides, E. M. Schiesser, M. J. Shoup III, M. Spilatro, B. Webb, D. Weiner, J. D. Z. Technology development for ultra-intense all-OPCPA systems. *High Power Laser Science and Engineering* **7**, (2019).
122. Fu, W. and Wise, F. W. Normal-Dispersion Fiber Optical Parametric Chirped-Pulse Amplification. *2018 Conference on Lasers and Electro-Optics, CLEO 2018 - Proceedings* **43**, 5331 (2018).
123. Fourcade-Dutin, C. and Bigourd, D. Modulation instability in a dispersion oscillating fibre pumped by a broad band pulse. *Journal of Modern Optics* **64**, 500–506 (2017).
124. Dubietis, A. and Couairon, A. *Ultrafast Supercontinuum Generation in Transparent Solid-State Media*. (Springer Nature, 2019).
125. Ding, Y., Xu, J., Ou, H. and Peucheret, C. Mode-selective wavelength conversion based on four-wave mixing in a multimode silicon waveguide. *IET Conference Publications* **2013**, 198–200 (2013).
126. Pan, W., Jin, Q., Li, X. and Gao, S. All-optical wavelength conversion for mode-division multiplexing signals using four-wave mixing in a dual-mode fiber. *Journal of the Optical Society of America B* **32**, 2417 (2015).
127. C. Fourcade Dutin. *et al.* Post-compression of high-energy femtosecond pulses using gas ionization. *Optics Letters* **35**, 253 (2010).
128. Kolesik, M., Katona, G., Moloney, J.V., Wright, E. M. Physical factors limiting the spectral extent and band gap dependence of supercontinuum generation. *Phys. Rev. Lett* **91**, (2003).
129. Saari, P. and Reivelt, K. X-Shaped Propagation-Invariant localized light waves. *Physical Review Letters* **79**, 4135–4138 (1997).
130. Tzortzakis, S. *et al.* Formation of a conducting channel in air by self-guided femtosecond laser pulses. *Physical Review E - Statistical Physics, Plasmas, Fluids, and Related Interdisciplinary Topics* **60**, (1999).
131. Poletti, F. and Horak, P. Description of ultrashort pulse propagation in multimode optical fibers. *Journal of the Optical Society of America B* **25**, 1645 (2008).
132. Poletti, F. and Horak, P. Dynamics of femtosecond supercontinuum generation in multimode fibers. *Optics Express* **17**, 6134 (2009).

133. Mussot, A., Sylvestre, T., Provino, L. and Maillotte, H. Generation of a broadband single-mode supercontinuum in a conventional dispersion-shifted fiber by use of a subnanosecond microchiplaser. *Optics Letters* **28**, 1820 (2003).
134. Köttig, F., Tani, F., Travers, J. C. and Russell, P. S. J. Self-focusing below the critical power in gas-filled hollow-core PCF. in *Optics InfoBase Conference Papers* vol. Part F81-E (2017).
135. Mecozzi, A., Antonelli, C. and Shtaif, M. Coupled Manakov equations in multimode fibers with strongly coupled groups of modes. *Optics Express* **20**, 23436 (2012).
136. Tani, F., Travers, J. C. and St.J. Russell, P. Multimode ultrafast nonlinear optics in optical waveguides: numerical modeling and experiments in kagomé photonic-crystal fiber. *Journal of the Optical Society of America B* **31**, 311 (2014).
137. Benabid, F., Knight, J. C., Antonopoulos, G. and Russell, P. S. J. Stimulated Raman Scattering in Hydrogen-Filled Hollow-Core Photonic Crystal Fiber. *Science (1979)* **298**, 399–402 (2002).
138. Poletti, F. Nested antiresonant nodeless hollow core fiber. *Optics Express* **22**, 23807 (2014).
139. Cregan, R. F. *et al.* Single-Mode Photonic Band Gap Guidance of Light in Air. *Science (1979)* **285**, 1537–1539 (1999).
140. Knight, J. C., Broeng, J., Birks, T. A. and Russell, P. S. J. Photonic band gap guidance in optical fibers. *Science (1979)* **282**, 1476–1478 (1998).
141. Alharbi, M. *et al.* Hypocycloid-shaped hollow-core photonic crystal fiber Part II: Cladding effect on confinement and bend loss. *Optics Express* **21**, 28609 (2013).
142. Agrawal, G. *Nonlinear Fiber Optics*. (Academic Press, 2012).
143. Hansson, T. *et al.* Nonlinear beam self-imaging and self-focusing dynamics in a GRIN multimode optical fiber: theory and experiments. *Optics Express* **28**, 24005 (2020).

Chapter 4. Design of a tunable infrared generation system by a four-wave mixing process in the fundamental mode.

4.1 Introduction

Ultra-fast optical parametric amplification (**OPA**) based on a four-wave mixing process, has become popular and well established to study in diverse configurations, wide-tunability, ultra-wide gain bandwidth and very high temporal contrast of ultra-short pulses[1,2]. The parametric amplification process was performed in a variety of materials, such a bulk non-linear crystals with second-order susceptibility and also in an isotropic medium with a third-order susceptibility [3]. In both cases, the interaction geometry is essential to get the optimal phase-matched condition that enables an efficient energy transfer from the pump to the target signal. Once enough power is reached to obtain the non linear process, it is possible to adjust the amplifier size or decrease the pulse peak power to keep the non-linearity under control. A common method for reducing the power of the pulse is to stretch it at the system input while the target pulse is compressed after amplification. This scheme is known as optical parametric chirped pulse amplification (**OPCPA**), is widely used to reach pulses with high energy and/or high peak power [4].

Another method for ultra-fast OPA is to carry out the process in guided systems which provide significant benefits because of the guiding geometry. Besides its robustness and its compact size, the optical interaction between the pulses involved is more efficient thanks to the beam collinearity, excellent spatial beam profiles and their superposition t directly provided by the waveguide. In particular, we investigated this process in single-mode solid photonic crystal fibers in which the generation and signal amplification are preformed using a four-wave mixing mechanism. Here, the interplay between the nonlinear phase of the pump and the dispersion of the fiber [5] allows to reach the phase-matching conditions. In another hand the power scalability can be achieved by increasing the diameter of the fiber while maintaining the appropriate dispersal profile or by stretching the pulses involved [6–8]. By using a gas-filled waveguide, higher intensities can be managed (∽10 ^{14} -10 ^{15} Wcm^{-2})[9], thanks its higher damage threshold. With gas-filled fibers, it is also possible to tune the dispersion in real-time, allowing the adjustment of the phase-matching condition.

Few groups have focused their research on amplification in gas-filled capillaries, with a large core, in visible[10], ultraviolet [11,12], and infrared [13,14]. In most cases, the amplification is achieved with a multi-modal phase matching in capillaries to amplify a targeted spectral range[13,15]. For example, it has been shown that a 9-cm long hollow core PCF with an inner diameter of 13 μm provides a higher transmission of the FWM signal by a factor of > 50 compared to a 10-cm long solid cladding hollow fiber with an inner diameter of 100 μm [16]. In addition, by using FWM in anti-resonant HCF and applying a gas pressure gradient, it is possible to produce almost an octave-spanning in the MIR with an energy of 10 μJ [17]. The gas-filled hollow-core fibers have many advantages for non-linear phenomena, because the pressure is a key ingredient to simultaneously adjust the dispersion and non-linearity. A straightforward example is in [17] where by adjusting the gas pressure and pulse pump chirp, a time-frequency mode structure is produced on the FWM bands [18].

Therefore, in this chapter, we present a study of the FWM process in a gas-filled capillary to properly understand the method using detailed numerical simulations. For the experimental results, we focus on the investigation of the broadband idler generation rather than the signal amplification and we only consider the fundamental mode to ensure a Gaussian-like profile at the output.
Consequently, one of the objectives of this work is to numerically and theoretically demonstrate the infrared pulse generation through the FWM in the fundamental mode. The results shown in this section have been published in Journal of the Optical Society of America B (Annex).

4.2 Numerical model

In the following section we calculate the spectral location of the lobes generated by the FWM using the phase matching equation. The signal and idler gains will also be calculated with the analytical solution of the coupled equation and NLSE. The last section discussed how the group velocity mismatch and linear chirp can affect the conversion efficiency in the FWM process.

4.2.1 Dispersion in Hollow Core Capillary

As an initial step for the FWM process in a HCC, it is necessary to calculate the propagation constant $\beta(\lambda)$ as the function of the wavelength. As it was described in chapters 2 and 3 the refractive index in HCC is calculated based on the properties of the waveguide and the refractive index of the filling gas [19].
For example, the second-order dispersion curve, β_2, as a function of the wavelength, for various argon pressures in a HCC with a core radius of 75 μm is shown in Fig. 4.1.
The refractive index $n_{gas}(\lambda)$, that depends on the wavelength, temperature, and pressure, is calculated with the Sellmeier equation [20]. The coefficients at standard conditions are given at Table 4-1.

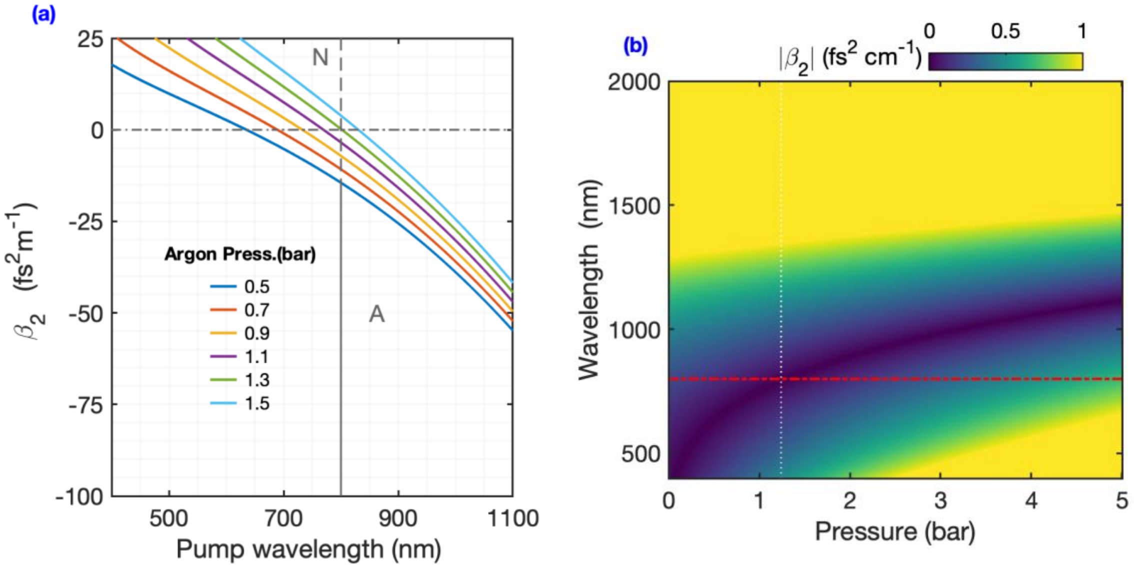

Fig. 4.1 a) Dispersion curves of the argon filled HCC. The core diameter is 150 µm and the pressure is tuned from 0.5 up to 1.5 bar. The normal dispersion is indicated with N and anomalous with A. b) Map of the absolute value of β_2 as the function of the pressure. The red line corresponds to the pump wavelength, at 800 nm. The white dotted line highlights the spectral bandwidth when $\beta_2 \approx 0$ (fs^{2}cm^{-1}).

In Fig. 4.1a., the negative GVD is indicated by letter A while the positive GVD is indicated by letter N. In this waveguide geometry conditions (argon filled HCC with a core diameter of 150 µm), the zero-dispersion wavelength (**ZDW**) at 800 nm, is indicated by the intersection between the grey and green lines. Thus, from Fig. 4.1a, we can see as the pressure increases, the ZDW shifts towards higher frequencies. In the case of a pump wavelength centered at 800 nm, the ZDW occurs at approximately 1.24 bar.

Table 4-1 Coefficients of the Sellmeier equation for argon at P_0= 1000 mbar and T_0= 273 K [2].

µm^2	**B_1 x10^{-8}**	**C_1x10^{-8}**	**B_2x10^{-8}**	**C_2x10^{-8}**
Argon	20332.29	206.12	34458.31	8.066

To adequately characterize fibers, it is necessary to know the $\beta_2(\lambda)$ value within a wavelength range. Therefore in Fig. 4.2, we indicate the landscape for absolute values of $\beta_2(\lambda)$ as function of the pressure. From the color bar, one can observe a bandwidth of 400 to 2000 nm with very small $\beta_2$values (<1 fs^{2}cm^{-1}). The red line indicates the wavelength of the pump at 800 nm while the white line represents the point where $\beta_2 \approx 0$ fs^2/cm. Thus, one can conclude that the bandwidth from 400 to 1300 presents very low chromatic dispersion values. We will see later the importance of these properties.

According to the numerical results in chapter 3, the key parameters such as core radius, gas types and pressures produce a different dispersion profile that affects the phase-matching conditions. One must pay attention to the selection of parameters. For example, depending on the input pump power, it is possible to achieve similar phase conditions by adjusting the filling gas type and core radius. The problem arises with a large core radius capillary, where the understanding of the dynamics is difficult because of the multi-mode propagation. In this sense, the first part of the research focuses only on the single-mode

FWM process. To begin with the numerical part, we chose an HCC with a 75 μm radius filled with argon.

4.2.2 Phase-matching condition

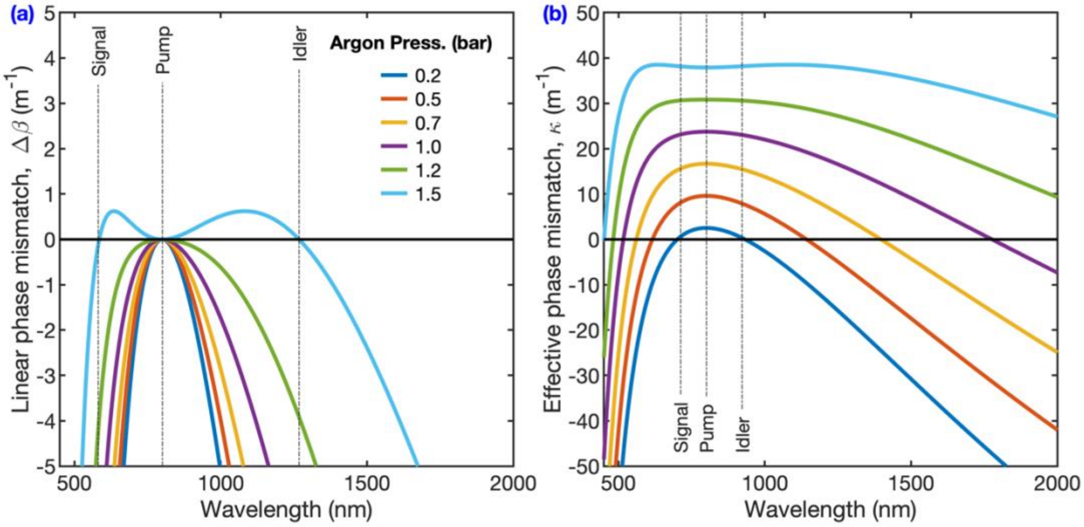

Fig. 4.2 (a) Linear mismatch in HCC for a 75 µm core radius. The argon pressure is tuned from 0.5 up to 1.5 bar. (b) Effective mismatch for input pump power of 1.67 GW, for the same pressure values as in (a).

The previous dispersion curve is used to calculate the effective phase mismatch κ and gain g from the analytical solution of the coupled equations, by considering an input pump power f 1.67 GW within a pressure range between 0.5 and 1.5 bar. The effective phase matching equation is divided into two main parts, one of these relates to a linear phase term ($\Delta\beta$), which is shown on the Fig. 4.2a. The condition for the blue line is being calculated for an argon pressure ~1.5 bar, which produces $\Delta\beta_L=0$ at the position of 1268 nm and 584 nm, respectively.

Accordingly, to Eq. (3-39), when a strong pump is involved, the non-linear contribution needs to be included in the phase-matching calculations [15]. The nonlinear contribution shifted the phase-matched curves, see Fig. 4.2 b. As a result, phase-matching takes place at wavelengths closer to the pump. This effect is caused by the nonlinear phase contribution in the phase matching equation.

In addition, there is an effective length where the four fields can exchange energy, which is the inverse of effective phase mismatch, $L_{coh}=2\pi/\kappa$. If L_{coh} value is small, the distance could be several meters and we can select a long fiber. Otherwise, if L_{coh} is high, the distance will be limited to few millimeters, i.e., we may select a short fiber.

4.2.3 Gain tuning by pressure

The double peak position of the FWM bands (signal and idler frequencies) is directly linked to n_2 and β_2. Thus, their bandwidth and gain can also be modified simultaneously (Fig. 4.3). The gain is calculated as the function of the pressure for a 70 cm-long argon filled HCC with a core radius of 75 µm.

The power gain increases while the peaks move away from the pump, see Fig. 4.3a. The gain bandwidth also increases with the pressure, but as soon as β_2 becomes positive, the gain bandwidth becomes narrower. In other words, at high pressure, the signal and idler gain region are clearly separate from the pump wavelength, appearing a region around the pump where the gain is weak, see Fig. 4.3b. The best conversion efficiency point is indicated by the white dashed line in the Fig. 4.3b, and it represents a pressure value around 1.3 bar. The corresponding central wavelength for idler and signal is 2439 and 478 nm respectively (± 252 THz).

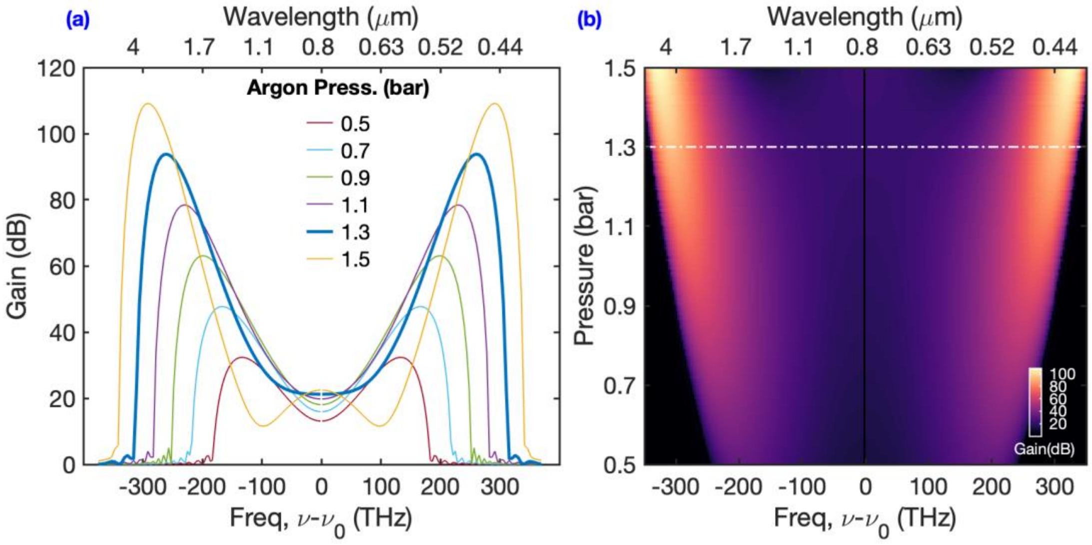

Fig. 4.3. (a) Signal and idler gain as function of the argon pressure. The input peak power is 1.67 GW. The core radius is 75 µm. and the HCC length is 70 cm. (b) Gain map, as a function of the frequency offset and argon pressure. The dote-dash line represents the point where $\beta_2 \approx 0$ fs^{2}cm^{-1}.

The gain is also calculated as a function of the input peak power and displayed in Fig. 4.4. The signal and idler positions shift away from the pump as the peak power increases. In this way, it is possible to generate an idler further in the infrared over 3 μm, with a good gain value.

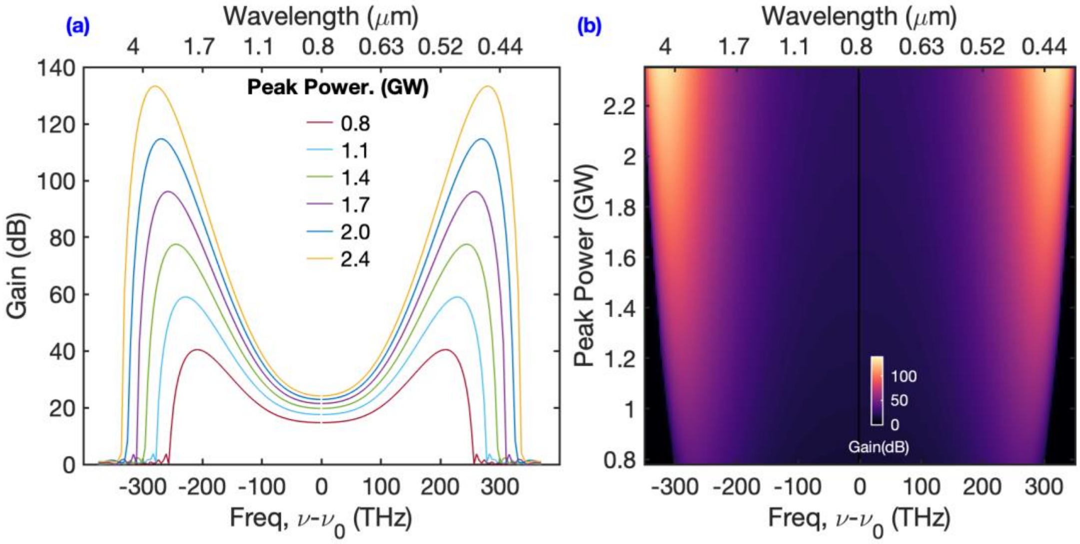

Fig. 4.4 Signal and idler gain vs argon pressure for input pump power from 0.8 up to 2.4 GW (b). Spectral gain map as function of pump power. The argon pressure is 1.3 bar.

4.2.4 Gain vs the HCC length

The gain at the lobe frequency obtained in an HCC length, is calculated by setting the input pressure at 1 bar and the peak power at 1.67 GW. In Fig. 4.5a, we show the evolution of the gain as the function of the HCC lengths from 1mm to 90 cm. Three spectra are also selected at specified lengths to show how the gain changes (Fig. 4.5b). As a result, by increasing the HCC length up to 90 cm it is possible to obtain high gain higher than 80 dB. The same gain value can also be obtained with a higher pressure and a shorter HHC (e.g. 80 dB for a length of 70 cm and a pressure of 1.3 bar, see Fig. 4.4). However, changing the parametric leads to a shift of the spectral band positions of the signal/idler due to the phase-matching conditions. In Fig. 4.4.b, the signal/idler lobes are closer to the pump, at 220 THz corresponding to 1935 and 504 nm.

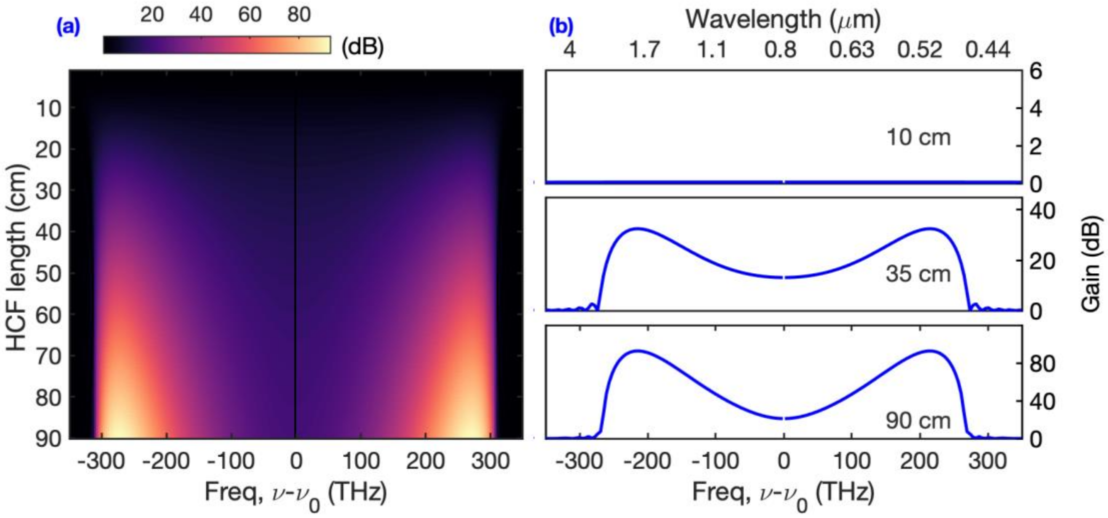

Fig. 4.5 Evolution of the spectrum along with an HCC as the function of the frequency offset from the pump at 800 nm and argon pressure of 1 bar (b) Selected spectrum at a length of 10, 35, and 90 cm.

4.2.5 The group delay mismatch in HCC

The spectral components of the pulse propagate at different speeds within a fiber due to the Group Delay Mismatch (**GDM**). Specifically, the nonlinear interaction between two optical pulses is reduced and then stops when the two pulses do not overlap, i.e. the faster pulse passes completely through the slower pulse. This feature is known as the temporal **walk-off length**, L_{WL}, defined by:

$$\mathbf{L}_{\mathbf{WL}}=T_0/\left|\mathbf{d}_{12}\right|, \qquad (4-1)$$

$$\mathbf{d}_{12}=\beta_1(\lambda_1)-\beta_1(\lambda_2), \qquad (4-2)$$

where λ_1 and λ_2 are the center wavelengths of each pulse and T_0 pulse width.

As an example, in the following, we consider a pulse duration of 100 fs (FWHM) for the pump, signal and idler. The pump and signal wavelengths are set at 800 and 550 nm, respectively. The calculated GDM is displayed in the Fig. 4.6 where two pulses are separated at a rate of=17.7 fs m^{-1}. This means the estimated walk-off length is $\simeq$ 5.6 m. According to the energy conservation law $\left(\frac{1}{\lambda_4}=\frac{2}{\lambda_1}-\frac{1}{\lambda_3}\right)$ the corresponding idler wavelength is $\sim$1666 nm. Thus, the idler pulse will separate from the pump at a rate of 69 fs m^{-1} (dashed line on the right side in Fig. 4.6) leading to a walk-off length of $\simeq$ 1.4 m. This value defines a limit of the HCC length.

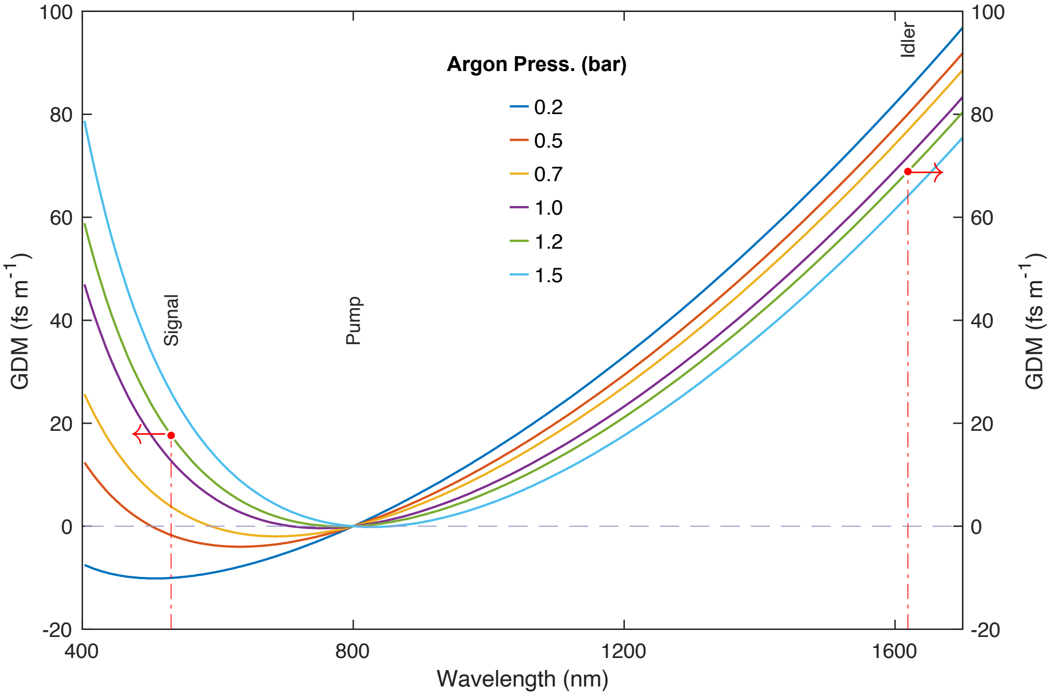

Fig. 4.6 Group Delay Mismatch in an HCC with a core diameter of 150 µm and an argon pressure varying from 0.2 up to 1.5 bar. The red dots represent the GDM value of the signal and idler for an argon pressure of ~1 bar.

4.2.6 Broadband pump

In addition to the GDM, another important key point for an ultrafast amplifier is its spectral bandwidth. Commonly in an OPA, an efficiently transfer energy occurs from a narrowband pump pulse to a broadband signa/idler pulse. The pump and the seed pulses must be temporally overlapped to exchange energy. In OPA often the seed signal is a white light continuum (**WLC**) which usually is temporally chirped due to its propagation in the generation medium. Therefore, by changing the relative delay between the pump and signal, specific frequency components of the signal can be amplified from a short pump pulse. This leads to a tunable signal amplification and idler generation, see Fig. 4.7a.

A broadband amplification occurs when the phase-matching conditions are fulfilled for a very broad spectral range of the signal[9] . Thus, it is often necessary to temporally stretch the pump pulse to achieve a better overlap with the signal, see Fig. 4.7b.

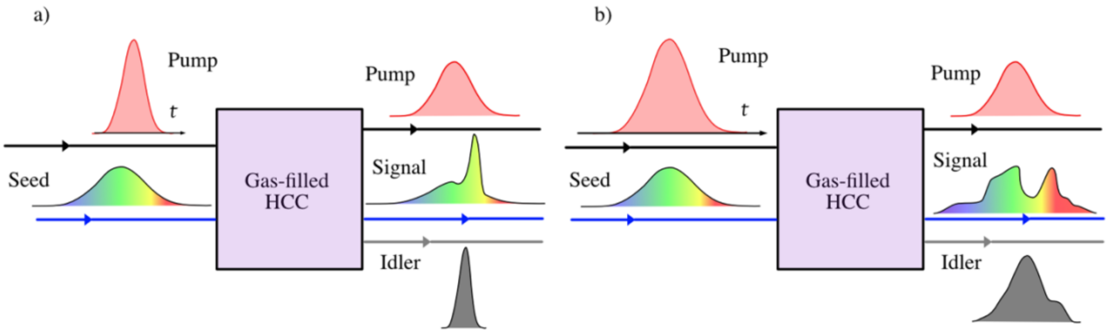

Fig. 4.7 Broadband amplification with a chirped seed signal and a short pump (a) or a long pump (b)

The analytical model described before does not fulfill explain the ultra-fast FWM because it does not include the contribution of the pump bandwidth. Therefore, from the derivation over the linear phase Eq. (3-42), we know β_2 term dominates the process and when $|\beta_2|$ is relatively small, one should include the β_4 term as well[21]. Moreover, each pump spectral component has an impact on the FWM, which depends on the odd terms of the dispersion[7].

In the following, we will define a chirped pump as the sum of the CW at various frequencies around the central frequency[22]. The chirped pump also affects the frequency generation. Then, the spontaneous photons will be generated with a temporal delay,τ, and a spectral distribution according to the matched FWM relation.

A simple model based on the spectral distribution of the pump has been developed to calculate the coherence length, imitating a broad band pump pulse with a adjustable wavelength from 750 to 850 nm, Fig. 4.8. The CL is also calculated for different pressure values and is represented by the lines. The results are displayed in Fig. 4.8a.

For example, in the 2D representation, Fig. 4.8b, the CL for a pressure of 1.25 bar, (line with a grey shadow on Fig. 4.8), the idler band expands from 1200 up to 3400 nm. At higher pressure, and the idler/signal bands also become narrower, the CL decreases, and the bands move away from the pump frequency.

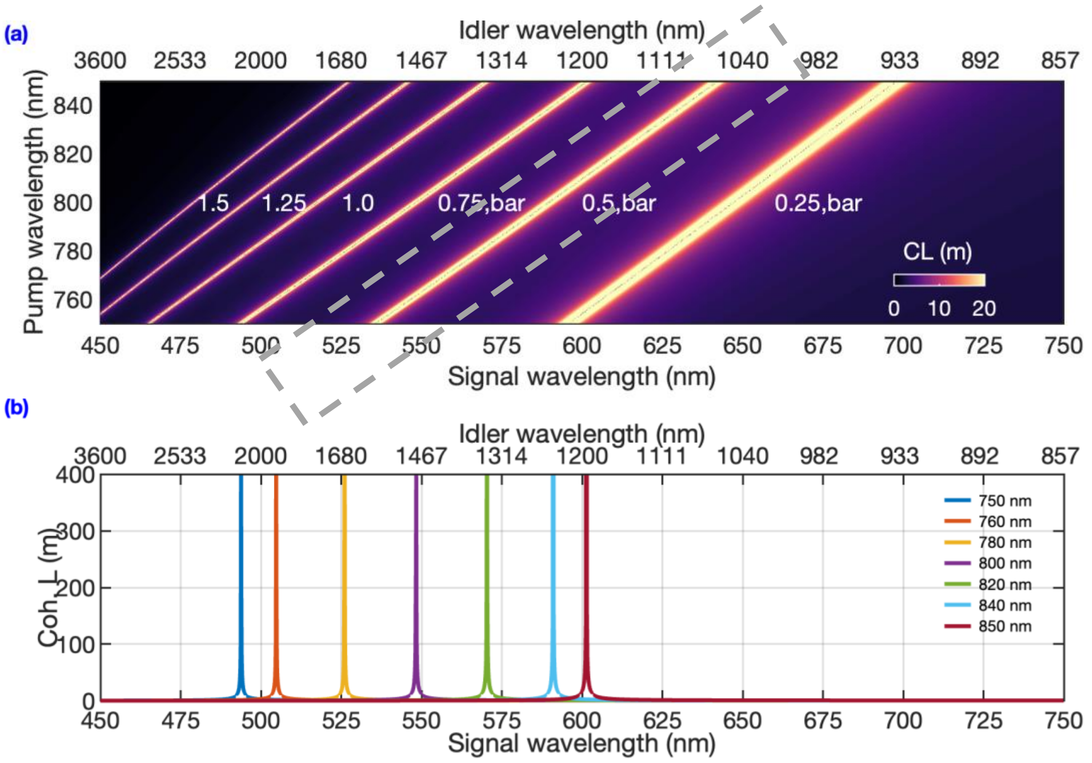

Fig. 4.8 a) Coherence length CL, for a tunable continuous pump wave at different argon pressure. b) FWM bands for an argon pressure of 1.25 bar and for tunable pump from 750 to 850 nm.

4.3 Pulse propagation by integrating the NLSE

When the pump is considered at the Fourier transform limit, all generated FWM bands temporally overlap. However, in most cases, the pump acquires a chirp when it propagates through the non-linear medium, even with low dispersion, such that its spectrum becomes modulated in phase. To validate the previous analytical model for a chirped pulse with broad bandwidth, numerical simulations were performed by integrating the NLSE using the split-step Fourier method.

The input configuration of the code is 2^{15} points and a temporal resolution of 1.3 fs. This leads to a total window of about ~±21 ps and a frequency span of ~± 374 THz. The global error is set at 1e^{-6}, and the initial step size h is 2 mm. The gain profile has been calculated by injecting a FT limited pump pulse with a central wavelength at 800 nm and a duration of ~120 fs at FWHM. The pump energy is 205 µJ leading to a peak power of 1.67 GW. Half photon per temporal mode is added as the initial condition, to mimic the random noise.

Fig. 4.9 shows the evolution of the total spectrum along 60-cm in the HCC filled with argon at 1.25 bar pressure ($\beta_{20} = -0.839\ fs^2m^{-1}, \beta_{30} = +40.73\ fs^3m^{-1}$). The pump spectrum broadens and after approximately 20 cm, the pulse starts to generates two lateral bands at around ± 225 THz and the spectral components are progressively amplified during propagation. This configuration shows an asymmetric broadening caused by the existing GVD property on the HCC [21]. As might be expected, the spontaneous side lobes of FWM become stronger as they propagate through the medium.

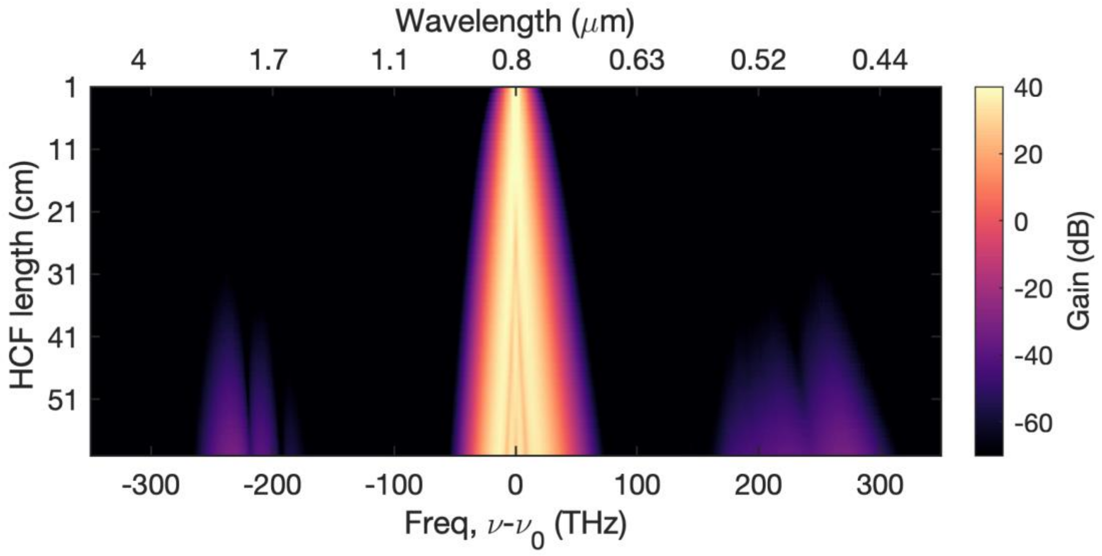

Fig. 4.9 Spectral evolution of the pulse along a 60 cm-long HCC filled with argon at a pressure of 1.25 bar. The spectral intensity is in logarithm scale. The pump wavelength is set at 800 nm. The peak power is 1.67 GW.

The output spectrum after the pulse propagates in 60 cm is displayed in the Fig. 4.10a, where two weak lobes appear with a frequency shift of ~± 225 THz (corresponding to ~500 and ~2000 nm). In Fig. 4.10b, the coherence length is shown for several tunable CW pump. In both cases, the signal and idler bandwidths match with each other. This means that the analytic solution could be an efficient tool to estimate signal or the idler bandwidth.

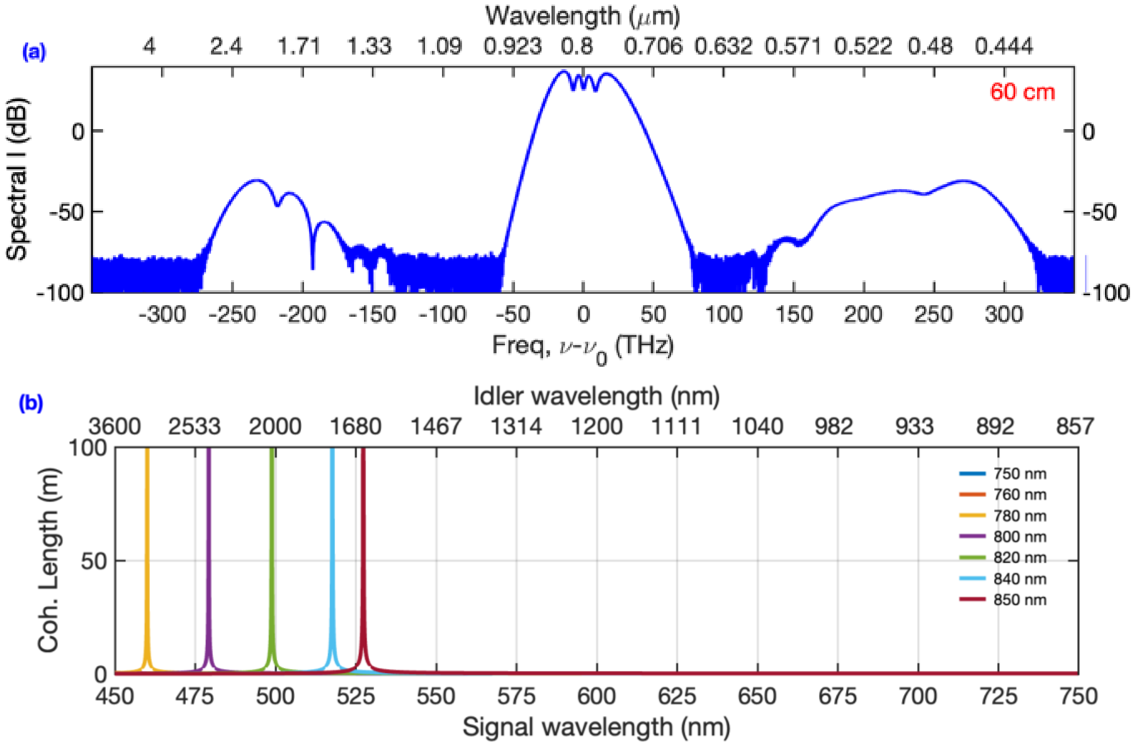

Fig. 4.10 (a) Output spectra calculated by the NLSE where the signal band extends from 444 up to 600 nm whereas idler band from 1.2 up to 3 µm. b) Coherence length calculated from a tunable CW pump where the signal band extends from 475 up to 550 nm and the idler bandwidth from 1.4 up to 3.6 µm.

4.3.1 Effect of the second order dispersion term

As the pump propagates in the HCC the pulse acquires some chirp. Its instantaneous frequency varies for each angular pump frequency over the entire bandwidth $\Delta\Omega_p$ [22]. If we considered a broadband pump as an ensemble of CWs, each pump frequency generates peaks at different frequency positions and different times. The second-order dispersion term for a broadband pump is not constant and it is possible to observe an asymmetrical spectral enlargement of the bands [21]. For example, when the central pump frequency is shifted, the bands are also shifted. As a result, the signal/idler components will not be offset by the same amounts, because β_{20} has different values (Fig. 4.1a). In our case, the dispersion curve is asymmetric, so the spectral change is more significant in signal components than on the idler [21]. Indeed, because of this large spectral shift, two subsequent peaks can be generated on the idler side but from a different pump frequency. By another hand, many bands are generated from a chirped pulse. If the spectral shift is not very large, the band cannot be distinguished within the spectral range since they overlap. As found in Fig. 4.10, the two lobes are symmetric as respect to the pump frequency. However, because the HCC is not pumped by CW, each pump component generates a specific FWM with their positions that vary with its own β_{20} value.

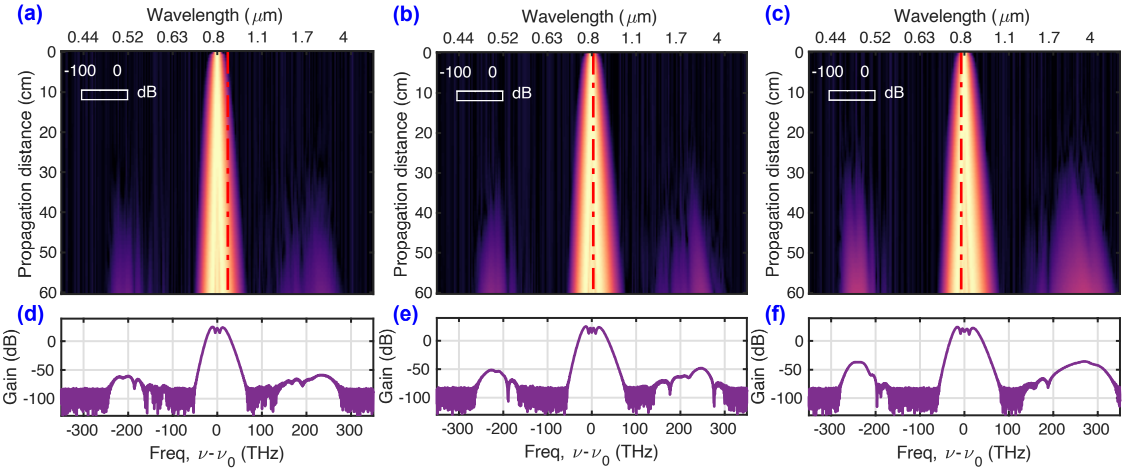

Fig. 4.11 (a) Spectral evolution of FWM simulated by the NLSE for HCC filled with three different pressures (a) 1 bar, β_{20}: -5.408 fs^{2}m^{-1} and β_{30}: 38.63 fs^{3}m^{-1}, (b) 1.24 bar, β_{20}: -0.839 fs^{2}m^{-1} and β_{30}: 40.65 fs^{3}m^{-1} (c) 1.4 bar, β_{20}: 1.90 fs^{2}m^{-1} and β_{30}: 42.0 fs^{3}m^{-1} Images (d),(e),(f) are the output spectrum at the HCC length of 60 cm.

Fig. 4.11 shows the spectral evolution of the pump in the same HCC, but with three different dispersion regimes adjusted by gas pressure. With a negative β_{20}. value the bandwidths lobes are more symmetric around the frequency pump. A positive value of β_{20}results in gain improving, but with a more asymmetrical shape.

4.3.2 Four-Wave Mixing Chirped Pulse Amplification

FWM can also be used to amplify a chirped broadband signal [17] by using a chirped pump with a relatively broad spectrum. With an input chirped pump pulse, it is also possible to limit the SPM contribution and to increase the injected pulse energy.

As the chirped pulse propagates into the HCC, each spectral component generates its own FWM spectrally shifted. For example, in the numerical calculations, the pump pulse is stretched to 180 fs by applying a positive second-order phase of 198 fs^2. The argon pressure is 1.24 bar. The generation of the FWM bands appears at ~30 cm and the lobes are centered at a frequency offset from the pump of ~225 THz (Fig. 4.12). However, the spectral bands are strongly modulated, resulting from interferences between the FWM bands generated at different time points from the modulated pump spectrum.

In the spectral evolution with the length (Fig. 4.12a) and the spectrogram (Fig. 4.12b), we can see that each instantaneous pump frequency generates a well-defined band at a given time. Both spectral bands are asymmetrical, such that the bandwidth is greater in the anti-Stokes side (visible spectral components). Referring to the spectrogram (Fig. 4.12b), the signal band (bottom) seems to have ascending slope, while the idler slope is nearly flat. This feature is useful when pretending to seed the amplifier with a chirped signal.

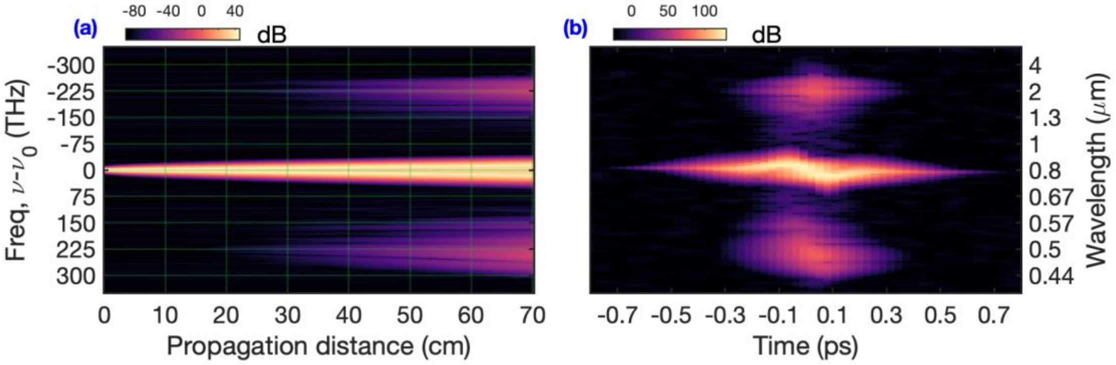

Fig. 4.12 Spectral evolution in the 70-cm long HCC filled with argon at pressure of 1.24 bar. The positive chirp is 198 fs^2. (b) Spectrogram of the total electric field at the HCC output.

The comparison between the output spectrum (*70-cm-long HCC*) when a positive and negative input chirped pump is shown in Fig. 4.13. The pump spectral broadening is slightly stronger when the pump is positively chirped, while in the time domain, the pulse is shorter. The pump bandwidth is always narrower in the case of a FT limit pulse (Fig. 4.13) due to the SPM contribution. The signal and idler band are not significantly affected by the sign of the chirp (Fig. 4.13a), in contrast, the spectral broadening of the pump and the lobes are stronger with the case of limit pulse FT (Fig. 4.13c). However, the spectral bands are strongly modulated for the case with the chirped pump, which probably results from the interference between the FWM bands generated at different delays.

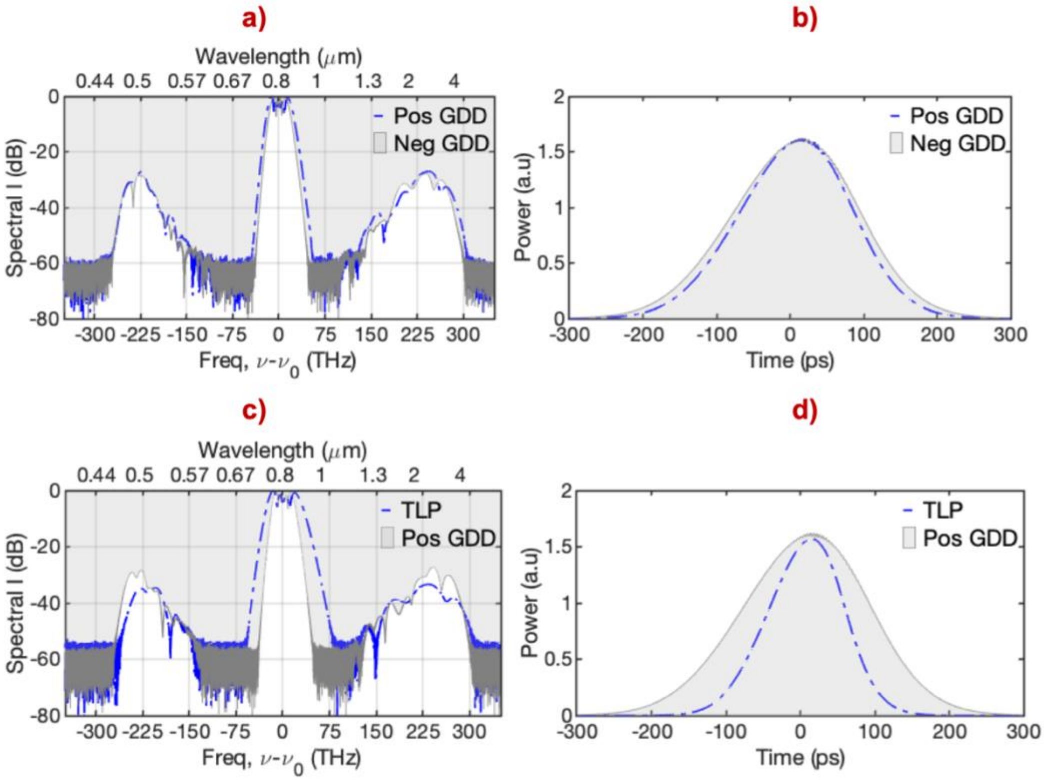

Fig. 4.13 a) spectral and b) temporal comparison of the output pump pulse with positive and negative chirped input pump in an HCC filled with argon at a pressure of 1.24 bar, c) spectral and d) temporal comparison of the output pump pulse with positive and FTL (TLP) pump in 60-cm long HCC filled with 1.2 bar argon.

4.4 Signal amplification and frequency generation in HCC

To increase the pulse energy [4], the pulses are often stretched to reduce the input peak power in the system and to avoid any damage in the material. At the output of the system, the targeted pulse is compressed after the amplification step. These schemes are known as Optical Parametric Chirped Pulse Amplifier (**OPCPA**). In this manuscript, the same idea is performed but, in a gas-filled guided system that provides significant advantages thanks to the guiding geometry. On the other hand, Four-wave Mixing in a gas medium has been successfully investigated for frequency conversion[16–18] and light amplification [11] in PCF and FWM in nonlinear crystals. To increase the bandwidth amplification and improve frequency conversion efficiency, a suitable selection of experimental parameters is required. For this reason, a combination of OPCA and FWM schema is evaluated in the following section.

From the previous simulation results, several characteristics were obtained, such as the gas pressure, dispersion regime, sign of chirp, the central wavelength of the sidebands, and their spectral bandwidths. Therefore, for the following simulations, a signal pulse is now injected with a central wavelength of 550 nm. The spectral bandwidth of the signal is 100 nm at FWHM (Fig. 4.14.a). The input peak power is set at 264 W.
The Table 4-2 summarizes the various combinations of GDD, pump and signal energy used in the numerical calculations.

Table 4-2 Spectral phase and time duration of the pump and signal pulses in the cases under study

Case	GDD - ΔT_o	Φ_p=0 fs^2 T_p=120 fs	Φ_p=0 fs^2 T_p=120 fs	Φ_p=5807 fs^2 T_p=200 fs	Φ_p=16524 fs^2 T_p= 400 fs
I a	Φ_s= 97 fs^2; T_s= 81 fs	E_{p1} = 200 uJ E_{s1}= 203 pJ			
I b	Φ_s=159 fs^2; T_s=132 fs		E_{p1} = 200 uJ E_{s1}= 503 pJ		
II a	Φ_s= 227 fs^2; T_s= 188 fs			E_{p1} = 342 uJ E_{s1}= 3.8 nJ	
II b	Φ_s=480 fs^2; T_s= 395 fs				E_{p2}= 689 uJ E_{s2}= 7.7 nJ

4.4.1 FWM generated with a FT limited Pump, (Case I).

In case I.a, the signal is positively chirped with a spectral phase equal to Φ_s=97 fs^2 such that the signal pulse duration is shorter (81 fs) than the FT-Limited pump. For Case I.b, the signal is chirped with a spectral phase equal to Φ_s=159 fs^2 and the duration is longer than the FT-Limited pump (Fig. 4.14.a). In both cases, the peak power is constant, i.e., the input energy changes, see Table 4-2 .

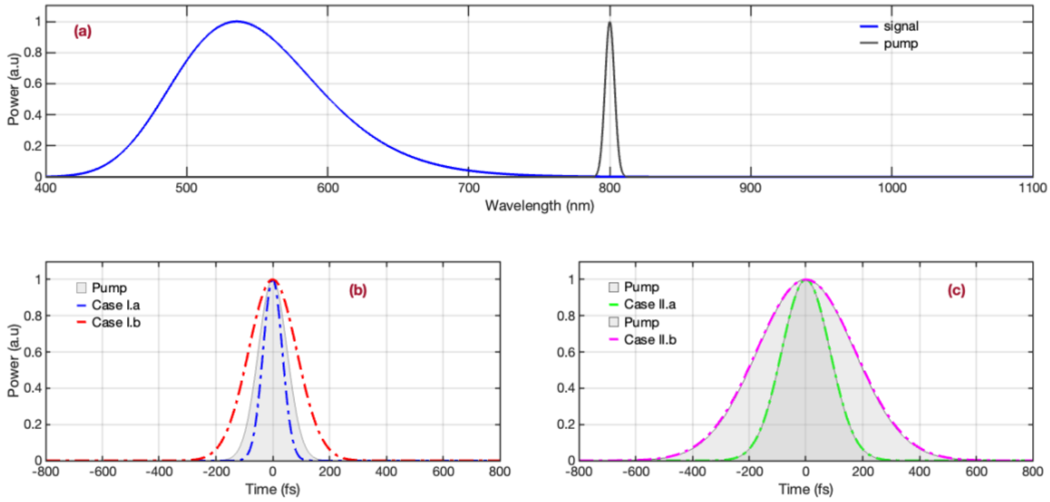

Fig. 4.14 Normalized spectral intensity of the pump (black line), and signal (blue line). B) Case Ia, Normalized temporal profile of the FT limited pump pulse (gray curve) and a stretched signal with Φ_s= 85 fs^2 (blue dotted-dash line). C) Case I. a, Normalized temporal profile of the FT limited pump pulse (gray curve) and a stretched signal with Φ_s= 214 fs^2 (red dotted-dash line)

The conversion efficiency is calculated as the ratio between the output signal power at z=L and the input pump power at z=0, such as,

$$\eta = P_s(z=L) / P_p(z=0) \qquad (4-3)$$

The efficiency curve for the positively chirped input signal is displayed in Fig. 4.15. For each case, the maximum efficiency (>10 %) is reached at a pressure between 1 and 1.25

bar. The signal side is higher than the idler side, because of the interplay between the GVD value and nonlinearity, that cooperates in establishing the phase condition within a shorter propagation distance.

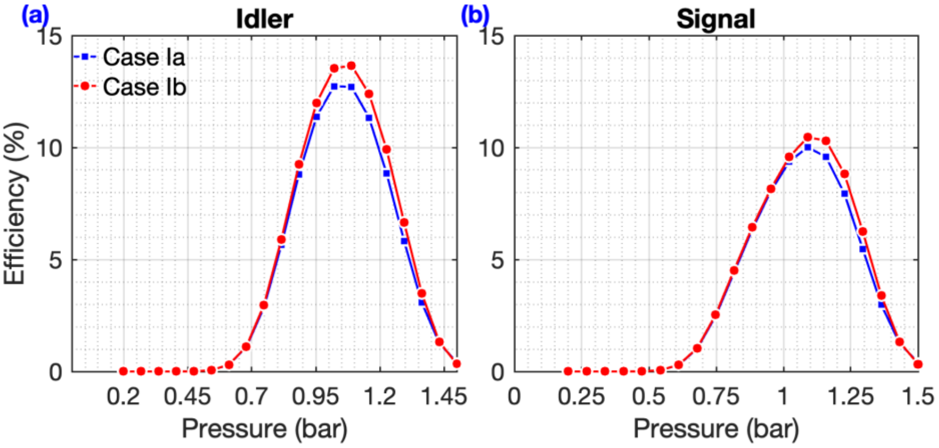

Fig. 4.15 a) The idler and signal efficiency of the FWM generated with a FT limited Pump and negatively chirped signal, with ϕ_s= 85 fs^2 (red line) and ϕ_s= 214 fs^2 (blue line). B) idler, and signal efficiency of FWM generated with a FT limited Pump and positively chirp signal, with ϕ_s= 85 fs^2 (red line) and ϕ_s= 214 fs^2 (blue line). The HCC length is 60 cm.

Based on the spectrograms shown in Fig. 4.11, we already knew that the generated spontaneous signal seems to have a positive slope. Therefore, we conclude that if a positive chirped pump is seeded in the amplifier, the process will be more efficient.

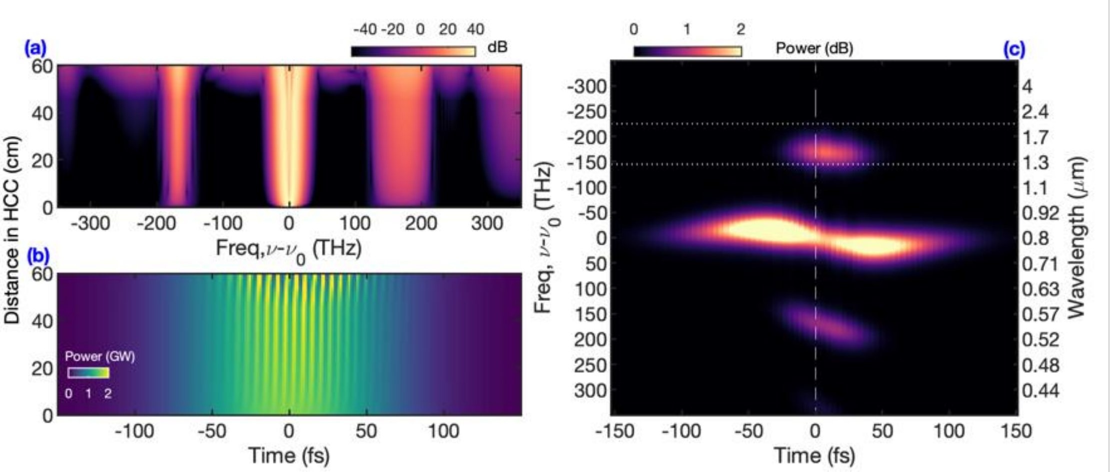

Fig. 4.16 a), b)Spectral and temporal evolution in a 60 cm-long HCC filled with an argon gas at 1.2 bar. c) Spectrogram of the output pulse of the 60 cm long HCC filled with 1.2 bar argon.

Fig. 4.16.a shows spectral and time evolution when a positively chirped signal propagates together with FT-Limited pump, through a 60-cm long HCC filled with argon at 1.2 bar. The spectral and temporal profiles at z=60 cm are displayed in Fig. 4.16.b. The generation of the FWM bands becomes clear after a few centimeters of propagation, and the spectral bandwidth is wider in the anti-Stokes side. The side lobes are centered at a pump frequency offset of ~180 THz.

In Fig. 4.16b, the optical beating between the signal and the pump is observed, which leads to the FWM observed in the time domain.

From the spectrogram Fig. 4.16.c we can note that each instantaneous pump frequency generates a well-defined band at a specific time.

The FWM bands is generated at maximum when the relative delay is ~20 fs from the pump center. Simultaneously, a portion of the pump power starts to deplete. The output FWM bands are marginally delayed from each other, and the idler generation is less efficient since the signal pulse does not overlap with the powerful part of the pump. This effect is the result of the GDM.

4.4.1-1 Group velocity mismatch effect

As noted in the previous section, there is a GDM because the signal and pump propagate at different speeds. For example, the signal may temporally overlap only with the trailing edge of the pump if the GDM values have the opposing sign. Thus, the transfer energy becomes affected since the interaction does not occur from the strongest part of the pump, see Fig. 4.17. In addition, in the spectral domain, since only a small amount of the signal spectral components interacts with the pump pulse, the amplification and generation bandwidth can be reduced.

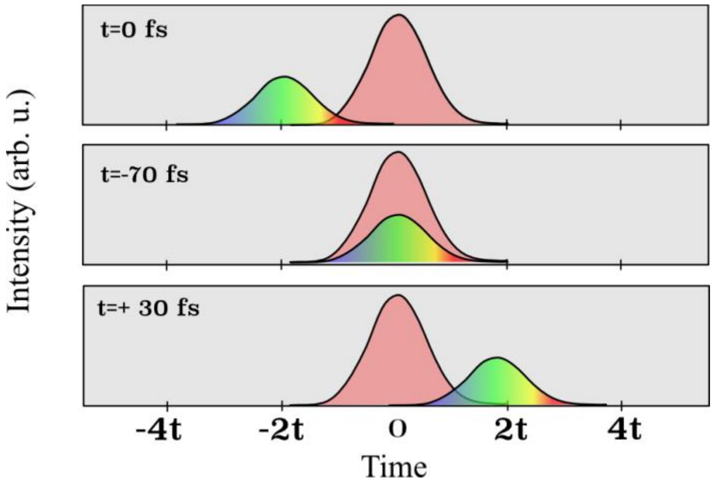

Fig. 4.17 Temporal overlap between the signal and pump pulses.

For instance, if a broadband chirped signal and a narrow pump are introduced into the amplifier, by changing the relative delay, different spectral components of the signal can overlap with the pump. This feature allows to have a free adjustment of the idler frequency.

Hence, as a conclusion, the GDM affects the corresponding phase conditions and also reshaped the idler/signal bandwidth. The output spectrum and spectrogram comparisons are shown on Fig. 4.18. In this case the argon pressure is 1.2 bar (case Ib).

When the signal is injected with a delay offset of -20 fs from the pump, the idler central wavelength is around 1.5 µm, with a bandwidth of ~70 THz whereas the signal has an amplification band of ~200 THz.

When the signal delay offset is + 20 fs from the pump, the generated idler lies close to the pump around 1.4 µm with a narrow bandwidth. The signal bandwidth amplification starts at 690 nm and its maximum amplification wavelength is ~550 nm. The shape of the modulated pump is more asymmetrical compared to the case when the delay on the signal is not null (grey shape).

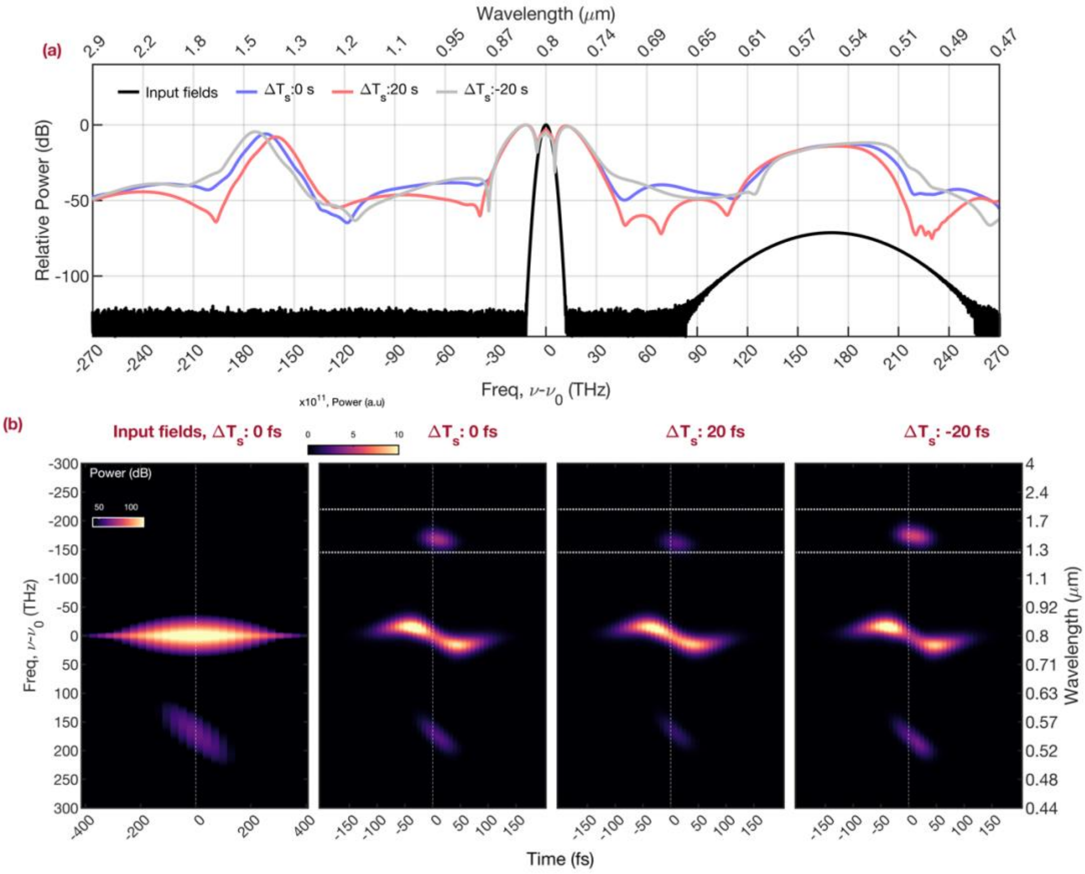

Fig. 4.18 a) Comparison of the output spectral profile for different relative delays b). Spectrogram for different delays (b) The 60-cm long HCC is filled with argon at a pressure of 1.2 bar.

In Fig. 4.18.b, in the second box, we can see three main bands around zero delay. They correspond to the signal, pump, and idler, respectively. The area around 1.4 μm is the idler generated by FWM. In the box number 4 ($\Delta T_s = -20$ fs) FWM seems to occur in the central part of the pump pulse, where the strongest portion of the pump is located. When the GDM is not well-compensated (the remaining spectrograms), the signal and pump spectral components do not have the best temporal overlapping. Only part of the pump is involved in the FWM process. Consequently, there are less spectral components in the idler band.

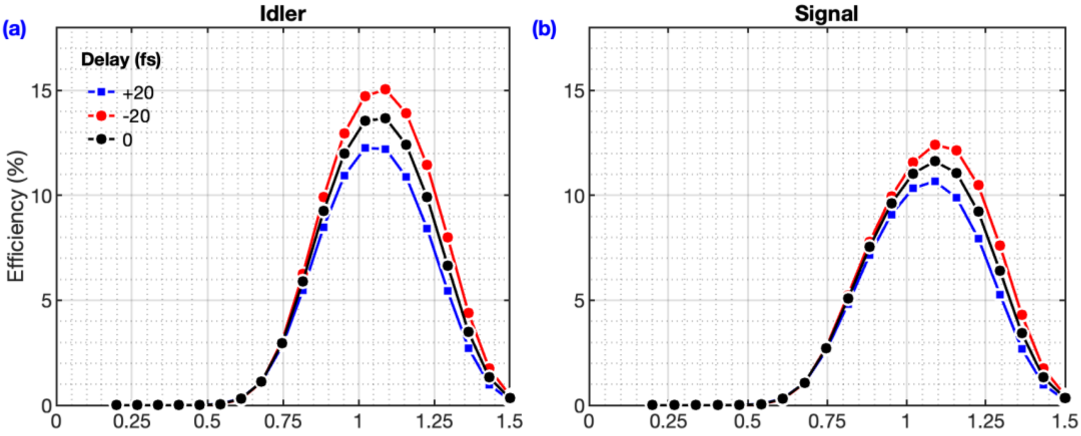

Fig. 4.19 Efficiency for several relative delays between the pump and signal, for Case Ib

As conclusion, the efficiency of the FWM process can be enhanced by setting the relative delay between the pump and the signal (Fig. 4.19). A higher amount of power is transferred to the signal and idler in the case with of a relative delay of -20 fs. This comparison provides a clear picture of the relationship between GDM and FWM performance.

4.4.2 FWM generated with Chirped pump, (Case II)

Case II a and Case II b.

We then applied a linear chirp on the two pulses to stretch them such that they have the same pulse duration (Fig. 4.14c). This configuration is called Case II (Table 4-2). The spectral bandwidth and central wavelength of the signal are the same as in Case I. The conversion efficiency is calculated as the function of the argon pressure, considering a 60-cm long HCC.

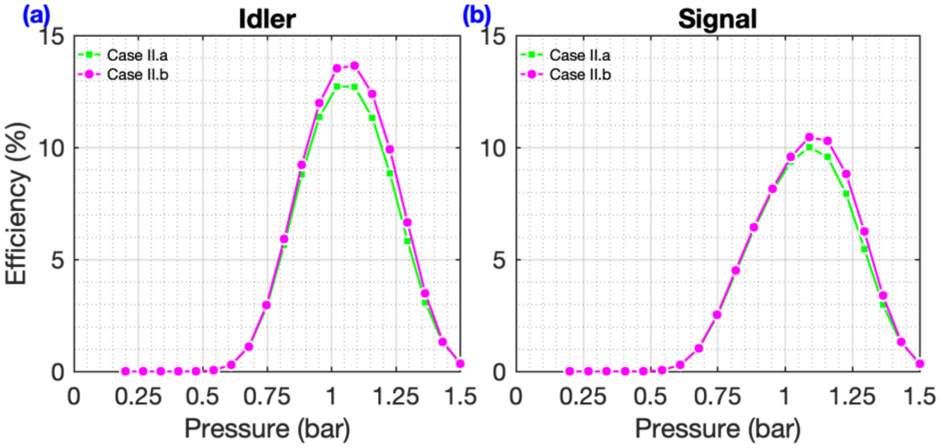

Fig. 4.20 a) Idler, and b) Signal efficiency when the pump and signal are negatively and positively chirped respectively. Bottom graph, idler, and signal efficiency when the pump and signal are both positively chirped Case II a, b.

A positively chirped pump produces a higher efficiency value than in the previous case, (Fig. 4.15). The highest point remains between 1 and 1.3 bar, with the pump propagating in the normal dispersion regime (pressure >1.0 bar).

The efficiency improvement is due to the fact that more signal spectral components can overlap temporally with the pump, thereby fulfilling the corresponding phase matching condition in a broad bandwidth. The idler conversion efficiency is 2% better than in Case Ib (Fig. 4.20).

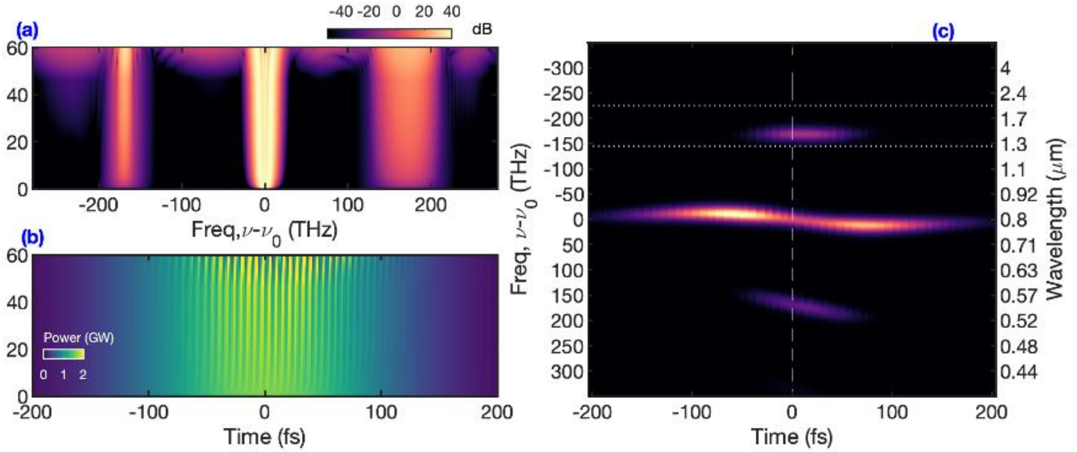

Fig. 4.21 a) spectral evolution b) temporal evolution in a 60-cm long HCC filled with an argon pressure of 1.2 bar c) Spectrogram of the output pulse in a 60 cm long HCC filled with argon at a pressure of 1.2 bar.

Fig. 4.21.a shows spectral and time evolution when a positively chirped signal propagates together with a positively chirped pump, through a 60-cm long HCC with a gas pressure of 1.2 bar. The generation of the FWM bands appears clearly after few centimeters of propagation and the side lobes are centered at a frequency offset of ~180 THz. The FWM spectral bandwidth is larger on the signal side. In the spectrogram of Fig. 4.21.c it can be pointed out that FWM bands appear at around 0 fs. The signal and the idler bands are slightly shifted towards the positive times due to the weak GDM effect. Accordingly, it can be concluded that the spectral components of the signal with the pump pulse have a better overlap when the pump and signal are stretched to a similar pulse duration. The signal band extends from 520 to 630 nm, with a central part around 570 nm, with a positive slope whereas the idler band is at ∼1.4 µm with a flat frequency slope.

4.4.2-1 Group Velocity Mismatch effect

The goal is to adjust the input delay between the pump and the signal to increase the efficiency and bandwidth of the idler, taking advantage of the GDM effect. We use the same configuration as Case IIb, but we applied a delay of +70 fs or -30 fs between the input pulses.

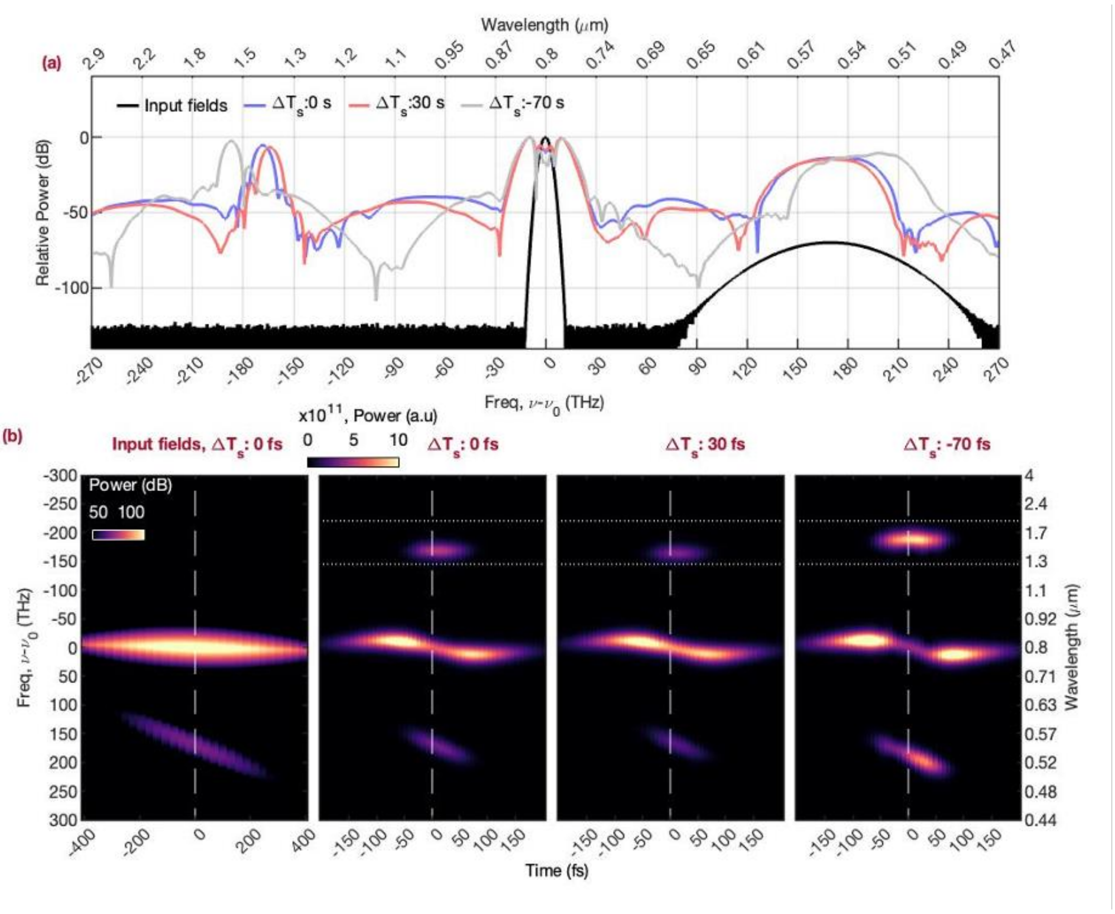

Fig. 4.22 a) Comparison of the output spectral profile for different relative delays. b) Spectrogram for different delay. The 60-cm long HCC is filled with argon at a pressure of 1.2 bar.

Fig. 4.22 shows the output spectrum and spectrograms using the previous input delays values. Regarding the spectrogram (Fig. 4.22 .b), the first image box is a spectrogram with the input fields. The following boxes are the spectrograms with different delays (0, 30, -70 fs). The blue line represents the case where the delay between the pump and the signal is null, i.e., the central wavelengths arrive at the same time at the entrance of the HCC, see Fig. 4.22.a. This case produces an idler with a central wavelength of ~1.4 µm, whereas the signal amplification band is almost ~100 THz, with a central wavelength around ~580 nm. When the signal is delayed by 30 fs, the idler band slightly shifts towards the pump, whereas its bandwidth does not significantly change from the previous case (Fig. 4.22). However, the signal and idler powers decrease because the signal spectral bandwidths involved in the process are narrower.

The case where the signal is delayed by 70 fs, the central wavelength of the idler moves closer to 1.7 µm while the signal shows stronger amplification around ~520 nm.

4.4.1 Comparison between Case I and Case II.

The case I represents the configuration when a FT limited pump is launched trough the HCC, while in case II, the pump is temporally stretched with pulses duration lower and higher than the one of the signal pulses. About the case, I a. and I b, the idler generation efficiency is a bit improved in case Ia.

In case II, the efficiency is higher on the idler side. Additionally, there is a slight increase in efficiency when the two pulses are stretched to longer pulse durations. This improvement is due to a better temporal overlap between the pump and broadband signal. In general, the efficiency remains nearly the same values in both cases (Fig. 4.23).

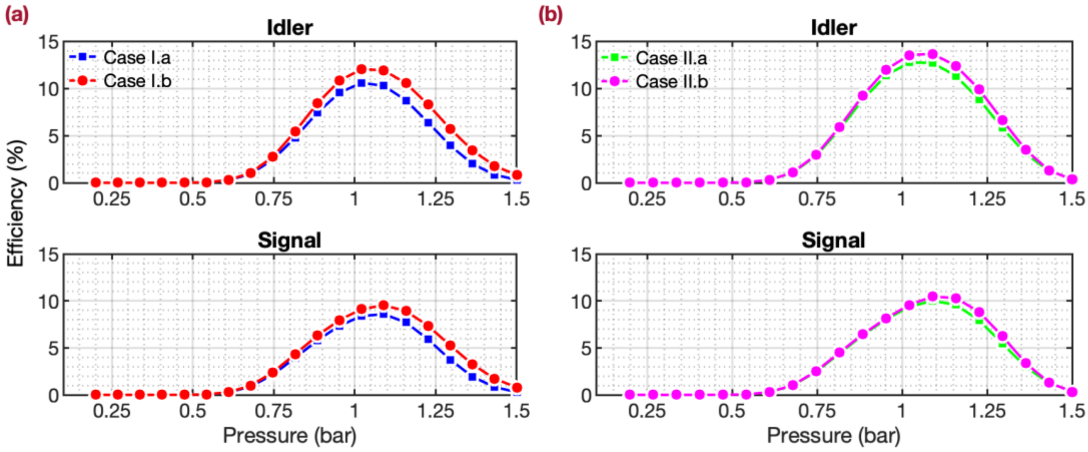

Fig. 4.23 Fig. 6. (a) Signal and idler efficiency for case I. (b) Signal and idler efficiency for case II.

4.5 Experimental setup

In terms of frequency conversion from a FWM process in a unique HCC filled with gas, Kida et al.[15] have done parametric amplification of supercontinuum signal with a gain up to 100, and the achieved amplification bandwidth supports sub-10-fs pulse. Faccio [13] reported light amplification using relatively narrowband input pulses with FWM phase matched considering high order modes. Similarly, [10] describes a tunable source of ultra-short tens-uJ-level visible pulses driven by two color pulses. However, the key parameters by which the process can be optimized are not yet clear. It is important to note that none of the work ensures that the phase-matched FWM occurs with only single mode as many parameters are involved in the process. Especially, the used hollow radius is large, and therefore, multi-mode propagation is expected.

Using the numerical results from the previous section, an experimental configuration was developed to study the phase-matched FWM in the single mode.

4.5.1 Configuration with a FT Limited pump pulse.

4.5.1-1 Experimental set up characterization

The configuration starts with a Ti:Sapphire amplifier system (Libra, Coherent Inc.) that delivers pulses with a pulse duration of ~120 fs (FWHM) at a repetition rate of 1 kHz. The maximum pulse energy is >800 µJ, and the spectrum is centered at 800 nm. The pulse from the amplifier is aligned to a 30 cm long HCC, which is located inside a home built metal chamber. The inner core diameter is 150 µm. The laser beam is focused with a plano-convex lens into the HCC, see Fig. 4.24. Three focal lengths have been tested and the coupling efficiency values are shown in Table 4 3. The focal spot size generated with the lens of f=500 mm, is about 92.33 x 72.09 µm (at 1/e2), which is close to the optimum size for the maximum coupling efficiency into EH11 fiber mode, by using the relationship shown in Chapter 2, eq (2-57).

Table 4-3 Coupling efficiency for different focal lenses.

Focal distance	**f=400 mm**	**f=450 mm**	**f=500 mm**
Input power (mW)	10.73	10.73	10.73
Output power (mW)	4.92	4.02	5.02
Efficience (%)	44.8	37.5	46.8

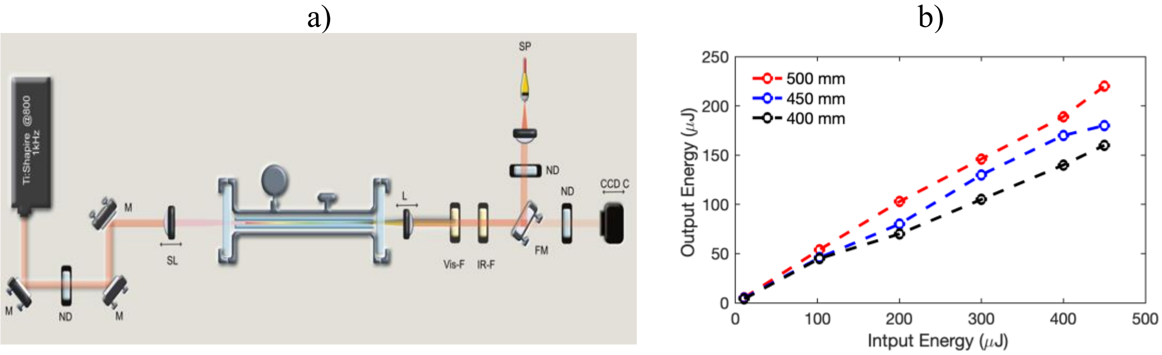
a)
b)

Fig. 4.24 a) Scheme of the setup developed for the pump coupling and chamber characterization, with input pump energy 100 μJ. M, Broadband Dielectric Mirror. ND, Neutral Absorber Filter, SL, Plan-convex Lens. Vis-F, IR-F, (Filters) BS, Beam Splitter, CCD C, Visible camera (Thorlabs BC106N-VIS), SP, visible spectrometer (Ocean optics USB 200) . b) output energy at the function of the input energy.

The chamber is composed of a stainless-steel tube with an entrance and exit 5 mm thick sapphire broadband window (Thorlabs WG31050). The chamber has also a gas input and output with a manometer. The beam is coupled into the hollow core. To avoid non-linear input effects at the fiber entrance, the air or gas was removed with a vacuum pump. Fig. 4.24.b shows the evolution of the output energy as the function of the input energy. This linear behavior confirms that not spurious effect perturbate the coupling. The output beam is collimated by a convex lens (f=250 mm) and then it splits into two paths. One to detect spectra and the other to observe the beam profile with a CCD camera (Thorlabs BC106N-VIS), Fig. 4.25.b. The output spectrum, when gas is not present in the chamber is shown in the Fig. 4.25. When the fiber is filled with air, the spectrum of the pump becomes broader, because of the interaction of light and air, SPM.

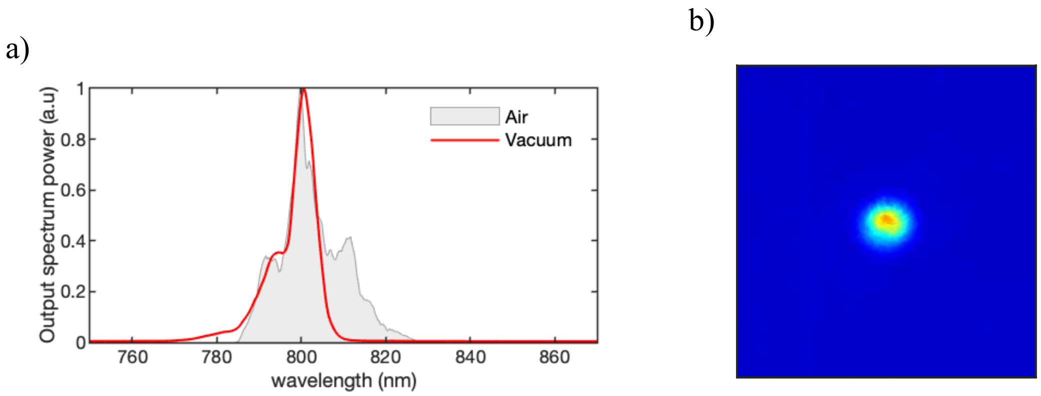

Fig. 4.25 a) Pump output spectrum using an input energy of 100 µJ when the HCC is filled with air (gray curve) and under vacuum (red line) b) Spatial distribution of the beam in the far-field at the output of HCC when the vacuum.

4.5.1-2 Set-up configuration

The scheme of the complete experimental set-up is displayed in Fig. 4.26. The light beam of the amplifier is divided in two paths with a beam splitter (90/10 %). The strongest portion is used as a pump while the weakest portion (~5 µJ) is focused on a 5 mm thick sapphire plate, and it is always placed a few millimeters before the focus point to avoid any optical damage. The pulse energy is controlled by a variable iris aperture, which allows the annular structure to be removed into the output beam. Under these circumstances, a smooth and stable white light continuum (**WLC**) is generated with a spectral bandwidth extending from 450-850 nm and is positively chirped. A 650 nm long-pass filter was placed after the collimation to remove the residual peak from the pump (FEL650 Thorlabs).

The output beam is collimated and pass through a delay line to allow temporal overlap between the pump and the signal pulses. The continuum and the pump beam are superimposed on a visible Cold Mirror (FM03). The two beams are coupled with help of their respective planoconvex lenses into the 30-cm long HCC. At the chamber output, the pump and signal energies are ~170 µJ and 0.539 nJ, respectively. The visible components are separated from the infrared part with a Hot Mirror UVFS (M254H45). Next, a low-pass filter (at 650 nm) and neutral absorbent density were fixed in front of the CCD camera (Thorlabs BC106N-VIS) and the visible spectrometer (Ocean optics USB 200). A long-pass dichroic mirror (DLMP900) is placed in the infra-red path to separate the pump from the idler components. In addition, the pump beam is attenuated by absorbing neutral density filters. By passing the visible beam through a BS, the beam profile (Genie Nano M640 Mono, Visible-Camera, sensitivity 400-850 nm) and the spectrometer signal (Ocean optics USB 400) can be measured at the same time. On the idler path to fully remove the pump components, the beam also passes through a long-pass filter (FELH1000). Finally, the beam is sent to a spectrometer (Stellar Net spectrometer DWARF-Star NIR) and another camera (CCD Hamamatsu IR-Camera, sensitivity of 900 to 1700 nm) with a flip mirror.
The experimental procedure is as followed. The pump is coupled in the capillary, once the air has been taken out of the chamber and subsequently filled with argon gas (up to 1 bar). Eventually, the input pump power was progressively increased to 400 µJ. The beam

is always set to keep the coupling efficiency all the time. Several data were recorded i) at a constant input power for different pressure values ii) at a given fixed pressure within a range of pump power.

The temporal overlap between the pump and the signal is set with a delay line. For each stage, it allows the superposition of different signal spectral components with the pump pulse, due to the signal chirp, so that different input configurations result in a different idler. Consequently, for each stage of the delay line, the data were recorded.

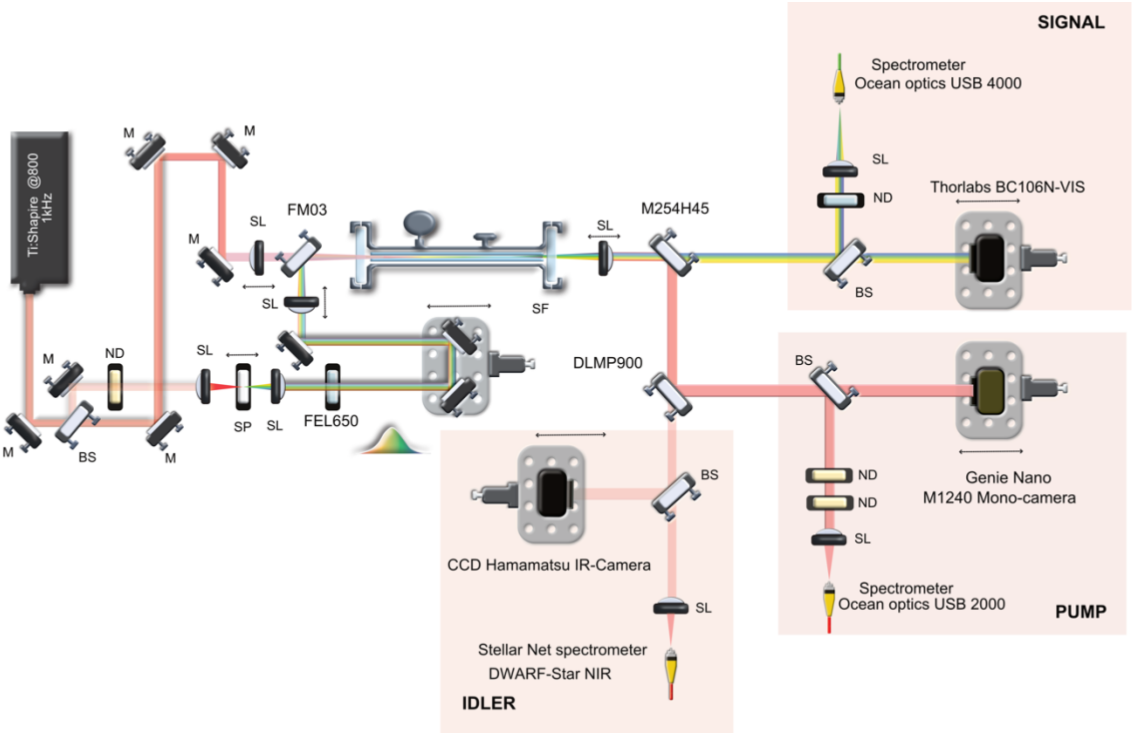

Fig. 4.26 Scheme of the complete experimental set-up. SL Plano Convex lens, BS, beam splitter, ND absorptive neutral density filter, DM, Cold mirror, LF long-pass filter, SF short-pass filter, SP Sapphire plate.

4.5.1-3 Characterization of the input pump and signal pulses.

To use the laser pulse correctly, careful characterization is required. Temporal measurements are the primary step to evaluate the duration and the spectral phase on the pump and signal. In the first instance, the pump is used directly, as it leaves the amplifier. So, the beam is sent to the spectrometer and the auto-correlator. The results of the temporal measurements are shown on Fig. 4.27a. By using the measured spectrum, the FTL shape is calculated (black line) and compared with those obtained by autocorrelation (blue line), with a pulse duration of 166 fs, assuming a Gaussian pulse shape. As part of a second set-up, the pump pulse propagates through an N-F2 glass dispersive block to temporally stretch the pump. Then, the pump is also characterized by the spectrometer and the auto-correlator. The results are displayed in Fig. 4.27b.

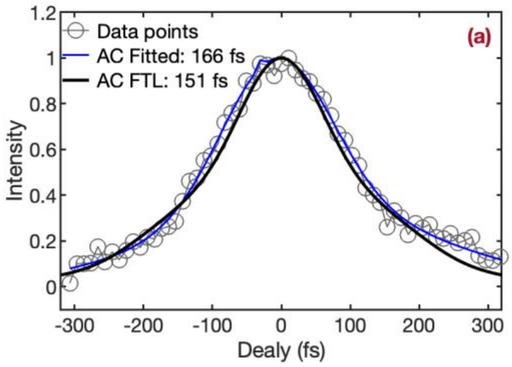

Fig. 4.27 (a) Autocorrelation trace of the unchirped pump pulse with a Gaussian fit. The duration is 166 fs (FWHM), (b) Autocorrelation trace of the stretched pump when it passed through a dispersive block of N-F2 with a Gaussian fit. The duration is 231 fs (FWHM).

As a signal is also coupled to the HCC, and its preliminary characterization is also necessary. The generated continuum is sent to the spectrometer and a FROG setup. The signal FROG traces were challenging because the phase-matching bandwidth in the crystal is usually too small. Furthermore, the signal has a spatial chirp, so only part of the bandwidth signal was taken for the FROG trace (shown in Fig. 4.28).

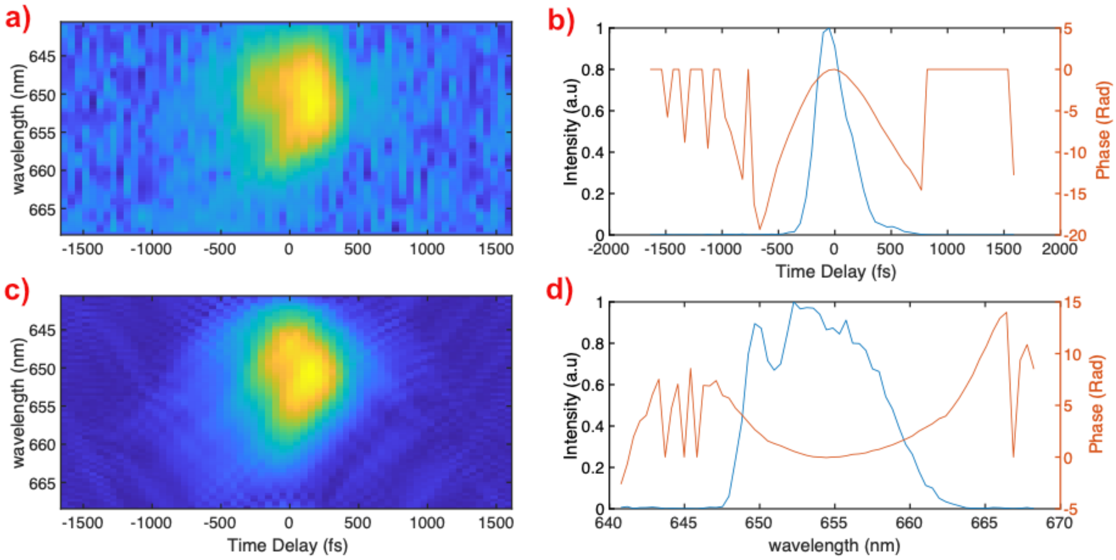

Fig. 4.28 Measured (a) and retrieved (c) SHG-FROG traces for the continuum signal at the HCC output with no gas in the chamber. Retrieved spectrum and spectral phase of the continuum signal (d). Retrieved temporal shape and phase of the continuum signal (b).

Fig. 4.28 displays the measured FROG trace and its retrieval shape, which is very similar This means that the input setting for the reconstruction algorithms provide the relevant results. The SH signal corresponds to only a portion of the complete WLC. The spectral range measured is between 645 nm and 665 nm, and its corresponding spectral phase is relatively smooth, with a predominantly quadratic phase contribution.

4.5.1-4 Experimental results

The air was firstly removed from the chamber. Then, we increase the input power at the entrance of the chamber to 503 µJ. Next, the output power of the pump was 202 µJ resulting in a 40% of coupling. The difference between the experimental and theoretical coupling value is linked to the spatial beam profile, which is not perfectly adapted to the hollow core shape, i.e., it is not completely circular, and the beam has an elliptical shape.

The signal and idler spectra are shown in Fig. 4.29 for a pressure of 1 bar. The tuning bandwidth was measured by changing the temporal overlap between the pump and signal, which depends on the micrometric offset of the delay line. The distance was divided into several stages (14 stages). The spectra of the pump, signal and idler were measured according to each step of the delay line. Both idler and amplified signal beam profiles were also measured at each step. The amplified signal component is tuned while the idler spectrum varies from 1.1 µm to 1.4 µm.
We can also observe in Fig. 4.29 the evolution of the signal spectrum as a function of the time overlaps. For longer delay, only one narrow band of the signal is amplified, around 575 nm. When the delays are below 300 fs, a second amplification band appears, and it continues to grow together with the first band. Although the signal gain is small, the IR idler is generated.

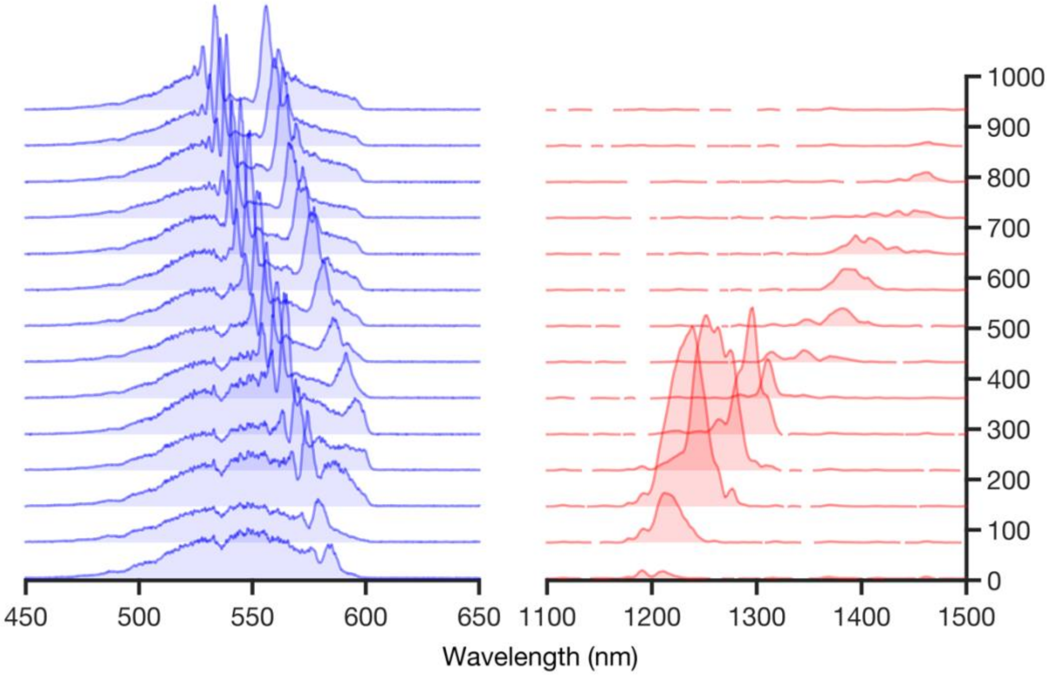

Fig. 4.29 Experimental generation of FWM. a) Generated output spectra of the amplified signal and b) idler in the HCC filled with argon at a pressure of 1 bar. The pump energy is 200 µJ. The delay corresponds to temporal overlap between the input pump and signal.

The idler beam profile images are shown in Fig. 4.30b, where the image number 3 is the sharpest, which means that this is highest conversion efficiency point.
The corresponding delay value is about 146 fs with a central wavelength at around 1238 nm. From the energy conservation equation with the pump at 800 nm, the wavelength of the corresponding amplified signal is 590 nm, which is very close to the experimental spectrum Fig. 4.29.

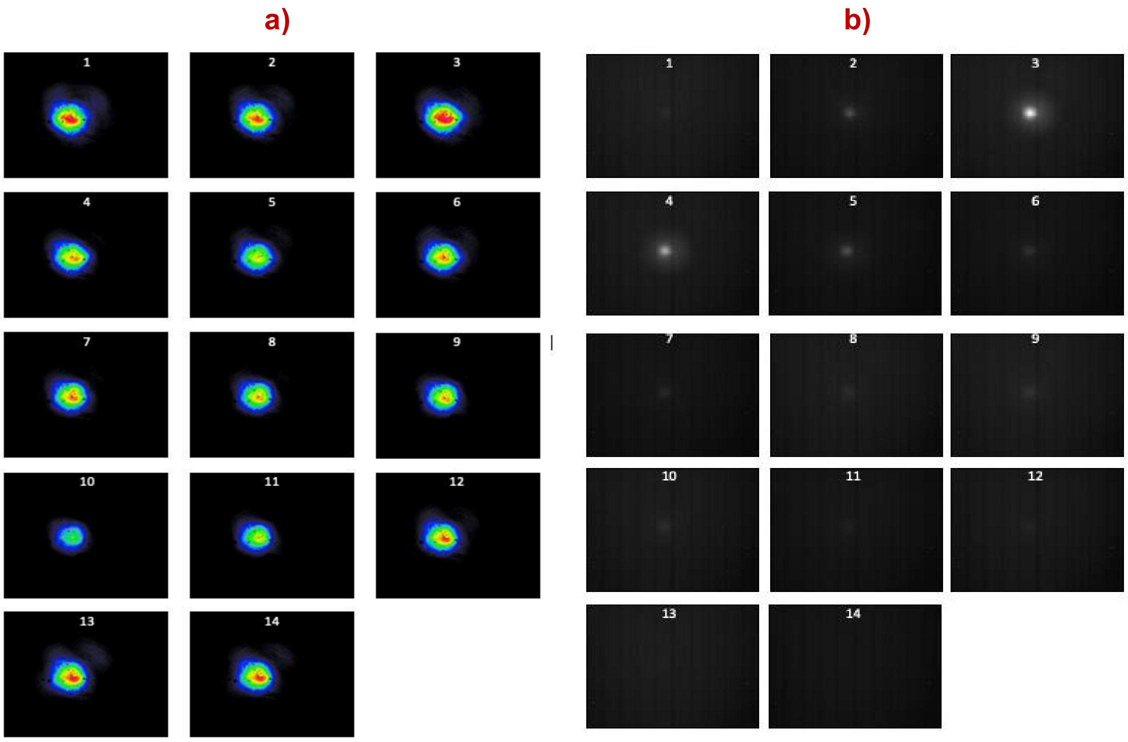

Fig. 4.30 Beam profile in the far-field as a function of delay step for the signal (a) and the idler (b). In the images 1 corresponds to the time delay of zero fs and continued until almost 1000 fs delay.

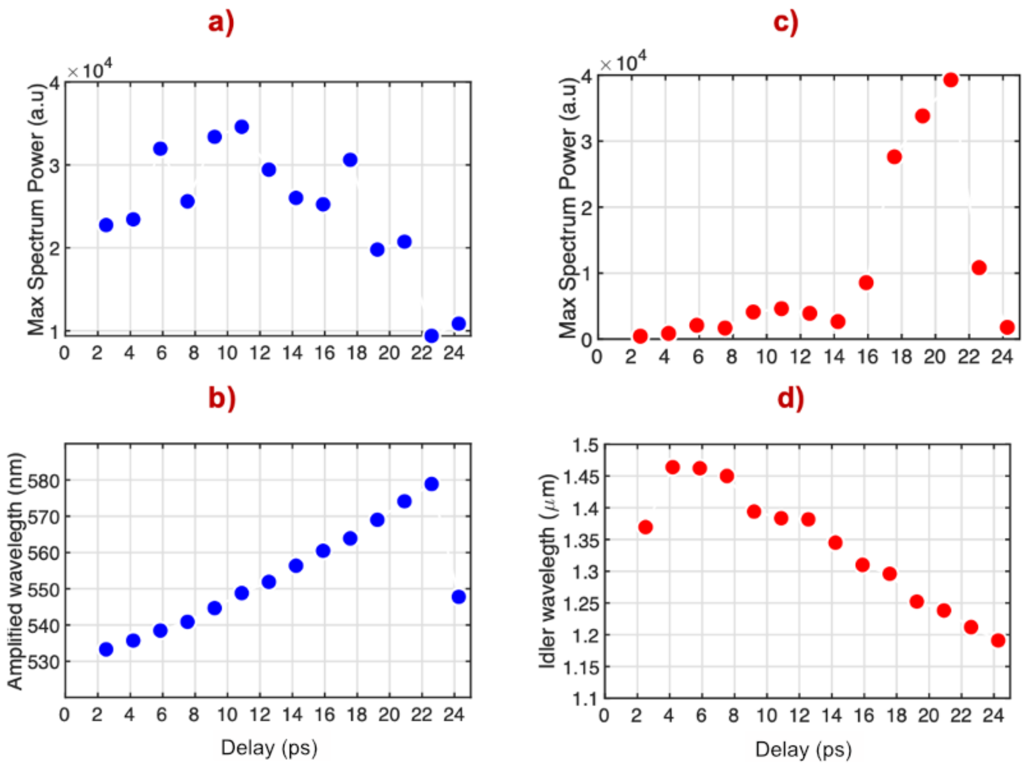

Fig. 4.31 Maximum experimental spectrum power as a function of the delay for the signal (a) and the idler (b). The central wavelength of the amplified signal as a function of the delay (b) the idler central wavelength as a function of the delay (d).

Fig. 4.31.a, shows the corresponding maximum spectral signal power as the function of the delay and its central wavelength (Fig. 4.31.b).

Since the idler is generated as the pump and signal propagate, we cannot represent the gain in the same way as the signal. So, we take only the maximum spectral power corresponding to each relative delay step, and its corresponding central wavelength seen (Fig. 4.31.c-d). The maximum power values are calculated from the spectrum integral on the wavelength rang. As we observe in Fig. 4.31 the wavelength of the idler and signal are nearly linear with the delay. This presents a large band of tunability.

4.5.2 Configuration with a chirped pump pulse.

As discussed in the numerical section, when a linear chirp is added to the pump, the amplification bandwidth should be enlarged and the conversion efficiency improved. In this way, a second experimental setup was developed.

The pump beam from the amplifier system passes through a piece of dispersive glass, to temporally stretched up to 231 fs (see Fig.4.27). For a higher peak power than 4.2 GW, the beam starts to self-focus in the dispersive block, and we limited the power to this value. The stretched pump was coupled into the HCC and the output beam was collimated by a convex lens (f=250 mm). The signal, pump and idler components were separated in the same manner as before. The complete experimental layout diagram is shown in Fig. 4.32. The cameras used to record the beam profile are surrounded by a grey box to indicate the flip mirrors.

We measured the spectra of the pump, signal, and idler, according to each stage of the delay line, for different argon pressures, (1.2, 1,3, 1.4, 1.6, 1.8, and 2.2 bar) and the pump power holds steady.

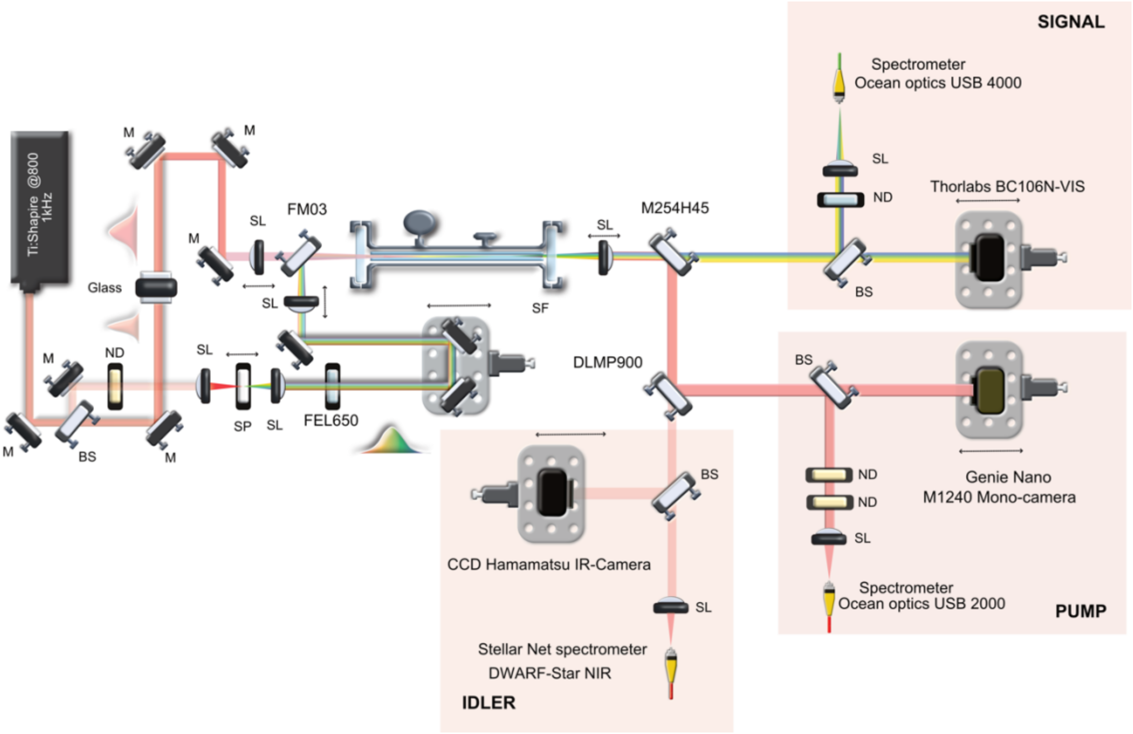

Fig. 4.32 Scheme of the complete experimental set-up for Ultra-broadband FWM. M, Broadband Dielectric Mirror, SL Plano-Convex lens, BS, beam splitter, ND absorptive neutral density filter, CM, Cold mirror, LF long-pass filter, SF short-pass filter, SP, Sapphire Plate.

4.5.2-1 Experimental results

Spectral tunability from the pressure changes

By modifying the delay, various components of the chirped signal interact with those of the chirped pump. Thus, experimentally, one expects that the maxima of the amplified signal and the generated wavelengths change with the relative delay. It is also expected the gains and conversion efficiencies changes for different gas pressures.

The output spectra of the signal and idler were firstly recorded, and then the maximum was selected for each delay. The corresponding power and central wavelength are displayed in Fig. 4.33.a. Similar curves are shown for the signal (Fig. 4.33.b).

The gain is calculated as before (the ratio between the amplified signal and the input signal) while the idler gain value is the spectrum integral on the wavelength range and the idler power is directly measured with a power meter at each delay.

The analysis of the data leads to the conclusion that the highest amplifier gain is reached at a pressure of 1.3 bar. Meanwhile, the highest spectral power occurs at 1.2 bar. The wavelengths at maximum power for the signal and the idler are 585 and 1250 nm, respectively. The pulse energy at 1250 nm, is relatively weak (few nJ) and is consistent with the low gain value (<5 dB).

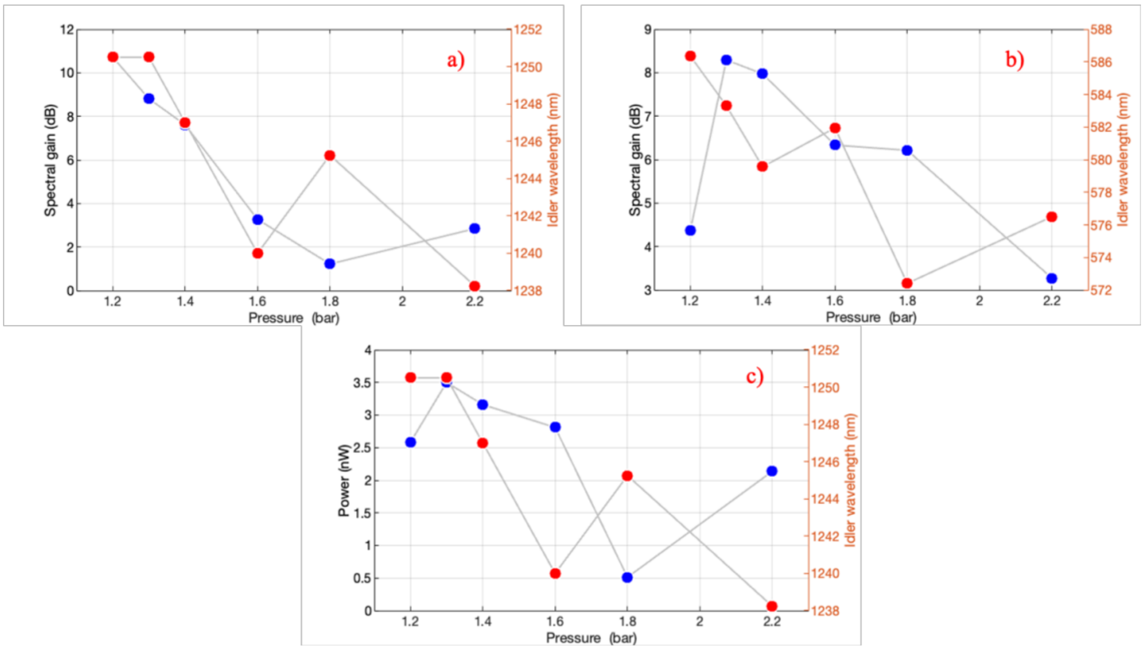

Fig. 4.33 Maximum spectral idler intensity and central idler wavelength as a function of pressure (a). Signal spectral gain and central signal wavelength as a function of pressure (b). Power of the idler as a function of pressure (c).

For higher pressure values, the energy transfer process is less efficient because the phase-matched is not reached. At higher-pressure values, we observe some other non-linearity that perturbate the FWM we will deeply investigate in chapter 5.

The tuning range for the amplified signal and idler is indicated in Fig. 4.34 at a pressure of 1.3 bar. On the signal side (blue curves), one band is mostly amplified at small temporal overlap. At longer delays, a second band of the signal becomes also amplified. Then the pump energy goes to two spectral signal bands, which increase the amplification bandwidth. In the idler side, the power spectrum decreases when a dual peak appears in the amplified signal.

The signal frequency variation is greater than one in the idler. It seems more than one FWM band can be amplified by adjusting the temporal overlap. Based on the experimental spectra, the amplified signal presents peaks with a clear separation between them whereas the idler spectra also present a structured but low power.

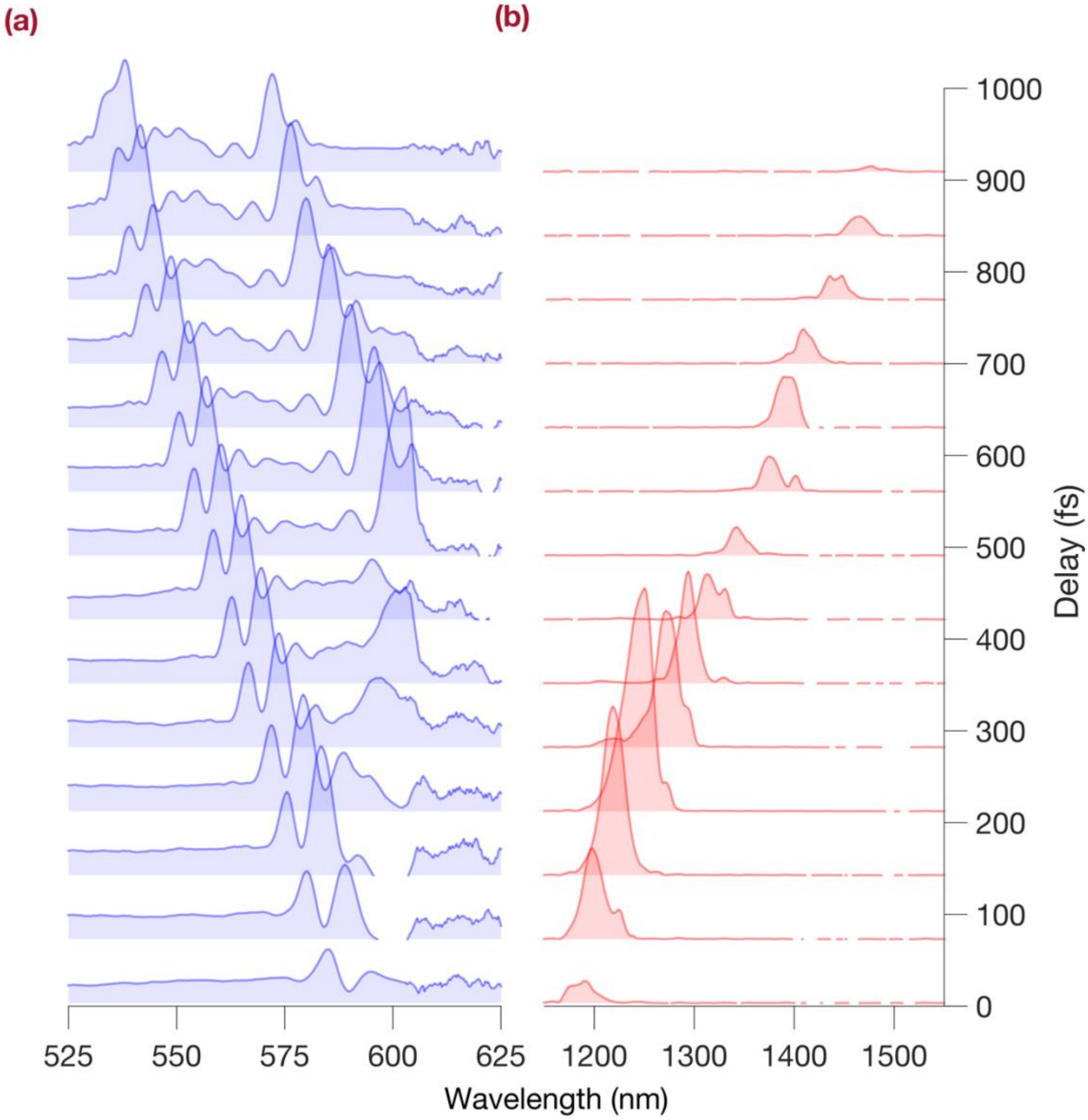

Fig. 4.34 Experimental generation of the FWM with a chirped pump pulse. a) Output spectra of the amplified signal and b) generated idler in the argon filled HCC. The pressure is 1.3 bar and the pump peak power is 1.1 GW. The delay corresponds to the relative temporal overlap between the input pump and signal.

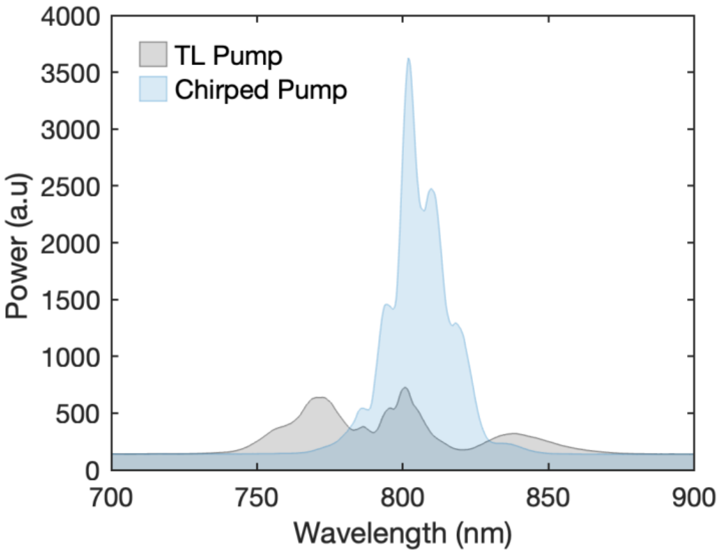

Fig. 4.35 Output pump spectrum when the HCC is filled with argon at a pressure of 1.3 bar. The gray curve is related to TL Fourier pump pulse. The blue curve represents the spectrum when a chirp is applied to the pump.

The idler and amplified signal beam profiles are displayed as the function of the relative delay in Fig. 4.36 and Fig. 4.37. The idler spectra recorded with the highest power correspond to the image number 4 (delay of 212 fs*)*. The powerful signal beam is observed in picture 8. It arises when the second peak appears on the spectrum.

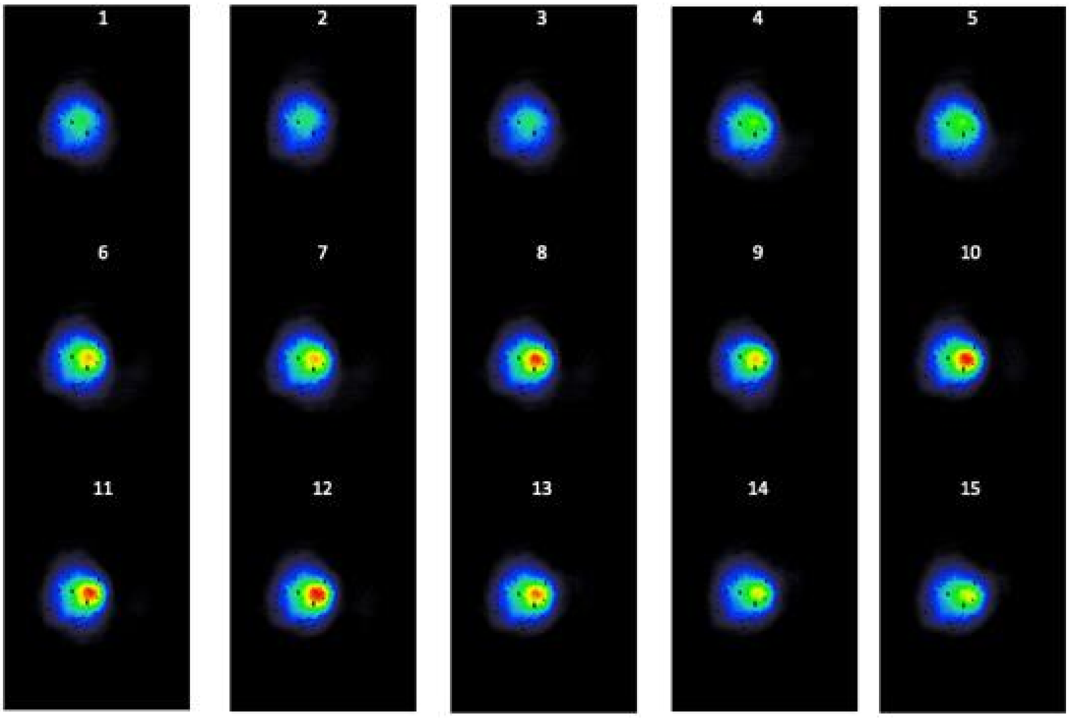

Fig. 4.36 Beam profile of the signal as a function of the step number, where 1 corresponds to the time delay of 0 fs and 15 ≈ 900 fs.

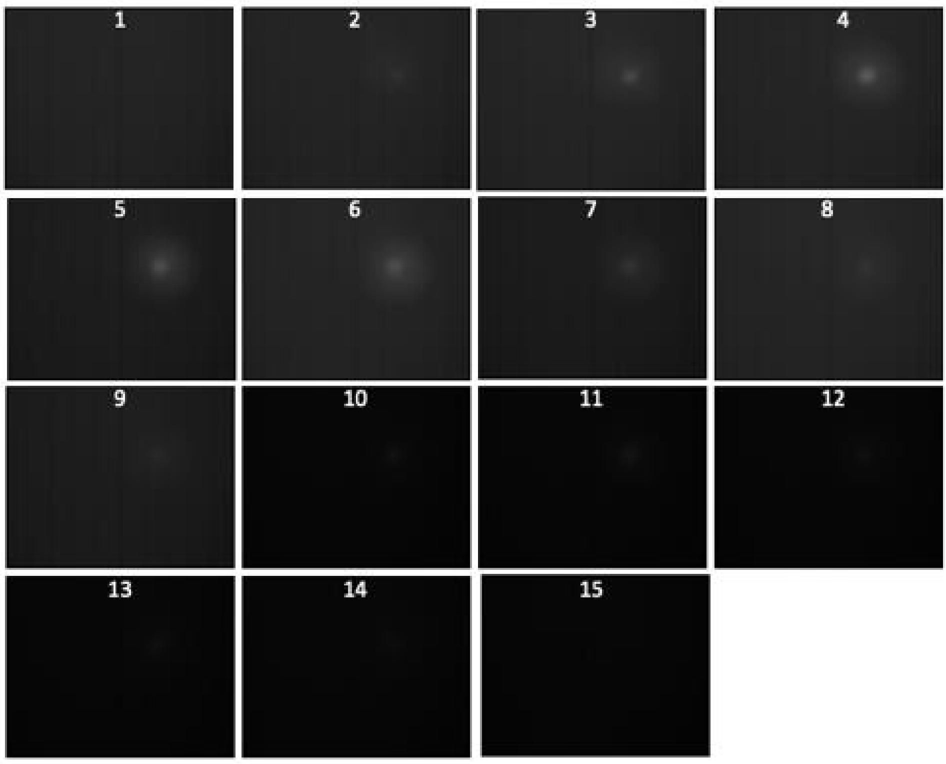

Fig. 4.37 Beam profile of the idler as a function of the relative delay, where 1 corresponds to the time delay of 0 fs and 15 ≈ 900 fs.

Fig. 4.38 shows the intensity autocorrelation trace of the idler pulse at a relative delay of 212 fs, where the conversion efficiency is the highest. The corresponding spectrum is centered at 1250nm. Assuming a Gaussian temporal profile, the pulse duration is 220 fs at FWHM with a pedestal at +600 fs because of an uncompensated spectral phase. The red line is the trace calculated from the spectrum when the spectral phase is compensated. The expected FT limited pulse duration is 45 fs. The pulse energy at 1250 nm is relatively weak and is ~ 4 nJ.

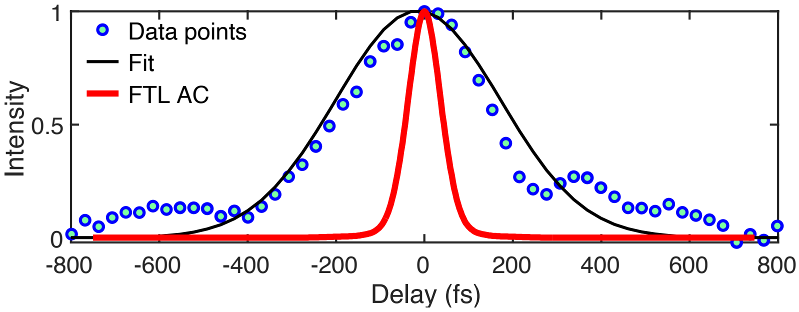

Fig. 4.38 The data points represent the autocorrelation trace of the idler generated. The black line is a Gaussian pulse fit. The red line corresponds to the FT limited pulse calculated from the spectrum.

In Fig. 4.39 displays the spectra of the signal, idler and pump at the input and after propagation through the HCC at this highest performance. The input signal is shown in grey. The output amplified signal spectrum has been measured and is shown in blue. This spectrum is shifted from the input signal due to a higher gain available for longer wavelengths, ~600 nm. The green color curve is the generated idler spectrum and has a bandwidth of 0.34 µm at FWHM. The central wavelength of the corresponding idler is

1250nm. The red curve represents the output pump spectrum that progressively expands on the longer wavelength sides.

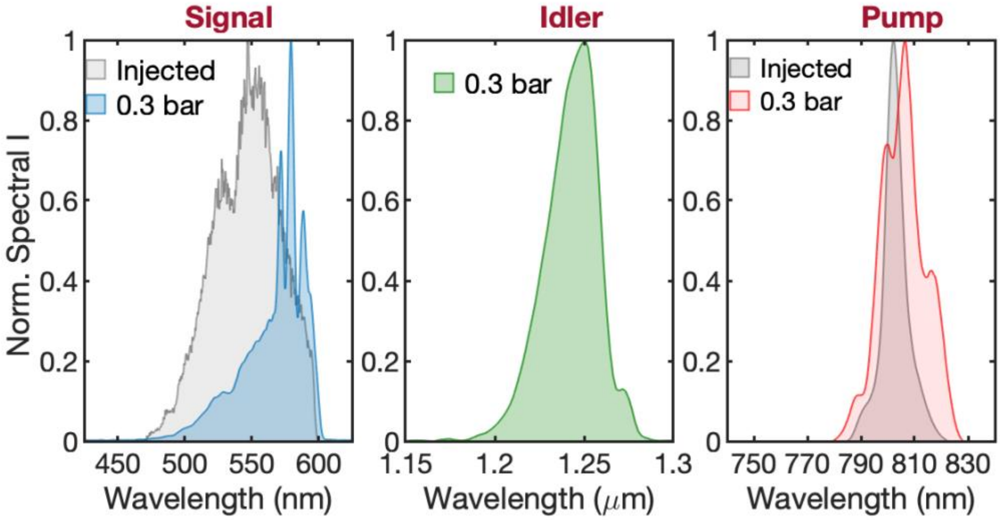

Fig. 4.39 Normalized spectra of the input signal (grey line), the amplified signal (blue line) and generated idler spectra (green line), pump spectrum (red line). The pump spectra under vacuum (grey line). The pressure is 1.3 bar.

4.6 Discussion

The comparison of the experimental results between the chirped pump and un-chirped pump is shown in Fig. 4.40. The red line indicates that the signal is linearly amplified with the delay. This behavior is due to the fact that the pump is less affected by the SPM when the pump is chirped. However, when the pump has a higher SPM effect due to higher peak power (see black line) a second amplified spectral range is produced around a delay of 200 fs. The interesting thing is that the second peak becomes stronger than the first peak. On the black line, there is a sudden change, that is the point around 300 fs where the second peaks get more amplified. Although the initial peak is less amplified it still evolved linearly towards shorter frequencies, see Fig. 4.40.a.

Fig. 4.40.b represents the idler wavelength at the maximum power recorded on the spectra as the function of the relative delay. The idler does not show different behavior. It appears that the idler is less affected by the pump frequency change since its wavelength position moves linearly in both cases. The numerical results were expected to improve the efficiency of the conversion by introducing a chirp into the pump. Experimentally, this assumption is verified in Fig. 4.40c. The red line represents the case with the chirped pulse, and we can observe that the amount of energy transferred to the idler is slightly higher than the other case. We expect to improve that behavior with a higher chirp value.

The measured tunability of the idler peak position for the two cases is shown in Fig. 4.41. In both cases, a tunable idler is achieved in the range from 1.2-1.5 µm. It is also important to note that, for different delays, there is a well-defined idler spectrum. Experimentally, this enables to better control the adjustment of the pulses. For the FT-Limited pump, the range of the idler tuning is shorter with harder control.

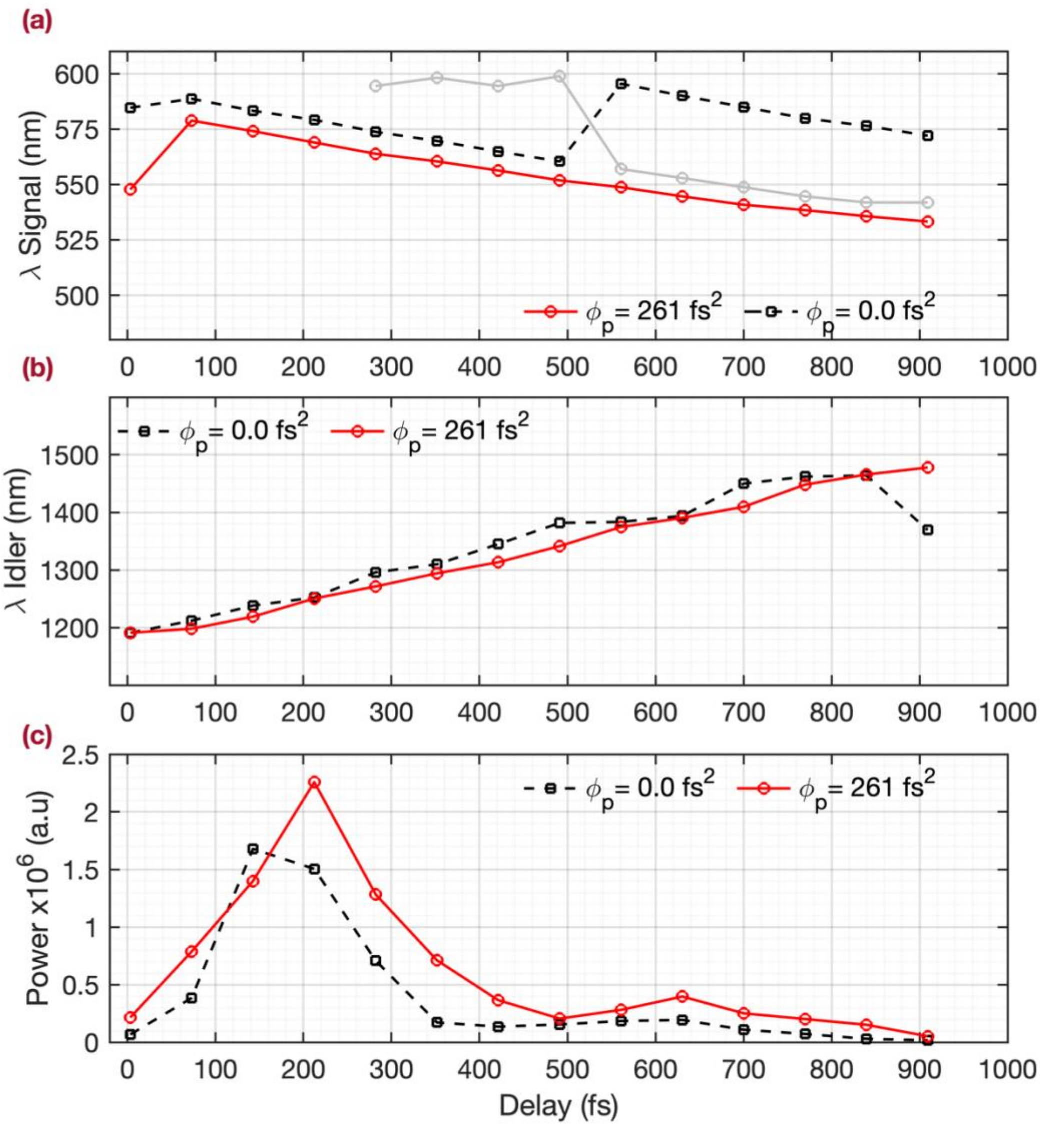

Fig. 4.40 a-b) Maximum of the band in the signal and idler sides as the function of the delay when the pump pulse is unchirped (black line) or chirped (red line). The grey line corresponds to a second maximum. c) Maximum intensity of the idler as the function of the delay.

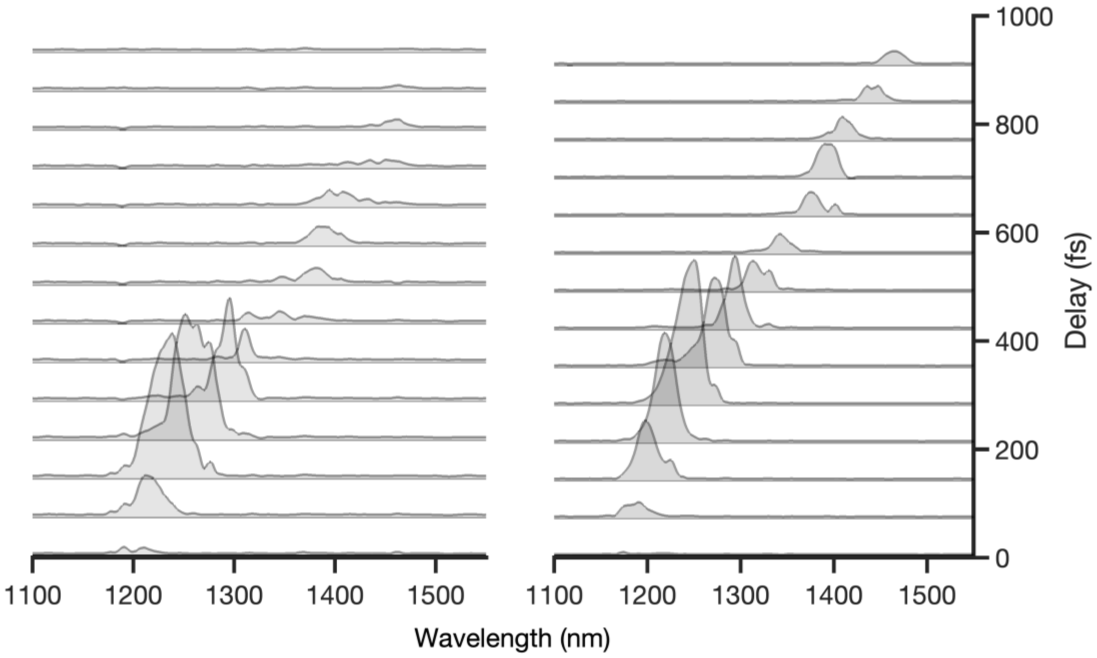

Fig. 4.41 The idler spectrum as the function of the delay for the FT limited pump pulse (a) and a chirped pump pulse (b).

4.7 Conclusion

This chapter summarizes the development of a source based on infrared generation on the FWM in the gas-filled HCC. The interaction of a visible broadband continuum with a chirped pump pulse results in the generation of a tunable pulse in the near infrared from 1.2 to 1.5 µm with the potentiality to reach the mid-infrared range. In the first part, the numerical simulations provide the full understanding of the role of key parameters such as the gas pressure, chirps and relative delays of the involved pulses.

The gain bandwidth and pulse duration of the signal and generated idler are strongly affected by the nonlinear phase contribution. Consequently, the pump power and pressure are adjusted and the temporal overlap is the signal allows to get a better conversion efficiency. From the numerical result, the signal and idler bandwidth are asymmetric. This change is due to the high order dispersion terms.

In this work, we take the advantage of the GDM and chirp to obtain a large tunability. Since the signal has a higher spectral width than the pump wave, it is possible to overlap different spectral components by adding a relative delay between the signal and the pump. This property is used to control the FWM process, resulting in a tunable idler. The concept was applied to the experimental configuration, which ends up with a system that produces an adjustable infrared pulse. For example, when the pump is temporal stretched, an idler is generated at 1.2 µm with a duration of ~220 fs at the direct output of the capillary, while a 45 fs pulse can be obtained with phase compensators.

We observed the optimal generation of the idler with the stretched pump at a pressure of 1.3 bar. This is in good agreement with the expected pressure (~1.2 bar) obtained from the simulation. We believe that some difference should be observed due to other nonlinear effects. Particularly, high order modes are excited during the propagation and are not included in this current simulation. Therefore, the pump beam is also self-focused and spatial oscillations can occur during the propagation [23]. This might lead to an increase in local intensity and a change of the nonlinearity condition. This is the subject to be covered in the next chapter.

4.8 References to Chapter 4

1. Schawlow, A. L. and Townes, C. H. Infrared and optical masers. *Physical Review* **112**, 1940–1949 (1958).
2. Maiman, T. H. Stimulated optical radiation in Ruby. *Nature* **187**, 493–494 (1960).
3. Hall, R. N., Fenner, G. E., Kingsley, J. D., Soltys, T. J. and Carlson, R. O. Coherent light emission from GaAs junctions. *Physical Review Letters* **9**, 366–368 (1962).
4. Javan, A., Bennett, W. R. and Herriott, D. R. Population inversion and continuous optical maser oscillation in a gas discharge containing a He-Ne mixture. *Physical Review Letters* **6**, 106–110 (1961).
5. Strickland, D. and Mourou, G. Compression of amplified chirped optical pulses. *Optics Communications* **56**, 219–221 (1985).
6. Koester, C. J. and Snitzer, E. Amplification in a Fiber Laser. *Appl. Opt* **3**, RP1 (2017).
7. Nilsson, J. *et al.* High-power wavelength-tunable cladding-pumped rare-earth-doped silica fiber lasers. *Optical Fiber Technology* **10**, 5–30 (2004).
8. Lavenu, L. *et al.* High-energy few-cycle Yb-doped fiber amplifier source based on a single nonlinear compression stage. *Optics Express* **25**, 7530 (2017).
9. Blow, K. J. and Wood, D. Theoretical Description of Transient Stimulated Raman Scattering in Optical Fibers. *IEEE Journal of Quantum Electronics* **25**, 2665–2673 (1989).
10. Franken, P. A., Hill, A. E., Peters, C. W. and Weinreich, G. Generation of optical harmonics. *Physical Review Letters* **7**, 118–119 (1961).
11. Bass, M., Franken, P. A., Hill, A. E., Peters, C. W. and Weinreich, G. Optical mixing. *Physical Review Letters* **8**, 18–18 (1962).
12. Giordmaine, J. A. and Miller, R. C. Tunable coherent parametric oscillation in LiNbO3 at optical frequencies. *Physical Review Letters* **14**, 973–976 (1965).
13. Maker, P. D. and Terhune, R. W. Study of optical effects due to an induced polarization third order in the electric field strength. *Physical Review* **137**, 507–509 (1965).
14. New, G.H.C. and Ward, J. F. Optical third-harmonic generation in gases,. *Phys. Rev. Lett.* **19**, 556–559 (1967).
15. McWane, P. D. and Sealer, D. A. New measurements of intensity-dependent changes in the refractive index of liquids. *Applied Physics Letters* **8**, 278–279 (1966).
16. Carman, R. L., Chiao, R. Y. and Kelley, P. L. Observation of degenerate stimulated four-photon interaction and four-wave parametric amplification. *Physical Review Letters* **17**, 1281–1283 (1966).

17. Brahms, C., Belli, F. and Travers, J. C. Infrared attosecond field transients and UV to IR few-femtosecond pulses generated by high-energy soliton self-compression. *Physical Review Research* **2**, 043037 1–8 (2020).
18. Manzoni, C. and Cerullo, G. Few-optical-cycle pulses from near-IR to UV by non linear frequency conversion. in *2015 IEEE Photonics Conference, IPC 2015* 206–207 (2015).
19. Tzankov, P. *et al.* 300 µJ noncollinear optical parametric amplifier in the visible at 1 kHz repetition rate. *Optics Letters* **31**, 3629–3631 (2006).
20. Odhner, J. H. and Levis, R. J. High-energy noncollinear optical parametric amplifier producing 4 fs pulses in the visible seeded by a gas-phase filament. *Optics Letters* **40**, 3814–3817 (2015).
21. Viotti, A.-L. *et al.* Supercontinuum generation and soliton self-compression in χ (2)-structured KTiOPO 4. *Optica* **5**, 711–717 (2018).
22. Andriukaitis, G. *et al.* 90 GW peak power few-cycle mid-infrared pulses from an optical parametric amplifier. *Optics Letters* **36**, 2755–2757 (2011).
23. Shamir, Y. *et al.* High-average-power 2 µm few-cycle optical parametric chirped pulse amplifier at 100 kHz repetition rate. *Optics Letters* **40**, 5546–5549 (2015).
24. Silva, F., Bates, P. K., Esteban-Martin, A., Ebrahim-Zadeh, M. and Biegert, J. High-average-power, carrier-envelope phase-stable, few-cycle pulses at 21 µm from a collinear BiB3O6 optical parametric amplifier. *Optics Letters* **37**, 933 (2012).
25. Gu, X. *et al.* Generation of carrier-envelope-phase-stable 2-cycle 740-µJ pulses at 21-µm carrier wavelength. *Optics Express* **17**, 62–69 (2009).
26. Robert, P. *et al.* Spectral correlation of four-wave mixing generated in a photonic crystal fiber pumped by a chirped pulse. *Optics Letters* **45**, 4148–4151 (2020).
27. Fourcade-Dutin, C. *et al.* Temporal distribution measurement of the parametric spectral gain in a photonic crystal fiber pumped by a chirped pulse. *Photonics* **6**, 1–9 (2019).
28. Fourcade-Dutin, C., Miranda, O. Z., Mounaix, P. and Bigourd, D. Toward mid-infrared ultra-short pulse generation in a gas-filled hollow-core photonic crystal fiber. in *Advanced Photonics Congress 2021* (2021). doi:10.1364/noma.2021.notu3c.5.
29. J. C. Travers, C. Brahms, F. Belli, T. F. Grigorova, A. L. M. S. Advances in nonlinear optics in gas-filled hollow-core fibers. in *in OSA Nonlinear Optics 2021, R. Boyd, C. Conti, D. Christodoulides, and P. Rakich, eds., OSA Technical Digest (Optical Society of America, 2021), paper NM2A.1.* (2021).
30. Travers, J. C., Grigorova, T. F., Brahms, C. and Belli, F. High-energy pulse self-compression and ultraviolet generation through soliton dynamics in hollow capillary fibres. *Nature Photonics* **13**, 547–554 (2019).
31. Kida, Y. and Imasaka, T. Optical parametric amplification of a supercontinuum in a gas. *Applied Physics B: Lasers and Optics* **116**, 673–680 (2014).
32. Ippen, E. P. Low-power quasi-cw raman oscillator. *Applied Physics Letters* **16**, 303–305 (1970).
33. Misoguti, L. *et al.* Generation of broadband VUV light using third-order cascaded processes. *Physical Review Letters* **87**, 013601/1-013601/4 (2001).
34. Adamu, A. I. *et al.* Deep-UV to Mid-IR Supercontinuum Generation driven by Mid-IR Ultrashort Pulses in a Gas-filled Hollow-core Fiber. *Scientific Reports* **9**, 1–8 (2019).

35. Wagner, N. L. *et al.* Self-compression of ultrashort pulses through ionization-induced spatiotemporal reshaping. *Physical Review Letters* **93**, 173902–173906 (2004).
36. Popmintchev, T. *et al.* Bright coherent ultrahigh harmonics in the kev x-ray regime from mid-infrared femtosecond lasers. *Science (1979)* **336**, 1287–1291 (2012).
37. Cabasse, A., Machinet, G., Dubrouil, A., Cormier, E. and Constant, E. Optimization and phase matching of fiber-laser-driven high-order harmonic generation at high repetition rate. *Optics Letters* **37**, 4618–4620 (2012).
38. Couch, D. E. *et al.* Ultrafast 1 MHz vacuum-ultraviolet source via highly cascaded harmonic generation in negative-curvature hollow-core fibers. *Optica* **7**, 832–837 (2020).
39. Brahms, C., Belli, F. and Travers, J. C. Infrared attosecond field transients and UV to IR few-femtosecond pulses generated by high-energy soliton self-compression. *Physical Review Research* **2**, 0–1 (2020).
40. Ciriolo, A. G. *et al.* Generation of ultrashort pulses by four wave mixing in a gas-filled hollow core fiber. *Journal of Optics* **20**, 125503-1 /125503-9 (2018).
41. Belli, F., Abdolvand, A., Travers, J. C. and Russell, P. St. J. Highly efficient deep UV generation by four-wave mixing in gas-filled hollow-core photonic crystal fiber. *Optics Letters* **44**, 5509 (2019).
42. Durfee, C. G., Backus, S., Kapteyn, H. C. and Murnane, M. M. Intense 8-fs pulse generation in the deep ultraviolet. *Optics Letters* **24**, 697 (1999).
43. Faccio, D., Grün, A., Bates, P. K., Chalus, O. and Biegert, J. Optical amplification in the near-infrared in gas-filled hollow-core fibers. *Optics Letters* **34**, 2918 (2009).
44. Kida, Y. and Kobayashi, T. Generation of sub-10 fs ultraviolet Gaussian pulses. *Journal of the Optical Society of America B* **28**, 139 (2011).
45. Fourcade-Dutin, C., Zurita-Miranda, O., Mounaix, P. and Bigourd, D. Mid-infrared ultra-short pulse generation in a gas-filled hollow-core photonic crystal fiber pumped by two-color pulses. *Fibers* **9**, 21 (2021).
46. Stolen, R. H., Bjorkholm, J. E. and Ashkin, A. Phase-matched three-wave mixing in silica fiber optical waveguides. *Applied Physics Letters* **24**, 308–310 (1974).
47. Hill, K. O., Johnson, D. C. and Kawasaki, B. S. Efficient conversion of light over a wide spectral range by four-photon mixing in a multimode graded-index fiber: erratum. *Applied Optics* **20**, 2769 (1981).
48. Agrawal, G. P. Nonlinear fiber optics: its history and recent progress [Invited]. *Journal of the Optical Society of America B* **28**, A1 (2011).
49. Nazemosadat, E., Pourbeyram, H. and Mafi, A. Phase matching for spontaneous frequency conversion via four-wave mixing in graded-index multimode optical fibers. *Journal of the Optical Society of America B* **33**, 144 (2016).
50. Rademacher, G., Warm, S. and Petermann, K. Analytical description of cross-modal nonlinear interaction in mode multiplexed multimode fibers. *IEEE Photonics Technology Letters* **24**, 1929–1932 (2012).
51. Mecozzi, A., Antonelli, C. and Shtaif, M. Nonlinear propagation in multi-mode fibers in the strong coupling regime. *Optics Express* **20**, 11673 (2012).
52. Mafi, A. Pulse Propagation in a Short Nonlinear Graded-Index Multimode Optical Fiber. *Journal of Lightwave Technology* **30**, 2803–2811 (2012).
53. Ding, E., Lefrancois, S., Kutz, J. N. and Wise, F. W. Scaling fiber lasers to large mode area: An investigation of passive mode-locking using a multi-mode fiber. *IEEE Journal of Quantum Electronics* **47**, 597–606 (2011).

54. Nazemosadat, E. and Mafi, A. Nonlinear switching in multicore versus multimode waveguide junctions for mode-locked laser applications. *Optics Express* **21**, 30739 (2013).
55. Mafi, E. N. and A. Nonlinear switching in a two- concentric-core chalcogenide glass optical fiber for passively mode-locking a fiber laser. *Opt. Lett.* **39**, 4675–4678 (2014).
56. Fu, S. *et al.* Passive Q-switching of an all-fiber laser induced by the Kerr effect of multimode interference. *Optics Express* **23**, 17255 (2015).
57. Einarsson, G. Pulse broadening in graded-index optical fibers: correction. *Applied Optics* **25**, 1030 (1986).
58. Renninger, W. H. and Wise, F. W. Optical solitons in graded-index multimode fibres. *Nature Communications* **4**, 1719 (2013).
59. S. Raghavan G. P. Agrawal. Spatiotemporal solitons in inhomogeneous nonlinear media. *Opt. Commun* **180**, 377–382 (2000).
60. Kibler, B. and Béjot, P. Discretized Conical Waves in Multimode Optical Fibers. *Physical Review Letters* **126**, (2021).
61. Faccio, D. *et al.* Spatio-temporal reshaping and X Wave dynamics in optical filaments. *Optics Express* **15**, 13077 (2007).
62. Konorov, S. O., Fedotov, A. B. and Zheltikov, A. M. Enhanced four-wave mixing in a hollow-core photonic-crystal fiber. *Optics Letters* **28**, 1448 (2003).
63. Ding, X., Selim Habib, Md., Amezcua-Correa, R. and Moses, J. Near-octave intense mid-infrared by adiabatic down-conversion in hollow anti-resonant fiber. *Optics Letters* **44**, 1084 (2019).
64. Finger, M. A., Joly, N. Y., Russell, P. S. J. and Chekhova, M. v. Characterization and shaping of the time-frequency Schmidt mode spectrum of bright twin beams generated in gas-filled hollow-core photonic crystal fibers. *Physical Review A* **95**, 053814 (2017).
65. Cordier, M. *et al.* Active engineering of four-wave mixing spectral correlations in multiband hollow-core fibers. *Optics Express* **27**, 9803 (2019).
66. Tempea, G. and Brabec, T. Theory of self-focusing in a hollow waveguide. *Optics Letters* **23**, 762 (1998).
67. Crego, A., Conejero Jarque, E. and San Roman, J. Influence of the spatial confinement on the self-focusing of ultrashort pulses in hollow-core fibers. *Scientific Reports* **9**, 9546 (2019).
68. Chapman, R. T. *et al.* Modal effects on pump-pulse propagation in an Ar-filled capillary. *Optics Express* **18**, 13279 (2010).
69. Mangini, F. *et al.* Self-imaging dynamics in nonlinear GRIN multimode optical fibers. *Frontiers in Optics / Laser Science* **28**, 24005–24021 (2020).
70. Wright, L. G., Wabnitz, S. W., Christodoulides, D. N. and Wise, F. W. Ultrabroadband dispersive radiation by spatiotemporal oscillation of multimode waves. in *Photonics and Fiber Technology 2016* (2016). doi:10.1364/NP.2016.NW4A.1.
71. Marhic, M. E. *Fiber optical parametric amplifiers, oscillators and related devices*. *Fiber Optical Parametric Amplifiers, Oscillators and Related Devices* vol. 9780521861 (Cambridge University Press, 2007).
72. Couairon, A. *et al.* Practitioner's guide to laser pulse propagation models and simulation. *European Physical Journal: Special Topics* **199**, 5–76 (2011).
73. Brabec, T. and Krausz, F. Intense few-cycle laser fields: Frontiers of nonlinear optics. *Reviews of Modern Physics* **72**, 545–591 (2000).

74. Agrawal, G. P. *Nonlinear fiber optics*. *Nonlinear Fiber Optics* (Academic Press, 2019). doi:10.1016/C2018-0-01168-8.
75. Boyd, R. W. *Nonlinear Fiber Optics*. (2008).
76. Marcatili, E. A. J. and Schmeltzer, R. A. Hollow Metallic and Dielectric Waveguides for Long Distance Optical Transmission and Lasers. *Bell System Technical Journal* **43**, 1783–1809 (1964).
77. Lehmeier, H. J., Leupacher, W. and Penzkofer, A. Nonresonant third order hyperpolarizability of rare gases and N2 determined by third harmonic generation. *Optics Communications* **56**, 67–72 (1985).
78. Couairon, A., Chakraborty, H. S. and Gaarde, M. B. From single-cycle self-compressed filaments to isolated attosecond pulses in noble gases. *Physical Review A - Atomic, Molecular, and Optical Physics* **77**, (2008).
79. Sinkin, O. V., Holzlöhner, R., Zweck, J. and Menyuk, C. R. Optimization of the split-step Fourier method in modeling optical-fiber communications systems. *Journal of Lightwave Technology* **21**, 61–68 (2003).
80. Marburger, J. H. Self-focusing: Theory. *Progress in Quantum Electronics* **4**, 35–110 (1975).
81. Milosevic, N., Tempea, G. and Brabec, T. Optical pulse compression: bulk media versus hollow waveguides. *Optics Letters* **25**, 672–674 (2000).
82. Stolen, R. H. and Lin, C. Self-phase-modulation in silica optical fibers. *Physical Review A* **17**, 1448–1453 (1978).
83. Dudley, J. M. and Taylor, J. R. *Supercontinuum generation in optical fibers*. *Supercontinuum Generation in Optical Fibers* vol. 9780521514 (2010).
84. Snitzer, E. Cylindrical Dielectric Waveguide Modes*. *J Opt Soc Am* **51**, 491 (1961).
85. Archambault, J. L., Black, R. J., Lacroix, S. and Bures, J. Loss Calculations for Antiresonant Waveguides. *Journal of Lightwave Technology* **11**, 416–423 (1993).
86. Hesketh, G. D., Poletti, F. and Horak, P. Spatio-Temporal Self-Focusing in Femtosecond Pulse Transmission Through Multimode Optical Fibers. *Journal of Lightwave Technology* **30**, 2764–2769 (2012).
87. Börzsönyi, A., Heiner, Z., Kalashnikov, M. P., Kovács, A. P. and Osvay, K. Dispersion measurement of inert gases and gas mixtures at 800 nm. *Applied Optics* **47**, 4856–4863 (2008).
88. Cros, B. *et al.* Eigenmodes for capillary tubes with dielectric walls and ultraintense laser pulse guiding. *Physical Review E - Statistical Physics, Plasmas, Fluids, and Related Interdisciplinary Topics* **65**, (2002).
89. M. Nisoli, S. Stagira, S. De Silvestri, O. Svelto, S. Sartinia Z. Cheng, G. Tempea, C. Spielmann, and F. K. Towards a terawatt-scale sub-10-fs laser technology. *IEEE J. of selected topics in quantum ELECTRONICS* **4**, (1998).
90. Trebino, R. *Frequency-Resolved Optical Gating: The Measurement of Ultrashort Laser Pulses*. *Frequency-Resolved Optical Gating: The Measurement of Ultrashort Laser Pulses* (2000). doi:10.1007/978-1-4615-1181-6.
91. Trebino, R. *et al.* Measuring ultrashort laser pulses in the time-frequency domain using frequency-resolved optical gating. *Review of Scientific Instruments* **68**, 3277–3295 (1997).
92. Stolen, R. Phase-matched-stimulated four-photon mixing in silica-fiber waveguides. *IEEE Journal of Quantum Electronics* **11**, 100–103 (1975).
93. Russell, P. Photonic Crystal Fibers. *Science (1979)* **299**, 358–362 (2003).
94. Knight, J. C. Photonic crystal fibres. *Nature* **424**, 847–851 (2003).

95. Bigourd, D., D'Augerès, P. B., Dubertrand, J., Hugonnot, E. and Mussot, A. Ultrabroadband fiber optical parametric amplifier pumped by chirped pulses. *Optics Letters* **39**, 3782 (2014).
96. Bigourd, D. *et al.* Parametric gain shaping from a structured pump pulse. *IEEE Photonics Technology Letters* **31**, 214–217 (2019).
97. Vanvincq, O., Fourcade-Dutin, C., Mussot, A., Hugonnot, E. and Bigourd, D. Ultrabroadband fiber optical parametric amplifiers pumped by chirped pulses Part 1: analytical model. *Journal of the Optical Society of America B* **32**, 1479 (2015).
98. Fourcade-Dutin, C., Vanvincq, O., Mussot, A., Hugonnot, E. and Bigourd, D. Ultrabroadband fiber optical parametric amplifier pumped by chirped pulses Part 2: sub-30-fs pulse amplification at high gain. *Journal of the Optical Society of America B* **32**, 1488 (2015).
99. Bigourd, D. *et al.* High-gain fiber, optical-parametric, chirped-pulse amplification of femtosecond pulses at 1 μm. *Optics Letters* **35**, 3480 (2010).
100. Bigourd, D., Lago, L., Mussot, A., Kudlinski, A. and Hugonnot, E. High gain fiber optical parametric chirped pulse amplification of femtosecond pulses at 1 μm. *Optics InfoBase Conference Papers* **35**, (2011).
101. Qin, Y., Batjargal, O., Cromey, B. and Kieu, K. All-fiber high-power 1700 nm femtosecond laser based on optical parametric chirped-pulse amplification. *Optics Express* **28**, 2317 (2020).
102. Qin, Y. *et al.* Watt-level all-fiber optical parametric chirped-pulse amplifier working at 1300 nm. *Optics Letters* **44**, 3422 (2019).
103. Ho, M. C., Uesaka, K., Marhic, M., Akasaka, Y. and Kazovsky, L. G. 200-nm-bandwidth fiber optical amplifier combining parametric and Raman gain. *Journal of Lightwave Technology* **19**, 977–981 (2001).
104. Lesvigne, C. *et al.* Visible supercontinuum generation controlled by intermodal four-wave mixing in microstructured fiber. *Optics Letters* **32**, 2173 (2007).
105. Tu, H., Jiang, Z., Marks, D. L. and Boppart, S. A. Intermodal four-wave mixing from femtosecond pulse-pumped photonic crystal fiber. *Applied Physics Letters* **94**, 101109 (2009).
106. Yuan, J. *et al.* Polarization-dependent intermodal four-wave mixing in a birefringent multimode photonic crystal fiber. *Optics Letters* **42**, 1644 (2017).
107. Dupiol, R. *et al.* Far-detuned cascaded intermodal four-wave mixing in a multimode fiber. *Optics Letters* **42**, 1293 (2017).
108. Yuan, J. *et al.* Experimental generation of discrete ultraviolet wavelength by cascaded intermodal four-wave mixing in a multimode photonic crystal fiber. *Optics Letters* **42**, 3537 (2017).
109. Velazquez-Ibarra, L., Diez, A., Silvestre, E. and Andres, M. V. Tunable Four-Wave Mixing Light Source Based on Photonic Crystal Fibers with Variable Chromatic Dispersion. *Journal of Lightwave Technology* **37**, 5722–5726 (2019).
110. Delagnes, J.-C. *et al.* High-power widely tunable ps source in the visible light based on four wave mixing in optimized photonic crystal fibers. *Optics Express* **26**, 11265 (2018).
111. Ryf, R. *et al.* Mode-Division Multiplexing Over 96 km of Few-Mode Fiber Using Coherent 6$\,\times\,$6 MIMO Processing. *Journal of Lightwave Technology* **30**, 521–531 (2012).
112. Wright, L. G., Christodoulides, D. N. and Wise, F. W. Controllable spatiotemporal nonlinear effects in multimode fibres. *Nature Photonics* **9**, 306–310 (2015).

113. Krupa, K. *et al.* Multimode nonlinear fiber optics, a spatiotemporal avenue. *APL Photonics* **4**, 110901 (2019).
114. Rashleigh, S. C. Origins and Control of Polarization Effects in Single-Mode Fibers. *Journal of Lightwave Technology* **1**, 312–331 (1983).
115. Taylor, J. R. *Theory of Dielectric Optical Waveguides. 2nd Edition*. *Journal of Modern Optics* vol. 39 (1992).
116. Stolen, R. and Bjorkholm, J. Parametric amplification and frequency conversion in optical fibers. *IEEE Journal of Quantum Electronics* **18**, 1062–1072 (1982).
117. Ferguson, A. I. *The Elements of Nonlinear Optics*. *Journal of Modern Optics* vol. 38 (1991).
118. Musheghyan, M. *et al.* Tunable, few-cycle, CEP-stable mid-IR optical parametric amplifier for strong field applications. *Journal of Physics B: Atomic, Molecular and Optical Physics* **53**, (2020).
119. B. Shao, Y. Li, Y. Peng, P. Wang, J. Qian,Y. Leng, R. L. Broad-bandwidth high-temporal-contrast carrier-envelope-phase-stabilized laser seed for 100 PW lasers. *Opt. Lett.* **45**, (2020).
120. E. Rubino, J. Darginavičius, D. Faccio, P. Di Trapani, A. Piskarskas, A. D. Generation of broadly tunable sub-30-fs infrared pulses by four-wave optical parametric amplification. *Opt. Lett* **36**, 382–384 (2011).
121. J. Bromage, S.-W. Bahk, I. A. Begishev, C. Dorrer, M. J. Guardalben, B. N. Hoffman, J. B. Oliver, R. G. Roides, E. M. Schiesser, M. J. Shoup III, M. Spilatro, B. Webb, D. Weiner, J. D. Z. Technology development for ultra-intense all-OPCPA systems. *High Power Laser Science and Engineering* **7**, (2019).
122. Fu, W. and Wise, F. W. Normal-Dispersion Fiber Optical Parametric Chirped-Pulse Amplification. *2018 Conference on Lasers and Electro-Optics, CLEO 2018 - Proceedings* **43**, 5331 (2018).
123. Fourcade-Dutin, C. and Bigourd, D. Modulation instability in a dispersion oscillating fibre pumped by a broad band pulse. *Journal of Modern Optics* **64**, 500–506 (2017).
124. Dubietis, A. and Couairon, A. *Ultrafast Supercontinuum Generation in Transparent Solid-State Media*. (Springer Nature, 2019).
125. Ding, Y., Xu, J., Ou, H. and Peucheret, C. Mode-selective wavelength conversion based on four-wave mixing in a multimode silicon waveguide. *IET Conference Publications* **2013**, 198–200 (2013).
126. Pan, W., Jin, Q., Li, X. and Gao, S. All-optical wavelength conversion for mode-division multiplexing signals using four-wave mixing in a dual-mode fiber. *Journal of the Optical Society of America B* **32**, 2417 (2015).
127. C. Fourcade Dutin. *et al.* Post-compression of high-energy femtosecond pulses using gas ionization. *Optics Letters* **35**, 253 (2010).
128. Kolesik, M., Katona, G., Moloney, J.V., Wright, E. M. Physical factors limiting the spectral extent and band gap dependence of supercontinuum generation. *Phys. Rev. Lett* **91**, (2003).
129. Saari, P. and Reivelt, K. X-Shaped Propagation-Invariant localized light waves. *Physical Review Letters* **79**, 4135–4138 (1997).
130. Tzortzakis, S. *et al.* Formation of a conducting channel in air by self-guided femtosecond laser pulses. *Physical Review E - Statistical Physics, Plasmas, Fluids, and Related Interdisciplinary Topics* **60**, (1999).
131. Poletti, F. and Horak, P. Description of ultrashort pulse propagation in multimode optical fibers. *Journal of the Optical Society of America B* **25**, 1645 (2008).

132. Poletti, F. and Horak, P. Dynamics of femtosecond supercontinuum generation in multimode fibers. *Optics Express* **17**, 6134 (2009).
133. Mussot, A., Sylvestre, T., Provino, L. and Maillotte, H. Generation of a broadband single-mode supercontinuum in a conventional dispersion-shifted fiber by use of a subnanosecond microchiplaser. *Optics Letters* **28**, 1820 (2003).
134. Köttig, F., Tani, F., Travers, J. C. and Russell, P. S. J. Self-focusing below the critical power in gas-filled hollow-core PCF. in *Optics InfoBase Conference Papers* vol. Part F81-E (2017).
135. Mecozzi, A., Antonelli, C. and Shtaif, M. Coupled Manakov equations in multimode fibers with strongly coupled groups of modes. *Optics Express* **20**, 23436 (2012).
136. Tani, F., Travers, J. C. and St.J. Russell, P. Multimode ultrafast nonlinear optics in optical waveguides: numerical modeling and experiments in kagomé photonic-crystal fiber. *Journal of the Optical Society of America B* **31**, 311 (2014).
137. Benabid, F., Knight, J. C., Antonopoulos, G. and Russell, P. S. J. Stimulated Raman Scattering in Hydrogen-Filled Hollow-Core Photonic Crystal Fiber. *Science (1979)* **298**, 399–402 (2002).
138. Poletti, F. Nested antiresonant nodeless hollow core fiber. *Optics Express* **22**, 23807 (2014).
139. Cregan, R. F. *et al.* Single-Mode Photonic Band Gap Guidance of Light in Air. *Science (1979)* **285**, 1537–1539 (1999).
140. Knight, J. C., Broeng, J., Birks, T. A. and Russell, P. S. J. Photonic band gap guidance in optical fibers. *Science (1979)* **282**, 1476–1478 (1998).
141. Alharbi, M. *et al.* Hypocycloid-shaped hollow-core photonic crystal fiber Part II: Cladding effect on confinement and bend loss. *Optics Express* **21**, 28609 (2013).
142. Agrawal, G. *Nonlinear Fiber Optics*. (Academic Press, 2012).
143. Hansson, T. *et al.* Nonlinear beam self-imaging and self-focusing dynamics in a GRIN multimode optical fiber: theory and experiments. *Optics Express* **28**, 24005 (2020).

Chapter 5. Multimode nonlinear contribution in a Hollow Core Capillary

5.1 Introduction

Nowadays, the development of ultrashort laser sources at high-peak power in the near and mid-infrared, are mostly based on the difference frequency mixing, optical parametric amplification and filamentation phenomena in dielectrics and semiconductors [1]. However, at high peak power, nonlinear effects in multimode optical fibers need to be included. Thus, the manipulation of temporal and spectral properties increases the difficulty on the dynamics.
On the other hand, fiber damage is the limiting factor in developing high-power peak fiber lasers. One solution is to increase the diameter of the fiber which tends to introduce a multimode propagation. The contribution of High Order Modes (**HOMs**) is highly investigated in telecommunications because they lead to get an extra communication channel and increases the bandwidth of the systems. The combination of mode-selective and wavelength conversion has been experimentally demonstrated by using FWM in a multimode silicon waveguide in which one mode is selected and converted to another wavelength [2]. Another approach presents optical wavelength conversion for mode-division multiplexing (**MDM**) by converting two modes simultaneously using FWM in a dual-mode fiber incorporating a pump with two modes. Lately, it was shown that it is also possible to reshape the transverse spatial beam profile via the multimode coupling fiber modes [3].

The strong interaction between an intense pulse with the matter leads to space and spectral modifications of the total electric field therefore, in solids, liquids and gases, the non-linear propagation of intense femtosecond laser pulses can produce filaments [4] in which many processes like, self-focus, diffraction, self-phase modulation, self-steepening, ionization, etc., are involved. From the interaction of those processes, it is also possible to generate a supercontinuum (**SC**) accompanied by resonant emissions.
Filamentation and SC generation could be generalized by employing the effective three-wave mixing model, which provides an unified picture, connecting the spectral broadening on the propagation axis with eventually colored conical emission [5], i.e. the transversal spatial distribution stops to be concentrated just around the propagation axis. These waves are considered as a linear superposition of monochromatic bessel beams having different number vectors at different frequencies that makes up a linear invariant solution of the Maxwell equations [6].
Conical emission is now considered as a signature of filamentation and it was observed in gases, liquids, and solids [7] and the beam spatial profile is strongly related to dispersion. X-shapes pattern or O-waves can occur in the normal and anomalous dispersion regime.

While bulk media can sustain several modes, the waveguides only support a discrete number of modes at a given frequency. In relation to this theory, B. Kibler and P. Bejot [8] reported a theoretical description of quantized wave formations in multimode mode fibers (**MMFs**). The numerical model is based on the unidirectional pulse propagation equation

(**MM-UPPE**), which takes into consideration the spatiotemporal shape of the field and its modal distribution. From a numerical model in a GRIN MMF and step-index MMFs, they conclude that quantized waves are generated when intense pulse nonlinearly propagates in a multimode waveguide, whatever the dispersion regime and geometry of the waveguide. Poletti[9] et al. highlighted that femtosecond pulses propagating in MMF lead to a permanent intermodal power transfer between modes. It can be observed even in the absence of any phase matching. From numerous research, two important scale lengths are established; the beat length and modal walk-off length.

Regarding the four-wave mixing process, phase matching conditions are also investigated in GRIN MMF in which the propagation constants of the modes are quantified at equal frequency spacing [10]. The key role of dispersion in the intermodal dynamics is also demonstrated in [11]. In the normal regime conditions, the formation of upshifted and downshifted spectral bands is observed with the intermodal oscillation of the power, and also the spectral bands produce a uniform spectrum that extends over several octaves with a large spectral power density. Alternatively, the anomalous dispersion regime is in favor of the generation of multimode solitons and dispersive waves (**DW**). The Intermodal FWM (**iFWM**) has been also demonstrated for the SC generation with multimode in Photonic Crystal Fibers (**PCFs**) [12]. The nonlinear frequency conversion is achieved with the combination of intermodal FWM and PCFs properties, where the pump propagates in the fundamental mode and the anti-Stoke and Stoke photons are generated in the high order modes. For example, by changing the input peak power, it is possible to modify the mode distribution at the output [13].

Intermodal phase-matchied FWM can also be quite efficiency. For example, two pump photons around 800 nm in the fundamental mode can be efficiently converted into anti-Stokes photon around 553 nm and one Stoke photon within the wavelength range 1445-1586 nm in the second-order mode, with a 16 to 21% conversion efficiency [14].

The numerical studies related to intermodal nonlinear effects of short pulses in multimode PCFs have been numerically studied by Poletti and Horak [9,11]. In their numerical approach, they have derived and simplified a set of coupled GNLSEs which describe the propagation of radially symmetrical modes. The model can be applied to study of the four-wave mixing in MMFs. Another interesting approached have been made by Mecozzi et al. [15,16] in which they show that a group of modes can be coupled throughout SPM and XPM, eliminating all four wave mixing terms.

Concerning the experimental works, Faccio et al. [17] reported the light amplification using a fundamental pulse and its harmonics to generate a near-infrared pulse through FWM by considering a phase matching condition with high order modes. Several numerical models to design pulse compression systems have been developed considering multimode propagation in gas environment, such as gas filled HCC [18]. As result, a periodic oscillation of the energy is usually observed and corresponds to a beating between modes where the energy transfer occurs from the fundamental mode to high-order modes because of spatial Kerr effect.

Many other works have shown that for intense ultrashort pulses and nonlinear intermodal phase-matching can cause spatio-temporal coupling (intermodal energy transfer) even below the critical power threshold [19,20].

Tani et al. [21] introduced a general full-field propagation equation for gas-filled waveguides, including both fundamental and HOMs. However, the key parameters in which the process can be optimized are not yet clear. In addition, it would be interesting to find an intermediate range, where the FWM phase-matched changes from a purely fundamental mode to multimode, which is the topic of this section.

Multimode fibers are also a very important concept in providing an alternative to current parametric optical amplification and frequency generation in intermodal FWM. Therefore, in this chapter, we will examine the interaction of the multimode coupling to understand the phase matching mechanism underlying the generation and eventual amplification of HOMs in gas-filled HCC.

5.2 Intermodal FWM and space-time interaction

In most of optical waveguides, light is confined in the core, where the refractive index is higher than in the surrounding medium. The propagation can be described with the rule given by total internal reflection. Other types of fibers are also investigated with other original guiding mechanisms, as in Kagome fibers [22], antiresonant fiber [23] or band gap photonic crystal fiber [24,25]. The principle of the Kagome fiber is based on an inhibited coupling between the silica cladding and guided hollow-core modes. Here, the cladding of the HC fiber does not exhibit any photonic bandgap but relies on a strong transverse mismatch between the continuum of cladding modes and those of the core, and the subsequent reduction of their field overlap integral [26], [27]. In the following, we specifically move to FWM with several modes inside of the HCC.

5.2.1 Intermodal standard FWM

The intermodal FWM scheme involves two pump photons in one mode (i.e., the fundamental mode) and the anti-Stokes and Stokes photons in the same or first high-order modes.

The effective phase-matching equation can be written as:

$$\Delta\kappa = \Delta\beta_L + \Delta\beta_{NL} = \beta^{n,k}(\omega_3) + \beta^{n,l}(\omega_4) - \beta^{n,m}(\omega_2) - \beta^{n,m}(\omega_1) + \Delta\beta_{NL}, \qquad (5-1)$$

where $\beta^{(r)}(\omega_q)$ is the propagation constant of the qth wave propagating in the rth fiber mode. Since the electric field is linearly polarized, thus just $J_{0,m}$ are considered because for $n \geq 1$, the modal field overlaps integrals will be zero [9]. Consequently, when the two pump are in the fundamental mode, the overlap integral in cylindrical coordinates can also be express as:

$$f_{i,j,k,l}^{1,m} = \left(\frac{1}{(N_i)^2 N_k N_l}\right) \int_0^{2\pi} d\phi \int_0^{\infty} r dr J_{01}\left(u_{11}\frac{r}{a}\right) J_{01}\left(u_{11}\frac{r}{a}\right) J_{0m}\left(u_{1k}\frac{r}{a}\right) J_{0m}\left(u_{1l}\frac{r}{a}\right), \qquad (5-2)$$

with $N_i^2 = 2\pi \int_0^{\infty} r\,dr \left| J_{0m}\left(u_{1m}\frac{r}{a}\right)\right|^2$, that corresponds to the effective area for each mode. $f_{i,j,k,l}$ is the combination of the wave numbers and $J_{(r)}$ wave propagating in the rth fiber mode.

The nonlinear phase equation and parametric gain depend on the overlap integral, such as [3,28]:

$$\Delta\beta_{NL}=2P_1\left(\left(\frac{n_2\omega_3}{c}\right)f_{13}+\left(\frac{n_2\omega_4}{c}\right)f_{14}-\left(\frac{n_2\omega_1}{c}\right)f_{11}\right) \qquad (5-3)$$

$$g^2=\left(\frac{n_2\omega_3}{c}\right)\left(\frac{n_2\omega_4}{c}\right)\left(f_{1134}P_1\right)^2-\left(\frac{\kappa}{2}\right)^2 \qquad (5-4)$$

The two first elements with $f_{i,j}$ on Eq. 5-3 are related to the mixing between the pump and signal/idler whereas the last element is the self-interaction of the pump, i.e., SPM.

The coherence length map is calculated using a CW wave at 800 nm in the fundamental mode coupled in a HCC with a core diameter of 150 µm. The peak power is 1.88 GW, and the HCC is filled with argon at different pressure. For the signal and idler waves, the first-order modes are considered calculating the potential phase matched process. The result is displayed in Fig. 5.1 (on the right). One can observe different lines that represent the coherence length (i.e. π/κ). The combinations of the modes used for each curve is graphically illustrated on the left panel in Fig. 5.1. The roots of the Bessel function are reminded in Table 5-1.

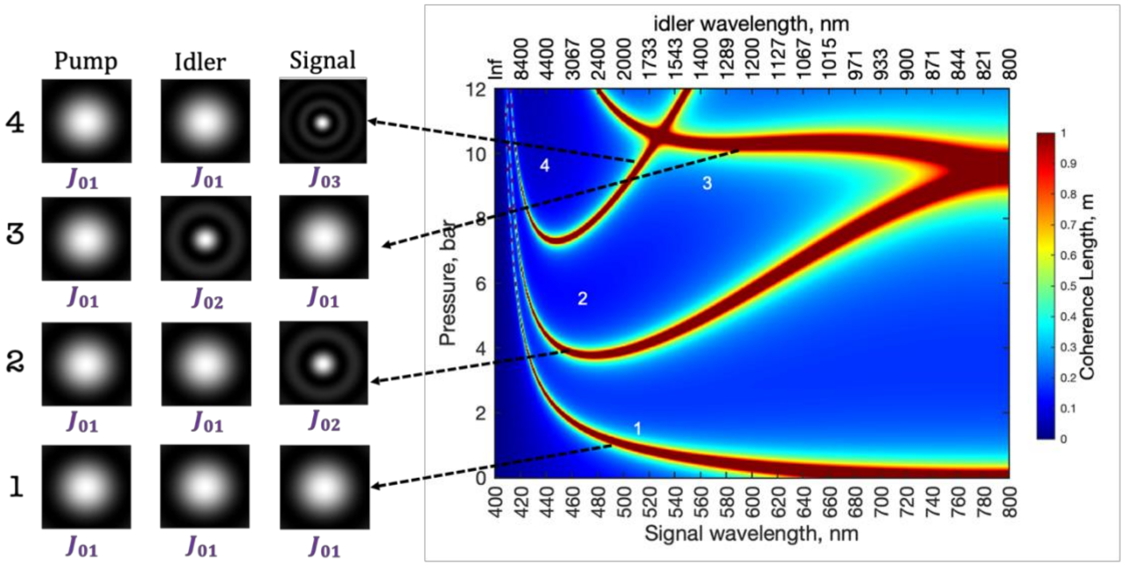

Fig. 5.1 Coherence length calculated from the analytical solution of the coupled equation considering $EH_{1,m}$ modes for the signal and idler waves. The pump wave is in the fundamental mode at 800 nm. The HCC has a core diameter of 150 µm and is filled with argon. The peak power is 1.88 GW.

Table 5-1 Root of the Bessel function used in Fig. 5.1

Curve #	Pump	idler	Signal
1	2.405	2.405	2.405
2	2.405	2.405	5.520

3	2.405	2.405	8.654
4	2.405	5.520	2.405

When the pump spectrum is at 800 nm and the power is 1.88 GW, the intermodal FWM can occur for several pressures. For example, for a pressure of 4 bar, the signal and idler wavelength positions are around ~500 nm and ~2000 nm, respectively. For this phase-matched condition, the pump and the idler remain in the fundamental mode while the signal is in the EH_{12} mode. The idler wavelength position may be adjusted by raising the pressure and two additional phase combinations are available at higher pressure values, see Fig. 5.1.

5.2.2 Intermodal contribution from space-time interaction

When a strong beam propagates with a transverse intensity gradient in the gas filled HCC, the spatial Kerr effect also produces a modification of the propagation [18]. For example, when the laser beam is coupled in the fundamental mode, the laser beam induces an increase in the refractive index proportional to the local intensity. This process leads to the creation of a lens. Thus, the beam is self-focused and the modal distribution is modified during the propagation [19,29]. By using a modal decomposition picture, spatial oscillations during the propagation can be described as a power transfer between different modes through an FWM process [18,29]. Similarly, to the previous discussion of the angular frequency also generated by FWM, one can define a coherence length Lcs between the fundamental mode and the high order modes as

$$\mathrm{Lcs} = 2\pi / \Delta\beta s \qquad (5-5)$$

With $\Delta\beta s = \beta_1 - \beta_m$ the wave vector mismatch between the high order mode m and the fundamental mode.

As Lcs considerably decreases with the mode order, it is usually possible to neglect the modes higher than EH_{12}. Therefore, by neglecting the loss and group velocity mismatch, the main part of the radiation transfer takes place from the fundamental beam to the EH_{12} mode. In addition, the maximum transfer is found to be proportional to $\Delta\beta s^2$ [18]. For example, in the case of a strong pump pulse at 800 nm that propagates in a hollow core capillary with a core diameter of 150 µm and filled with argon at 3 bar, the power transfer from the two first modes appears with a period of Lcs=2.25 cm.

In the case of the ultra-short pulse regime, the temporal domain simultaneously adds some modification of the angular frequency through the temporal Kerr effect. In most cases, the pump spectrum broadens due to self-phase modulation in the HCC for a length in the range of the characteristic nonlinear length $L_{NL} = 1/\gamma P_0$. For example, L_{NL}=8.3 cm for the same parameters outlined above.

Including the high order modes, the transverse spatial effect complicates the analyses since each mode has its own dispersion and nonlinear modal parameters. The spatial modulation also leads to a local increase in the intensity that might generate periodic waves. It means that new frequencies can be generated within the same spatial period.

In this manuscript, we focus on the high order modes generated together with the self-phase modulated spectrum. When the pump undergoes a large spectral broadening through SPM together with the spatial oscillation, some frequency components are generated in other modes. The concept is illustrated in Fig. 5.2.

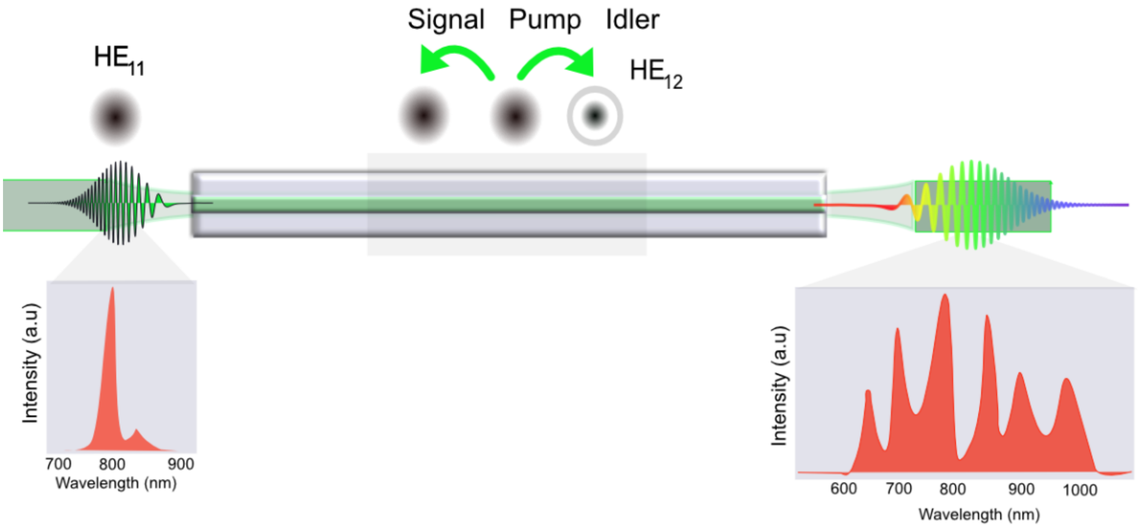

Fig. 5.2 Schematic representation of the new frequencies and new modes from the space to time interaction.

5.3 Experimental part

5.3.1 Experimental set-up

The experimental set-up is summarized in Fig. 5.3. It starts with a Ti: sapphire amplifier system (Libra, Coheren Inc.) that delivers pulses with a duration of ~120 fs (FWHM) at a repetition rate of 1 kHZ. The maximum pulse energy is ~800 µJ, and the spectrum is centered at 800 nm. The pulse coming from the amplifier is injected in a 30 cm-long HCC with an inner diameter of 150 µm. The HCC is placed inside of a home-built metal chamber. The laser beam is focused with a plano-convex lens (f=500 mm) into the fiber with a coupling efficiency of 40 %. We assume that the pump is mostly coupled in the HE_{11} mode.

The output beam is split into two paths, one is well-collimated with a lens (f=150 mm) to measure the far-field image with a CMOS camera (Genie Nano M1240 Mono), whereas the remaining path is used to record the near field image with a second CMOS camera (Genie Nano MM2590 Mono). For example, to record the spectrum and signal profile, the FES650 filter has been installed in the filter area, see Fig. 5.3, and with a mirror (flip mounts) the filter beam is directed towards the visible spectrometer. In the same way, others filters were also placed to select various spectral components (Table 5-2), and the far-field and near-field images were measured after alignment optimization. Their corresponding spectra were simultaneously recorded.

Table 5-2 Filters to select part of the spectrum

Spectral components	**Filters**
Signal	Thorlabs, FES0650
Pump	Thorlabs, FELH0700 and FESH1000
Idler	Thorlabs, FELH0900

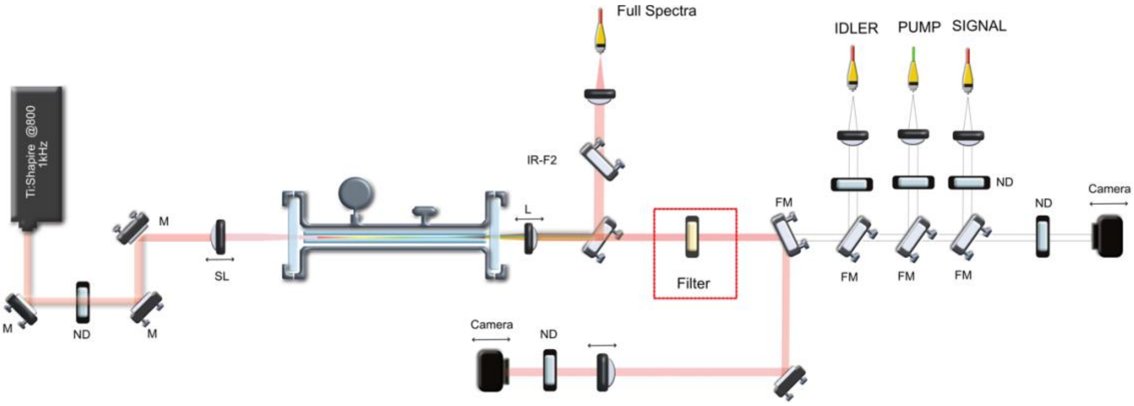

Fig. 5.3 Experimental set-up .SL Plano Convex lens, BS, beam splitter, ND absorptive neutral density filter, FM, Flip Mirror, C, CMOS Camera.

5.3.2 Effect of the gas pressure at a fixed input peak power

As part of the characterization procedure, the laser beam spectrum, near and far field images were firstly measured when the chamber was empty (Fig. 5.4). One can observe that the pump spectrum is centered at 800 nm whereas the near and far images have shapes close to HE_{11} mode patterns.

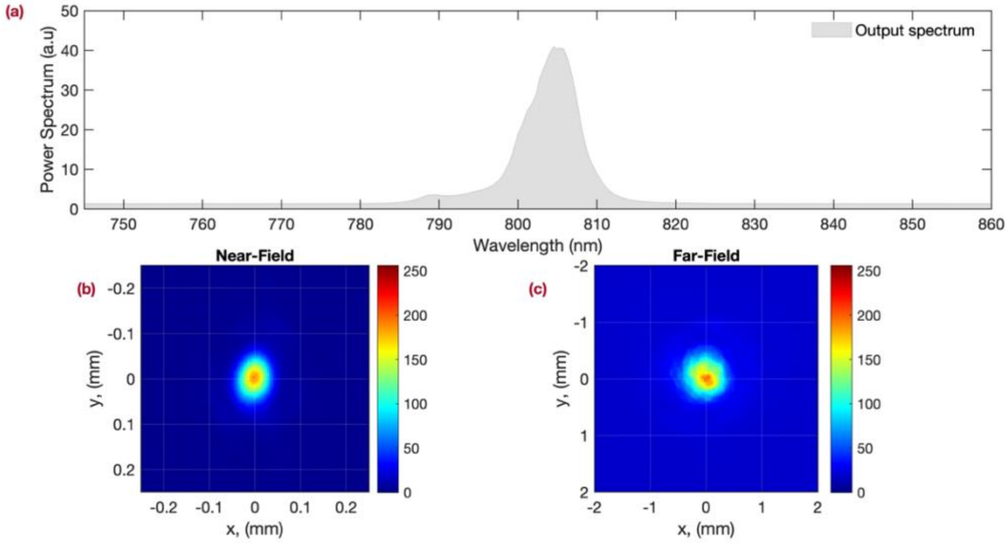

Fig. 5.4 (a) Pump spectrum. Corresponding near (b) and far (c) field distributions. The peak power is 1.6 GW and the HCC is under vacuum.

Case at a pressure of 3 bar

The chamber was filled with the argon gas up to ~3 bar , while the pump peak power is maintained at 1.61 GW at the HCC input. The pump spectrum presents a spectral broadening mostly from self-phase modulation during the nonlinear interaction between the gas and the beam (see Fig. 5.5). The spectrum extends from 700 nm to 900 nm with a strong peak around 850 nm. In order to evaluate the time-space coupling, beam profiles for selected spectral ranges need to be measured since we expect to get a part of the energy coupled into high-order modes. Experimentally, the central and the edge parts are selected from the complete spectrum. We define the signal and idler as the lower and higher wavelength regions, respectively. Consequently, several filters were placed in the path using few flip mounts (Fig. 5.3).

The entire spectrum without filters is displayed in Fig. 5.5.a. Subsequently, a short-pass filter (see Table 5-2) was used to observe visible components (signal path) and the spectrum is displayed on Fig. 5.5.b. and the associated beam profiles Fig. 5.5e, h.
Next, the filter for the measurement of the pump spectrum was placed on the beam path. The spectrum and its corresponding spatial profiles are displayed in Fig. 5.5.f, i.
Finally, to see the infrared side (idler) the corresponding filters have been set on the beam path and the corresponding beam profiles are shown in Fig. 5.5 g, j.

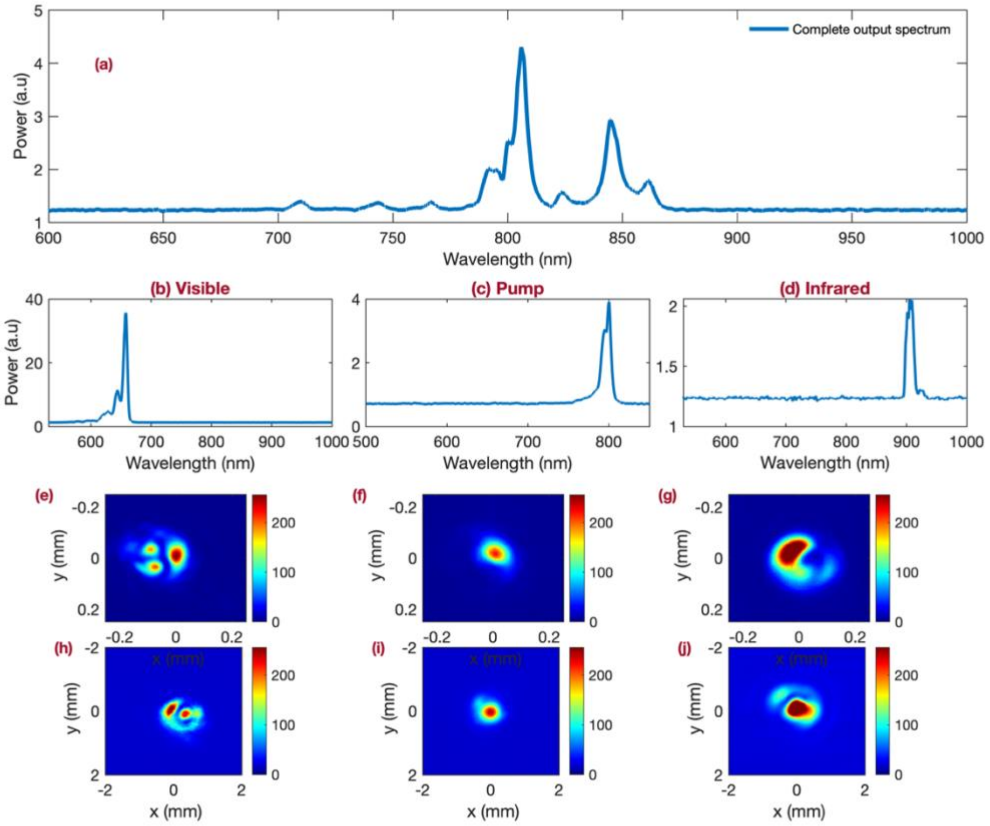

Fig. 5.5 a) Complete spectrum of the pump. The individual spectra of the b) signal e) pump and h) idler. In addition, the near and far field distributions of e,h) signal f,i) pump and g,j) idler. The 30 cm long HCC is filled with Argon at ~3 bar. The input pump peak power 1.6 GW.

The central part of the spectrum, i.e., the pump, has a clear circular shape and is close to an HE$_{11}$ as the one recorded under vacuum (see Fig. 5.5). The beam profiles of the signal and idler have several structures and do not clearly represent the fundamental mode. Since the filters select only a wide spectral range, the profile takes also into account the space-spectrum distribution. We expect that the recorded beam profiles originated from a mixing of several beam profiles.
From the simulation described in Section 5.2, we will conclude that the spectral part closed to the center remains within the HE$_{11}$ mode, while the edge propagates with the HE$_{12}$ mode. It is worth noting that the calculated coherence length Lc does not explain the generation of new waves with high order modes, Fig. 5.1.

Case at a pressure of 4 bar

Once the pressure was increased at around 4 bar, the spectral broadening is enhanced and some other maximum bands have been observed (Fig. 5.6.a). The power is more transferred from the pump center to other frequencies on the edges. The signal profile distribution in the near field and far-field displays a pattern with a maximum surrounded by a ring (Fig. 5.6. e,h). This shape has a well-defined profile compared to the previous case and looks similar to the HE$_{11}$ mode. In the idler region, the spatial distribution is less clear and presents a fashion pattern with a low ring with a decentralized maximum. This configuration appears as a mix of the fundamental-HE$_{11}$ and the HE$_{22}$ modes.

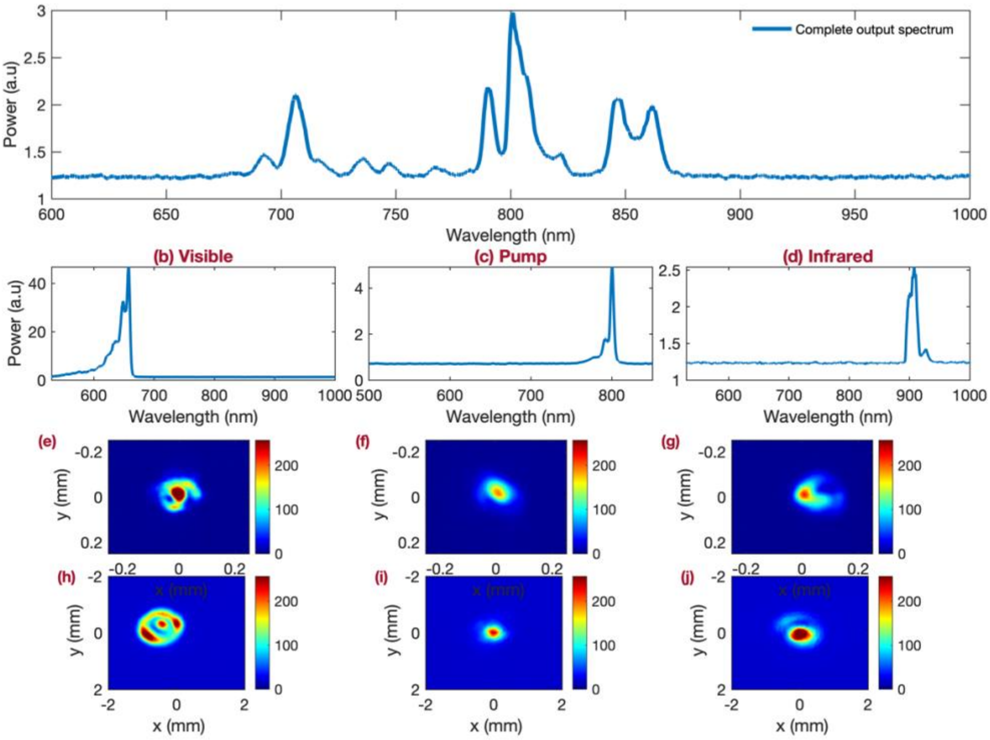

Fig. 5.6 a) Complete spectrum of the pump. The individual spectra of the b) signal e) pump and h) idler. In addition, the near and far field distributions of eh) signal f,i) pump and g,j) idler. The 30 cm long HCC is filled with Argon at ~ 4 bar. The input pump peak power 1.6 GW.

Case at a pressure of 5 bar

When the argon pressure approaches ~5 bars, the full spectrum develops a stronger modulation and the visible part becomes stronger, at about 700 nm. The infrared components become weaker compared to the previous case. The spectral broadening reaches ~ 900 nm (Fig. 5.7a). The interesting part happens within the spatial distribution profiles because the idler pattern develops a clearer ring shape as for the visible profile, (Fig. 5.7c, d). Thus, we can conclude when the spectrum broadens through SPM, the beam profile at the spectrum center has a fundamental shape, while the signal and idler parts tend to display a shape close to the HE_{12} mode.

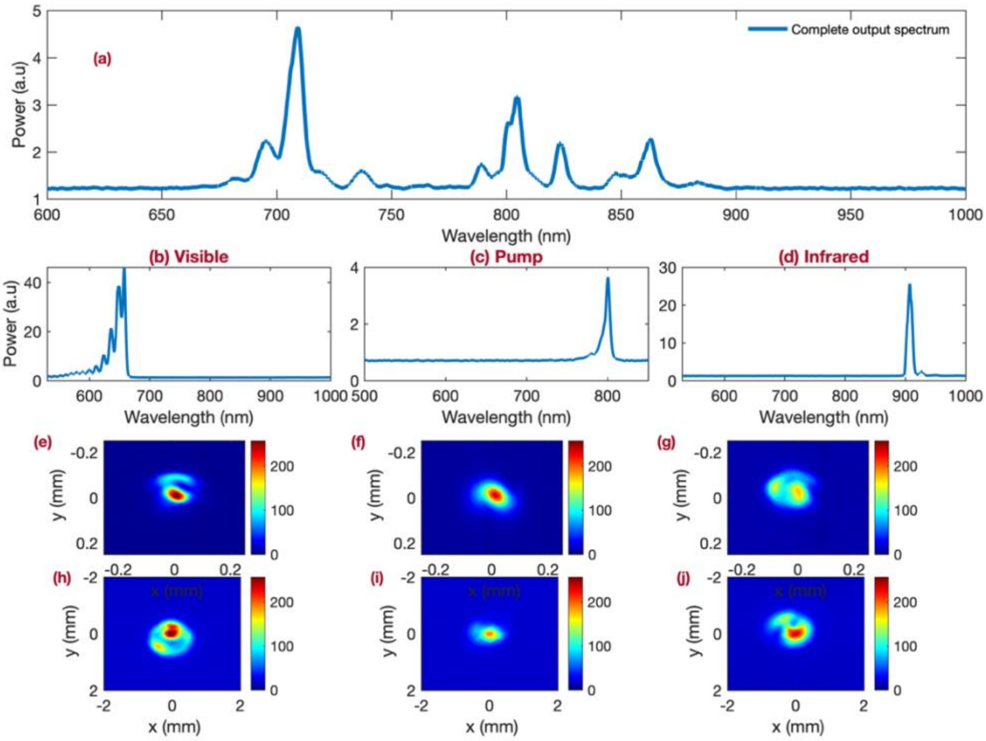

Fig. 5.7 a) Complete spectrum of the pump. The individual spectra of the b) signal e) pump and h) idler. In addition, the near and far field distribution of e,h) signal f,i) pump and g,j) idler. The 30 cm long HCC is filled with Argon at ~5 bar. The input pump peak power 1.6 GW.

5.3.3 Effect of the peak power at a fixed pressure

A similar experiment was carried out, but by keeping a constant gas pressure inside the chamber while the coupled energy/power in the HCC is increased. Fig. 5.8 and Fig. 5.9 display results for a peak power at the HCC input of 0.8 or 1.1 GW. We can see that the full spectrum is clearly different from each other. At low peak power, the infrared components are almost not present Fig. 5.8.a while at high peak power, it appears to be stronger Fig. 5.9.a. The spatial profile images in the signal part present a maximum surrounded by a ring in both cases, at high and low peak powers. We could therefore confirm that the signal components are generated in a high order mode, mostly in the HE_{12} mode. As for the idler, the spatial profile images are also less clearly defined, but a weak ring arises and stays at high power.

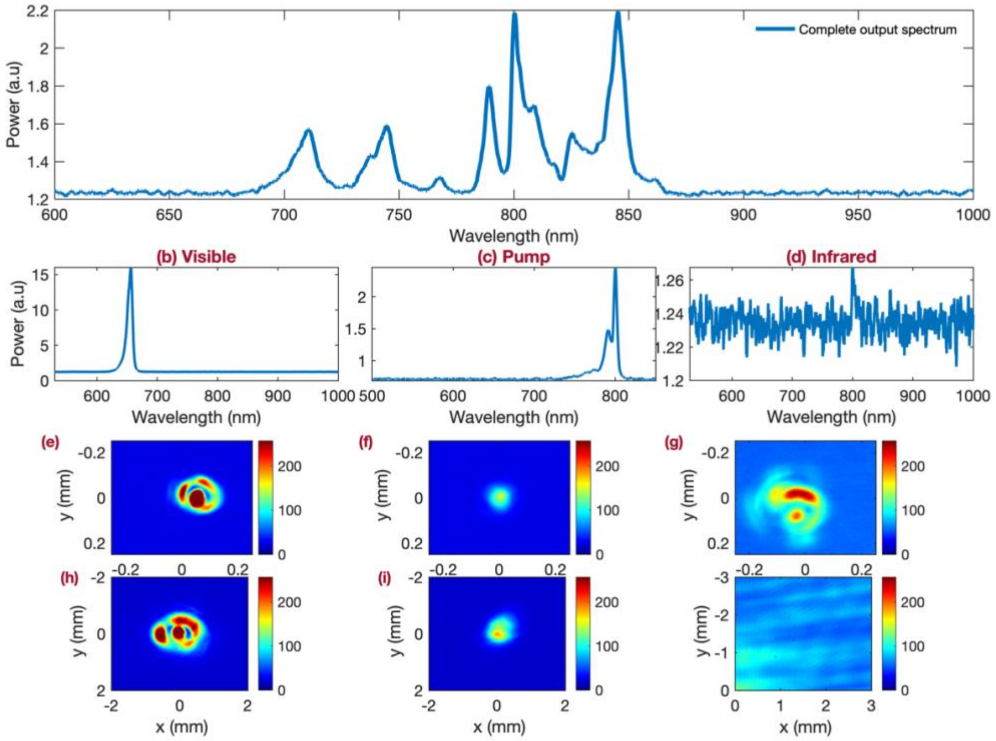

Fig. 5.8 a) Complete spectrum of the pump. The individual spectra of the b) signal e) pump and h) idler. In addition, the near and far field distribution of e,h) signal f,i) pump and g,j) idler. The 30 cm long HCC is filled with Argon at ~5 bar. The input pump peak power 0.8 GW.

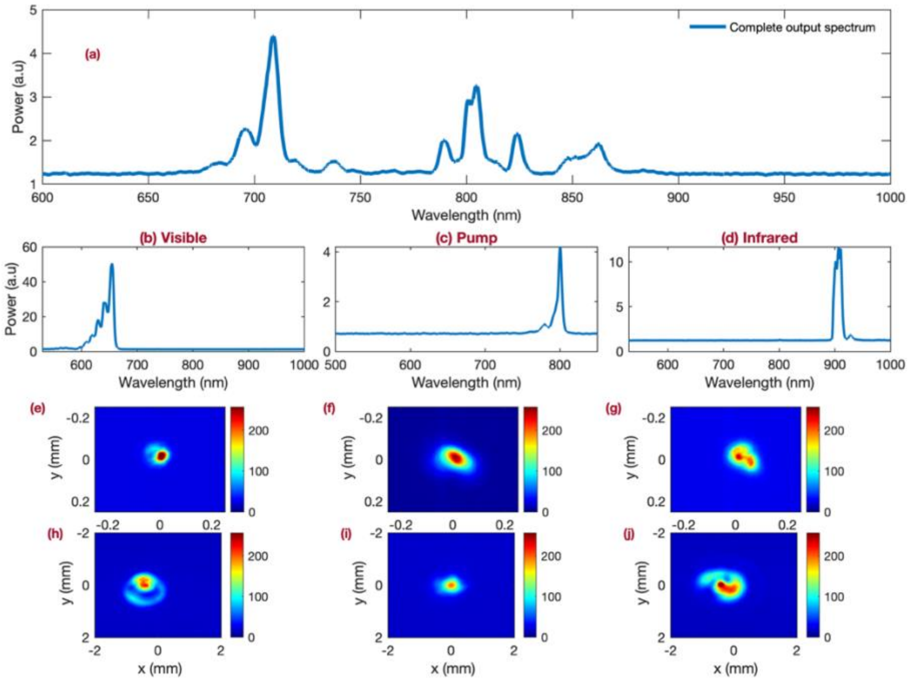

Fig. 5.9 a) Complete spectrum of the pump. The individual spectra of the b) signal e) pump and h) idler. In addition, the near and far field distribution of e,h) signal f,i) pump and g,j) idler. The 30 cm long HCC is filled with Argon at ~5 bar. The input pump peak power 1.1 GW.

From all these cases, one can conclude that when the spectrum broadens through SPM, the beam profile at the spectrum center has a fundamental shape, while the signal and idler parts tend to display a shape close to the HE_{12} mode. The ring structure looks more sensitive to parameters, as the pressure and peak power in the infrared part.

The HE_{12} profile does not always appear very distinct for few reasons. First, the filters select a relatively broad part of the full spectrum and, therefore, we may observe different profiles within this spectral range. We will confirm with numerical simulations, at the end of the chapter, that the beam profiles mix the HE_{11} and HE_{12} modes. Secondly, the beam at the HCC output propagates, is collimated, and passes through lenses, and several optics. Some chromatic and geometrical aberrations are expected and will influence the recorded profiles. Third, the pump profile at the HCC input is not perfectly symmetric and will produce some asymmetry in the output beam shape.

5.3.4 Measurement with an imaging spectrometer

The setup, including the imaging spectrometer, is shown in Fig. 5.10. The output laser beam is collimated as it passes through a lens and several filters. A few centimeters after a far field image are created and sent to the imaging spectrometer. The instrument generates an output plane in which the horizontal axis shows the spectral distribution with a wavelength scale, while the vertical axis represents the spatial distribution. We are then able to place a camera at the imaging plane to record the complete two-dimensional pattern.

The wavelength scale is easily calibrated by adjusting the central wavelength within the spectrometer and the relation to the number of pixels on the camera. The alignment is carried out when the chamber is free of gas, to detect only the 800 nm.

The goal with the imaging spectrometer in the experiment is to observe and record simultaneously all the spectrum and profile as a function of parameters (pressure and power).

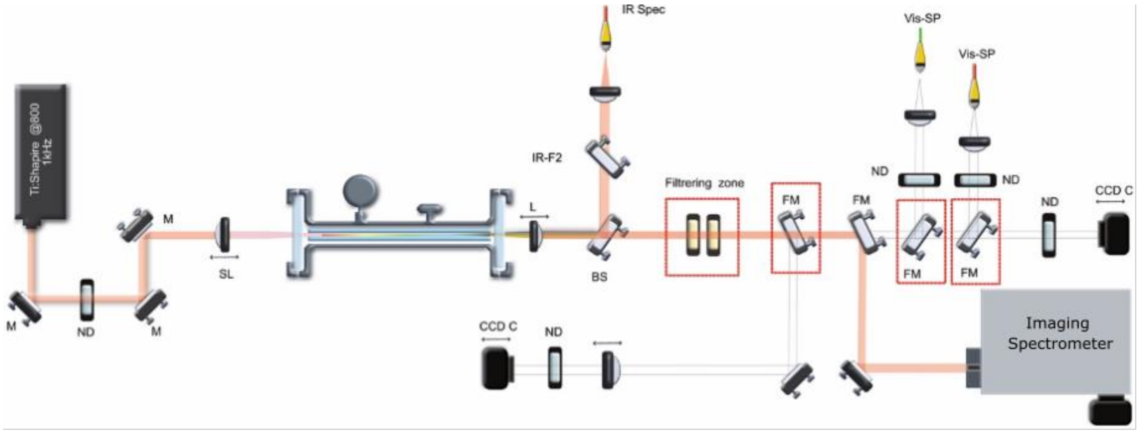

Fig. 5.10 Experimental configuration with the imaging spectrometer.

The chamber was filled with argon gas up to ~ 3 bar, while the input pump peak power is maintained at 1 GW.

Fig. 5.11 presents an example of a spectrum measured when the pressure is ~3 bars. Some spectral components are detected with the idler and the signal spectrometers. The signal and idler spatial profiles look like the HE_{11} mode. Thus, under these experimental conditions, the new frequencies generated remain in the fundamental mode.

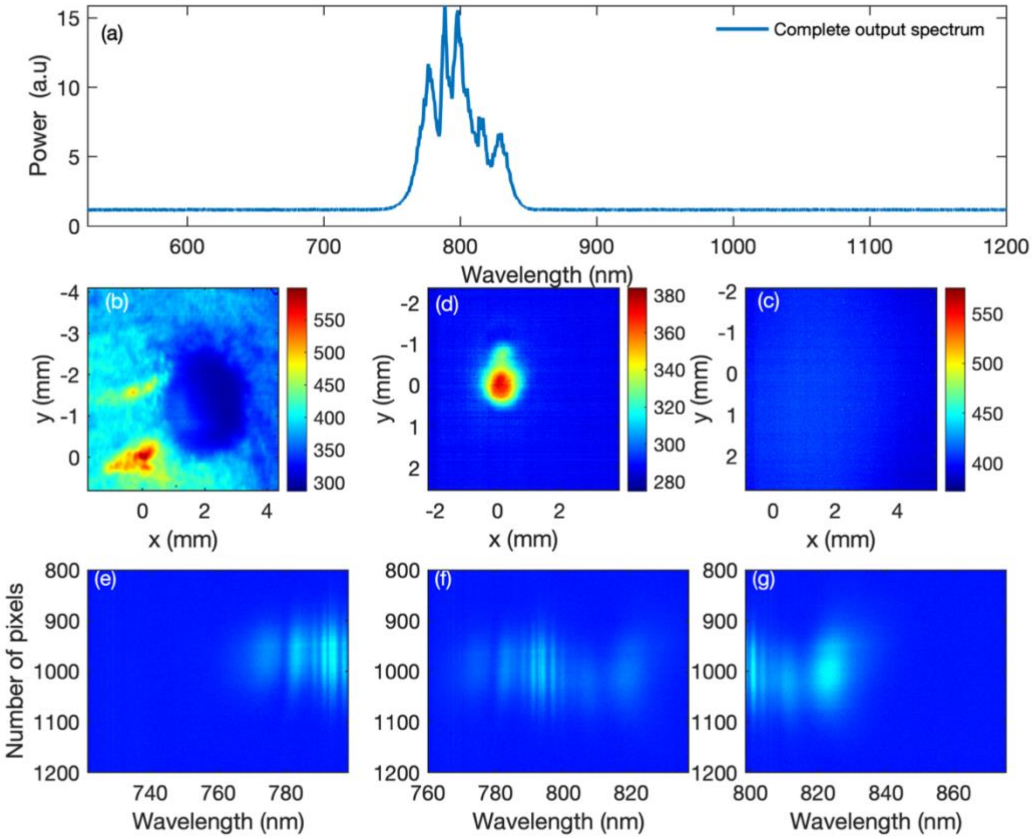

Fig. 5.11 a) The complete beam spectrum. The far field distribution measured with the camera for b) signal d) pump c) idler. Spatio-spectral profile recorded with the imaging spectrometer, after propagation through 30-cm-long -HCC filled with argon at 3 bar. The input pump power is 1GW.

Fig. 5.12 presents an example of a spectrum measured by increasing the pressure to ~5 bars. The signal and idler spatial profile displays a distorted pattern because of the higher order mode. On the other hand, the measurements of the imaging spectrometer display bands corresponding to the red and blue shift emissions in Fig. 5.12.a-b. whereas the radial intensity distribution remains only in the central region. This distribution indicates that the new frequency components follow a spatial distribution corresponding to the lower order of the Bessel function, J_{01}.

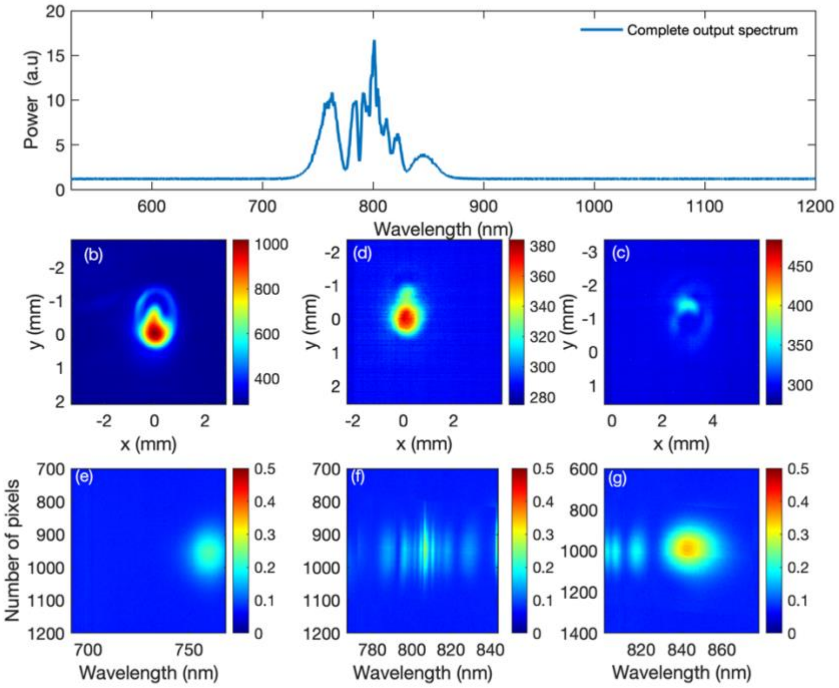

Fig. 5.12 a) The complete beam spectrum. The far field distribution measured with the camera for b) signal d) pump c) idler. Spatio-spectral profile recorded with the imaging spectrometer, after propagation through 30-cm-long -HCC filled with Argon at 5 bar. The input pump power is 1GW.

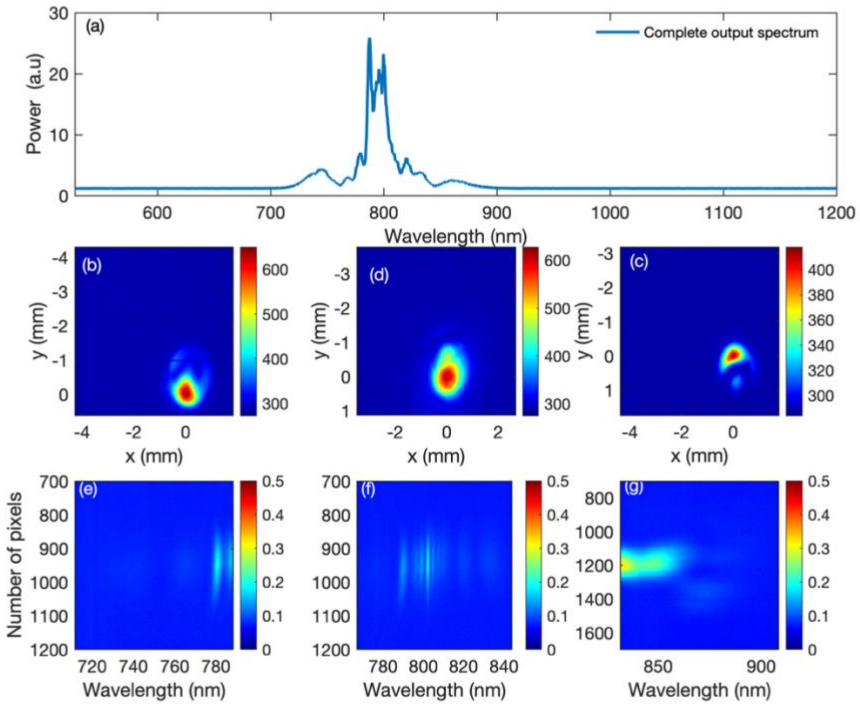

Fig. 5.13 The complete beam spectrum. The far field distribution measured with the camera for b) signal d) pump c) idler. Spatio-spectral profile recorded with the imaging spectrometer, after propagation through 30-cm-long -HCC filled with Argon at 7 bar. The input pump power is 1GW.

Fig. 5.13 depicts the results when the pressure is approximately ~7 bar. The entire spectrum represents an even larger spectrum than in the previous one. The spectral profile has more structures and ripples. The results are displayed on the spatial profiles (Fig.

5.13.b-c) recorded with a camera in the far-field, and the spatio-spectral intensity profile recoded by an imaging spectrometer (Fig. 5.13. f-g). The idler beam profile (Fig. 5.13 .c), displays a shape with a ring surrounding a central part. This pattern could confirm the existence of a higher order mode, a shape closes to the HE_{12} mode. The interesting section concerns the results of the imaging spectrometer (spatio-spectral profile), because the band has a different spatial distribution. In other words, the energy is distributed around the vertical axis as well. It seems that the spectral components around ~870 nm have a spatial distribution corresponding to another vertical distribution, i.e the energy is split in two areas. This result confirms that the idler frequencies are in the high-order mode.

5.4 Seeded FWM

5.4.1 Experimental configuration

As discussed in the previous section, a transfer process occurs during the multimode propagation of the intense pump in the HCC. The spectrum broadens mostly through SPM and the spectral edges exhibit a HOM content. In this case, the process is generated from the broadening of the pump itself, i.e., the signal and idler bands are originated from the pump.

To enhance the conversion efficiency, the system was seeded with a broadband and weak signal. The signal passes through a delay line to adjust the temporal overlap between the pump and the signal. Then, the signal was coupled into the capillary in the fundamental mode simultaneously with the pump. The output chamber beam is collimated and separated through various filters to visualize the signal and idler components.

5.4.2 Initial conditions

To perform this experiment, it was necessary to make sure that the signal and the pump are coupled in the fundamental mode. The spatial distribution of the pump and signal in the far field were verified at the beginning of each test, without any gas in the chamber. When the gas enters the HCC, the spatial pattern has been observed in several conditions to understand exactly the origin of the modal distortions. The experiment was carried out under the following conditions: the gas pressure is at 3 bar, the pump and signal peak powers are 1.2 GW and 4.5 MW respectively. The initial beam characterization is depicted in Fig. 5.14.

The output beam is separated in the signal and idler components by using several filters. The central part, the pump, is also attenuated. Each individual path is sent to the corresponding visible and infra-red camera and spectrometers. This is labeled as "visible side" and "infra-red side" in the Fig. 5.14. The spectrometers and cameras are for the visible side, the Ocean optics USB 4000, CCD camera (Thorlabs BC106N-VIS). For the infrared side, those are, Stellar Net spectrometer (DWARF-Star NIR) and CCD Hamamatsu (IR-Camera, sensitivity between 900 to 1700 nm). The pump spectrum and its beam profile were measured with the Ocean optics USB 2000 and the camera Genie Nano M1240 Mono (Visible-Camera, sensitivity between 400-850 nm).

In Fig. 5.14a, the spatial profile is displayed when only the signal is coupled and propagated through the capillary. Since the signal is weak, there is no nonlinear interaction between the signal and the gas. Thus, the spatial profile of the signal remains unchanged (Fig. 5.14.a). One can conclude that the beam is mostly injected into the fundamental mode. Fig. 5.14b. Of course, the idler is not generated and no beam profile is detected (Fig. 5.14c-d).

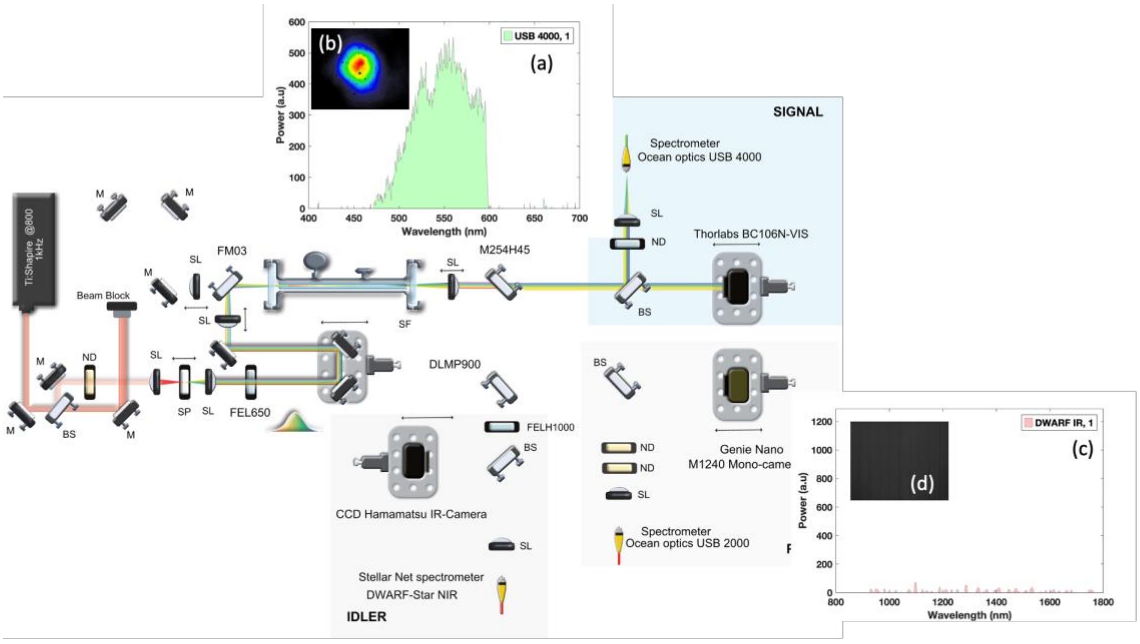

Fig. 5.14 Experimental configuration for the initial characterization when only the signal is injected into the capillary a) spectrum and b) beam profile of the signal, c)spectrum and d) beam profile of the idler.

Fig. 5.15.f shows the beam profile when the pump is coupled only in the capillary. When the pressure is ~3 bar, the spectrum in the visible and infrared are filtered at the output, similarly to the experiment described in the previous section. The signal part presents a strong peak around 580 (Fig. 5.15.a) while the idler spectrum is around 1.1 μm (Fig. 5.15.c). The spatial profile shows a ring around a centered maximum (Fig. 5.15.b) in the infrared while the signal is mostly circular (Fig. 5.15.d).

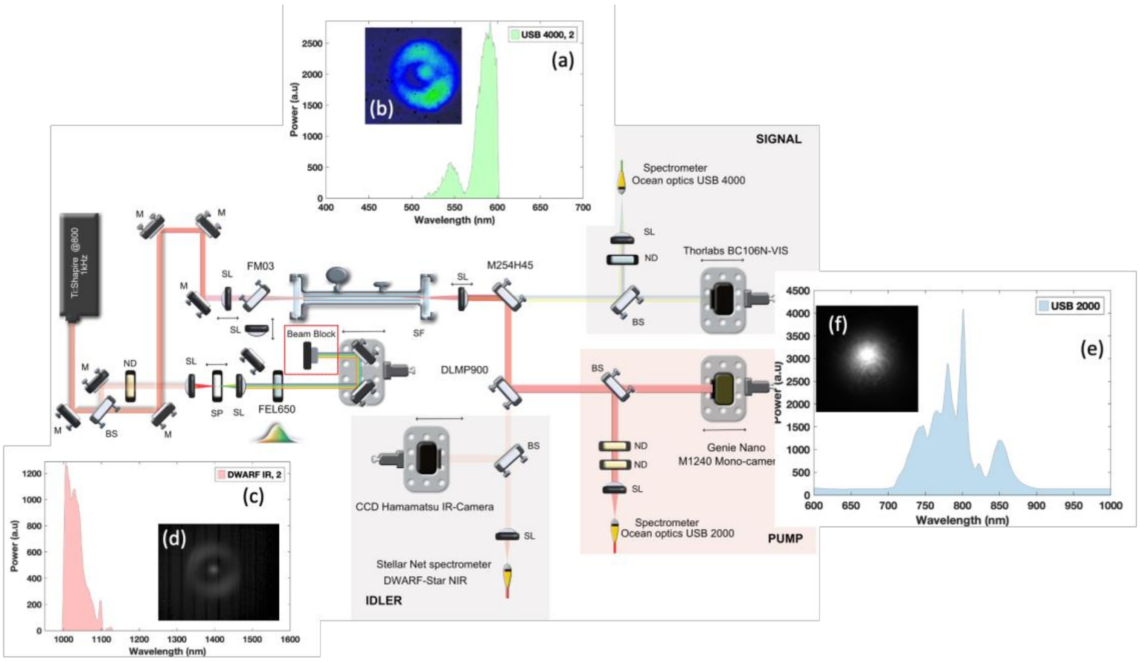

Fig. 5.15 Experimental configuration for initial characterization when only the pump is injected into the capillary a) spectrum and b) beam profile of the signal, c)spectrum and d) beam profile of the idler side.

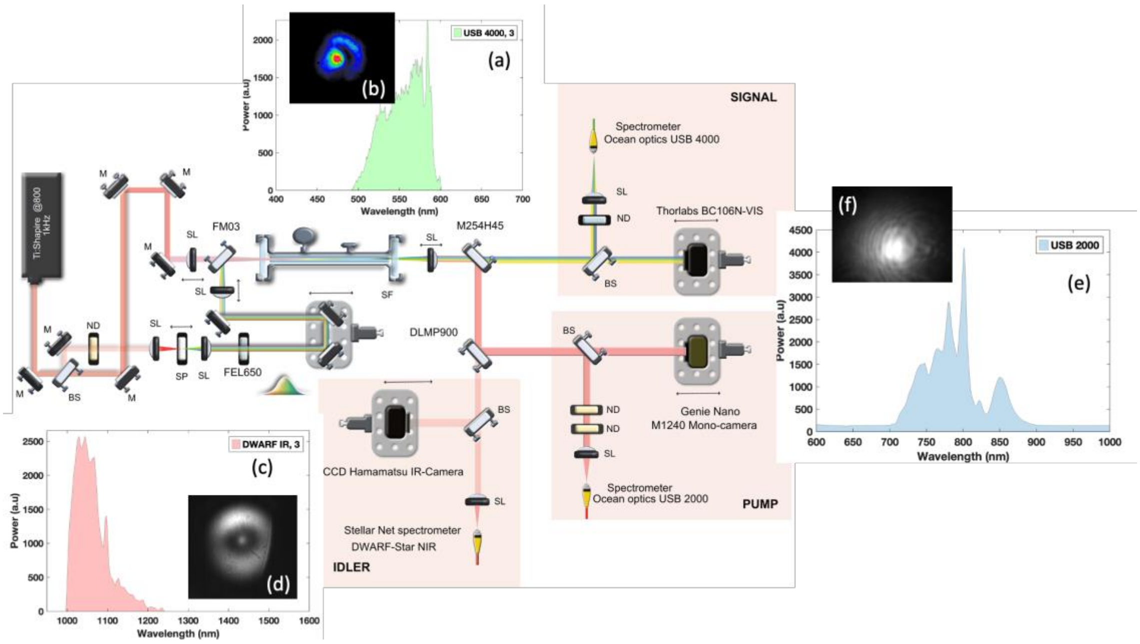

Fig. 5.16 Experimental configuration when both only the signal and pump are injected into the capillary a), spectrum and b) beam profile of the signal, c) spectrum and d) beam profile of the idler side and f) spectrum and e) beam profile of the pump.

Fig. 5.16 represents the case when the pump and signal are coupled together into the capillary. From the comparison between spectra, we can observe a weak amplification of the signal when the pump is injected, while the idler spectrum gets stronger. In addition, when the signal seeds the HCC, the spectral structures in the visible change: the maximum at 580 nm (Fig. 5.16.a) becomes stronger when the signal is injected as expected from Fig. 5.15.a. Concerning the spatial profile of the beams, the ring becomes stronger in the signal and idler in both cameras when the signal is injected due to the amplification (Fig. 5.16.b) although the signal injected is in the fundamental mode. The idler exhibits a strong ring (and Fig. 5.16.d) while the pump (and Fig. 5.16.f) has a beam profile near the fundamental mode.

In the following, the temporal delay between the pump and the signal is adjusted and the spectrum is recorded at each step. In Fig. 5.17, the amplified signal is represented in blue while the generated idler is in red. The idler is generated from 1.1 to 1.2 μm. and the highest power is obtained for a spectrum centered at ~1200 nm. The generated idler presents a broadband spectrum due to a better overlap between the signal components and the pump. Simultaneously, the signal is broadly amplified at this delay.

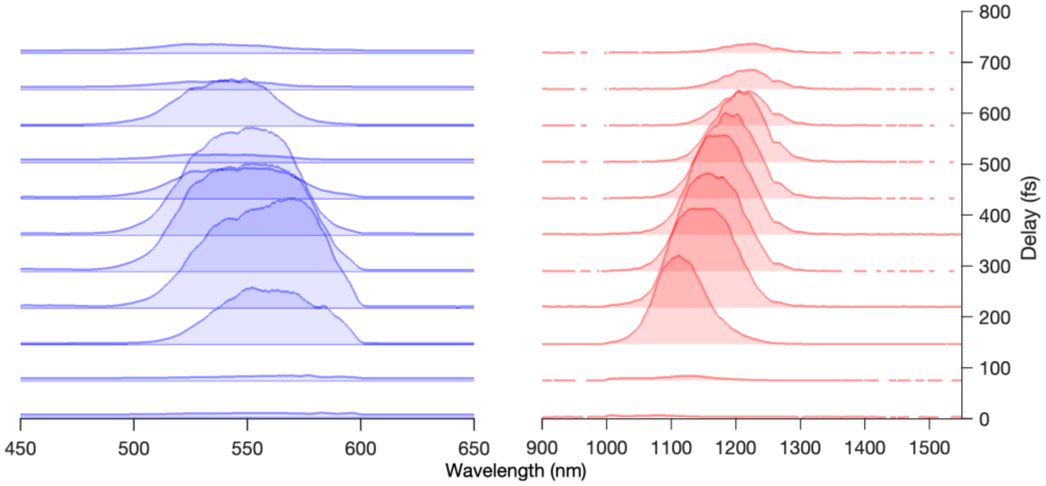

Fig. 5.17 Evolution of signal and idler spectra as a function of the temporal overlap between the injected signal and the pump

For each delay step, the spatial beam profile of the signal and idler has also been recorded (Fig. 5.18 and Fig. 5.19). When the temporal overlap between the pump and the signal is not present, the signal beam is mostly in the fundamental mode, as seen in Fig. 5.14b. A large and weak ring is also observed, and it is originated from the interaction with the pump. Once the signal and the pump pulses overlap, the signal beam starts to be distorted. The signal beam profiles are recorded as a function of the delay, and it is possible to observe how the energy goes to the outer ring. For example, for a delay of ~289 fs the intensity of the ring is the highest. Generally, for all delays, the shape remains in EH_{12}, except in the last case, where the shape appears to be in EH_{11} at delay 718 fs, because the nonlinear interaction between the signal and pump is reduced.

Similarly, the idler has also a ring shape due to the pump contribution (as in the previous section). The following images show the evolution of the structured shape, exhibiting a ring around a centered maximum Fig. 5.19. The beam profile pictures has always an HE_{12} shape when the signal pulses overlap or not with the pump, because the generated frequency is spontaneously produced in the HE_{12} mode.

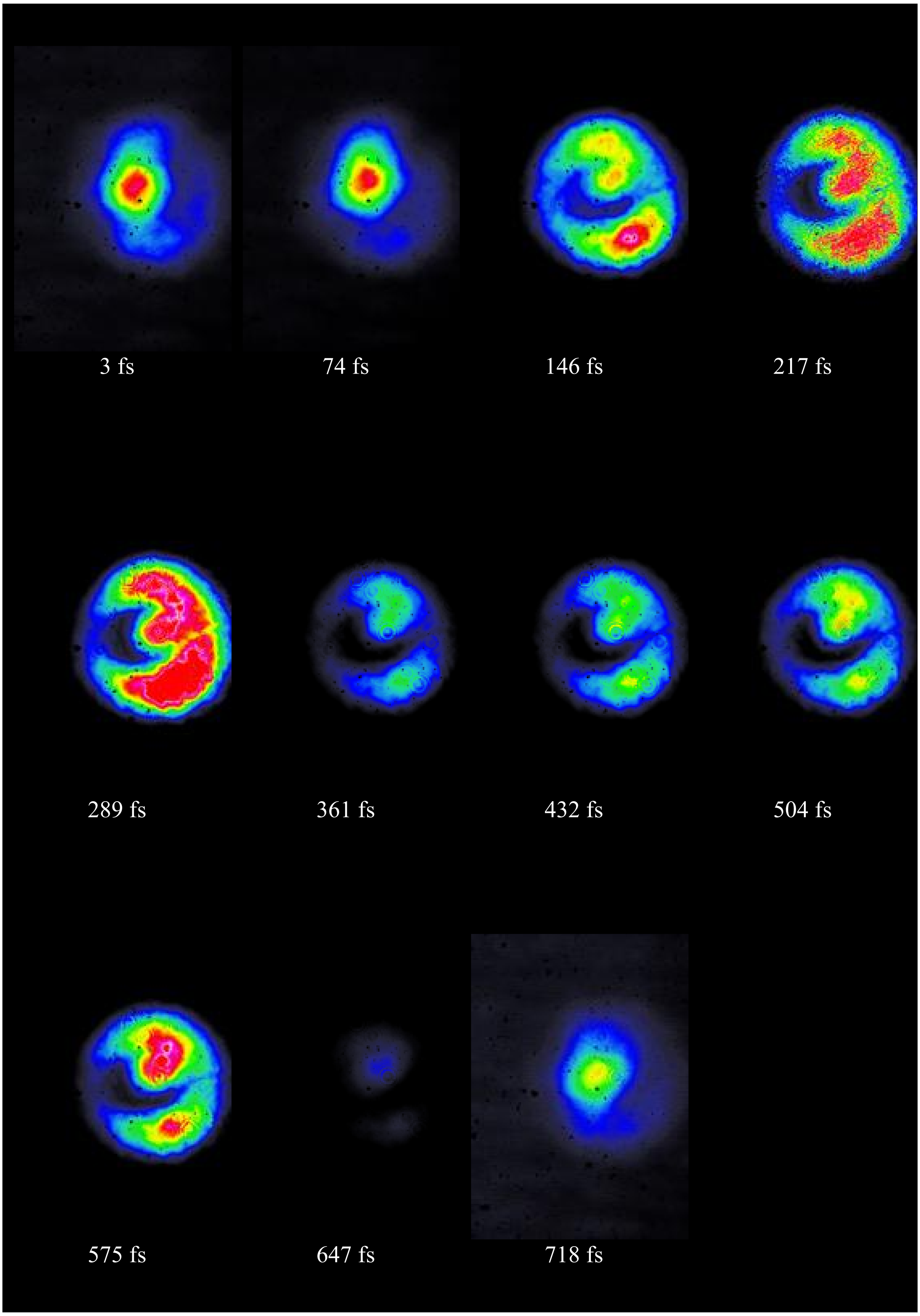

Fig. 5.18 Evolution of a spatial profile of the signal as a function of the relative delay with the pump.

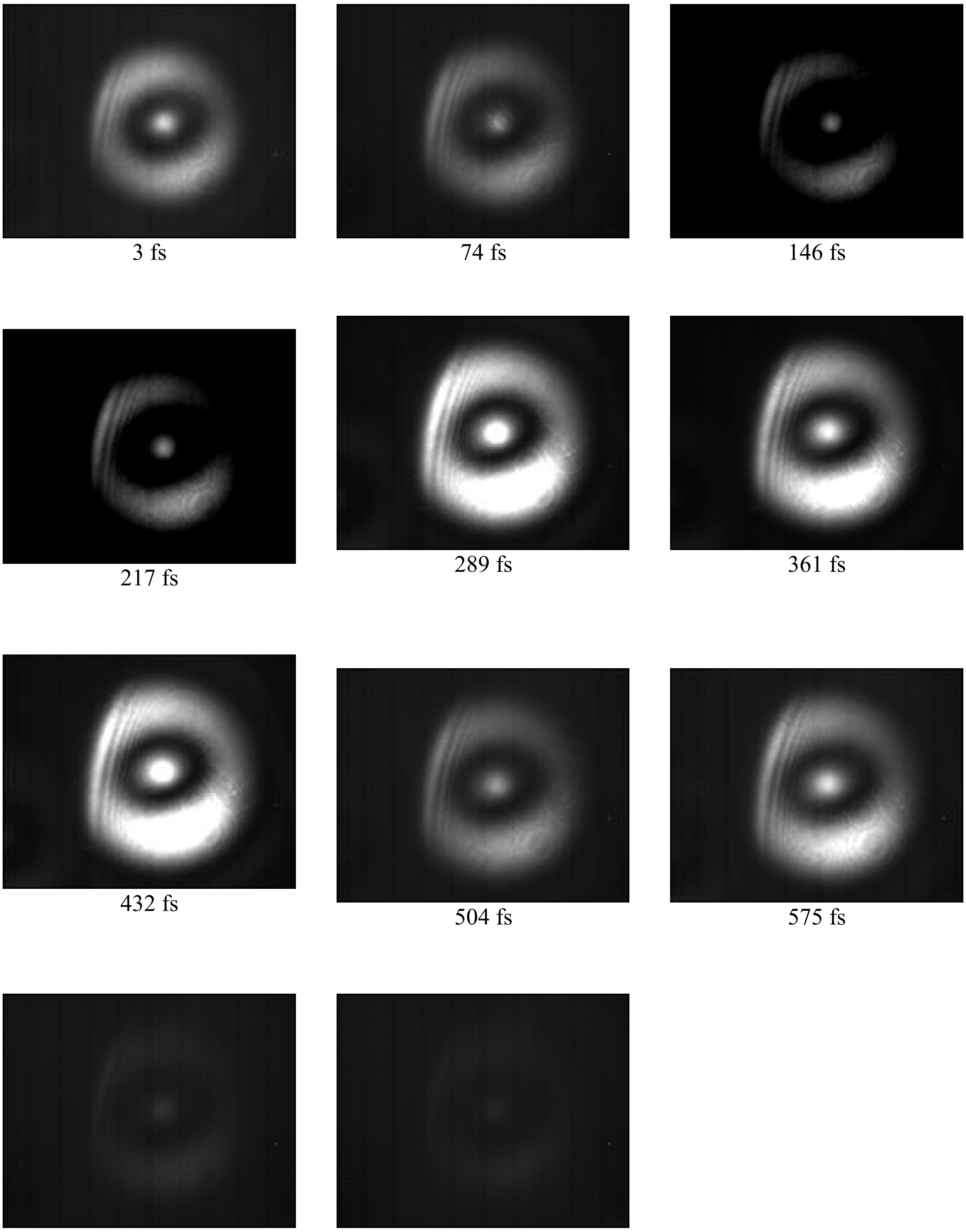

3 fs

74 fs

146 fs

217 fs

289 fs

361 fs

432 fs

504 fs

575 fs

647 fs

718 fs

Fig. 5.19 Evolution of a spatial profile of the idler as a function of the relative delay with the pump.

The average power of the generated idler as a function of the delay is shown in Fig. 5.20. The highest value is obtained when the overlap between the signal and the pump is optimal (217 fs), and it closes to the best signal amplification.

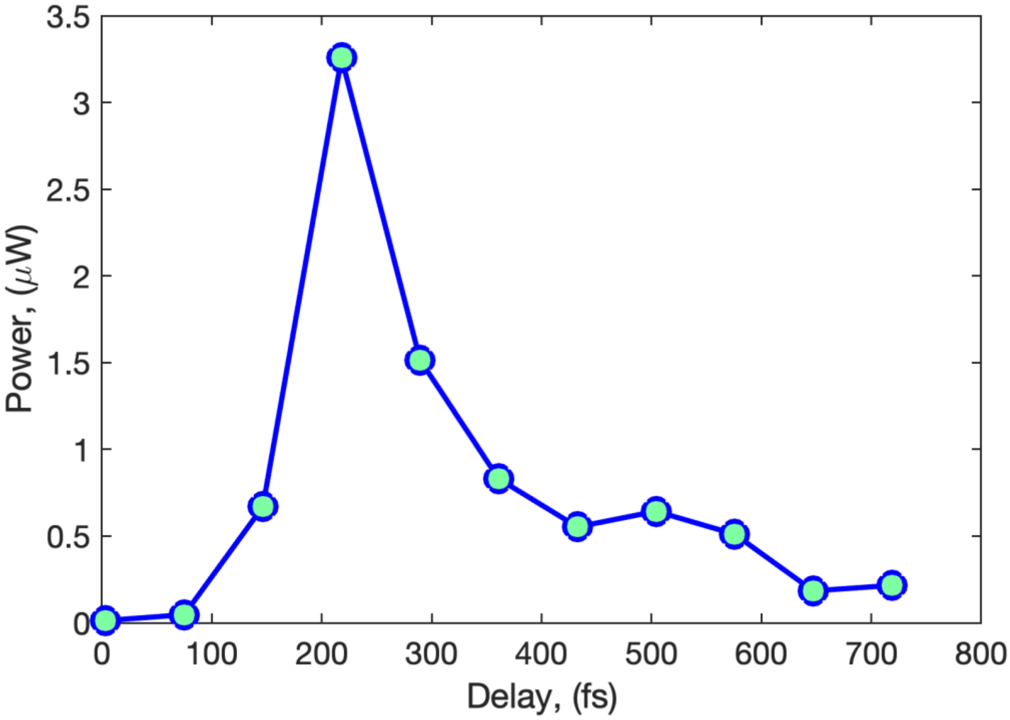

Fig. 5.20 Idler average power as a function of the relative delay between the pump and signal.

5.5 Advanced numerical simulations

The purpose of this section is to study in detail the mechanism of the mode generation through the spatiotemporal coupling in the gas-filled HCC. As the analytical description of the spectral FWM does not provide a strict explanation for the experimental configuration, we used advanced numerical simulations to include both the spatial and temporal Kerr effect.

The numerical simulations have been done by P. Béjot at the laboratory "Interdisciplinaire Carnot de Bourgogne". They are based on the resolution of the unidirectional pulse propagation equation (**UPPE**) generalized to structured media (i.e. media embedding a transversal distribution of the refractive index) expressed in the modal basis [8]. It includes the gas-filled waveguides with the HOMs, the modal linear dispersion, and the Kerr effect. The spatio-temporal coupling is automatically included in the simulation. In the following, the simulation also takes into account the asymmetry of the input beam profile by using the m,n eigenvalues. At the input, 1% of the field is injected into the HE_{12} mode, whereas the remaining part is in the fundamental mode.

Here, we simulate the nonlinear propagation of 100-fs Gaussian pulses coupled in a 40-cm long HCC filled with 4 bar of argon. The core diameter is 150 µm and the peak power is 1.3 GW. The spectrum is firstly recorded as the function of the HCC length (Fig. 5.21). As expected, the spectrum gradually broadens, mostly by SPM, along the propagation.

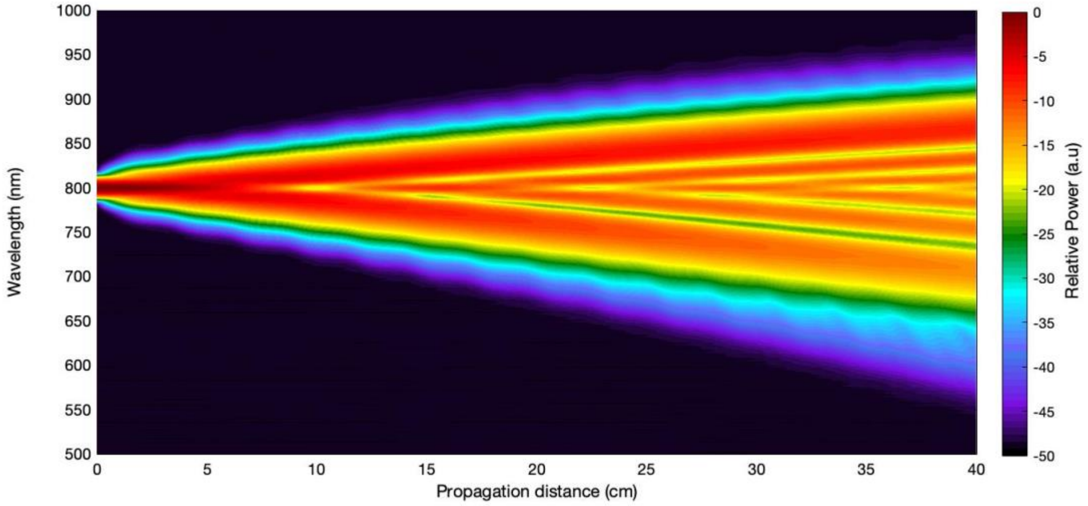

Fig. 5.21 Spectrum as a function of the argon filled HCC. The pressure is 4 bar and the input peak power is 1.3 GW

Simultaneously with the spectral broadening, the fluence oscillates during the propagation since the beam stretch and compress along the length (Fig. 5.22). This effect corresponds to the power transfer the fundamental mode to the HE_{12} mode due to the spatio-temporal coupling. Indeed, during propagation, the laser beam induces an increase in the refractive index proportional to the local intensity and thus the beam is exposed to a high index at the center a lower index at the edges. However, in contrast to a linear lens focusing, self-focusing is a cumulative effect along the propagation so that the beam is increasingly intense in its center, producing self-focused beam. In the absence of any saturation effect, self-focusing would end up in a singularity at a finite propagation distance. However, self-focusing always competes with diffraction/propagation. Then, the beam spreads and shrinks, resulting in an oscillatory propagation characterized by defocus-refocusing cycles [1]. A similar effect is shown in the GRIN fibers, where Spatial self-imaging (**SSI**) results in a longitudinal oscillation of the beam width and beam intensity along the fiber. In this way, the combination of the Kerr effect and SSI produces a dynamic similar to a long period of grating [30]. The spatial oscillation can be interpreted as a periodic transfer of the power between modes, and the period depends to phase relationship of the modes, i.e., the wave-vector mismatch. The periodic exchange of power between modes eventually ceases as the modes go through a walk-off process because of intermodal group-velocity mismatch. The observed period is directly linked to the coherence length (Eq. 5.5) and in our conditions, Lcs equals to ~2.25 cm. As the consequence of the local intensity increase, specific nonlinearity can be produced periodically, Fig. 5.22

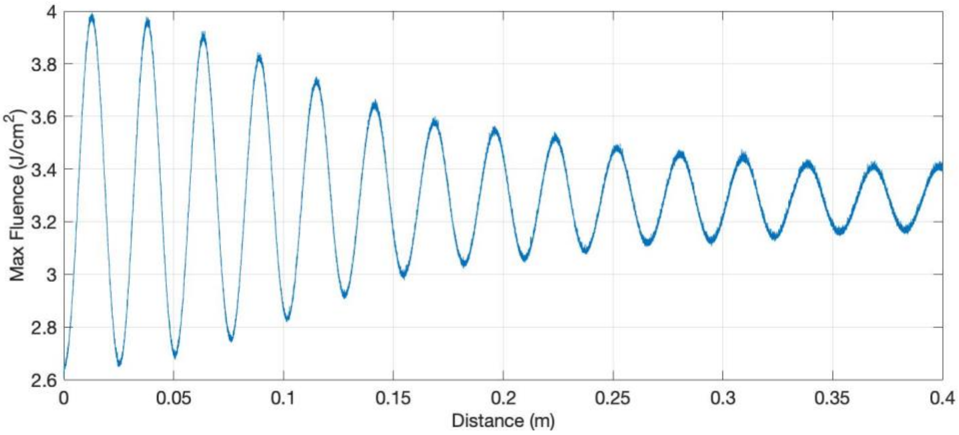

Fig. 5.22 The fluence or the intensity profile relative to the propagation distance.

In order to compare the numerical simulation at the HCC output with the experimental results, the spectrum is filtered in the shorter or longer wavelength part; λ<660nm or λ>900nm .Then, the beam profile is calculated and the fluence or the intensity profiles are plotted. In the signal part (Fig. 5.23), we can clearly see an HE12 mode as observed in the experiment. In addition, a slight asymmetry in the intensity of the ring is observed, i.e., the left part is more intense than on the right. This asymmetry was obtained when an elliptical beam profile was launched at the input. Therefore, the beam input shape also affected the power distribution of the modes. This observation also explains the experimental quality of the beam profiles.

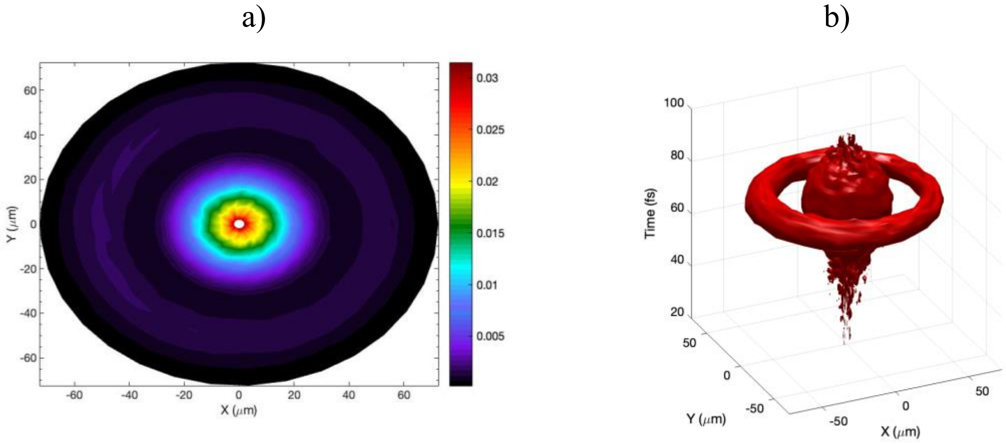

Fig. 5.23 a) Beam profile of the signal when the spectrum is filtered at a wavelength <660 nm b)Corresponding contour plot.

For the idler beam profile (Fig. 5.24), it has a shape closed to the fundamental mode, and it does not fit with the experimental observation. However, the beam profile strongly depends on the filter edge. Indeed, the center of the spectrum is mostly in the fundamental mode and therefore shifting the filter away from the middle spectra would change the profile.

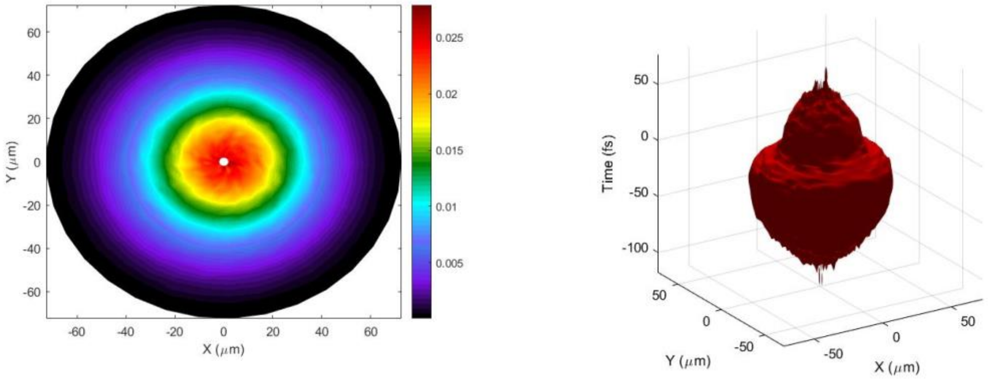
a) b)

Fig. 5.24 a) Beam profile of the idler when the spectrum is filtered at a wavelength >900 nm b) corresponding contour plot .

Accordingly, the idler profiles are shown when the filter is set for λ>920nm (Fig. 5.25a-b) and λ>930nm (Fig. 5.26c-d). For the first case, the ring structure starts to appear and an uncentered maximum is also observed, as in the experiment. When the filter is shifted even further away from the pump, the shape is clearer, with a maximum surrounded by a ring.

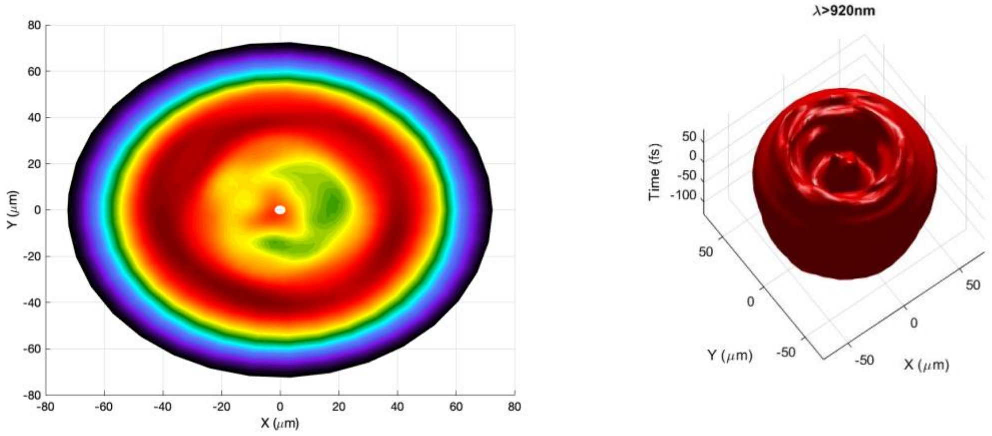
a) b)

Fig. 5.25 a) Beam profile of the idler when the spectrum is filtered at a wavelength >920 nm b) corresponding contour plot .

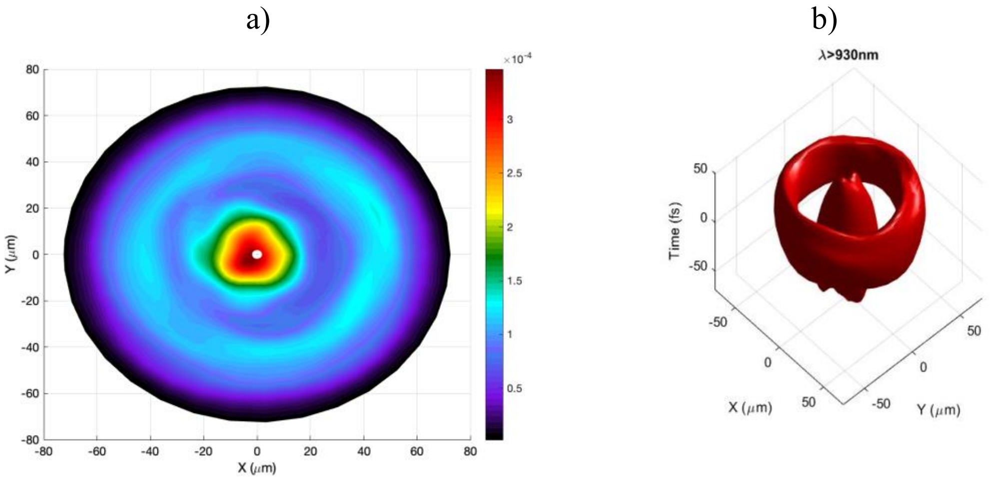

Fig. 5.26 Beam profile of the idler when the spectrum is filtered at a wavelength >930 nm b) corresponding contour plot

5.6 Conclusions

This chapter summarizes the work on the high order modes generated together with the self-phase modulated spectrum during the laser pulse propagation in a gas-filled hollow core capillary. Thus, as the first approach, the frequency generation was calculated based on a FWM process considering the phase matched with $HE_{1,m}$ modes. The analytical solution results in 4 different phase-conditions by increasing the pressure. Thus, an experimental configuration was developed to corroborate the multimode frequency generation. The signal and idler beam profiles were recorded with various experimental conditions, pressure, and pump peak power. The beam profiles of the signal and idler have several structures and do not clearly represent the fundamental mode. Since the filters select only a wide spectral range, the profile takes also into account the space-spectrum distribution. We conclude that the recorded beam profiles originated from a mixing of several beam profiles, such as the spectral part closed to the center remains within the HE_{11} mode while the edge propagates with the HE_{12} mode.

During propagation the spectrum broadens mostly through SPM and the spectral edges exhibit a HOM. In this case, the process is generated from the broadening of the pump itself, i.e., the signal and idler bands are originated from the pump. In order to enhance the conversion efficiency, the system was seeded with a broadband and weak signal. From this experiment, we observe the evolution of the signal and idler profiles in which a structured shape exhibiting a ring around a centered maximum. This is due to the contribution of several modes (HE_{11} and HE_{12}) within the signal bandwidth. The idler presents a HE_{12} shape that remains even when the signal pulses do not overlap with the pump. The stronger idler was centered at 1200 nm with a power of 3.5 μJ.

From advanced numerical simulations based on the resolution of the unidirectional pulse propagation equation generalized to structured media, we found the local intensity increases periodically. This process produces a spatial oscillation during the beam propagation, and it can be described as a power transfer between HE_{11} and HE_{12}. Moreover, the propagating light inside the fiber is directly dependent on the initial coupling conditions, i.e., of the combination of initially excited modes which can be self-modulated because of the mode beating and Kerr effect. The beam profile strongly depends on the filter position. Indeed, the center of the spectrum is mostly in the fundamental mode and therefore shifting the filter away from the middle spectrum would change the profile as we observed in the experimental beam profiles. These findings are of interest for applications involving multi-mode fiber laser development, and all-optical beam processing with multi-mode fibers. Future work aims to develop an analytical description to agree with the experimental observations.

5.7 References to Chapter 5

1. Dubietis, A. and Couairon, A. *Ultrafast Supercontinuum Generation in Transparent Solid-State Media*. (Springer Nature, 2019).
2. Ding, Y., Xu, J., Ou, H. and Peucheret, C. Mode-selective wavelength conversion based on four-wave mixing in a multimode silicon waveguide. *IET Conference Publications* **2013**, 198–200 (2013).
3. Pan, W., Jin, Q., Li, X. and Gao, S. All-optical wavelength conversion for mode-division multiplexing signals using four-wave mixing in a dual-mode fiber. *Journal of the Optical Society of America B* **32**, 2417 (2015).
4. C. Fourcade Dutin. *et al.* Post-compression of high-energy femtosecond pulses using gas ionization. *Optics Letters* **35**, 253 (2010).
5. Kolesik, M., Katona, G., Moloney, J.V., Wright, E. M. Physical factors limiting the spectral extent and band gap dependence of supercontinuum generation. *Phys. Rev. Lett* **91**, (2003).
6. Saari, P. and Reivelt, K. X-Shaped Propagation-Invariant localized light waves. *Physical Review Letters* **79**, 4135–4138 (1997).
7. Tzortzakis, S. *et al.* Formation of a conducting channel in air by self-guided femtosecond laser pulses. *Physical Review E - Statistical Physics, Plasmas, Fluids, and Related Interdisciplinary Topics* **60**, (1999).
8. Kibler, B. and Béjot, P. Discretized Conical Waves in Multimode Optical Fibers. *Physical Review Letters* **126**, (2021).
9. Poletti, F. and Horak, P. Description of ultrashort pulse propagation in multimode optical fibers. *Journal of the Optical Society of America B* **25**, 1645 (2008).
10. Nazemosadat, E., Pourbeyram, H. and Mafi, A. Phase matching for spontaneous frequency conversion via four-wave mixing in graded-index multimode optical fibers. *Journal of the Optical Society of America B* **33**, 144 (2016).
11. Poletti, F. and Horak, P. Dynamics of femtosecond supercontinuum generation in multimode fibers. *Optics Express* **17**, 6134 (2009).
12. Mussot, A., Sylvestre, T., Provino, L. and Maillotte, H. Generation of a broadband single-mode supercontinuum in a conventional dispersion-shifted fiber by use of a subnanosecond microchiplaser. *Optics Letters* **28**, 1820 (2003).
13. Köttig, F., Tani, F., Travers, J. C. and Russell, P. S. J. Self-focusing below the critical power in gas-filled hollow-core PCF. in *Optics InfoBase Conference Papers* vol. Part F81-E (2017).
14. Konorov, S. O., Fedotov, A. B. and Zheltikov, A. M. Enhanced four-wave mixing in a hollow-core photonic-crystal fiber. *Optics Letters* **28**, 1448 (2003).
15. Mecozzi, A., Antonelli, C. and Shtaif, M. Coupled Manakov equations in multimode fibers with strongly coupled groups of modes. *Optics Express* **20**, 23436 (2012).

16. Mecozzi, A., Antonelli, C. and Shtaif, M. Nonlinear propagation in multi-mode fibers in the strong coupling regime. *Optics Express* **20**, 11673 (2012).
17. Faccio, D., Grün, A., Bates, P. K., Chalus, O. and Biegert, J. Optical amplification in the near-infrared in gas-filled hollow-core fibers. *Optics Letters* **34**, 2918 (2009).
18. Tempea, G. and Brabec, T. Theory of self-focusing in a hollow waveguide. *Optics Letters* **23**, 762 (1998).
19. Crego, A., Conejero Jarque, E. and San Roman, J. Influence of the spatial confinement on the self-focusing of ultrashort pulses in hollow-core fibers. *Scientific Reports* **9**, 9546 (2019).
20. Chapman, R. T. *et al.* Modal effects on pump-pulse propagation in an Ar-filled capillary. *Optics Express* **18**, 13279 (2010).
21. Tani, F., Travers, J. C. and St.J. Russell, P. Multimode ultrafast nonlinear optics in optical waveguides: numerical modeling and experiments in kagomé photonic-crystal fiber. *Journal of the Optical Society of America B* **31**, 311 (2014).
22. Benabid, F., Knight, J. C., Antonopoulos, G. and Russell, P. S. J. Stimulated Raman Scattering in Hydrogen-Filled Hollow-Core Photonic Crystal Fiber. *Science (1979)* **298**, 399–402 (2002).
23. Poletti, F. Nested antiresonant nodeless hollow core fiber. *Optics Express* **22**, 23807 (2014).
24. Cregan, R. F. *et al.* Single-Mode Photonic Band Gap Guidance of Light in Air. *Science (1979)* **285**, 1537–1539 (1999).
25. Knight, J. C., Broeng, J., Birks, T. A. and Russell, P. S. J. Photonic band gap guidance in optical fibers. *Science (1979)* **282**, 1476–1478 (1998).
26. Alharbi, M. *et al.* Hypocycloid-shaped hollow-core photonic crystal fiber Part II: Cladding effect on confinement and bend loss. *Optics Express* **21**, 28609 (2013).
27. Snitzer, E. Cylindrical Dielectric Waveguide Modes*. *J Opt Soc Am* **51**, 491 (1961).
28. Agrawal, G. *Nonlinear Fiber Optics*. (Academic Press, 2012).
29. Hesketh, G. D., Poletti, F. and Horak, P. Spatio-Temporal Self-Focusing in Femtosecond Pulse Transmission Through Multimode Optical Fibers. *Journal of Lightwave Technology* **30**, 2764–2769 (2012).
30. Hansson, T. *et al.* Nonlinear beam self-imaging and self-focusing dynamics in a GRIN multimode optical fiber: theory and experiments. *Optics Express* **28**, 24005 (2020).

General conclusion

This thesis deals with ultra-short pulses propagating inside a gas filled hollow-core capillary to generate nonlinear effects as SPM and FWM. We studied the generation and the tunability of infrared pulses through FWM processes since ultra-short pulse-based sources with long wavelengths are becoming increasingly important tools in a wide range of applications.
The choice of a hollow-core capillary filled with gas is due to the fact that the dispersion and non-linearity are linked to the filling gas species, the core radio and the gas pressure. When one of these properties changes, the refractive index of the gas is also modified in a linear manner, which has a direct impact on the propagating pulses within the medium. The choice of parameters are the key ingredients to simultaneously achieve spectral broadening and FWM, leading to Stokes and anti-Stokes bands. Considering the FWM as one of the main processes, the combination of all degree of freedom results in a different gain with adjustable magnitude at a tunable spectral position of the bands.

A numerical model based on the integration of the nonlinear Schrödinger equation was developed to provide the full understanding of the parameters including the chirps and the relative delay between the pump and a seed. These simulations have been achieved assuming all the pulses propagate in the fundamental mode. We found that stretching the pump and signal allows to get a better interaction between the fields and improved conversion efficiency. The generated signal presents a large bandwidth whereas the idler bandwidth is narrower due to the high order dispersion terms of the fiber. Therefore, the amplifier was seeded by a broadband signal to overlap different spectral components by adding a relative delay between the chirped signal and pump pulses. This property is a good approach to control the interaction process, resulting in the generation of a tunable idler in the near infrared. The concept was implemented to an experimental configuration and the developed system produced an adjustable infrared femtosecond source between 1.2 and 1.5 μm. For example, an idler pulse was generated at 1.2 μm with a duration of ~220 fs at the direct output of the capillary. The duration could be reduced to 45 fs with phase compensators.

As a second part of this PhD activity, the nonlinear interaction in a gas filled HCC was subsequently investigated by considering the multimode content. According to the analytical description of the multimode FWM, we highlighted that it was possible to find several phase matchings conditions with several modes by adjusting the parameters (type of gas, pressure, core radius and peak power). In fact, by increasing the pressure in the previous experiment, we found that several phase-matched processes can be obtained when high order modes are considered for the signal and idler pulses. Thus, an experimental configuration was developed to analyzed more deeply the multimode FWM. We found the signal and idler beam profiles have several structures with a clear representation of higher order modes. In order to enhance conversion efficiency, the system was seeded with a broadband and weak signal. From this experiment, we observe the evolution of the signal and idler profiles in which a structured shape exhibits a ring around a centered maximum. This is due to the contribution of several modes (HE_{11} and HE_{12}) within the signal bandwidth. The idler has an HE_{12} shape which remains even when the signal pulses do not overlap with the pump. The most powerful idler was centered at 1200 nm with a power of 3.5 μW. An imaging spectrometer system was also included in the experiment together with the measurement of near and far field images. From all the

experimental results, we conclude that the spectrum broadens mostly through SPM and the spectral edges exhibit HOM from the interaction with the pump, i.e the signal and idler bands are originated from the broadening of the pump components.
However, the observed process was not in good agreement with the analytical description of the FWM, in particular with the expected gas pressure. Consequently, to investigate deeply this mechanism, we performed advanced numerical simulations based on the resolution of the unidirectional pulse propagation equation generalized to structured media. The numerical results show that the local intensity increases periodically, which produces a spatial oscillation during the beam propagation. The oscillation corresponds to a beating between modes. The energy transfer from the fundamental mode to high-order modes is due to spatial Kerr effect and the nonlinear intermodal phase-matching can cause spatio-temporal coupling when the pump is below the critical power threshold. In our case the power transfer occurs mostly between the HE_{11} and HE_{12} mode with a beating period of ~2.25 cm. An important conclusion is the simulation confirms that the beam profiles depend strongly on the selected spectral range as observed in the experiment. Indeed, the center of the spectrum is mostly in the fundamental mode while the wings are mostly in other modes. Therefore, shifting the filter away from the middle part of the spectrum would change the profile.

These results might be relevant for applications involving the development of multimode fiber lasers and for all-optical beam processing with multi-mode fibers. Future work involving more advanced models and experimental methods that includes the study of spatiotemporal dynamics. Another perspective of the research project is to focus on phased-matched FWM with HOMs in fiber with larger effective areas to enhance the tunning of the pressure range. In addition, the goal will be to seed the amplifier with a signal in a high order mode to deeply understand the nonlinear interaction with the pump and to generate an idler pulse toward the mid-infrared in the ultra-short pulse regime.

Appendix

Analytical solution of the coupled wave equations for four waves mixing in the absence of pump depletion

In the degenerate FWM case, the coupled wave equations (Eq. 3-8,3-11) are reduced to three equations for the pump, signal and idler waves. The electrical field envelopes (Eq. 3-6) of these three waves (A_1, A_2, A_3) are therefore described by:

$$\frac{dA_1}{dz} = \frac{in_2\omega_1}{c}\left[\left(f_{11}|A_1|^2 + 2\left(f_{13}|A_3|^2 + f_{14}|A_4|^2\right)\right)A_1 + 2f_{1134}A_3A_4A_1^* e^{i\Delta\beta z}\right] \quad \text{(A-1)}$$

$$\frac{dA_3}{dz} = \frac{in_2\omega_3}{c}\left[\left(f_{33}|A_3|^2 + 2\left(f_{31}|A_1|^2 + f_{34}|A_4|^2\right)\right)A_3 + f_{3411}A_1^2A_4^* e^{-i\Delta\beta z}\right] \quad \text{(A-2)}$$

$$\frac{dA_4}{dz} = \frac{in_2\omega_4}{c}\left[\left(f_{44}|A_4|^2 + 2\left(f_{41}|A_1|^2 + f_{43}|A_3|^2\right)\right)A_4 + f_{4311}A_1^2A_3^* e^{-i\Delta\beta z}\right], \quad \text{(A-3)}$$

where n_2 nonlinear index

ω_j wave frequency

f_{ij}mode field overlap

The mode field overlap integral is described as

$$f_{ijkl} = \frac{\langle F_i^* F_j^* F_k F_l \rangle}{\left[\langle |F_i|^2\rangle\langle |F_j|^2\rangle\langle |F_k|^2\rangle\langle |F_l|^2\rangle\right]^{1/2}}, \quad \text{(A-4)}$$

where F_{ijkl} is the modal field distribution of each interacting wave.

Since the signal and idler power are weak in comparison with the pump power, the XPM and FWM processes are neglected in equation (A-1). SPM and XPM involving only A2 and A3 can be removed in equation (A-2) and (A-3).

Assuming the pump remains undepleted during the FWM process, the coupled equations are as follow:

$$\frac{dA_1}{dz} = \frac{in_2\omega_1}{c}\left[f_{11}\left(|A_1|^2\right) A_1\right] \quad \text{(A-5)}$$

$$\frac{dA_3}{dz} = \frac{in_2\omega_3}{c}\left[2f_{31}\left(|A_1|^2\right)A_3 + f_{3411}\,(A_1)^2 A_4^* \;\exp(-i\Delta\beta z)\right] \quad \text{(A-6)}$$

$$\frac{d\mathbf{A}_4}{dz} = \frac{i n_2 \omega_4}{c}\left[2\mathrm{f}_{41}\left(\left|\mathrm{A}_1\right|^2\right)A_4 + \mathrm{f}_{4311}\,(\mathrm{A}_1)^2 A_3^* \exp(-i\Delta\beta z)\right] \tag{A-7}$$

Then, we assume that the four waves propagate in the fundamental mode EH$_{11}$, such as the overlap integral is constant.

$$f_{ijkl} \approx f_{ij} \approx \frac{1}{A_{eff}} \quad , \tag{A-8}$$

We also ignore the relatively small difference in optical frequency of the four waves and the nonlinear parameter γ is introduced by using the following definition

$$\gamma = \frac{n_2 \omega_1}{c A_{eff}}, \tag{A-9}$$

By replacing the non-linear parameter in Eq. (A-5) to Eq. (A-7)

$$\frac{d\mathbf{A}_1}{dz} = i\gamma\left[\left|\mathrm{A}_1\right|^2\right] A_1 \tag{A-10}$$

$$\frac{d\mathbf{A}_3}{dz} = i2\gamma\left(\left|A_1\right|^2\right)A_3 + i\gamma(A_1)^2 A_4^* \exp\,(-i\Delta\beta z) \tag{A-11}$$

$$\frac{d\mathbf{A}_4}{dz} = i2\gamma\left(\left|A_1\right|^2\right)A_4 + i\gamma(A_1)^2 A_3^* \exp\,(-i\Delta\beta z) \tag{A-12}$$

The solution of Eq. (A-10) is as follow:

$$\mathrm{A}_1(z) = A_1(0)\exp\left[i\gamma P_1 z\right] = A_1(0)\exp(i\,p_1 z)\,, \tag{A-13}$$

where, $P_1 = \left|A_1(0)\right|^2$ and $p_1 = \gamma P_1$

By substituting Eq. (A-13) in Eq. (A-11) and Eq. (A-12), we obtain two linear coupled equations for the signal and idler.

$$\frac{d\mathbf{A}_3}{dz} = i2\gamma P_1 A_3 + i\gamma A_1(0)\,A_1(0)\,A_4^* \exp i(2\gamma P_1 - \Delta\beta)\,z, \tag{A-14}$$

$$\frac{d\mathrm{A}_4}{dz} = i2\gamma P_1 A_4 + i\gamma A_1(0)\,A_1(0)\ A_3^*\ \exp i(2\gamma P_1 - \Delta\beta)\,z, \qquad \text{(A-15)}$$

Then we use the following notation:

$$\frac{d\mathbf{A_k}}{dz} = ipA_k + \ ir\ \exp(\,i\,qz)\,A_l^*, \qquad \text{(A-16)}$$

where

$$p = 2\gamma P_1 = 2\,p_1$$
$$r = \gamma\ [A_1(\,0)\,]^2$$
$$q = 2p_1 - \Delta\,\boldsymbol{\beta}$$

$$k = 3{,}4 \qquad l = 7 - k$$

To solve this equation, we introduce the following transformation

$$B_k = A_k \exp(\,-ip)\,z$$
$$A_k = B_k \exp\,(\,ip)\,z$$
$$A_l^* = B_l^* \exp(\,-ip)\,z$$

After the first derivate of B_k

$$\frac{d\boldsymbol{B}_k}{dz} = \left[A_k\right]\left[(\,-ip)\,\exp(\,-ipz)\,\right] + \left[\frac{dA_k}{dz}\right]\left[\exp(\,-ipz)\,\right], \qquad \text{(A-17)}$$

Substituting Eq. (A-16) in Eq. (A-17)

$$\frac{dB_k}{dz} = [A_k]\left[(\,-ip)\ \exp(\,-ipz)\,\right] + \left[ipA_k + \ irA_l^*[\exp(\,iqz)\,]\right]\left[\exp(\,-ipz)\,\right]$$

$$\frac{dB_k}{dz} = [\ irA_l^*\,[\exp\ (\ iqz)\ ]\left[\exp(\ -\ iz)\ \right]$$

Writing the equation only as a function of B_k.

$$\frac{d\boldsymbol{B}_k}{dz} = ir\left[B_l^*\exp\,(\,-\,ipz)\,\right]\left[\exp\,(\,i\mathrm{q}z)\,\right]\left[\exp\,(\,-\,ipz)\,\right] \qquad \text{(A-17)}$$

Then for k=3

$$\frac{dB_3}{dz} = \ irB_4^*\left[\exp - i(\,2\gamma P_1)\,z\right][\exp\,i\left(2p_1 - \Delta\beta\right)]\left[\exp - i(\,2\gamma P_1)\,z\right]$$

Then, the effective phase matched condition is given as being the exponential term:

$$\kappa=\gamma 2P_1+\Delta\beta \tag{A-18}$$

To resolve the Eq. (A-17), the second derivate of $\boldsymbol{B_3}$ is applied

$$\frac{dB_3}{dz}=ir\left[B_4^*\right]\left[\exp(-i\kappa z)\right] \tag{A-19}$$

$$\frac{d^2B_3}{dz^2}=ir\exp(-i\kappa z)\left[\frac{dB_4^*}{dz}\right]-i\kappa\left[\frac{dB_3}{dz}\right], \tag{A-20}$$

replacing $\frac{dB_4^*}{dz}$, in Eq. (A-20)

$$\frac{d^2B_3}{dz^2}=ir\exp(-i\kappa z)\left[-\boldsymbol{ir}[\boldsymbol{B}_3][\mathbf{exp}(i\kappa z)]\right]-i\kappa\left[\frac{dB_3}{dz}\right]$$

$$\frac{d^2B_3}{dz^2}=r^2[B_3]-i\kappa\left[\frac{dB_3}{dz}\right]$$

$$\frac{\boldsymbol{d^2B_3}}{\boldsymbol{dz^2}}=\left[\gamma^2\boldsymbol{P}_1(0)^2\right][\boldsymbol{B}_3]-\mathbf{i}\,\boldsymbol{\kappa}\left[\frac{\boldsymbol{dB_3}}{\boldsymbol{dz}}\right] \tag{A-21}$$

$$\frac{\boldsymbol{d^2B_4^*}}{\boldsymbol{dz}}=\left[\gamma^2\boldsymbol{P}_1(0)^2\right][\boldsymbol{B}_4^*]+\mathbf{i}\,\boldsymbol{\kappa}\left[\frac{\boldsymbol{dB_4^*}}{\boldsymbol{dz}}\right] \tag{A-22}$$

To resolve the Eq. (A-21) and Eq. (A-22), we applied the next transformation

$$C_k=B_k\exp i\left(\kappa/2\right)z$$

By replacing $B_k=A_k\exp(-ipz)$

$$C_k=A_k\left[\exp i\,(\kappa/2-p)\,z\right]$$
$$C_l^*=A_l^*\left[\exp-i(\kappa/2-p)\,z\right]$$

By making the first derivation.

$$\frac{\boldsymbol{dC_k}}{\boldsymbol{dz}}=\boldsymbol{i}\left[\frac{\boldsymbol{\kappa}}{2}\right]\boldsymbol{C}_k+\boldsymbol{ir}\left[\boldsymbol{C}_l^*\right],$$

By using the transformation for the propagation problems. (A1.1) [1], it leads to:

$$\frac{d^2C_k}{dz^2} - g^2(z)\,C_k = 0, \tag{A-23}$$

$$g(z)^2 = r^2 - \frac{(\kappa)^2}{4} + \frac{i\kappa'}{2},$$

When g is constant the solution is a linear combination of the exponential $\exp(gz)$ and $\exp(-gz)$. That represents a complex propagation constant, where its real part corresponds to the gain or attenuation, while the imaginary part corresponds to the phase. In this case we considered g as constant over a short length. Also is considered the non-pump depletion. Therefore, the parametric gain coefficient is given by:

$$g^2 = \left(\gamma^2 P_1(0)^2\right) - \left(\frac{\kappa}{2}\right)^2, \tag{A-24}$$

The signal and idler output fields are obtained as a linear contribution, so the general solution of Eq. (A-23) is the form:

$$C_K(z) = a_k\left(e^{g_k z}\right) + b_k\left(e^{-g_k z}\right) \tag{A-25}$$

To calculate the constant a_k *and* b_k, we used the following equations.

$$C_K(0) = a_k + b_k, \tag{A-26}$$

$$\frac{C(z)'_k}{g_k} = \left[a_k\left(e^{g_k z}\right)\right] - \left[b_k\left(e^{-g_k z}\right)\right], \tag{A-27}$$

$$b_k = \left[\frac{1}{2}\right]\left[C_K(0) - \frac{C(0)'_k}{g_k}\right] \quad a_k = \left[\frac{1}{2}\right]\left[C_K(0) + \frac{C(0)'_k}{g_k}\right], \tag{A-28}$$

Replacing Eq. (A-28) into Eq. (A-25)

$$C_K(z) = C_K(0)\left[\cosh(gz)\right] + \frac{C(0)'_k}{g_k}\left[\sinh(gz)\right], \tag{A-29}$$

By using the initial condition for the signal and idler (z=0) in the following expression and the solution are substituting in Eq. (A-29)

$$C(0)_k = A_k(0)$$

$$\frac{dC_k(0)}{dz} = i\left[\frac{\kappa}{2}\right] A_k(0) + ir\left[A_l^*(0)\right]$$

$$C_K(z) = A_k(0)\left[\cosh(gz)\right] + \frac{i}{g}\left[\left[\frac{\kappa}{2}\right] A_k(0) + r\left[A_l^*(0)\right]\right]\left[\sinh(gz)\right], \tag{A-30}$$

This corresponds to its matrix form:

$$\begin{bmatrix} C_K(z) \\ C_l^*(z) \end{bmatrix} = \begin{bmatrix} \cosh(gz) + \frac{i}{g}\frac{\kappa}{2}\sinh(gz) & \frac{ir}{g}\sinh(gz) \\ -\frac{ir}{g}\sinh(gz) & \cosh(gz) - \frac{i}{g}\frac{\kappa}{2}\sinh(gz) \end{bmatrix} \begin{bmatrix} A_K(0) \\ A_l^*(0) \end{bmatrix} \tag{A-31}$$

From the matrix solution, the electric field $\boldsymbol{A}_k(z)$ at distance z is the form:

$$\boldsymbol{A}_k(z) = \boldsymbol{C}_K(z)\exp\left[i\left(p - \frac{\kappa}{2}\right)z\right] \tag{A-32}$$

Substituting Eq. (A-30) into Eq. (A-32), the signal and idler field are:

$$A_k(z) = \left\{A_k(0)\left[\left[\cosh(gz)\right] + \frac{i}{g}\left[\frac{\kappa}{2}\right]\left[\sinh(gz)\right]\right] + \left[\frac{ir}{g}\left[\sinh(gz)\right]\right]\left[A_l^*(0)\right]\right\}\exp\left[i\left(p - \frac{\kappa}{2}\right)z\right] \tag{A-33a}$$

$$A_l^*(z) = \left\{A_l^*(0)\left[\left[\cosh(gz)\right] - \frac{i}{g}\left[\frac{\kappa}{2}\right]\left[\sinh(gz)\right]\right] - \left[\frac{ir}{g}\left[\sinh(gz)\right]\right]\left[A_k(0)\right]\right\}\exp\left[-i\left(p - \frac{\kappa}{2}\right)z\right] \tag{A-33b}$$

Considering the amplitude of the idler at the input fiber is zero, $A_4(0) = 0$. The signal and idler gain are respectively.

$$h_3 = \frac{A_3(z)}{A_3(0)} = \left\{\left[\cosh(gz)\right] + \left[\frac{i}{g}\frac{\kappa}{2}\right]\left[\sinh(gz)\right]\right\}\exp\left[i\left(2\gamma P_1 - \frac{\kappa}{2}\right)z\right] \tag{A-34a}$$

$$h_4 = \frac{A_4(z)}{A_3^*(0)} = \left\{ i\frac{r}{g}\left[\sinh(gz)\right]\right\} \exp\left[i\left(2\gamma P_1 - \frac{\kappa}{2}\right) z\right] \tag{A-34b}$$

The signal and idler power $P_3 = \left|A_3\right|^2$ grows with z as:

$$P_3(z) = P_3(0)\left[1 + (1 + \kappa^2/4g^2)\ \sinh^2(gz)\right], \tag{A-35a}$$

$$P_4(z) = P_3(0)\left[(1 + \kappa^2/4g^2)\ \sinh^2(gz)\right], \tag{A-35b}$$

Signal to-Idler power conversion efficiency $G_4(z) = \left|h_4(z)\right|^2$ and the signal power $G_3(z) = \left|h_3(z)\right|^2$

$$G_4(z) = \left|\frac{r}{g}\left[\sinh(gz)\right]\right|^2, \tag{A-36a}$$

$$G_3(z) = G_4(z) + 1 \tag{A-36b}$$

References

[1] M. E. Marhic, *Fiber Optical Parametric Amplifiers, Oscillators and Related Devices* (Cambridge University Press, 2007), Vol. 9780521861.

SPIM
école doctorale **sciences pour l'ingénieur et microtechniques**

UBFC
UNIVERSITÉ
BOURGOGNE FRANCHE-COMTÉ

Université Bourgogne Franche-Comté
32, avenue de l'Observatoire
25000 Besançon, France